



**HAL**  
open science

# Propagation of Galactic Cosmic Rays and Dark Matter indirect Detection

Timur Delahaye

► **To cite this version:**

Timur Delahaye. Propagation of Galactic Cosmic Rays and Dark Matter indirect Detection. Mathematical Physics [math-ph]. Université de Savoie; Università degli studi di Torino, 2010. English. NNT: . tel-00530422v1

**HAL Id: tel-00530422**

**<https://theses.hal.science/tel-00530422v1>**

Submitted on 28 Oct 2010 (v1), last revised 23 Nov 2010 (v3)

**HAL** is a multi-disciplinary open access archive for the deposit and dissemination of scientific research documents, whether they are published or not. The documents may come from teaching and research institutions in France or abroad, or from public or private research centers.

L'archive ouverte pluridisciplinaire **HAL**, est destinée au dépôt et à la diffusion de documents scientifiques de niveau recherche, publiés ou non, émanant des établissements d'enseignement et de recherche français ou étrangers, des laboratoires publics ou privés.



# THESIS

submitted for the degrees of

DOCTEUR DE L'UNIVERSITÉ DE SAVOIE  
DOTTORE DELL'UNIVERSITÀ DEGLI STUDI DI TORINO

by

TIMUR DELAHAYE

## Propagation of Galactic Cosmic Rays and Dark Matter indirect Detection

Defended publicly the 7<sup>th</sup> of July 2010 with the authorisation of the referees:

Prof. Carlos MUÑOZ    Referee  
Prof. Günter SIGL    Referee

in front of the following jury :

Prof. Jean ORLOFF            President  
Prof. Nicolao FORNENGO    Ph.D. advisor  
Prof. Martin LEMOINE  
Prof. Carlos MUÑOZ           Referee  
Prof. Pierre SALATI          Ph.D. advisor  
Prof. Günter SIGL            Referee  
Prof. Joseph SILK



*Canim anneannemin anisina*



# Contents

<b>Acknowledgments</b>	<b>ix</b>
<b>Introduction</b>	<b>1</b>
<b>1 Dark matter in the Standard Model of Cosmology</b>	<b>5</b>
1.1 Friedmann-Lemaître-Robertson-Walker’s Cosmology . . . . .	6
1.1.1 The formalism . . . . .	6
1.1.2 The possible scenarios . . . . .	8
1.1.2.1 The open Universe . . . . .	10
1.1.2.2 The closed Universe . . . . .	10
1.1.2.3 The critical Universe . . . . .	10
1.1.3 Observational results . . . . .	10
1.1.3.1 The Hubble parameter . . . . .	10
1.1.3.2 $\Omega_\gamma$ . . . . .	11
1.1.3.3 $\Omega_T$ . . . . .	11
1.1.3.4 $\Omega_m$ . . . . .	12
1.1.3.5 $\Omega_\Lambda$ . . . . .	13
1.2 Evidences for dark matter . . . . .	14
1.2.1 On cosmological scales . . . . .	14
1.2.1.1 Constraining dark matter with relic density . . . . .	15
1.2.1.2 Constraining dark matter with Big Bang Nucleosynthesis . . . . .	17
1.2.1.3 Large Scale Structures formation . . . . .	17
1.2.2 On the scale of clusters of galaxies . . . . .	19
1.2.3 On galactic scales . . . . .	20
1.3 Escape ways from the dark matter problem . . . . .	21
1.3.1 Modifying gravity . . . . .	21
1.3.2 Changing cosmological paradigm . . . . .	21
<b>2 The Standard Model of Particle Physics and beyond</b>	<b>23</b>
2.1 The Standard Model of Particle Physics . . . . .	24
2.2 Problems of the Standard Model of Particle Physics . . . . .	28
2.2.1 Muon anomalous momentum . . . . .	28
2.2.2 Neutrinos . . . . .	28
2.2.3 Matter antimatter asymmetry . . . . .	29
2.2.4 Dark matter . . . . .	29

2.2.5	Theoretical problems . . . . .	29
2.2.5.1	Quantum Chromodynamics and the strong $CP$ problem . . . . .	30
2.2.5.2	Parameters problem . . . . .	30
2.2.5.3	Unification . . . . .	30
2.2.5.4	Hierarchy problem . . . . .	31
2.3	Supersymmetry . . . . .	32
2.4	Extra-Dimensions . . . . .	34
2.4.1	Large extra dimensions . . . . .	34
2.4.2	Warped extra dimensions . . . . .	34
2.4.3	Universal Extra Dimensions . . . . .	35
2.5	Other models . . . . .	35
2.5.1	Little Higgs . . . . .	35
2.5.2	Technicolor . . . . .	36
2.6	Phenomenological models . . . . .	36
2.6.1	Minimal Dark Matter . . . . .	36
2.6.2	Exciting Dark Matter . . . . .	36
<b>3</b>	<b>Cosmic Rays</b> . . . . .	<b>39</b>
3.1	A short history of Cosmic Rays . . . . .	40
3.1.1	Discovery . . . . .	40
3.1.2	A tool for particle physics . . . . .	40
3.1.3	A new era of astrophysics . . . . .	41
3.2	Modern Cosmic Ray detection methods . . . . .	41
3.2.1	Balloons . . . . .	41
3.2.1.1	CREAM . . . . .	41
3.2.1.2	ATIC . . . . .	41
3.2.2	Satellites . . . . .	42
3.2.2.1	PAMELA . . . . .	42
3.2.2.2	Fermi . . . . .	42
3.2.2.3	AMS . . . . .	43
3.2.2.4	CALET . . . . .	43
3.2.3	Ground-based detectors . . . . .	44
3.2.3.1	HESS . . . . .	44
3.2.3.2	KASCADE Grande . . . . .	45
3.2.3.3	Pierre Auger . . . . .	45
3.2.3.4	LOFAR . . . . .	46
3.3	Current understanding of Cosmic Rays . . . . .	46
3.3.1	Energy spectrum . . . . .	46
3.3.2	Composition . . . . .	47
3.3.3	Isotropy . . . . .	49
3.3.4	Greisen-Zatsepin-Kuzmin cut-off . . . . .	49

<b>4</b>	<b>Cosmic Ray sources</b>	<b>53</b>
4.1	Primary Cosmic Rays . . . . .	54
4.1.1	Supernova remnants . . . . .	55
4.1.1.1	Fermi acceleration mechanism . . . . .	55
4.1.1.2	Released cosmic ray energy spectrum . . . . .	57
4.1.2	Pulsars . . . . .	61
4.1.3	Distribution in the Milky Way . . . . .	63
4.2	Secondary Cosmic Rays . . . . .	64
4.2.1	Production cross-sections . . . . .	64
4.2.1.1	Pion to muon . . . . .	66
4.2.1.2	Muon to electron . . . . .	67
4.2.1.3	Pion to electron . . . . .	67
4.2.1.4	Kaon to electron . . . . .	69
4.2.1.5	Proton to pion (or kaon) . . . . .	70
4.2.1.6	Dealing with other particles . . . . .	72
4.2.1.7	Comparison . . . . .	73
4.2.2	Projectile cosmic ray fluxes . . . . .	73
4.2.3	Galactic distribution of targets . . . . .	76
4.3	Exotic Cosmic Rays . . . . .	76
4.3.1	Dark matter . . . . .	76
4.3.1.1	Annihilating dark matter . . . . .	76
4.3.1.2	Decaying dark matter . . . . .	77
4.3.1.3	Energy spectra . . . . .	77
4.3.1.4	Smooth distribution of dark matter . . . . .	78
4.3.1.5	Clumps . . . . .	80
4.3.1.6	Intermediate Mass Black Holes . . . . .	82
4.3.2	GRB, AGN etc. . . . .	82
<b>5</b>	<b>Propagation</b>	<b>87</b>
5.1	Diffusion model . . . . .	88
5.1.1	The model . . . . .	88
5.1.2	The propagation parameters . . . . .	91
5.2	Energy losses . . . . .	92
5.2.1	Energy losses in the disc . . . . .	92
5.2.2	Energy losses everywhere: radiative losses . . . . .	93
5.2.2.1	Synchrotron . . . . .	93
5.2.2.2	Inverse Compton . . . . .	95
5.2.3	Comparisons . . . . .	97
5.3	Semi-analytical solutions of the diffusion equations . . . . .	97
5.3.1	Smooth distribution of sources everywhere in the halo . . . . .	99
5.3.1.1	Bessel–Fourier expansion technique . . . . .	100
5.3.1.2	The Green functions technique . . . . .	102
5.3.2	Smooth distribution of sources in the disc only . . . . .	103
5.3.2.1	Radial propagators . . . . .	104

5.3.2.2	Vertical propagators . . . . .	105
5.3.3	Time dependent solution . . . . .	106
5.4	Solar modulation . . . . .	108
5.5	Improving the model . . . . .	110
5.5.1	Boundary conditions . . . . .	110
5.5.2	Anisotropic propagation . . . . .	110
5.5.3	Time dependence . . . . .	111
<b>6</b>	<b>Positrons and electrons</b>	<b>115</b>
6.1	Secondaries . . . . .	116
6.1.1	The electron and positron fluxes and their uncertainties . . . . .	116
6.1.1.1	Propagation . . . . .	116
6.1.1.2	Source . . . . .	118
6.1.1.3	Local bubble . . . . .	120
6.1.1.4	Proton retro-propagation . . . . .	121
6.1.1.5	Diffusive reacceleration and full energy losses . . . . .	121
6.1.2	Discussion . . . . .	124
6.2	Primaries . . . . .	124
6.2.1	Astrophysical sources . . . . .	124
6.2.1.1	Smooth distribution of sources . . . . .	126
6.2.1.2	Local supernova remnants . . . . .	129
6.2.1.3	Local pulsars . . . . .	136
6.2.2	Dark matter . . . . .	137
6.2.2.1	The Galactic halo . . . . .	138
6.2.2.2	Decaying dark matter . . . . .	147
6.2.2.3	The clumps . . . . .	148
6.3	Discussion . . . . .	149
<b>7</b>	<b>Photons</b>	<b>155</b>
7.1	Gamma rays . . . . .	156
7.1.1	Gamma rays from $\pi^0$ decay . . . . .	156
7.1.1.1	Production cross-section . . . . .	157
7.1.1.2	Primary cosmic ray flux . . . . .	159
7.1.1.3	Target distribution . . . . .	161
7.1.1.4	Results . . . . .	161
7.1.2	Gamma rays from Bremsstrahlung . . . . .	162
7.1.3	Gamma rays from inverse Compton scattering . . . . .	165
7.1.4	Gamma rays from radio isotopes . . . . .	166
7.1.5	The extra galactic component . . . . .	167
7.1.6	Gamma rays from dark matter . . . . .	167
7.2	Radio emission from synchrotron radiation . . . . .	171

<b>8</b>	<b>Dark matter indirect detection</b>	<b>177</b>
8.1	Recent Data . . . . .	178
8.1.1	PAMELA . . . . .	178
8.1.2	ATIC . . . . .	179
8.1.3	Fermi . . . . .	180
8.1.4	HESS . . . . .	180
8.1.5	WMAP . . . . .	180
8.2	An optimistic interpretation . . . . .	180
8.3	A more realistic interpretation . . . . .	185
	<b>Conclusion</b>	<b>195</b>
<b>A</b>	<b>Technical details in cosmology</b>	<b>197</b>
A.1	Distances in Robertson-Walker metric . . . . .	197
A.1.1	Angular distance . . . . .	197
A.1.2	Luminosity distance . . . . .	198
A.1.3	Hubble distance . . . . .	199
A.2	Computing the relic density . . . . .	200
<b>B</b>	<b>Technical details concerning propagation</b>	<b>203</b>
B.1	Bessel expansions . . . . .	203
B.2	Primary cosmic rays retro-propagation . . . . .	205
B.3	Taking into account diffusive reacceleration . . . . .	207
B.3.1	The electron case . . . . .	207
B.3.2	The proton case . . . . .	209
B.4	Taking into account a local bubble . . . . .	209
B.5	The radial image . . . . .	210
B.6	Adiabatic losses . . . . .	213
<b>C</b>	<b>Dark matter distribution</b>	<b>215</b>
C.1	The Galactic centre . . . . .	215
C.2	Determining the local dark matter density . . . . .	216
C.3	Boundary conditions of the diffusion equation and dark matter . . . . .	217
<b>D</b>	<b>Description of the Milky Way</b>	<b>219</b>
D.1	Gas distribution . . . . .	219
D.1.1	Molecular gas distribution . . . . .	219
D.1.2	Atomic gas distribution . . . . .	220
D.1.3	Ionised gas distribution . . . . .	220
D.1.4	Thin disc approximation . . . . .	221
D.2	The Galactic magnetic field . . . . .	222
D.3	Determining the distance of the Sun to the Galactic centre . . . . .	224



# Acknowledgments

I would like to thank Patrick Aurenche and Fawzi Boudjema, former and present directors of LAPTh for hosting me in their institution for my thesis. I am also grateful to Prof. Mauro Anselmino, head of the theoretical physics department of the university of Turin for allowing a co-supervision of my doctorate at his institution. I thank Prof. Giovanni Fiorentini and the scientific council of IDAPP for allowing me to take part to the very nice joint doctorate program they organise.

During these last three years, I have attended many schools and conferences and this would not have been possible without the financial support of many organisations, I am very grateful to CNRS, Université de Savoie, the Région Rhône-Alpes, the GDR SuSy, PCHE and Terascale, INFN, the doctorate school PHAST, the network Universenet, IDAPP and to the organisers of the rencontres de Moriond and of ISSCSMB'09. More generally I am extremely thankful to the French state which financially supported me for seven years. I have been extremely lucky to benefit from such a generous system.

I am very thankful to Profs. Carlos Muñoz and Günther Sigl, who very kindly accepted to refer this work. I also thank Prof. Joseph Silk, Jean Orloff and Martin Lemoine who accepted to attend my thesis defence. I am all the more grateful to Martin Lemoine since he is the one who advised me to contact Pierre Salati with his recommendation while I was looking for a Ph.D.

Of course my warmest thanks go to Pierre Salati and Nicolao Fornengo, my Ph.D. advisors. This is also the place to thank all the people who showed me the path in the dark forest that physics is: Julien Lavalley, Roberto Lineros, Fiorenza Donato, Céline Bøehm, Armand Fiasson, Pierre Brun, David Maurin, Richard Taillet. Thank you for all the scientific discussions we had and which taught me so much. I especially thank Roberto and Armand who were so patient in teaching me how to struggle with gnuplot, root and the very scary Mesocenter for computation *MUST*.

I would like to thank Richard Taillet and Céline Bøehm for having corrected parts of this work.

Avant toute chose, je remercie très sincèrement les différents professeurs qui m'ont donné le goût des sciences depuis ma tendre enfance jusqu'aux plus récentes années: mesdames Chekroun, Magail, Margaria et Berline, mademoiselle Lebœuf, messieurs Lebsir, Deville, Fagebaum, Frajmann, Fleury, Basdevant, Rougé, Lemoine, Langlois, Aspect, Dauxois, Gawedzki, Salati et tant d'autres... Merci aussi à Gilles Chabrier et Chrisophe Winidoerffer qui m'ont aidé à faire mes premiers pas dans la recherche.

Je souhaiterais remercier ceux qui ont contribué au fait que mon séjour à Annecy s'est si

bien déroulé. Je pense bien évidemment à tous ceux qui mettent une si bonne ambiance au LAPTh, Éric, Fawzi, Richard, Pierre, Livia<sup>a</sup>...

Merci aussi à ceux qui m'ont accueilli au sein des Dahus : Laurent, Éric, Geneviève, Dominique, Guy, Anne et tous les autres qui m'ont emmené skier dans les belles montagnes des Aravis. Je remercie également les membres de l'AVOC avec lesquels je me suis bien amusé et qui m'ont poussé à me dépasser : les Denis, Sandrine, Émilie, Romain, Benoît, Xavier, Gilles, Bertrand, tous les autres et surtout la dream team de la Saintélyon : Marion, Iro et Virginie<sup>b</sup>.

Je remercie mes camarades de galère, ceux qui étaient dans les chiourmes avant la mienne : Grégory, Nans, Samuel et Wessel, ceux qui étaient dans la mienne : Victor et Guillaume et aussi les petits qui suivent : Daniel et Guillaume. Les premiers pour m'avoir conseillé et surtout avoir été de bons amis, les derniers pour m'avoir laissé vieux-chouffiser tout mon soûl sans jamais se plaindre.

Bien sûr je remercie également les petits LAPPins, auxquels on pardonne volontiers d'être expérimentateurs tellement ils sont sympas : Olivier, Mathieu, Julien, Florent, Loïc, Dudu, Louis, Nelly<sup>c</sup>, Xavier, Dimitra, Armand et Iro. Une mention spéciale pour Magali.

Je remercie tous ceux qui m'ont aidé à essayer de faire mentir Mme de Stael<sup>d</sup> : Caroline, Bénédicte, Rachel, Armand et Iro<sup>e</sup>. Ça n'était pas facile mais nous avons réussi à nous amuser à Annecy !

Merci à ceux qui n'ont pas hésité à braver des distances astronomiques pour venir me rendre visite : Florent L., Layane, Damien et Sandrine, Maïté, Guillaume, Clément, Delphine, Fabrice et Matthieu.

Je remercie aussi mon super oncle qui m'a prêté sa Fiat Panda qui a tant fait mon succès, qui s'est si gentiment soucié de moi et surtout qui m'a fait plein de cousins plus géniaux les uns que les autres. Et mes grands-parents qui m'ont souvent envoyé leur amour alors même que je ne les visitais pas assez régulièrement.

Enfin je remercie ceux avec lesquels j'ai partagé mon appartement à Annecy : Arnaud puis Guillaume. Ça a été un vrai plaisir de vivre avec vous.

Ringrazio anche la *mafia straniera* che mi ha immediatamente accettato nel suo gruppo : Victoria, Mariana, Jan, David, Dario, Alison, Bruna, Bianca, Maria-Pilar... grazie per le pizze, gli aperitivi, il carnevale d'Ibrea, i tulipani e tutte le feste che abbiamo fatto insieme.

Ringrazio i carissimi ragazzi *underground* che hanno avuto la pazienza di insegnarmi l'italiano e la gentilezza di farmi scoprire la loro bella città di Torino. È stato un piacere mangiare ogni giorno con voi e discutere senza fine di caffè e di tutte le lingue latine. Grazie a Stefano, Daniele, Parsa, Stefano, Ana, Iván, Riccardo, Diogo, Mario e Roberto. Grazie ancora di più a Riccardo per i concerti e a Daniele per il meraviglioso fine settimana a Genova.

Grazie anche a Silvia di non odiarmi dopo la formidabile scuola estiva a Karlsruhe.

---

<sup>a</sup>o è Lidia ? non mi ricordo mai.

<sup>b</sup>Je continue à penser que ta blessure n'existe pas.

<sup>c</sup>hop ! dans le même panier !

<sup>d</sup>Les grandes villes seules conviennent aux personnes qui sortent de la règle commune, quand c'est en société qu'elles veulent vivre ; comme la vie y est variée, la nouveauté y plaît ; mais dans les lieux où l'on a pris une assez douce habitude de la monotonie, l'on n'aime pas à s'amuser une fois, pour découvrir que l'on s'ennuie tous les jours. *in Corinne ou l'Italie*.

<sup>e</sup>Vous êtes là bien souvent dans ces pages vous deux, c'est louche.

In fine grazie ai vini piemontesi e toscani, ai formaggi buonissimi, ai musei e alla gente che fanno del'Italia un paese così piacevole.

Ve tabii ki aileme teŝekkür etmek istiyorum. Beni her zaman aşkla beslediler, bana daima inandılar ve tüm ihtiyaçlarımı karşıladılar. Dedeciğim, anneciğim, babacığım, Nilciğim, her zaman göstermezsem de, sizleri çok seviyorum.



# Introduction

The ability to quote is a serviceable substitute for wit.

*William Somerset Maugham*

Since the discovery by Zwicky of the mismatch between luminous and gravitational masses of local galaxy clusters in 1933 [2], the issues of missing masses in the Universe have gone increasing in number. What Zwicky has called dark matter is still today evading detection from our instruments, however the new generation of experiments is giving us new hopes of shedding light on this darkness.

Three different methods have been proposed so far. The first one is the production at colliders, though this can prove that a particle having the good properties to be a dark matter candidate exist, such an man-made production will never prove that this particle is actually what dark matter is made of, nor will it give us its amount in the Universe. The Tevatron, the Large Hadron Collider and the future International Linear Collider, among other things, aim at this detection. The second method is called direct detection and consist in measuring the recoil energy of protons or neutrons impinged by Galactic dark matter particle passing through the Solar system, the Earth and our detectors. Many experiments are dedicated to this mission: DAMA–Libra, CDMS, Edelweiss, Xenon, Cogent... The problem is that these experiments require extreme shielding and background rejection, so even in the case that a signal is detected, suspicion of misidentification are very difficult to dismiss. In fact, the DAMA–Libra experiment does not any background rejection but rather looks for a modulation in the overall signal, so their problem is more that it is difficult to prove that their signal actually comes from dark matter. Moreover, this kind of detection would give little information about the properties of dark matter, except it spin dependent and spin independent coupling to hadrons. The third and last detection scheme the indirect detection, consists in looking not for the dark matter particle itself but rather for its annihilation or decay stable products. This can express itself as a neutrino population coming from dark matter particle trapped at the center of the Sun or the Earth, as high energy photons coming from regions where dark matter is dense (dwarf spheroidal galaxies, the Galactic center, intermediate mass black holes...) or as high energy charged particles coming from all over the Galaxy.

A very nice idea, first proposed by Silk & Srednicki [1], to detect dark matter is to look for its decay or annihilation products in the high energy particles travelling through space that we call cosmic rays: the so called dark matter *indirect* detection. If this detection mode is extremely interesting, because it would give us a wonderful insight to the deep nature of dark matter, it is however handicapped by the fact that our understanding of cosmic rays is far from perfect. For this reason it has been proposed to look preferentially to anti matter cosmic rays. Indeed, dark matter annihilation (or decay) should produce as much matter as anti matter, however the astrophysical background is expected to be much lower for anti matter, hence easing the emergence of a signal.

The target of this thesis has been to contribute, as much as I could, to the development and refinement of the diffusion model of Galactic cosmic rays, that aims to compute the flux of these high energy particles and to understand their sources. This means to predict the dark matter signal but also to understand the astrophysical background and to size the uncertainties related to it. Initially, this work was meant to concentrate mainly on positrons which has long been considered a promising channel. However the recent harvest of data did not concern positrons fluxes but either the positron fraction or the sum of electrons and positrons, this rose the need to understand electrons as well. Interpreting the recent data put light on the question of locality: is the cosmic ray electron flux the same everywhere in the Milky Way? Are we

sitting at the best place to see a dark matter signal to emerge from the background? Is not the Solar environment and especially its wind and magnetic field, hiding important information from us? Obviously, it is technically impossible to measure cosmic ray fluxes somewhere else than where we sit. This fact notwithstanding, photons emitted by cosmic rays radiating while they travel in the Galaxy, can bring us information about what is happening out there. This is even more relevant now that the Fermi  $\gamma$  telescope and the Planck infra-red observatory are on orbit.

After explaining the modern motivations to look for dark matter in chapters 1 and 2 from cosmology and particle physics point of view respectively, this work presents our current knowledge of cosmic rays in chapter 3. In chapter 4 and the following it only focuses on *low* energy cosmic rays, *id est* those that have an energy lower than  $\sim 10$  TeV, which are the only one relevant for dark matter indirect detection. Chapter 4 describes the sources of Galactic cosmic rays, while chapter 5 presents the the model used to describe their propagation in the Galaxy. It then focuses on positrons and electrons in chapter 6 and on  $\gamma$  rays in chapter 7. Finally chapter 8 sums up our current status in indirect dark matter research, and provides some ideas to start constraining dark matter models.

## Bibliography

- [1] Silk, J. & Srednicki, M. 1984, Phys. Rev. Lett., 53, 624 2
- [2] Zwicky, F. 1937, ApJ, 86, 217 2



# Chapter 1

## Dark matter in the Standard Model of Cosmology

Ogni punto d'ognuno di noi coincideva con ogni punto di ognuno degli altri in un punto unico che era quello in cui stavamo tutti. [...] Si stava così bene tutti insieme, così bene, che qualcosa di straordinario doveva pur accadere. Bastò che a un certo momento [la signora Phi(i)Nk<sub>0</sub>] dicesse: - Ragazzi, avessi un po' di spazio, come mi piacerebbe farvi le tagliatelle! - E in quel momento tutti pensammo allo spazio che avrebbero occupato le tonde braccia di lei muovendosi avanti e indietro con il mattarello sulla sfoglia di pasta, il petto di lei calando sul gran mucchio di farina e uova che ingombrava il largo tagliere mentre le sue braccia impastavano impastavano, bianche e unte d'olio fin sopra al gomito; pensammo allo spazio che avrebbero occupato la farina, e il grano per fare la farina, e i campi per coltivare il grano, e le montagne da cui scendeva l'acqua per irrigare i campi, e i pascoli per le mandrie di vitelli che avrebbero dato la carne per il sugo; allo spazio che ci sarebbe voluto perché il Sole arrivasse con i suoi raggi a maturare il grano; allo spazio perché dalle nubi di gas stellari il Sole si condensasse e bruciasse; alle quantità di stelle e galassie e ammassi galattici in fuga nello spazio che ci sarebbero volute per tener sospesa ogni galassia ogni nebula ogni sole ogni pianeta, e nello stesso tempo del pensarlo questo spazio inarrestabilmente si formava.

*Le Cosmicomiche, Italo Calvino*

## 1.1 Friedmann-Lemaître-Robertson-Walker's Cosmology

### 1.1.1 The formalism

At the beginning of the previous century, observational and experimental results led to a shift of paradigm in our understanding of our space-time and of gravitation. Thanks to the incredible progresses of differential geometry done by geniuses like Minkowski, Christoffel, Riemann, Ricci-Curbastro, Levi-Civita, Weyl and Bianchi in the early 20th century, Albert Einstein has been able to reformulate the gravitational interaction as a consequence of the geometry of space and time. Linking energy, matter (described by the energy-momentum tensor  $T_{\mu\nu}$ ), geometry (through Ricci curvature tensor  $R_{\mu\nu}$ , the scalar curvature  $R$  and the metric  $g_{\mu\nu}$ ), and only two constants (Newton's gravitational constant  $G$  and an integration constant  $\Lambda$  which can be interpreted as a cosmological constant) in one sole equation:

$$R_{\mu\nu} - \frac{1}{2}Rg_{\mu\nu} + \Lambda g_{\mu\nu} = 8\pi G T_{\mu\nu}, \quad (1.1)$$

he opened the way to a formalisation of the history of the Universe itself. This achievement, result of a wonderful interaction among mathematicians and physicists, allowed the following generation of physicists to discover black holes, gravitational lensing, to explain the trajectory of Mercury and to build the G.P.S. The cosmological constant term  $\Lambda$  cannot be forbidden by differential geometry nor physics and seems to be consistent with observations though its interpretation is still open for debate.

Considering that at extremely big scales (larger than  $\sim 100$  Mpc) the Universe seems to be homogeneous and isotropic, Friedmann on one side and Lemaître on the other suggested it was possible to solve Einstein's equation 1.1 and to find the metric of the Universe. Robertson and Walker showed that the only compatible metric had to have this expression:

$$ds^2 = -dt^2 + a^2(t) \left[ \frac{dr^2}{1 - kr^2} + r^2 (d\theta^2 + \sin^2(\theta)d\phi^2) \right]. \quad (1.2)$$

where  $k$  can only take the values  $-1, 0$  and  $1$ . This metric implies that it is possible to slice space-time into homogeneous and isotropic space-like slices  $\Sigma_t$  and therefore that it exists a comoving time  $t$ . The factor  $a(t)$  is called the scale factor and corresponds to the freedom to change the scale from one slice  $\Sigma_t$  to another. It also allows to size the physical distance, indeed two objects that are separated by a comoving coordinate distance  $l$  will actually see each other (for instance by exchanging photons) at a distance  $a(t)l$  which can vary with time. It is then logical to associate an apparent relative velocity to these two objects:  $v = \dot{a}(t)l$ . To get rid of the comoving distance  $l$  it is usual to consider the Hubble parameter:

$$H(t) = \frac{\dot{a}}{a},$$

named after the astronomer Edwin Hubble who first showed this linear relation between apparent distance and apparent velocity thanks to the observation of red-shifted galaxies. As we will see later 1.1.3.1, this parameter is not zero. This was a hint that the Universe was not static and led to the present model.

The computation of the Ricci curvature tensor gives:

$$R_{tt} = -3 \left( \frac{\ddot{a}}{a} \right) \quad \text{and} \quad R_{ij} = a^2 \left( \frac{\ddot{a}}{a} + 2 \frac{\dot{a}^2}{a^2} + 2 \frac{k}{a^2} \right) g_{ij}, \quad (1.3)$$

and the other coefficients are zero. Its contraction, the scalar curvature is:

$$R = 6 \frac{\ddot{a}}{a} + 6 \frac{\dot{a}^2}{a^2} + 6 \frac{k}{a^2} \quad (1.4)$$

The homogeneity-isotropy hypothesis not only constrains the left-hand side of Einstein's equation but also the right-hand side. Indeed, in a co-moving frame, the flux of energy has to be null in every direction (so the  $T_{0i} = 0$ ) and the spatial part has to be proportional to the metric, the proportionality coefficient being the density of  $\langle \vec{p}^2 / (3E) \rangle$  which is consistent with the definition of the pressure  $p$  in the comoving frame. Conservation of energy imposes that the energy-momentum tensor is:  $T_{\mu\nu} = \text{Diag}(-\rho, p, p, p)$  where  $\rho$  is the energy density. This also allows us to move the  $\Lambda g_{\mu\nu}$  term to the right-hand side and to integrate it in  $T_{\mu\nu}$ , thus we can interpret  $\Lambda$  as a vacuum-like fluid with negative pressure. In this framework, Einstein's tensorial equation 1.1 becomes two scalar equations, known as Friedmann's equations:

$$3 \left( \frac{\dot{a}}{a} \right)^2 = 8\pi G \rho - 3 \frac{k}{a^2} \quad \text{and} \quad (1.5)$$

$$\frac{\ddot{a}}{a} = -\frac{4\pi G}{3} (\rho + 3p). \quad (1.6)$$

Combining these two equations leads to the continuity equation:  $\dot{\rho} + 3 \frac{\dot{a}}{a} (\rho + p) = 0$ . If pressure is related to energy density through an equation of state of the kind  $p = \omega \rho$ , it is straightforward to obtain:

$$\rho = \rho_0 \left( \frac{a}{a_0} \right)^{-3(\omega+1)} = \rho_0 \hat{a}^{-3(\omega+1)},$$

where the subscript  $_0$  stands for present value and  $\hat{a}$  is the scale parameter divided by its present value. For most cosmological components, this equation of state is valid. For relativistic gas,  $\omega = 1/3$ ,  $\omega \simeq 0$  for non-relativistic matter and  $\omega = -1$  for vacuum-like fluids.

At this point, it is convenient to introduce the critical density:

$$\rho_c(t) = \frac{3H^2}{8\pi G},$$

and its present value

$$\rho_c = \frac{3H_0^2}{8\pi G} \simeq 0.92 h_{70}^2 10^{-26} \text{kg m}^{-3} \simeq 5.16 h_{70}^2 \text{GeV}/c^2 \text{m}^{-3}, \quad (1.7)$$

where  $h_{70} = H_0 / (70 \text{ km s}^{-1} \text{ Mpc}^{-1})$  allows us to give numerical values consistent with the best measurement of the Hubble constant. Together with  $\rho_c$  we will introduce the density parameters “ $\Omega$ ” which are the ratios of the various densities with the critical one, both at present values. Taking  $t = t_0$  for equation 1.5, one can express  $k$  as  $H_0^2 a_0^2 (\Omega_T - 1)$ , where

$$\Omega_T = \Omega_\Lambda + \Omega_m + \Omega_\gamma$$

is the total density to the critical density ratio.  $\Omega_\Lambda$  stands for  $\Lambda/\rho_c$ ,  $\Omega_m$  represents all non-relativistic matter and  $\Omega_\gamma$  all relativistic matter (not only photons). Let us now re-express the Friedmann equations 1.5 and 1.6:

$$H(t)^2 = H_0^2 (\Omega_m \hat{a}^{-3} + \Omega_\gamma \hat{a}^{-4} + \Omega_\Lambda + (1 - \Omega_T) \hat{a}^{-2}) \quad \text{and} \quad (1.8)$$

$$\ddot{a} = -H_0^2 a_0 \left( \frac{\Omega_m}{2} \hat{a}^{-2} + \Omega_\gamma \hat{a}^{-3} - \Omega_\Lambda \hat{a} \right) \quad (1.9)$$

As it can be seen in figure 1.1, the Hubble parameter is dominated successively by each component and only for few values of  $\hat{a}$  two components are in competition. The actual measurements seem to indicate that we live in the very particular time where vacuum just started to rule the Hubble parameter over dust. This is quite puzzling and has risen the suspicion that maybe the cosmological constant is not a constant. Curvature domination can take place after matter domination. Even though it is not possible to find an easy analytical solution to the full equation 1.8, because one can consider separately each regime, it is possible to discuss the various evolutions of the Universe for the various values of the  $\Omega$ 's. During radiation domination one has:

$$\hat{a}_\gamma(t) \propto \sqrt{2H_0 \sqrt{\Omega_\gamma} t}.$$

During matter domination one has:

$$\hat{a}_m(t) \propto \left( 2H_0 \sqrt{\Omega_m} t / 3 \right)^{2/3}. \quad (1.10)$$

During curvature domination, which happens only if the universe is subcritical ( $\Omega_T < 1$ ), one has:

$$\hat{a}_k(t) \propto H_0 \sqrt{1 - \Omega_T} t.$$

During vacuum domination one has:

$$\hat{a}_\Lambda(t) \propto \exp(H_0 \sqrt{\Omega_\Lambda} t).$$

Let us have a look to the various possible histories of the Universe.

### 1.1.2 The possible scenarios

Whatever the values of the parameters, the past of our Universe is rather clear: as we can measure a positive Hubble parameter  $H_0$ , it means that the scale parameter was smaller at earlier times. We do not know if the scale parameter  $a$  ever reached the null value and hence if time has a beginning (Big Bang), however we know that because it was much smaller, the Universe was much denser and therefore much warmer. So warm that according to particle physics, all particles in the Universe, including those who do not exist any more outside our colliders, were at thermal equilibrium, it was Gamow's Ylem. As the Universe cooled down, particles started to decouple from the ylem. The stable ones would freely follow their evolution while the unstable ones would decay. The photons that decoupled from baryonic matter when the first atoms formed, at  $\sim 4,000$  K have been free of interaction ever since (except for a

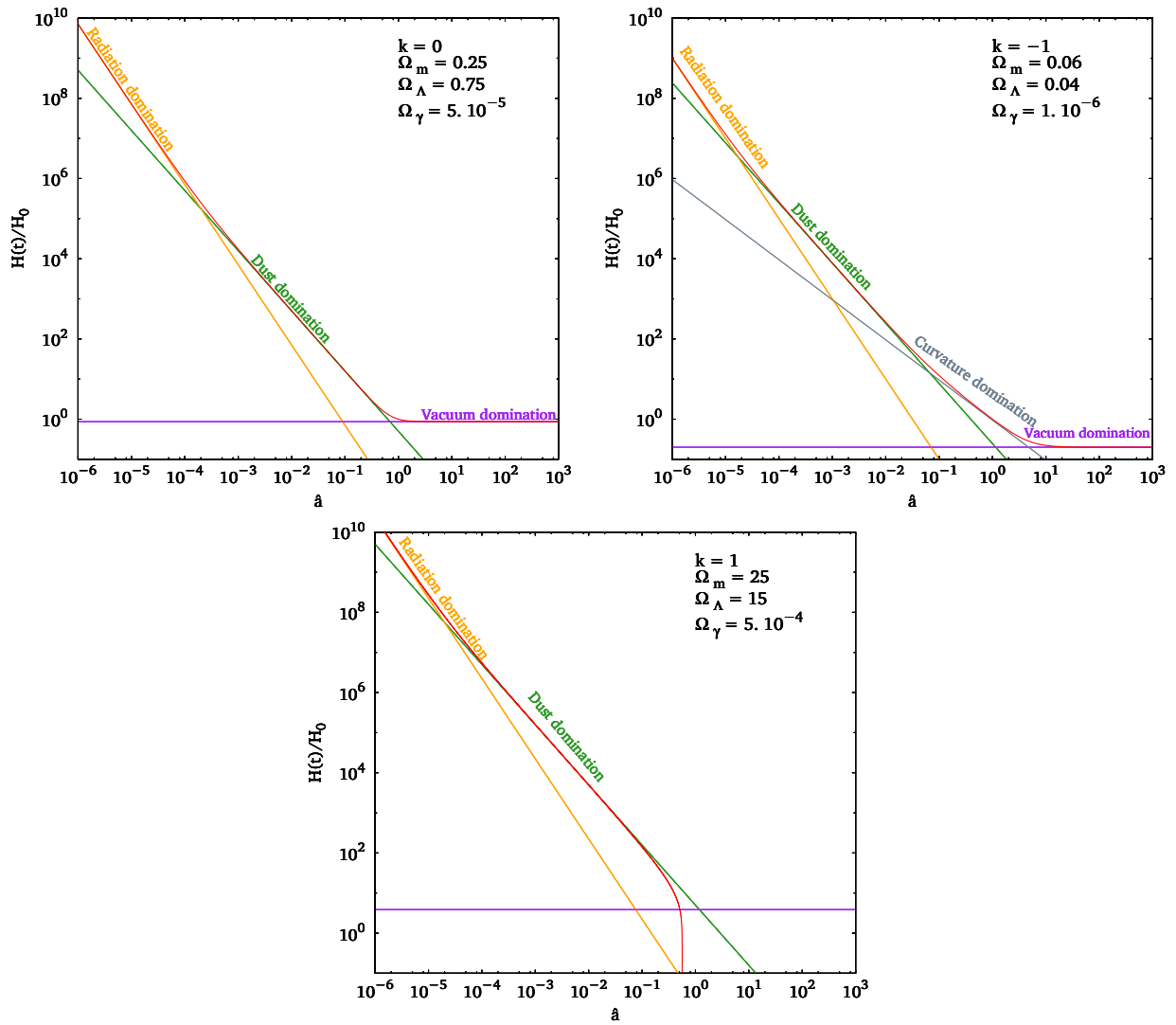


Figure 1.1: The red curve represents the Hubble parameter as a function of the scale parameter  $\hat{a}$  for various values of the  $\Omega$ 's. The other curves represent the same Hubble parameter if only radiation (orange), dust (green), curvature (grey) and cosmological constant (purple) were taken into account. The evolution of the Universe is ruled successively by radiation, non-relativistic matter, curvature and cosmological constant.

reheating during the re-ionisation of the Universe), because of expansion they have cooled down to the actual 2.725 K temperature they have been measured at. This sea of black body photons, called the Cosmic Microwave Background, discovered in 1964 has been considered as a proof of the Big Bang model. It is believed that there should also be a Cosmic Neutrino Background and a Cosmic Gravitational Wave Background. However, because these particles decoupled much earlier and have not been reheated by electron-positron annihilation, they are colder than the photons of the microwave background, hence very difficult to detect. Moreover, neutrinos and gravitational waves, interact much more weakly with our detectors than photons.

Concerning massive particles, once they have decoupled from the ylem, they have started to condensate because of gravitation, to form halos, galaxies, stars, planets and everything else we know in the Universe. Though particle physics is not able to tell us how many stable particle species may have decoupled from the ylem<sup>a</sup>, we are able never the less to compute the correct amount of light elements created during this phase of the history of the Universe (Big Bang Nucleosynthesis).

The future of our Universe is however less clear than its past and depends more on the values of the parameters of Friedmann equations.

### 1.1.2.1 The open Universe

If the Universe is subcritical,  $\Omega_T < 1$ , then gravitation is not strong enough to hold the Universe together. Either there is a cosmological constant (which is the case showed on the upper right panel of figure 1.1 and the Universe will exponentially grow, or, if there is no cosmological constant, curvature will prevail and the universe will expand linearly. In both case, the geometry of the universe is hyperbolic and this cold fate is called the Big Freeze.

### 1.1.2.2 The closed Universe

If the Universe is over-critic,  $\Omega_T > 1$ , then the geometry of the Universe is spherical. This means that curvature will cancel the other terms of Friedmann's equation 1.8 – see lower panel of figure 1.1. At this point if  $\ddot{a}$  is negative (see equation 1.9) then the Universe will recollapse on itself (the Big Crunch). However, if  $\Omega_\Lambda$  is large enough, then  $\ddot{a}$  can be positive and the Universe will nevertheless expand for ever.

### 1.1.2.3 The critical Universe

If the Universe is critical,  $\Omega_T = 1$ , then its geometry is Euclidean. In absence of cosmological constant, the Universe would slowly decelerate because of gravity,  $\dot{a}$  asymptotically going to zero.

It clearly appears from this discussion that it is extremely interesting to have a precise knowledge of the various density parameters  $\Omega$ . Last 30 years observational cosmology have been dedicated to the measurement of these parameters.

## 1.1.3 Observational results

### 1.1.3.1 The Hubble parameter

In 1929, Edwin Hubble realised that the Doppler-Fizeau effect was more important for further objects. This can be explained by an expanding Universe, the measured redshift of an astrophysical object  $z = \frac{\lambda_{received}}{\lambda_{sent}} - 1$  is, at the first order, equal to  $z = H_0 d / c$ , where  $d$  stands for the comoving distance between the observed object and the detector.

---

<sup>a</sup>Each model of physics beyond the standard model may provide this information but none of these models can be taken for granted yet.

The present value of the Hubble parameter  $H_0$  is of utmost importance for all other measurements. Indeed it appears in both Friedmann equations 1.8 and 1.9. Using various data, the Wilkinson Microwave Anisotropy Probe (WMAP) team estimated this parameter [13]. Their results are summed up in Table 1.1. Though the precision is extremely good, this estimation is indirect and relies on the fact that our cosmological model is correct.

Data set	$H_0$ [km s <sup>-1</sup> Mpc <sup>-1</sup> ]
WMAP 5years	71.9 <sup>+2.6</sup> <sub>-2.7</sub>
WMAP 5years + BAO	70.9 ± 1.5
WMAP 5years + high- $z$ SNe	69.6 ± 1.7
WMAP 5years + BOA + high- $z$ SNe	70.1 ± 1.3

Table 1.1: Estimations of the  $H_0$  parameter by the WMAP team making use or not of Baryonic Acoustic Oscillation (BAO) and high redshift supernovæ (high- $z$  SNe) data.

More recently, the Hubble Space Telescope collaboration, did a model independent estimation of the Hubble parameter, based only on redshift and distance estimations of local objects. They have reached the best precision achieved until now with this method. Even though they still have a 5% error, it does not suppose anything about the cosmological model. They have found  $H_0 = 74.2 \pm 3.6$  km s<sup>-1</sup> Mpc<sup>-1</sup> [16]. All these estimations are rather consistent. We will carry on using the  $h_{70} = H_0/70$  km s<sup>-1</sup> Mpc<sup>-1</sup> for our numerical estimations.

### 1.1.3.2 $\Omega_\gamma$

The only parameter that can be measured in a model independent way is the photon density  $\rho_\gamma$ . The temperature of the Cosmic Microwave Background has been measured precisely by COBE[15], which found  $T = 2.725 \pm 0.002$  K, an even better measurement will soon be performed by Planck. Using Stefan-Boltzmann law, corrected by a geometrical factor, one gets  $\rho_\gamma = 4 \sigma T^4 / c = (2.604 \pm 0.008) \times 10^5$  eV m<sup>-3</sup>. It is then straightforward to get  $\Omega_{CMB} = 5.05 h_{70}^{-2} \times 10^{-5}$ . Because  $\rho_\gamma \propto \hat{a}^{-4}$ , it is easy to see that  $\hat{a}_{rec}^{-1} = \frac{T_{rec}}{T_{CMB}}$  which gives  $z_{rec} \sim \hat{a}_{rec}^{-1} \sim 1,400$ . A full numerical computation[11] (taking reionisation into account) would actually give  $z_{rec} \sim 1,100$  However we should not forget that neutrinos also contribute to  $\Omega_\gamma$ . By considering entropy and energy conservation before and after neutrino decoupling, it is possible to show that  $\rho_\nu = (7/8)(4/11)^{4/3}\rho_\gamma$  for each neutrino (and anti-neutrino?) species. For three neutrino species, one gets  $\Omega_\gamma = 8.48 h_{70}^{-2} \times 10^{-5}$ .

### 1.1.3.3 $\Omega_T$

At the time of electron-proton recombination, when the Cosmic Microwave Background appeared, the Universe was matter dominated, therefore  $\Omega_T \sim \Omega_m(w_{rec})$  (this can be checked a posteriori). At that time the largest anisotropies were of the size of the Hubble distance  $d_H = H^{-1} = \frac{1}{H_0(\Omega_m \hat{a}^3 + (1-\Omega_m)\hat{a}^2)^{1/2}}$ . Indeed super-Hubble fluctuations are frozen (they modify the evolution of the scale parameter  $a$  and collapse is exactly compensated by dilution and

vice-versa) whereas sub-Hubble scales are already oscillating (due to pressure/gravitation competition). According to the definition of angular distance  $d_A$  (see equation A.1 in the Appendix), the angular size of the largest anisotropies of the Cosmic Microwave Background is:

$$\theta_H = \frac{d_H}{d_A} = \frac{d_H(1+z_{rec})}{a_0\chi_{rec}},$$

where the notations are the same as in the appendix A. We will consider three cases.

For  $\Omega_T \ll 1$

$$\theta_H \sim \frac{1}{2 - \ln(\Omega_m)}. \quad (1.11)$$

The matter density of the Universe is at least larger than its baryon density,  $\Omega_m \geq \Omega_b = 0.04$  (see section 1.2.1) hence the smallest value we can consider for  $\theta_H$ <sup>b</sup> is  $11^\circ$ .

For  $\Omega_T = 1$

$$\theta_H \sim \frac{1}{2\sqrt{1+z_{rec}}} \times \begin{cases} 1 & \text{if } x \geq 1 \\ f(x) = \frac{2}{\sqrt{x(1+x)}} & \text{if } x \leq 1 \end{cases}.$$

where  $x^3 = \frac{\Omega_m}{\Omega_\Lambda}$ . Because we still see outer clusters of galaxies,  $\Omega_\Lambda$  cannot be much bigger than  $\Omega_m$ . For the sake of numerical comparison, let us take an upper limit of  $\Omega_\Lambda = 100 \times \Omega_m$ . This gives  $x = 0.2$ . Between 0.2 and 1,  $f(x)$  varies from 4 to 1, hence we expect values of  $\theta_H \gtrsim \frac{1}{2\sqrt{1+z_{rec}}} = 0.86^\circ$ .

For  $\Omega_T \gg 1$  we have an upper bound:

$$\theta_H < \frac{1}{2\sqrt{1+z_{rec}}} = 0.86^\circ,$$

The angular spectrum of the Cosmic Microwave Background measured by WMAP and displayed in the left panel of Figure 1.2 clearly exhibits the highest anisotropies around  $1^\circ$ . This is a good reason to believe that our Universe is flat and  $\Omega_T = 1$ . A complete numerical analysis performed by the WMAP collaboration [11] gave:  
 $-0.0179 < \Omega_T - 1 < 0.0081$  (95% CL).

#### 1.1.3.4 $\Omega_m$

The real-space matter spectrum  $P(k)$  of the structures of the Universe is closely related to  $\Omega_m h$ . Indeed it concerns only virialised objects which do not feel the effect of a putative cosmological constant. The Sloan Digital Sky Survey [19] performed such a study using 200,000 galaxies. They corrected for possible luminosity bias<sup>c</sup> and found a  $P(k)$  consistent with many other studies, see right panel of Figure 1.2. They concluded that  $h_{70}\Omega_m = 0.287 \pm 0.020$ .

<sup>b</sup>beware that  $\theta_H$  was replaced by  $\sin(\theta_H)$  in equation 1.11 because the small angle approximation was not valid any more.

<sup>c</sup>The main bias comes from the fact that luminous objects are more easily detected than dim one. The other source of error is the proper motion of the object which can add or subtract a Doppler redshift to the cosmological one.

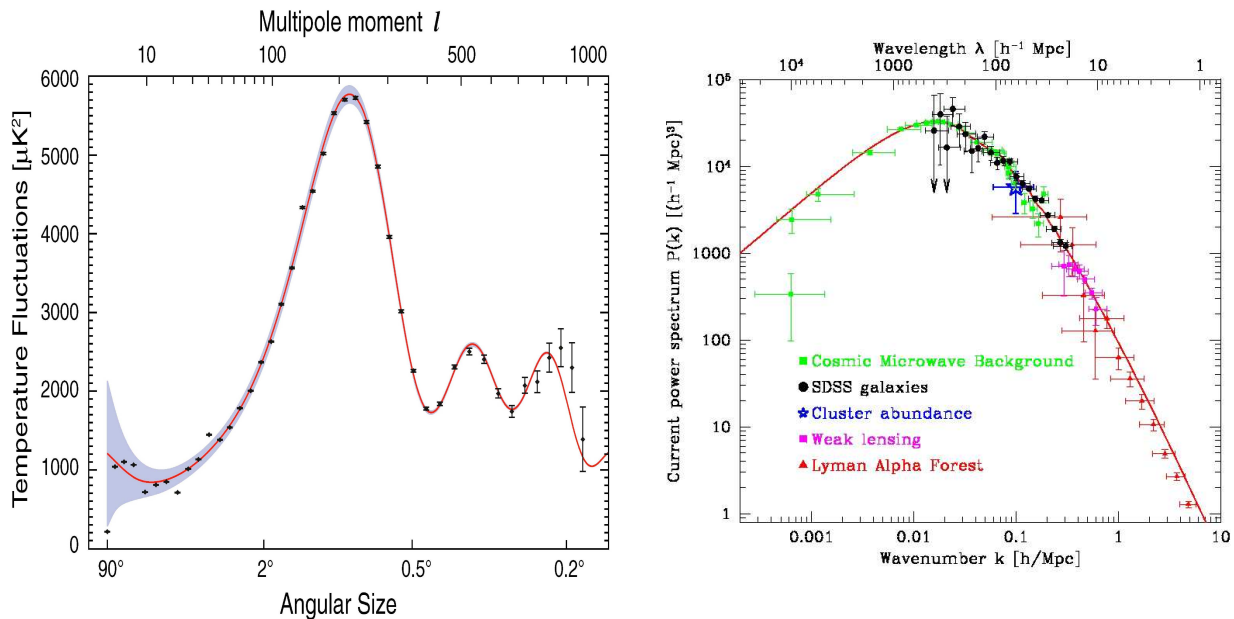


Figure 1.2: *Left panel:* The angular spectrum of the Cosmic Microwave Background as measured by WMAP. *Source WMAP website* *Right panel:* Real-space matter spectrum obtained compiling data from Cosmic Microwave Background measurements, galaxy surveys, cluster abundance, weak lensing and Lyman  $\alpha$  forest observations. *Source SLOAN website*

### 1.1.3.5 $\Omega_\Lambda$

It is finally time to use the second Friedmann equation 1.9. Let us introduce the deceleration parameter  $q_0 = -H_0^{-2} \frac{\ddot{a}}{a} \Big|_{t=t_0}$ . As we know that  $\Omega_\gamma$  can be neglected today, we get:

$$q_0 = \frac{\Omega_m}{2} - \Omega_\Lambda.$$

It was believed that all type Ia supernovae, because they all explode at the precise same mass, do have the same luminosity  $L_{SN}$ . It is now known that actually because the environment can make the star explode anisotropically, the received luminosity is not always the same. However we have now enough statistics on these objects to reconstruct the luminosity thanks to the duration of the emission and hence to use them as standard candles. Using the results from equations A.4 and A.5, one can show that the received flux  $\phi$  by nearby objects should go as:

$$\phi = \frac{L_{SN}}{4\pi} \frac{H_0^2}{z^2} (1 + (q_0 - 1)z)$$

This means that one should expect a deviation from Hubble law with increasing redshift. A good measurement of this deviation have been performed by the High-z SN project [10] and they found

$$\Omega_\Lambda = 0.71_{-0.06}^{+0.05}.$$

However it is important to stress that this measurement relies on the hypothesis that  $\Omega_T = 1$  otherwise the error bars would be much larger. In the future the Sloan Digital Sky Survey

SuperNova Survey (SDSS SN survey) and the SuperNova Acceleration Probe (SNAP) should give better results.

First thing we should tell about these measurements, is that, though they are extremely complex and suffer uncertainty, they agree remarkably well with each other. We indeed find that  $\Omega_T \sim \Omega_m + \Omega_\gamma + \Omega_\Lambda$  even though they are measured independently. However, as one can see from figure 1.3, it is also possible to combine the results from all these experiments and some others to get even better constraints on all our parameters. The up-to-date results are summed up in Table 1.2.

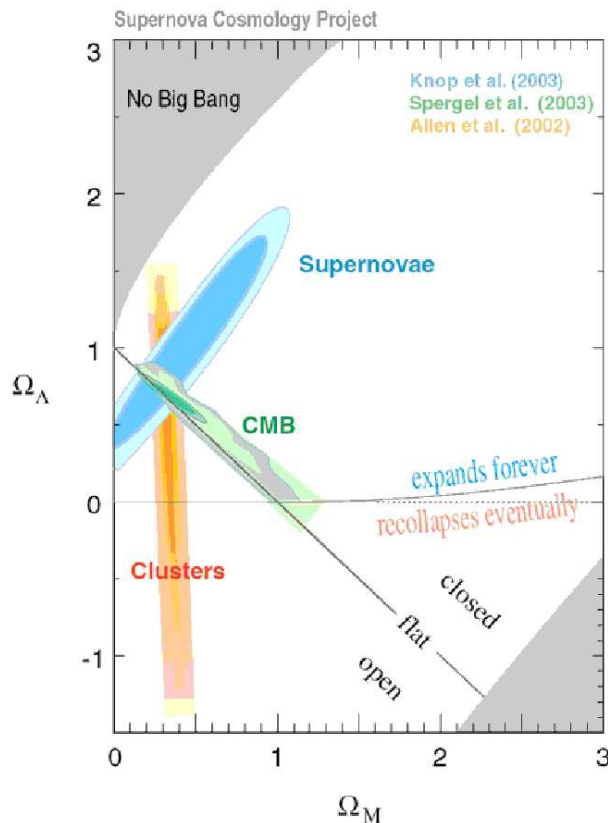


Figure 1.3: Combining different experimental result gives even better results. *Source SNAP website*

## 1.2 Evidences for dark matter

### 1.2.1 On cosmological scales

Cosmic Microwave Background anisotropies can also give us interesting information about the baryonic content of the Universe. Indeed, the peaks visible in the angular spectrum of the left panel of figure 1.2 are due to oscillation caused by pressure that interfered with the gravitational collapse. The speed of sound of the hot photon-electron-proton plasma is related to

Parameter	Value
$H_0$	$70.5 \pm 1.3 \text{ km s}^{-1} \text{ Mpc}^{-1}$
$\Omega_T$	$1.0050^{+0.0060}_{-0.0061}$
$\Omega_m$	$0.273 \pm 0.0145$
$\Omega_\Lambda$	$0.726 \pm 0.015$

Table 1.2: Up-to-date estimations of cosmological parameters by the WMAP team using Cosmic Microwave Background, Baryonic Acoustic Oscillation (BAO) and supernovæ data.

the baryon to photon density ratio  $\eta = n_b/n_\gamma$ . Estimation of this quantity thanks to primordial nucleosynthesis (see paragraph 1.2.1.2) or later measurements by the WMAP collaboration lead to a density parameter of baryons of

$$\Omega_b = 0.0456 \pm 0.0015.$$

Obviously this is one order of magnitude less than what is obtained from density power spectrum for non-relativistic matter density. One possible explanation to this surprising disagreement is that most of the matter of the Universe is not baryonic and because it was not contributing to pressure during recombination, this matter was necessarily decoupled from the ylem already. Neutrinos are extremely weakly coupled to electrons and not to other particles hence they were decoupled from the ylem then. However it is possible to estimate the neutrino density parameter. The WMAP collaboration estimated an upper limit of

$$\Omega_\nu \leq 0.0145$$

which rules out the neutrino explanation. The only possible solution that does not require us to change our cosmological paradigm is to invoke one or more new particles to which we will globally refer to as dark matter.

Adding a new ingredient to the ylem is dangerous because it may spoil the soup. Indeed, if this new particle is too unstable or annihilates too much and produces standard model particles, it will re-inject non-thermal protons and electrons to the ylem which would perturb the baryon to photon ratio  $\eta$  hence also what we call the Big Bang Nucleosynthesis (see paragraph 1.2.1.2) that is the cosmological formation of light nuclear elements. Of course this new particle has to have the correct density parameter.

### 1.2.1.1 Constraining dark matter with relic density

For a non-relativistic particle<sup>d</sup>  $\chi$ , the equation ruling its density  $n_\chi$  is called the Boltzmann equation:

$$\frac{dn_\chi}{dt} = -3\frac{\dot{a}}{a}n_\chi + \sum_{i,j,k} n_i n_j \langle \sigma_{ij \rightarrow \chi k} v \rangle - n_\chi \sum_{i,j,k} n_k \langle \sigma_{\chi k \rightarrow ij} v \rangle \quad (1.12)$$

<sup>d</sup>Here, as in the following,  $\chi$  will denote any dark matter particle and not necessarily the Supersymmetric neutralino which usually has the same notation.

where each term respectively corresponds to dilution from expansion, creation and annihilation with cross-sections  $\sigma_{ij \rightarrow \chi k}$  and  $\sigma_{\chi k \rightarrow ij}$  respectively.  $i, j$ , and represent the particles with which  $\chi$  can interact. The speed  $v$  is the relative speed of the interacting particles. In the case where the  $\chi$  particle can only annihilate with itself, one gets

$$\frac{dn_\chi a^3}{da^3} = \frac{\sum_{i,j} n_i n_j \langle \sigma_{ij \rightarrow \chi \chi} v \rangle - n_\chi^2 \sum_{i,j} \langle \sigma_{\chi \chi \rightarrow ij} v \rangle}{3\dot{a}/a}.$$

Because the particle has been in equilibrium with the ylem when it was very warm, one can write that  $\sum_{i,j} n_i(T) n_j(T) \langle \sigma_{ij \rightarrow \chi \chi} v \rangle_T = n_\chi(T)^2 \sum_{i,j} \langle \sigma_{\chi \chi \rightarrow ij} v \rangle_T$ . If the annihilation cross-section of  $\chi$  does not depend much on the temperature<sup>e</sup>, the annihilation rate simply reads:  $\Gamma = n_\chi \sum_{i,j} \langle \sigma_{\chi \chi \rightarrow ij} v \rangle$  and to simplify the previous equation as:

$$\frac{dn_\chi a^3}{da^3} = \frac{\Gamma}{3\dot{a}/a} \frac{n_\chi(T)^2 - n_\chi^2}{n_\chi},$$

which is easier to interpret. There are two regimes:

- if  $\Gamma \gg \dot{a}/a$ , that is if the annihilation rate is much larger than the expansion rate, then  $n_\chi$  is forced to  $n_\chi(T)$  (indeed if it gets larger, its derivative is negative and vice-versa).
- if  $\Gamma \ll \dot{a}/a$  then the right-hand side of the equation vanishes and  $n_\chi$  goes as  $a^{-3}$ .

The transition from one regime to another is called freeze-out and happens at a temperature  $T_f$  defined by

$$n_\chi(T_f) \sum_{i,j} \langle \sigma_{\chi \chi \rightarrow ij} v \rangle \sim H(T_f). \quad (1.13)$$

Using the laws of thermodynamics for the early Universe, as it is described in the appendix [A.2](#), it is possible to find a solution. The current value of the density parameter for  $\chi$ , the so called relic density, is numerically computed and is:

$$\Omega_{DM} h_{70}^2 \sim 0.227 \frac{1.9 \times 10^{-26} \text{cm}^3 \text{s}^{-1}}{\langle \sigma v \rangle} \quad (1.14)$$

where  $1.9 \times 10^{-26} \text{cm}^3 \text{s}^{-1}$  actually corresponds to an electro-weak scale cross-section. We will see in next chapter why this value is interesting. It is not surprising to see that the larger the annihilation cross-section, the less the amount of  $\chi$  left in the Universe today.

The main information one can keep in mind from this, is that the annihilation cross-section, and hence the coupling to the standard model particles, cannot be very large and that detection of such a particle will not be easy.

---

<sup>e</sup>Note that this hypothesis will not be valid any more when we will speak about Sommerfeld enhancement in chapter [8](#)

### 1.2.1.2 Constraining dark matter with Big Bang Nucleosynthesis

Much less straightforward, the constraints coming from Big Bang Nucleosynthesis are nevertheless interesting. Our understanding of the early Universe history, together with the standard model of particle physics, have been incredibly successful in predicting the amount of the light elements (all isotopes of hydrogen, helium, beryllium and lithium). As one can see on figure 1.4, except for  ${}^7\text{Li}$ , the abundances predicted by cosmology are in very good agreement with the observational estimations. It is not very clear today whether the discrepancy we see for  ${}^7\text{Li}$  is due to observational biases, later time stellar evolution or new physics, either in cosmology or in particle physics.

Acting very minimally and adding only one dark matter particle, not coupled to the standard model particles should not spoil the Big Bang Nucleosynthesis. However, as we will see in the next chapter, there are reasons to believe that particle physics is much richer than that. It is probable that dark matter is only the *visible* pit of the iceberg and is actually a tracer of a much more complex particle physics scenario. It is possible to include the new scenario into Big Bang Nucleosynthesis and to see, depending on the scenario and the parameters chosen, if it does any harm to the element abundances prediction. Therefore the constraints one can get from Big Bang Nucleosynthesis strongly depend on the particle physics model chosen to explain dark matter and cannot be handled in a generic way.

### 1.2.1.3 Large Scale Structures formation

The Cosmic Microwave Background clearly proves us that the Universe has been extremely homogeneous a long time ago; indeed the temperature spatial fluctuations, which are a good tracer of matter density fluctuations, measured by WMAP are of order  $\sim \mathcal{O}(10^{-5})$ . However it is obviously not the case any more: there are planets, stars, galaxies, clusters of galaxies and voids. The study of the growth of the fluctuations in the framework of an expanding Universe is interesting for the problem of dark matter. As long as a particle species is in equilibrium in the ylem, its small fluctuations cannot grow under the effect of gravitation because interaction with other species maintains the pressure. As we have seen in section 1.1.3.3, only fluctuations smaller than the Hubble distance can collapse. Moreover if the species is relativistic when it decouples from the ylem, over-densities will free-stream and dilute instead of collapsing. The largest coordinate distance that a relativistic particle  $\nu$  can go between its freeze-out and the time  $t_m$  it cools down to non-relativistic speeds is:

$$\chi_{fs} = \int_{t_f}^{t_m} \frac{cdt}{a(t)} \sim \frac{\hat{a}_m - \hat{a}_f}{H_0 a_0 \sqrt{\Omega_\gamma}}.$$

At the time the species became non-relativistic, we had  $T_\gamma(t_m) \sim m_\nu$ , as  $T_\gamma \propto a^{-1}$ , it is straightforward to see that  $\hat{a}_m \sim T_\gamma(t_0)/m_\nu$ . Today this corresponds to a distance of

$$a_0 \chi_{fs} = 60 \text{ Mpc} \frac{10 \text{ eV}}{m_\nu}.$$

which means that all fluctuations smaller than 60 Mpc should have been smeared out by free-streaming<sup>f</sup>. This result shows that neutrinos, though we know they have a mass, cannot be

<sup>f</sup>There are models where the small structures come from the fragmentation of larger structures, however this top-down scenario is disfavoured by numerical simulations.

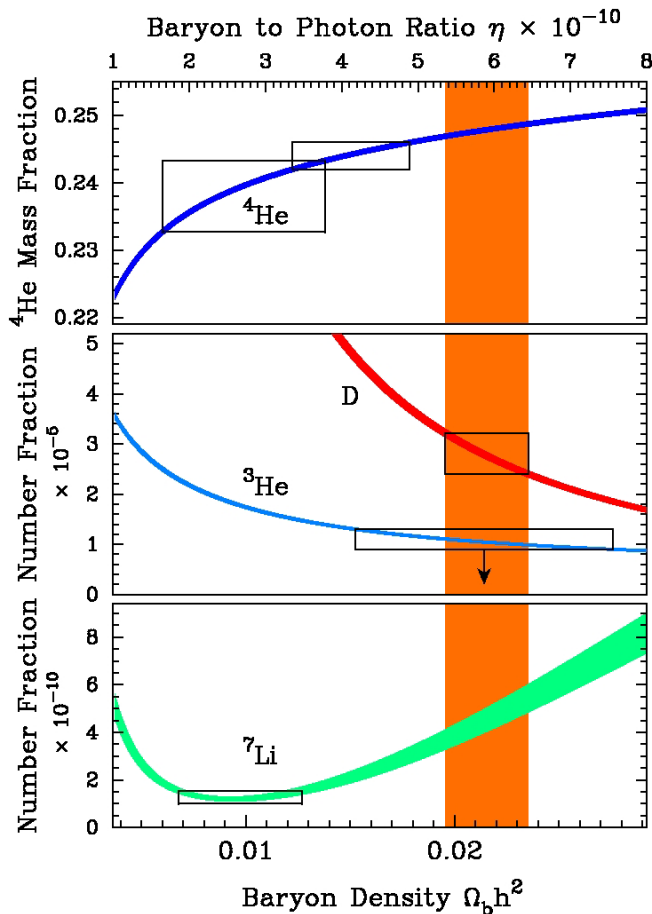


Figure 1.4: Theoretical predictions of the cosmological amount of  $^4\text{He}$ , Deuterium,  $^3\text{He}$  and  $^7\text{Li}$  compared to the hydrogen abundance (coloured bands) plotted against the baryon relic density  $\Omega_b$ . The orange band corresponds to the last measurement of  $\Omega_b$  and the black boxes shows the measured values of the various abundances. The tension that appears between observation and theoretical prediction concerning  $^4\text{He}$  are believed to be due to systematic effects in abundance estimations. *Source [12]*

the dark matter. This is why it is believed that dark matter should have been non-relativistic already when it decoupled from the ylem. This class of models is usually referred to as Cold dark matter models and is the only one considered in this work.

Another suggestion is that dark matter is actually baryonic and hidden in compact objects or very cold molecular gas clouds. Weak lensing surveys have been unable to detect a big enough amount of these objects. Moreover, Joe Silk has shown [18] that at the time of electron-proton recombination, free-streaming photons would fly away from over-dense regions to under-dense ones. Because of residual Compton scattering, these photons have pushed away some of the electrons, which themselves have pushed the hadrons. This has damped the fluctuations of the galactic size, hence baryons only could not have formed the galaxies. The Silk

damping is actually what explains the fact that the harmonic peaks of the angular spectrum of the Cosmic Microwave Background are smaller and smaller when  $l$  gets larger, as it can be seen of figure 1.1. There are some ways out of the Silk damping issue, for instance invoking isocurvature perturbation of the baryon to photon ratio instead of density fluctuations for the anisotropies of the Cosmic Microwave Background, however these models require fine-tuning.

Finally, numerical simulations using a cold dark matter decoupling before the electron-proton recombination have been successful to reproduce the correct amount of clusters and of galaxies in our Universe. The fact that this is coherent with our theoretical framework and observations is not a proof of the existence of cold dark matter of course but the fact that the models that do not require exotic component fail to explain the formation of large scale structure is a good reason to keep looking for dark matter.

We have seen that dark matter is an essential ingredient of our cosmological model, however introducing a new species in such amount should also have consequences on scales smaller than the whole Universe.

### 1.2.2 On the scale of clusters of galaxies

Historically, the idea of dark matter, has been first proposed in 1933 by the astronomer Fritz Zwicky who was studying the Coma cluster. By studying the speed distribution of seven galaxies of the cluster, he computed the dynamical mass of the cluster and found that it was about four hundred times larger than the luminous mass he computed by estimating the quantity of warm gas and stars. His conclusion was that most of the mass of a cluster of galaxy does not emit light. This is why he called it dark matter and we still use this name today. By that time the measurements suffered from a lot of uncertainties, however even with modern techniques, the discrepancy between dynamical and luminous masses holds for all the clusters we know. This is absolutely in agreement with what cosmology tells us: eighty percent of the matter content of our Universe is made of a non-relativistic species which interacts very little with photons and hence has decoupled from the ylem quite early.

Most recent studies[17] by the Sloan Digital Sky Survey found a mass to luminosity ratio of  $\langle M/L \rangle b^{-2} = 362 \pm 54h$  (statistical) for big clusters. This result leads to  $\Omega_m b^{-2} = 0.20 \pm 0.03$ , independent of  $H_0$ . The  $b^2$  parameter is a function of bias which takes into account low luminosity galaxies. It is important to note that since Zwicky, the method has changed, and now the mass is not only computed by velocity dispersion of single objects but also using the gravitational lensing of the cluster itself, or even of the whole sample. When it is possible, masses are also measured thanks to the X-ray emission of warm gas.

Another hint toward the existence of dark matter at cluster scale is the now famous Bullet cluster [14]. This object consists of two clusters of galaxies that have collided recently. On the one hand, it is possible to trace the gas distribution of the object thanks to X-ray emission and on the other hand, lensing provides a distribution of the total amount of matter. As it can be seen of figure 1.5 the two are clearly separated. Indeed the two gas distributions of both clusters have actually collided whereas the dark matter halos, which are collisionless just crossed each other. This is the first example where baryonic matter is clearly decorrelated from

the gravitational potential which proves that dark matter is actually a particle<sup>§</sup> and probably not only an effect of our misunderstanding of gravity.

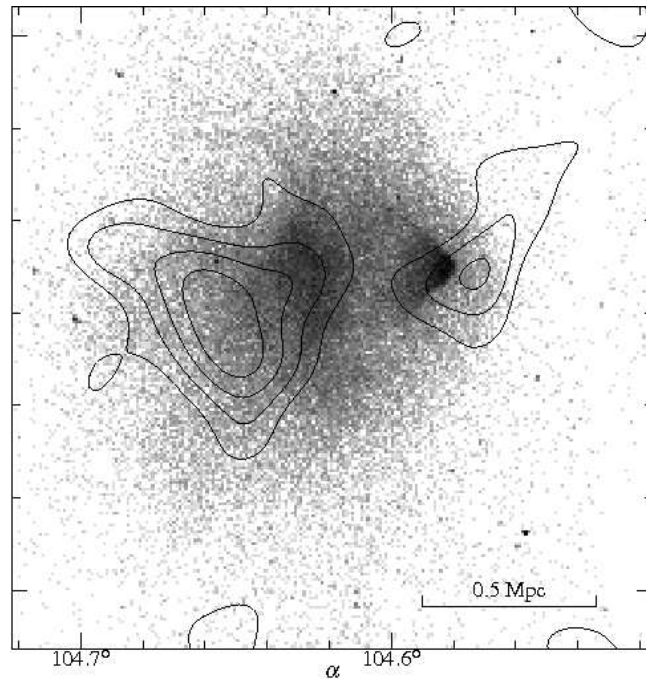


Figure 1.5: This is the bullet cluster 1E0657-56. The contours represent the dark matter distribution deduced by gravitational lensing whereas the black halo corresponds to the X-ray emission from the gas heated by the collision.

### 1.2.3 On galactic scales

A typical spiral galaxy like the Milky Way is constituted by a very heavy bulge (containing a super-massive black hole and thousands of heavy stars) surrounded by a thin disk of radius  $\sim 20$  kpc and thickness  $\sim 200$  pc. Most of the stars and gas we can see is located in the centre of the galaxies, therefore, according to Newton's law, one would expect a gravitational potential weaker and weaker further away from the centre. In a virialised object like a galaxy, this should translate into less kinetic energy for stars moving far away from the galactic centre. However, as it can be seen on figure 1.6 the rotational speed of stars far away from the centre is the same for most distances. One way to solve this problem is to consider that galaxies are in fact embedded in a large dark matter halo, the mass of which actually dominates the gravitational potential. The astronomers Vera Rubin and Albert Bosma have been the first ones to point this rotation curve problem in 1970 for the first one and five years later for the second.

---

<sup>§</sup>however cold dark matter is not necessary to explain the bullet cluster and if neutrinos are as heavy as a few eV they can explain it with some modification of gravity.

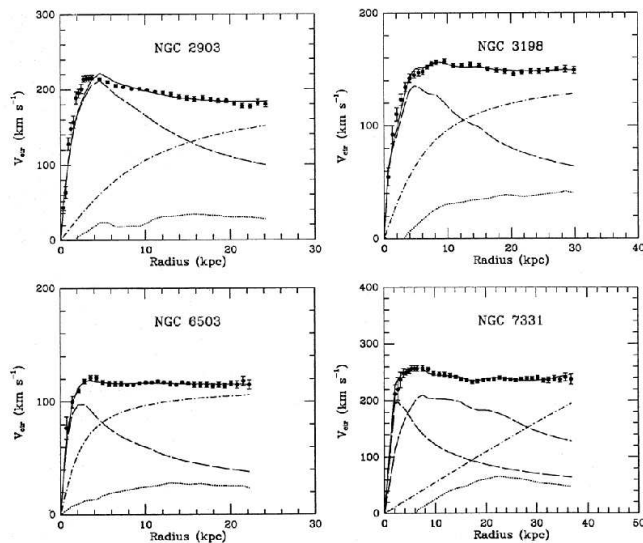


Figure 1.6: Rotation curves of elliptical galaxies. Long dashed curves correspond to the rotation curves one would expect from the star distribution, the dotted ones to the gas distribution, dotted-dashed curves are for a dark matter halo and the solid curves are for the sum of these three components. *Source [9]*

## 1.3 Escape ways from the dark matter problem

### 1.3.1 Modifying gravity

Our whole cosmological model relies on General Relativity. This theory has been tested at various scales but not much larger than the Solar system. It has been proposed that modifying gravity at galactic scales ( $\sim$ few kpc) may explain dark matter. Some attempts have been successful to explain galactic rotation curves however they fail to explain Large Scale Structure formation for the moment.

### 1.3.2 Changing cosmological paradigm

Friedmann and Lemaître's hypothesis is that the Universe is homogeneous and isotropic. Though the Cosmic Microwave Background observation is absolutely in agreement with that, the Friedmann equations imply it is still the case today. It is argued that averaging over space after treatment of the time-evolution creates counter-terms which may explain the cosmological constant. If cosmological constant is to be ruled out then we would have to reconsider our cosmological model as a whole, which includes dark matter.

## Conclusion

The cold dark matter is something that could solve so many problems we are faced with. We have gravitational hints of its existence in very different systems both dynamical and at

equilibrium and at many different scales, from the cosmological to the galactic one. Moreover it appears in problems we deal with either in Newtonian scheme or General Relativity. For all these reasons, it is a reasonable hypothesis to say that dark matter exists. However all these hints only concern gravity, what has particle physics to say about a new weakly interacting massive particle?

## Bibliography

- [1] This chapter is mainly based on the wonderful book [2] and the very nice lectures [4, 5, 6, 7, 8] I had the opportunity to attend.
- [2] Rich, J. Principes de la cosmologie. Ed. École polytechnique 2002 22
- [3] Langlois, D. Géométrie et gravitation. Ed. École polytechnique 2006
- [4] Seljak, U. Introduction to CMB anisotropies. Lectures given at the ICTP summer school in cosmology. Trieste, 2008 22
- [5] Kofman, L. Introduction to cosmology. Lectures given at the ICTP summer school in cosmology. Trieste, 2008 22
- [6] Wands, D. Inflation and cosmological perturbation. Lectures given at the ICTP summer school in cosmology. Trieste, 2008 22
- [7] Hui, L. Large Scale Structures. Lectures given at the ICTP summer school in cosmology. Trieste, 2008 22
- [8] Salati, P. Astrophysique des particules. Lectures given at the Master of the École Normale Supérieure de Lyon. Lyon, 2007 22
- [9] Begeman, K. G., Broeils, A. H., & Sanders, R. H. 1991, MNRAS, 249, 523 21
- [10] Clocchiatti, A., Schmidt, B. P., Filippenko, A. V., *et alii* . 2006, ApJ, 642, 1 13
- [11] Hinshaw, G., Weiland, J. L., Hill, R. S., *et alii* . 2009, ApJS, 180, 225 11, 12
- [12] Kirkman, D., Tytler, D., Suzuki, N., O’Meara, J. M., & Lubin, D. 2003, ApJS, 149, 1 18
- [13] Komatsu, E., Dunkley, J., Nolta, M. R., *et alii* . 2009, ApJS, 180, 330 11
- [14] Markevitch, M., Gonzalez, A. H., Clowe, D., *et alii* . 2004, ApJ, 606, 819 19
- [15] Mather, J. C., Fixsen, D. J., Shafer, R. A., Mosier, C., & Wilkinson, D. T. 1999, ApJ, 512, 511 11
- [16] Riess, A. G., Macri, L., Casertano, S., *et alii* . 2009, ApJ, 699, 539 11
- [17] Sheldon, E. S., Johnston, D. E., Masjedi, M., *et alii* . 2009, ApJ, 703, 2232 19
- [18] Silk, J. 1968, ApJ, 151, 459 18
- [19] Tegmark, M., Blanton, M. R., Strauss, M. A., *et alii* . 2004, ApJ, 606, 702 12

## Chapter 2

# The Standard Model of Particle Physics

Le beau est toujours bizarre.

*Charles Baudelaire*

## and beyond

For we are now in the region of 'perhaps' and 'appears'.

*Virginia Woolf in Orlando*

As we have seen in the previous chapter, cosmology requires at least one new neutral stable particle, produced with the correct density and able to initiate the formation of large scale structures. In a thermal production mechanism, the simplest way would be to have a weakly interacting massive particle (WIMP). Does such a particle exist? The answer to this question is to be asked to particle physicists. In this chapter, I present, in its broad lines, the current understanding of particle physics (the so called Standard Model), the issues it encounters and some (but certainly not all) of the models proposed to go beyond it and that give a dark matter particle candidate.

## 2.1 The Standard Model of Particle Physics

The Standard Model of Particle Physics is the model that describes the interactions of the smallest constituents of matter. It has been built progressively during the last century, based on quantum field theory. In this model there are three interactions called electro-magnetism, weak interaction and strong interaction. And there are various particles: six quarks which can feel the three interactions and exist in three colour states each, charged leptons which can feel only the first two ones and neutrinos that can only interact through the weak interaction. Every particle has an antiparticle which has the same mass but opposite quantum numbers. Each interaction respects a number of symmetries which can be described as the following:  $G_{\text{SM}} = SU(3)_c \otimes SU(2)_w \otimes U(1)_Y$ . The particles of the standard model hence have to be understood as representations (within the meaning of group theory) of  $G_{\text{SM}}$  with one charge (eventually null) for each subgroup, *id est* a colour, a weak charge and a hypercharge.

The interactions between particles can be computed from the following Lagrangian:

$$\mathcal{L}_{SM} = \mathcal{L}_{\text{YM}} + \mathcal{L}_{\text{D}} + \mathcal{L}_{\text{Yukawa}} + \mathcal{L}_{\text{Higgs}}. \quad (2.1)$$

The Yang-Mills term corresponds to the kinetic term for the gauge bosons:

$$\mathcal{L}_{\text{YM}} = -\frac{1}{4g_1^2} B_{\mu\nu} B^{\mu\nu} - \sum_{a=1}^3 \frac{1}{4g_2^2} W_{\mu\nu}^a W^{a\mu\nu} - \sum_{A=1}^8 \frac{1}{4g_3^2} G_{\mu\nu}^A G^{A\mu\nu} \quad (2.2)$$

where

$$B_{\mu\nu} = \partial_\mu B_\nu - \partial_\nu B_\mu,$$

$$W_{\mu\nu}^a = \partial_\mu W_\nu^a - \partial_\nu W_\mu^a - \sum_{b,c=1}^3 \epsilon^{abc} W_\mu^b W_\nu^c,$$

and

$$G_{\mu\nu}^A = \partial_\mu G_\nu^A - \partial_\nu G_\mu^A - \sum_{B,C=1}^8 f^{ABC} G_\mu^B G_\nu^C.$$

The tensors  $\epsilon^{abc}$  and  $f^{ABC}$  respectively stand for the structure constants of the generators of the  $SU(2)_w$  and  $SU(3)_c$ . Being abelian,  $U(1)_Y$  does not have any.

The kinetic term for the fermions is given by Dirac's Lagrangian:

	Name	Notation	SU(3) <sub>c</sub>	SU(2) <sub>w</sub>	U(1) <sub>Y</sub>	U(1) <sub>em</sub>	spin	flavour
Fermions	quarks	$Q_L = \begin{pmatrix} u_L \\ d_L \end{pmatrix}$ $u_R$ $d_R$	3 $\bar{3}$ $\bar{3}$	2 1 1	1/3 -4/3 2/3	2/3 -1/3 -2/3 1/3	1/2	up, charm, top down, strange, bottom
	leptons	$L_L = \begin{pmatrix} \nu_L \\ e_L \end{pmatrix}$ $e_R$	1 1	2 1	-1 2/3	0 -1 1	1/2	$e, \mu, \tau$
Bosons	gauge	$G^{A=1..8}$ $W^{a=1..3}$ B	8 1 1	1 3 1	0 0 0	0 0, ±1 0	1	
	Higgs	$H = \begin{pmatrix} \phi^+ \\ \phi_0 \end{pmatrix}$	1	2	-1	1 0	0	

Table 2.1: Particles of the Standard Model

$$\mathcal{L}_D = \sum_{i=1}^3 L_i^\dagger \sigma^\mu D_\mu L_i + \bar{e}_i^\dagger \sigma^\mu D_\mu \bar{e}_i + Q_i^\dagger \sigma^\mu D_\mu Q_i + \bar{u}_i^\dagger \sigma^\mu D_\mu \bar{u}_i + \bar{d}_i^\dagger \sigma^\mu D_\mu \bar{d}_i \quad (2.3)$$

where the various covariant derivatives, that ensures gauge transformations, are explicated hereafter.

$$\begin{aligned} D_\mu L_i &= \left( \partial_\mu + \sum_{a=1}^3 \frac{i}{2} W_\mu^a \tau^a - \frac{i}{2} B_\mu \right) L_i \\ D_\mu \bar{e}_i &= \left( \partial_\mu + \frac{2i}{6} B_\mu \right) \bar{e}_i \\ D_\mu Q_i &= \left( \partial_\mu + \sum_{A=1}^8 \frac{i}{2} G_\mu^A \lambda^A + \sum_{a=1}^3 \frac{i}{2} W_\mu^a \tau^a + \frac{i}{6} B_\mu \right) Q_i \\ D_\mu \bar{u}_i &= \left( \partial_\mu + \sum_{A=1}^8 \frac{i}{2} (G_\mu^A \lambda^A)^* - \frac{2i}{3} B_\mu \right) \bar{u}_i \\ D_\mu \bar{d}_i &= \left( \partial_\mu + \sum_{A=1}^8 \frac{i}{2} (G_\mu^A \lambda^A)^* + \frac{i}{3} B_\mu \right) \bar{d}_i \end{aligned} \quad (2.4)$$

The matrices  $\tau^a$  and  $\lambda^A$  are those of  $SU(2)$  and  $SU(3)$  respectively. It is interesting that actually in this Lagrangian, no particle has an explicit mass term. Indeed a term of the kind  $m_e e_R e_R^c$  would explicitly break the  $SU(2)_w$  symmetry and it would be difficult to explain why left handed and right handed electrons have the same mass but not the neutrino. An explicit mass term for the gauge bosons would also create the same problem. However experiments tell us that all known fermions have mass and so have three bosons: the  $Z$ , the  $W^+$  and the  $W^-$ . This means that  $G_{\text{SM}}$  is actually a broken symmetry. A nice and "natural" way to break a symmetry is the Higgs mechanism. This mechanism implies that the kinetic term of the Lagrangian still respects all symmetries, so does a potential term but not its vacua. It is not possible for a particle having a non zero spin to have a non trivial potential, otherwise, the minimum of the potential energy would not be the same for all observers. However, a scalar particle has no Lorentz index so its ground states (vacua) can be non zero. So we need a new particle (the yet known composite scalar particles, like the pion, do not work): the Higgs boson. As far as we know, colour charge is conserved but not the hypercharge nor the weak charge, however another charge is conserved: the electric charge. This means that the vacuum breaks  $SU(2)_w \otimes U(1)_Y$  but is stable under  $SU(3)_c$  and a remaining symmetry  $U(1)_{em}$ .

The Higgs Lagrangian deals with the Higgs boson self-interaction.

$$\mathcal{L}_{\text{Higgs}} = (D_\mu H)^\dagger (D^\mu H) - V(H) \quad (2.5)$$

where the covariant derivative and the potential are as follows:

$$D_\mu H = \left( \partial_\mu + \sum_{a=1}^3 \frac{i}{2} W_\mu^a \tau^a - \frac{i}{2} B_\mu \right) H \quad (2.6)$$

$$V(H) = \mu^2 H^\dagger H + \lambda (H^\dagger H)^2 \quad (2.7)$$

However, the Higgs being still to be discovered, it is possible that the expression of its potential is different, if the particle exists at all. Note that this expression of the potential  $V(H)$  is the simplest form invariant under  $SU(2)_w \otimes U(1)_y$  and renormalisable. To be physical, the potential must have minima, hence  $\lambda \geq 0$ . Furthermore, to have non trivial vacua we need  $\mu^2 \leq 0$ , so the lowest vacuum's value is  $\frac{|v|}{\sqrt{2}} = \sqrt{-\frac{\mu^2}{\lambda}}$ . If one chooses a vacuum and expands the fields around it, one gets:

$$H = \exp\left(\frac{i}{v} \xi_i(x) \sigma_i\right) \begin{pmatrix} 0 \\ \frac{v+h(x)}{\sqrt{2}} \end{pmatrix}. \quad (2.8)$$

where the three  $\xi_i$  and  $h$  vanish at the vacuum. The proper choice of gauge (called the unitary gauge) allows us to rewrite the previous Lagrangian:

$$\begin{aligned} \mathcal{L}_{\text{Higgs}} = & \frac{1}{2} \partial_\mu h \partial^\mu h + \frac{1}{8} (g_1 B_\mu - g_2 W_{3\mu}) (g_1 B^\mu - g_2 W_3^\mu) (v+h)^2 \\ & + \frac{1}{8} (g_2 W_{1\mu} - i g_2 W_{2\mu}) (g_2 W_1^\mu + i g_2 W_2^\mu) (v+h)^2 + \lambda v^2 h^2 + \lambda v h^3 + \frac{\lambda}{4} h^4 - \lambda \frac{v^2}{4}. \end{aligned} \quad (2.9)$$

To make this expression easier to understand, it is convenient to introduce new fields:

$$W_\mu^\pm = \frac{1}{\sqrt{2}} (W_{1\mu} \mp i W_{2\mu}) \quad (2.10)$$

and

$$\begin{pmatrix} Z^\mu \\ A^\mu \end{pmatrix} = \begin{pmatrix} \cos \theta_w & -\sin \theta_w \\ \sin \theta_w & \cos \theta_w \end{pmatrix} \begin{pmatrix} W_3^\mu \\ B^\mu \end{pmatrix}. \quad (2.11)$$

With  $m_h^2 = 2\lambda v^2$ ,  $m_W^2 = \frac{g_2^2 v^2}{4}$ ,  $m_Z^2 = \frac{v^2}{4}(g_1^2 + g_2^2)$  and  $\cos^2 \theta_w = \frac{m_W^2}{m_Z^2}$ , the equation 2.9 becomes:

$$\mathcal{L}_{\text{Higgs}} = \frac{1}{2} \partial_\mu h \partial^\mu h + \frac{1}{2} m_Z^2 Z_\mu Z^\mu + \frac{1}{2} m_W^2 W_\mu^+ W^{-\mu} + \left( \frac{2h}{v} + \frac{h^2}{v^2} \right) \left( \frac{1}{2} m_Z^2 Z_\mu Z^\mu + \frac{1}{2} m_W^2 W_\mu^+ W^{-\mu} \right) + V$$

This naturally gives a mass to the  $Z$  and  $W$ s bosons (but not to the photon  $A_\mu$ ) and completely constrains their coupling to the Higgs boson.

Finally, the Yukawa term leads to the particle interactions with the Higgs which generates a mass term for the fermions.

$$\mathcal{L}_{\text{Yukawa}} = \sum_{i,j=1}^3 iY_{ij}^e L_i^T \sigma_2 \bar{e}_{jL} H^* + iY_{ij}^u Q_i^T \sigma_2 \bar{u}_{jL} \tau_2 H + iY_{ij}^d Q_i^T \sigma_2 \bar{d}_{jL} H^* + \text{c.c.} \quad (2.12)$$

It is always possible to find a basis for which the first Yukawa matrix  $Y_{ij}^e$  is diagonal and to redefine  $L_i$  and  $\bar{e}_{jL}$  accordingly into eigenvectors. For the quarks however, this choice is not possible for both terms simultaneously (because  $Q_i^T$  appears in both terms). At best, one can diagonalise one and leave the second in the same basis with a unitary matrix  $\mathcal{V}$  called the Cabibbo-Kobayashi-Maskawa (CKM) matrix.

$$\mathcal{L}_{\text{Yukawa}} = \sum_{i,j=1}^3 i y_{ij}^e L_i^T \sigma_2 \bar{e}_{jL} H^* + i y_{jj}^u Q_i^T \sigma_2 \mathcal{V}_{ji} \bar{u}_{jL} \tau_2 H + i y_{ii}^d Q_i^T \sigma_2 \bar{d}_{jL} H^* + \text{c.c.} \quad (2.13)$$

Transforming the Higgs field as previously (see equation 2.8) and absorbing the unitary matrix coming from the gauge choice into the fields definition, naturally give mass terms to the charged leptons:  $\frac{v}{\sqrt{2}} y_{ii}^e = (m_e, m_\mu, m_\tau)$ , a coupling equal to  $m_i/h$  and no mass to the neutrinos.

Concerning the quarks, it is possible to do to down quarks what we have done for leptons, however for up quarks, because of the  $\mathcal{V}$  matrix the mass states and the interaction states will not be the same. Indeed, the changes in the field will transfer the CKM matrix to the previous parts of the Lagrangian. The interpretation of the terms of the matrix then becomes clear: they represent the probability of quark to decay into another one. The measure of the nine terms of this matrix (plus a possible phase) is an on going work which involves many experiments. Recently BABAR [10] and BELLE [5] have measured with unprecedented precision the terms of the mixing matrix.

$$\mathcal{V} = \begin{pmatrix} 0.97418 \pm 0.00027 & 0.2255 \pm 0.0019 & 0.00393 \pm 0.00036 \\ 0.230 \pm 0.011 & 1.04 \pm 0.06 & 0.0412 \pm 0.0011 \\ 0.00874_{-0.00037}^{+0.00026} & 0.0407 \pm 0.0010 & 0.999133_{-0.000043}^{+0.000044} \end{pmatrix} \quad (2.14)$$

Though some tension exists, these values are in agreement with a unitary matrix.

Up to now the standard model of particle physics has been extremely successful. Indeed it has been able to explain almost all precise measurements and to predict the existence of

particle before they were discovered by the CERN ( $Z$  [11] and  $W^\pm$ [12]) and by the Tevatron (top quark [4, 6]). But it has also been extremely successful in predicting accurate results for high precision tests. From a theoretical point of view it is extremely satisfactory because it is renormalisable and at the perturbative level automatically conserves baryon and lepton quantum numbers without invoking any discrete symmetry. However the standard model fails to explain some observables.

## 2.2 Problems of the Standard Model of Particle Physics

### 2.2.1 Muon anomalous momentum

One of the greatest successes of the standard model is the agreement between theoretical predictions and experimental values for the magnetic moment of the electron. From Dirac's equation (which is obtained from the Dirac part of the standard model Lagrangian), one can get the magnetic moment of the electron:

$$\vec{\mu} = g_e \frac{e}{2m} \vec{S}$$

where  $g_e$  comes from quantum mechanics. At tree level  $g_e = 2$  but loop corrections lead to  $g_e - 2 = 0.002319304400(80)$ . The experimental value is  $g_e - 2 = 0.002319304384(20)$  in extremely good agreement.

The calculi can be done for the muon. As of November 2006, the experimentally measured value [13] is  $g_\mu - 2 = 0.002\,331\,841\,6(13)$ , compared to the theoretical prediction of  $g_\mu - 2 = 0.002\,331\,836\,1(10)$ . This is a quite large difference.

The muon  $g$ -factor can be affected by physics beyond the Standard Model because new particles can enter the loops affecting this quantity. However, one should be aware that chromodynamics correction may be responsible for this anomaly.

### 2.2.2 Neutrinos

The Standard Model requires neutrinos to be massless and left-handed only (because it violates parity every time it interacts). However, many observations prove that neutrinos can change flavour when they propagate, *id est* that for example a neutrino created as an electron neutrino can be detected as a muon neutrino. The Sun produces a large amount of electron neutrino by nuclear processes which can be computed quite precisely (though it depends a little on the Solar dynamics model); cosmic rays, when producing an air shower (see paragraph 3.2.3) produce twice as much muon neutrinos as electron neutrinos; nuclear reactors produce electron anti-neutrino; and particle accelerators enable us to produce neutrino beams either with electron or muon flavour. All these sources are used by various experiments to measure the oscillation properties of neutrinos.

How is it possible for neutrinos to change flavour as they propagate? The only possibility is that, flavour states and propagation states have different basis. This can only be if the three masses of the neutrinos are different. Hence at least two of them have to be massive, in contradiction with the Standard Model. As for the quark it is convenient to introduce a

mixing matrix: the Pontecorvo–Maki–Nakagawa–Sakata (PMNS) matrix. The matrix is often parametrised as follow:

$$U = \begin{bmatrix} 1 & 0 & 0 \\ 0 & c_{23} & s_{23} \\ 0 & -s_{23} & c_{23} \end{bmatrix} \begin{bmatrix} c_{13} & 0 & s_{13}e^{-i\delta} \\ 0 & 1 & 0 \\ -s_{13}e^{i\delta} & 0 & c_{13} \end{bmatrix} \begin{bmatrix} c_{12} & s_{12} & 0 \\ -s_{12} & c_{12} & 0 \\ 0 & 0 & 1 \end{bmatrix} \begin{bmatrix} e^{i\alpha_1} & 0 & 0 \\ 0 & e^{i\alpha_2} & 0 \\ 0 & 0 & 1 \end{bmatrix} \quad (2.15)$$

And flavour and mass states are related by:

$$|\nu_i\rangle = U|\nu_\alpha\rangle,$$

where  $i = 1, 2$  or  $3$  designate the mass states and  $\alpha = e, \mu$  or  $\tau$  the flavour eigenstates. The coefficients  $c_{ij}$  and  $s_{ij}$  respectively mean  $\cos(\theta_{ij})$  and  $\sin(\theta_{ij})$  where  $\theta_{ij}$  is the mixing angle of mass states  $i$  and  $j$ . The phases  $\alpha_1$  and  $\alpha_2$  are non zero if the neutrinos are Majorana particles (*id est* if they are their own anti-particles). Finally  $\delta$  is the  $CP$  violation phase.

The fact that neutrinos oscillate and that the matrix  $U$  is not the identity matrix is not open to debate anymore as many experiments have measured these angles. The question is now whether this matrix is unitary or not. If it is not, this would mean that a fourth neutrino exists or that new physics is involved.

The neutrinos having a mass coming from a mechanism that is not the Higgs mechanism does not mean that the Standard Model of particle physics is wrong but it clearly means that it is incomplete.

### 2.2.3 Matter antimatter asymmetry

The observed Universe seems to be made of matter exclusively and not of antimatter. Of course antimatter exists in cosmic rays and in very violent phenomena but no planet, star nor galaxy made of antimatter has been detected so far. This is quite puzzling because if all matter was actually created by Gamow's ylem (see previous chapter) then matter and antimatter should have been produced in the exact same amount. Hence, when cooling down all the protons should have annihilated with all the antiprotons and the same for electrons and positrons. This is not completely true because the standard model predicts some violation of the  $CP$  symmetry through the weak interaction. However precise calculations show that this violation is not enough to explain the amount of matter left today. This may mean that a new physics, which breaks  $CP$  symmetry, is at play at high energies hence that the standard model should be enhanced.

### 2.2.4 Dark matter

As we have seen in chapter 1, cosmology requires a massive stable neutral particle. There is no such particle in the standard model. If cosmology is correct, this is clearly a shortcoming of the model and a call to go beyond it.

### 2.2.5 Theoretical problems

Unlike the previous points which are maybe loopholes of the standard model, the following points are maybe more philosophic as they are more answered questions than real issues of the

model itself.

### 2.2.5.1 Quantum Chromodynamics and the strong $CP$ problem

As it can be seen from equations 2.4, the weak interaction maximally violates the  $CP$  symmetry: indeed  $W^a$  bosons are only coupled to left-handed particles. There is actually no known reason why the strong interaction should not break, at least partially, the  $CP$  symmetry. Indeed, one would expect a term of the kind:

$$\mathcal{L} \supset \theta \sum_{A=1}^8 \frac{1}{4\pi^2} G_{\mu\nu}^A (\epsilon^{\mu\nu\sigma\rho} G_{\sigma\rho}^A) \quad (2.16)$$

added to the Yang–Mills Lagrangian to be satisfactory. The changes this term would imply in the covariant derivative, would break  $CP$  symmetry. Though a priori the parameter  $\theta$  is allowed to take any value between 0 and  $2\pi$ , experimental constraints imply that it is smaller than  $10^{-9}$ . One way to explain why this parameter has such a small value is the Peccei–Quinn mechanism [24] as restated by Weinberg [28] and Wilczek [29], is to invoke a new  $U(1)$  symmetry and to see the parameter  $\theta$  as a pseudo–scalar field called the axion. A priori the vacuum expectation value of the axion can be anything but QCD phase transition would force it to be zero.

Axion is a good candidate for dark matter as it can form Bose–Einstein condensates which would act as a cold dark matter. Current experimental and observational constraints impose its mass to be much lower than 1 eV. This means that the axion, if it exists cannot decay nor annihilate into high energy particles, hence it is not of great interest in the scope of this work.

However the fact that the standard model is not able to explain why  $CP$  violation is so low (if not null) for the strong sector is a problem.

### 2.2.5.2 Parameters problem

One frustrating thing with the standard model is that though it explains how particles gets a mass from coupling to the Higgs, it does not explain the hierarchy among the masses, their mixings. Twenty free parameters appear like given features of the theory and it would be satisfactory to understand whether these values come from a mechanism we do not understand yet or are fundamental constants of the Universe.

Moreover, there is no explanation to the fact that the standard model particle content is made of three similar families. Cosmology constrains the existence of a forth family but a fundamental reason would be more satisfactory.

### 2.2.5.3 Unification

Unification is an old dream of physicists. Since Maxwell has been able to unify electric and magnetic field, people have tried to go further, the hope being to describe every interaction with a single field. The standard model goes one step further as it considers that electromagnetism and weak interaction are intrinsically correlated as being the result of the breaking of a larger symmetry group. However it still requires three coupling constants.

A nice feature of the standard model is that it is renormalisable. Hence all the corrections at the loop level can be interpreted as a running of the coupling constants. What is interesting is that the three constants of the standard model almost converge to a common value at very high energy. Almost but not quite. This is often considered as a hint that, at high energy, new physics should be present. One of its effects would be to make the constants exactly converge at high energy.

Moreover the standard model cannot take into account one of the known interactions: gravity.

#### 2.2.5.4 Hierarchy problem

By construction, the masses of all the particles we know, cannot be larger than the scale at which the  $SU(2)_w \otimes U(1)_Y$  breaks down. The theory does not predict this scale. The only fundamental energy scale of physics is the Planck one which is completely defined by fundamental constants of physics:

$$m_P = \sqrt{\frac{\hbar c}{8\pi G}} \sim 2.43 \times 10^{18} \text{ GeV}.c^{-2}.$$

This is the scale at which quantum effects should start to affect gravity. This scale is about 17 orders of magnitude higher than the electroweak one ( $\sim m_W$ ). What is causing the breaking of the electroweak symmetry at such a low energy? Moreover, if one computes the quantum corrections to the Higgs mass, many terms proportional to the scale  $\Lambda$  at which the symmetry has broken down will appear:

$$\begin{aligned} \delta m_h^2 &= -\frac{y_f^2}{16\pi^2} (2\Lambda^2 + 6m_f^2 \log(\Lambda/m_f) + \dots) \\ \delta m_h^2 &= \frac{\lambda_S}{16\pi^2} (\Lambda^2 - 2m_S^2 \log(\Lambda/m_S) + \dots) \end{aligned} \quad (2.17)$$

where the first one comes from fermion loops and the second one from scalar loops. If the correct scale for  $\Lambda$  is the Planck scale, this means that these terms have to cancel out each other with a precision of order  $10^{-32}$  which would require an extreme fine tuning. This is absolutely not satisfactory from a theoretical point of view and may be interpreted as a hint that an intermediate energy scale should involve new physics.

Because of these more or less important issues, many new models of particle physics have been proposed in the past decades. The most obvious constraint is that any new theory has to be consistent with the standard model at low energies. Up to now no model which fix all the issues listed above have been proposed, however, some theories are considered as good steps forward in the direction of solving them. None of them are fundamental theories (in the sense that they are not able to unify all the interactions in a coherent pattern) but are effective theories, *id est* theories valid up to some energy scale, the same way as the standard model.

## 2.3 Supersymmetry

The Poincaré group is the group of the isometries of Minkowski's space–time. Its algebra is defined by the following commutation relations:

$$\begin{aligned} [P_\mu, P_\nu] &= 0 \\ [M_{\mu\nu}, P_\rho] &= \eta_{\mu\rho}P_\nu - \eta_{\nu\rho}P_\mu \\ [M_{\mu\nu}, M_{\rho\sigma}] &= \eta_{\mu\rho}M_{\nu\sigma} - \eta_{\mu\sigma}M_{\nu\rho} + \eta_{\nu\rho}M_{\mu\sigma} - \eta_{\nu\sigma}M_{\mu\rho} \end{aligned}$$

where  $\eta_{\mu\nu}$  is Minkowski's metric and  $P_\mu$  and  $M_{\mu\nu}$  are the generators of translations and Lorentz transformations respectively. Coleman–Mandula theorem forbids any extension of the Poincaré algebra<sup>a</sup>. However it is possible to extend it into a superalgebra, *id est* by adding anticommutation relations between the new generators instead of commutation relations. This means that it is possible to add new transformations which charges will be transformed as spinors by Poincaré transformation. This seems a natural extension of the logic that has ruled the construction of the standard model and it is why supersymmetry appears in many fundamental theories. However, in this section I will limit the discussion to what is often referred to as low energy supersymmetry.

In this class of models, one adds a charge  $Q = \begin{pmatrix} Q_\alpha \\ \bar{Q}^{\dot{\alpha}} \end{pmatrix}$  which transforms like a spin 1/2:

$$\begin{aligned} [M_{\mu\nu}, Q_\alpha] &= \frac{1}{2} (\sigma_{\mu\nu})_\alpha^\beta Q_\beta \\ [M_{\mu\nu}, \bar{Q}^{\dot{\alpha}}] &= -\frac{1}{2} (\bar{\sigma}_{\mu\nu})^{\dot{\beta}}_\alpha \bar{Q}^{\dot{\beta}} \\ [Q_\alpha, P_\mu] &= 0 \\ [\bar{Q}^{\dot{\alpha}}, P_\mu] &= 0 \end{aligned}$$

and satisfies the anticommutation relations:

$$\{Q_\alpha, \bar{Q}^{\dot{\beta}}\} = 2(\sigma^\mu)_{\alpha\dot{\beta}} P_\mu \tag{2.18}$$

$$\{Q_\alpha, Q_\beta\} = 0. \tag{2.19}$$

This charge commute with the mass operator ( $P^2 = P_\mu P^\mu$ ) but not with the spin operator ( $W^2 = \frac{1}{4}\epsilon_\mu^{\nu\rho\sigma} P_\nu M_{\rho\sigma} \epsilon^{\mu\lambda\kappa\gamma} P_\lambda M_{\kappa\gamma}$ ). This means that supersymmetric multiplets are made of particles with the same mass but with different spin. Equation 2.19 implies that it is always possible to find a particle (defined by its spin  $s$  and momentum  $p$ ) that satisfies  $Q_\alpha|s, p\rangle = 0$ . Here we will consider that  $\alpha$  and  $\beta$  can only take the values 1 and 2. Making use of equation 2.18 one gets  $\bar{Q}_1|s, p\rangle = 0$  and

$$\bar{Q}_2|s, p\rangle = \sqrt{4E} \left| s - \frac{1}{2}, p \right\rangle. \tag{2.20}$$

This means that each fermion has a scalar super partner which has exactly the same mass. This is what we needed to cancel out the term of order  $\Lambda^2$  in equation 2.17 and to solve the hierarchy

---

<sup>a</sup>except of course with internal symmetries

problem. However a scalar particle with the same mass as an electron (511 keV) and the same couplings, if it existed, should have been discovered already. This means that if supersymmetry exists, it is a broken symmetry and the scale at which it has been broken is higher than the electroweak scale.

Supersymmetry implies that the particle content is at least twice<sup>b</sup> as big as the one currently known. Usually the scalar partners of fermions are called sfermions (selectron, smuon, stau, sneutrino, squarks) and the fermionic partners of gauge bosons are called gauginos (wino, bino, gluino). A study of the triangle diagrams reveals that avoiding anomalies requires two higgs doublets on top of the singlet one. Their superpartners are called higgsinos.

Because electroweak symmetry breaking happens after supersymmetry breaking, some mixing can happen between neutral higgsinos and gauginos (neutralinos  $\chi^0$ ) as well as among charged ones (charginos  $\chi^\pm$ ). The precise phenomenology of supersymmetric theories depends on the supersymmetry breaking mechanism. So it is difficult to draw general conclusions. An important point however is that supersymmetry predicts fast proton decay because lepton and baryon numbers are not conserved any more. This is in contradiction with present experimental limits on proton lifetime. This issue is solved by invoking a new conservation law:  $R$ -parity. It states that the quantity  $R = (-1)^{3B-3L+2s}$  is conserved by all processes. This is already the case for all standard model interactions and stabilises the proton. Another consequence of this parity is that supersymmetric particle can only be created in pairs. This means that one needs an energy at least twice as large as their masses, so that only high energy colliders can produce them. This also implies that the lightest supersymmetric particle (LSP) is stable.

If the lightest supersymmetric particle is a neutralino (this depends on the values of the many free parameters of the theory), it is a suitable candidate for dark matter as it is stable, neutral, and ranges in the electroweak scale. This case is favourable to us as this kind of particle would also annihilate, and in the case of a dark matter halo, produce cosmic rays. However, the neutralino being a Majorana, its annihilation into leptons is helicity suppressed so it would produce little electron-positron pairs.

It is however noteworthy that some supersymmetric models predict the lightest supersymmetric particle to be the gravitino (the superpartner of the graviton). In this case, it can also be a suitable candidate for dark matter but would produce absolutely no signal for indirect detection.

Finally it is important to stress that supersymmetric theories can solve the hierarchy problem and the muon anomalous magnetic moment issue but is of no use for the other issues stated previously. As an effective theory, it does not achieve unification of gauge couplings but improves it considerably.

There are many supersymmetric models, more or less constrained, with more or less free parameters. The Large Hadron Collider will probe many supersymmetric models and if supersymmetry really breaks at low energy it has a great chance to discover it.

---

<sup>b</sup>Here we have considered only one supersymmetric charge however if there are more than one, the number of superpartners increases.

## 2.4 Extra-Dimensions

This section is mainly inspired by the lectures of Rizzo [27].

Instead of introducing new physics at an intermediate scale between the electroweak and the Planck ones, another idea to solve the hierarchy problem is to lower the Planck scale. If there are  $n$  extra spatial dimensions<sup>c</sup> but for some reason we (and all the standard model particles we are made of) cannot see them, then the Planck scale we measure in four dimensions  $M_p$  is lower than the fundamental reduced Planck scale  $M_D = \sqrt{\frac{\hbar c}{8\pi G}} \sim 2 \times 10^{18}$  GeV. Indeed, gravity being a geometrical effect, it feels all the existing dimensions and by Gauss theorem we can relate them as

$$M_p^2 = \left(\frac{c}{\hbar}\right)^n V_n M_D^{n+2}, \quad (2.21)$$

where,  $V_n$  is the volume of the extra space. The volume  $V_n$  has to be defined because we would be sensitive to an infinite dimension. Depending on the exact nature of the dimensions, it is possible to get  $M_p$  as low as the electroweak symmetry breaking scale so that there is no hierarchy problem. Let us consider the most popular models:

### 2.4.1 The Arkani-Hamed, Dimopoulos, Dvali (ADD) [9] models

In these models, also called large extra dimensions, all extra dimensions are compactified so  $V_n = (2\pi)^n \prod_{i=1}^n R_i$ ,  $R_i$  is the radius of each extra dimension. Short scale tests of gravity constrain  $n$  to be at least as large as two if one wants  $M_p$  to be of the order of 1 TeV. Because the extra-dimensions are compactified, the momentum of the graviton (the only particle able to propagate everywhere in the bulk *id est* the full space) in the extra directions is quantised and acts like a mass term. These states are called Kaluza-Klein excitations. As shown by Grard & Nuyts [21], the exact mass hierarchy (the KK-tower) strongly depends on the boundary conditions imposed and so does the stability of the excited states. Some of these states can be viable candidates for dark matter but their couplings are so low that they are of no interest for indirect detection. Moreover, if dark matter comes from another mechanism, these models could nevertheless have an impact. Indeed short range gravity would be modified and this can change dark matter self interaction and its interaction with standard particles (see Qin *et alii* [25]).

### 2.4.2 The Randall-Sundrum (RS) [26] models

In this class of models, also called warped extra dimensions, there is only one extra dimension (with coordinate  $y$ ) which is compactified on the  $S^1/Z_2$  orbifold (*id est* a torus with a parity symmetry which make the points  $y = 0$  and  $y = \pi R$  fixed points under symmetry and

---

<sup>c</sup>It is possible to also add extra time dimensions but they induce particles with negative mass (tachyons) which, if they interact with standard model particles, can damage causality.

periodicity). The brane (*id est* the subspace)  $y = 0$  is called the Planck wall and the brane  $y = \pi R$  is called the standard model (or TeV) wall. The metric of the space is:

$$ds^2 = e^{-2k|y|} \eta_{\mu\nu} dx^\mu dx^\nu - dy^2, \quad (2.22)$$

where  $\eta_{\mu\nu} = \text{diag}(1, -1, -1, -1)$  is the Minkowski metric and  $k$  is a measure of the curvature of this space. Equation 2.21 gives  $M_p^2 = \left(\frac{c}{\hbar}\right) \frac{M_D^3}{k} (1 - e^{-2\pi k R})$ . To avoid any hierarchy problem,  $k$  is taken to be of order  $M_D$  so actually  $k \sim M_D \sim M_P$  and so are all other masses but a look at the action shows that the masses we measure in the TeV wall are  $m e^{-k\pi R}$  hence of the TeV order. So the hierarchy problem is solved. Moreover, the coupling of the excited states of the graviton to the other particles is of the weak scale, making it a nice candidate for dark matter indirect detection.

Many variations of this model can be found in the literature, either with more branes, more dimensions, or gauge bosons and fermions allowed to live in the bulk. The interested reader can look for Rizzo [27] and the references therein. These modifications are quite interesting as they can also solve the flavour problem.

### 2.4.3 Universal Extra Dimensions (UED) [7] models

In the case where some of the dimensions are large enough to lower the Planck scale and others are small enough to allow standard model particles to propagate in them, they can also have KK-towers. Again, the phenomenology strongly depends on the boundary conditions. However this is quite dangerous as it can spoil many electroweak precision tests. One way to get rid of this problem is to introduce a Kaluza–Klein parity, its main effect is to suppress single odd Kaluza–Klein excitation states coupling to the standard model. A side effect is that the lightest excited particle (LKP) is stable and lies in the electroweak range, making it a perfect dark matter candidate. There is little difference between a lightest supersymmetric particle and a lightest Kaluza–Klein state particle, except for the spin. This means that the Large Hadron Collider (LHC) will have a hard time to distinguish UED from supersymmetry, unless the radii of the extra dimensions are small enough to allow production of the second excitation state. If the LKP is the excited photon, then its coupling to leptons is large, which is interesting for us.

Kaluza–Klein parity does not have to be imposed by hand but can naturally arise from topology and Lorentz invariance, see for instance Cacciapaglia *et alii* [15]. In such a case, the parity would sound much less ad hoc than  $R$ -parity.

## 2.5 Other models

Many other models of physics beyond the standard model have been proposed in the last few years. Too many to be described in this thesis, so I will only quote the most famous ones.

### 2.5.1 Little Higgs

Proposed by Arkani-Hamed *et alii* [8], this model suggests that the mass of the Higgs is protected by a spontaneously broken global symmetry. This means that the Higgs would be a

pseudo–Nambu–Goldstone boson. The stabilisation of the Higgs mass is ensured by the the new couplings which explicitly break the electroweak symmetry. The new symmetry also implies a set of new particles, symmetric to the standard model and with the same spin, that protects each mass from quadratic divergences. Because this would also affect electroweak precision measurements, a parity has to be added. This  $T$ –parity cancels out tree level coupling to the standard model. A side effect of this parity is that the lightest  $T$ –odd particle (LTP) is stable and is a good candidate for dark matter. In many cases the LTP is the heavy symmetric partner of the photon (see Cheng & Low [16]), the coupling of which is quite strong with fermions.

## 2.5.2 Technicolor

Introduced by Eichten & Lane [19] and Dimopoulos & Susskind [18], this model addresses the hierarchy problem by considering a dynamical symmetry breaking. Hence the Higgs boson should not exist and  $W$  and  $Z$  get their mass from new gauge bosons and quarks and leptons from a condensate of *technifermions*. The first versions of this model has been excluded by precision measurements so it is a little out of fashion now. However, extensions of the original technicolor theory (walking technicolor) that are in agreement with all experimental constraints exist. These models predict viable candidates for dark matter which have a correct relic density and, in some cases, can annihilate copiously into fermion pairs (see for instance Kainulainen *et alii* [22]). However, again, an ad hoc discrete symmetry is necessary to stabilize the dark matter candidate.

## 2.6 Phenomenological models

The models I will quickly present here are less theoretically motivated as they only try to address the dark matter issue and not the known “problems” of the standard model.

### 2.6.1 Minimal Dark Matter

Cirelli *et alii* [17] have investigated what is the simplest ingredient one could add to the standard model in order to provide a satisfactory dark matter candidate. They looked for extra multiplets with minimal spin, isospin and hypercharge quantum numbers which stable and satisfies all the usual dark matter constraints. This model does not require any new interaction so its predictions are quite straightforward. Depending on which data are considered as dark matter signal, the favoured multiplet is not always the same. However, requiring the candidate to be stable and to agree with direct detection constraints imply it has to be a fermionic 5-uplet or scalar 7-uplet. This sounds a little unnatural as nothing higher than a triplet exists in the standard model, however as long as no other new physics has been proven to be true, there is no reason not to consider this scenario.

### 2.6.2 Exciting Dark Matter

Following the idea of Boehm *et alii* [14], Finkbeiner & Weiner [20] initially introduced exciting dark matter to explain the 511 keV emission observed by INTEGRAL [23], this model

requires the dark matter particle to have an excited state 1 or 2 MeV above the ground state which can de-excite by emitting electron-positron pairs. It has been then successively modified to explain many other data, each time adding new excited states at the required energy.

## Conclusion

Though the standard model of particle physics does not provide a correct particle for dark matter, it is nice to see that many models destined to improve the standard model propose a viable dark matter candidate as a by product. The fact that new physics is expected at the electroweak scale, the same scale necessary for a thermally produced dark matter is surprising. This coincidence is some times referred to as the WIMP miracle and is one of the main reason to believe in dark matter rather than in a change in the laws of gravitation. However many candidates exist, and even the Large Hadron Collider may have a hard time to distinguish all of them. This is why it is important to look for direct and indirect detection of dark matter. This can provide very useful complementary information. But before one can distinguish an exotic signal from dark matter in cosmic rays, one needs to understand them properly.

## Bibliography

- [1] This chapter is mainly based on the lectures [2, 3] I had the opportunity to attend.
- [2] Deandrea, A. Interactions électrofaibles et introduction à la supersymétrie. Lectures given at the Master of the École Normale Supérieure de Lyon. Lyon, 2007 37
- [3] Masiero, A. The Standard model of particle physics, and beyond. Lectures given at the ISAPP summer school. Madrid, 2008 37
- [4] Abachi, S., Abbott, B., Abolins, M., *et alii* . 1995, Phys. Rev. Lett., 74, 2422 28
- [5] Abashian, A., Gotow, K., Morgan, N., *et alii* . 2002, Nuclear Instruments and Methods in Physics Research Section A: Accelerators, Spectrometers, Detectors and Associated Equipment, 479, 117 27
- [6] Abe, F., Akimoto, H., Akopian, A., *et alii* . 1995, Phys. Rev. Lett., 74, 2626 28
- [7] Appelquist, T., Cheng, H.-C., & Dobrescu, B. A. 2001, Phys. Rev., D64, 035002 35
- [8] Arkani-Hamed, N., Cohen, A. G., & Georgi, H. 2001, Phys. Lett., B513, 232 35
- [9] Arkani-Hamed, N., Dimopoulos, S., & Dvali, G. R. 1998, Phys. Lett., B429, 263 34
- [10] Aubert, B. *et alii* . 2002, Nucl. Instrum. Meth., A479, 1 27
- [11] Bagnaia, P. *et alii* . 1983, Phys. Lett., B129, 130 28
- [12] Banner, M. *et alii* . 1983, Phys. Lett., B122, 476 28

- 
- [13] Bennett, G. W. *et alii* . 2006, Phys. Rev., D73, 072003 28
  - [14] Boehm, C., Hooper, D., Silk, J., Casse, M., & Paul, J. 2004, Physical Review Letters, 92, 101301 36
  - [15] Cacciapaglia, G., Deandrea, A., & Llodra-Perez, J. 2010, JHEP, 03, 083 35
  - [16] Cheng, H. & Low, I. 2004, Journal of High Energy Physics, 8, 61 36
  - [17] Cirelli, M., Fornengo, N., & Strumia, A. 2006, Nuclear Physics B, 753, 178 36
  - [18] Dimopoulos, S. & Susskind, L. 1979, Nucl. Phys., B155, 237 36
  - [19] Eichten, E. & Lane, K. D. 1980, Phys. Lett., B90, 125 36
  - [20] Finkbeiner, D. P. & Weiner, N. 2007, Phys. Rev. D, 76, 083519 36
  - [21] Grard, F. & Nuyts, J. 2006, Phys. Rev., D74, 124013 34
  - [22] Kainulainen, K., Virkajärvi, J., & Tuominen, K. 2010, Journal of Cosmology and Astro-Particle Physics, 2, 29 36
  - [23] Knödseder, J., Lonjou, V., Jean, P., *et alii* . 2003, A&A, 411, L457 36
  - [24] Peccei, R. D. & Quinn, H. R. 1977, Phys. Rev. Lett., 38, 1440 30
  - [25] Qin, B., Pen, U., & Silk, J. 2005, ArXiv e-prints [astro-ph/0508572](https://arxiv.org/abs/astro-ph/0508572) 34
  - [26] Randall, L. & Sundrum, R. 1999, Phys. Rev. Lett., 83, 3370 34
  - [27] Rizzo, T. G. 2004 34, 35
  - [28] Weinberg, S. 1978, Phys. Rev. Lett., 40, 223 30
  - [29] Wilczek, F. 1978, Phys. Rev. Lett., 40, 279 30

## Chapter 3

# Cosmic Rays

Cette obscure clarté qui tombe des étoiles.

*Pierre Corneille in Le Cid*

## 3.1 A short history of Cosmic Rays

### 3.1.1 Discovery

Since its invention by William Gilbert (1544–1603) around 1600, it is known that an electroscopes discharges with time. This is due to phenomena that ionises the apparatus. It took some time to discover and understand the main one but after Henri Becquerel’s (1852–1908) discovery of radioactivity, it was understood that this ionisation was caused by natural radioactivity of the Earth. The first real study dedicated to the ionisation of the atmosphere has been performed by Charles Wilson (169–1959), it actually led him to build the first particle detector: a cloud chamber for which he received the Nobel Prize in 1927. However in 1910 a German Jesuits, Theodor Wulf (1868–1946), had the surprising idea to measure the ionisation of his electroscopes on the top of the Eiffel tower and realised that the ionisation increased rather than decrease as one should expect for a phenomenon caused by the Earth itself. Two years later, the Austrian physicist Victor Hess (1883–1964) did the same experiment with much more precise apparatus he designed and in a balloon, hence at much higher altitude. He showed that indeed the radiation causing ionisation was less and less intense within the first kilometre above the ground but increasing again from one to five kilometres. He also did a flight during the solar eclipse of April the 12th 1912 to show that the radiation had no solar origin [20]. Victor Hess concluded that the ionising radiation was not only due to Earth radioactivity but also had a cosmic origin. All his life long, Victor Hess carried on improving the technique of cosmic rays detection and his efforts were awarded by a Nobel prize in 1936 “for his discovery of cosmic radiation”.

### 3.1.2 A tool for particle physics

The year Victor Hess received his Nobel prize, so did Carl Anderson (1905–1991) “for his discovery of the positron”. Indeed in 1930, Robert Millikan (1868–1953) and Carl Anderson, following the idea Dmitri Skobelzyn (1892–1990) had three years before, used a cloud chamber to detect cosmic rays at the ground. Thanks to the magnet they applied to their detector, they found that positive and negative particles were present in the same quantity in cosmic rays. They first thought that the positive unit charge particles were protons (as it was the only known particle of the kind), however kinematic studies clearly showed the mass was consistent with the one of the electron. It is only after this discovery of positrons in cosmic rays that Chadwick, Blackett and Occhialini discovered  $\beta^+$  radio-activity and Curie and Joliot saw electron–positron pair production by  $\gamma$  radiation. Hence the first discovery of anti–matter and the confirmation of Dirac’s electron theory came from cosmic rays [7].

A few years later, other new particles were discovered in cosmic rays. Anderson again discovered muons in 1936, Powell and his collaborators discovered the charged pions in 1937, Rochester and Butler discovered the kaon in 1947, the same year strangeness was first discovered through the  $\Lambda$  baryon seen in cosmic ray induced hadronic interaction. It is only in 1948 that the technology to artificially produce new particles through collisions became available at the Berkeley synchrotron. It was the beginning of modern particle physics as we know it. Because colliders are able to produce collisions in copious amount they have led the experimental research up to the present day, however it seems that after the generation of linear colliders that should follow the

Large Hadron Collider of CERN, it will probably not be possible to reach higher energies and some people suggest we should go back to cosmic rays to study particle physics. However, this will be faced by very low luminosity issues.

It is also important to stress that the study of cosmic rays, not only allowed the discovery of many particles but it also motivated the development of new technologies to detect, and to analyse high energy particles. Cloud chambers, expansion chambers, photographic emulsions etc. were all invented for the study of cosmic rays.

Finally it is nice to see that even now, most particle physics experiments (ATLAS, CMS, T2K, etc.) use cosmic rays to calibrate their instruments, making cosmic rays a major ingredient of modern particle physics.

### 3.1.3 A new era of astrophysics

Of course the study of cosmic rays did not stop with the invention of colliders as cosmic rays are a subject of study themselves. Thanks to Victor Hess, many cosmic ray observatories flourished all over the world, mainly on the top of mountains (Mont Wilson, Pic du Midi, Chacaltya etc.). Analysis of the spectra, the mass composition and the anisotropies of cosmic rays is an on-going work.

## 3.2 Modern Cosmic Ray detection methods

### 3.2.1 Balloons

Since the first balloon launched in the United Kingdom by Cecil Powell (1938), techniques have done tremendous progresses and this technology is still in use today in spite of the development of satellites because it is cheaper and more convenient.

#### 3.2.1.1 CREAM

The Cosmic Ray Energetics And Mass[10] experiment is a set of various particle detectors (a Timing Charge Detector (TCD), a Čerenkov Detector (CD), a Transition Radiation Detector (TRD), a Čerenkov Camera (CherCam), a Silicon Charge Detector (SCD), scintillating fiber hodoscopes, and a tungsten-scintillating fiber calorimeter). It is able to measure charges up to 26 elementary charges and energies between  $10^{11}$  and  $10^{15}$  eV. It has already performed five flights above the Antarctica at height of 38–40 km. CREAM is presently the best experiment to measure the ratios of secondaries to primaries which are extremely important for constraining cosmic ray propagation, as we will see in Sect. 5.1.2.

#### 3.2.1.2 ATIC

The Advanced Thin Ionization Calorimeter[23] is quite similar to CREAM but is interested in lower energies (10 to 300 GeV/n), though it has been specifically designed for hadronic cosmic rays, it has been able to measure electrons (without distinction of charge) as well. It has performed two successful science flights above Antarctica, however less long and less high than the CREAM flights.

### 3.2.2 Satellites

A balloon cannot get much higher than a few tens of kilometres, the atmosphere being 800 km thick, understanding the data from balloon-borne detectors requires to model the interaction of cosmic rays with the air. Though we believe we understand these interactions, it cannot be excluded that some unknown systematic effects are taking place and falsify our data. This is why the new generation of cosmic ray detectors is placed at much higher altitudes.

#### 3.2.2.1 PAMELA

A Payload for Antimatter Matter Exploration and Light-nuclei Astrophysics [2] is an Italian particle detector installed on-board the Russian Resurs-DK1 satellite. It flies at an altitude ranging between 350 and 610 km and, thanks to its calorimeter and its magnetic spectrometer, it is probably the best instrument looking at cosmic rays of energies lower than 1 TeV, at the moment. It was launched the 15<sup>th</sup> of June 2006 and is taking data since. PAMELA is designed to measure cosmic ray fluxes on energy ranges never explored before, its design capabilities are recalled in Table 3.1. Though the collaboration has already started to release data, which will be discussed in paragraph 8.1, most of it is still to come. It is hoped that PAMELA will stay operational for a few more years.

Particle	Energy range for PAMELA	Energy range for AMS-02
$\bar{p}$	80 MeV - 190 GeV	up to 400 GeV
$e^+$	50 MeV - 270 GeV	up to 400 GeV
$e^-$	up to 400 GeV	around 1 TeV
$p$	up to 700 GeV	around a few TeV
$e^+ + e^-$	up to 2 TeV	around 1 TeV
Light nuclei ( $Z \leq 6$ )	up to 200 GeV/n	around a few TeV
Light isotopes (D, $^3\text{He}$ )	up to 1 GeV/n	up to 8 GeV/n
Antinuclei search	sensitivite to $10^{-7}$ in $\overline{\text{He}}/\text{He}$	$10^{-9}$ in $\overline{\text{He}}/\text{He}$

Table 3.1: PAMELA and AMS design goal performances. These numbers are taken from the PAMELA web-page<sup>c</sup> and the presentation of F. Barao in Annecy for the AMS: status and perspectives workshop<sup>d</sup>.

#### 3.2.2.2 Fermi

The Fermi Gamma-ray space telescope [17] is the result of a worldwide collaboration. It has been launched the 11<sup>th</sup> of June 2008 and is watching the sky ever since. It has not been designed for cosmic-ray study, yet, as it is actually a particle detector (tracker and calorimeter), it can be used to measure cosmic ray fluxes. However, as Fermi is not equipped with a magnet, it cannot distinguish positive from negative charge particles. Because its orbit is quite high

<sup>c</sup><http://tinyurl.com/yc6ok4g>

<sup>d</sup><http://tinyurl.com/ybzyceq>

(550 km) and with a small inclination with respect to the Equator ( $28.5^\circ$ ), the instrument has a lot of statistics and is not too sensitive to Earth magnetic field variations. The Fermi collaboration has already published electron plus positron fluxes from 7 GeV to 870 GeV (see paragraph 8.1) and may even measure the proton flux. Indeed, though the calorimeter is quite short for proton showers to develop, its large aperture may compensate this and allow a proton energy reconstruction (See Ref. [29]). Of course the most ground breaking results are to be expected in the diffuse gamma emission and gamma-ray sources.

### 3.2.2.3 AMS

Though it was initially scheduled for 2005, the Alpha Magnetic Spectrometer[6] is not in operation yet, but should be installed on the International Space Station (ISS) by the American shuttle Endeavour in November 2010. After a first test flight in 1998, the simplified version AMS-01 gave incredible results. AMS-02 should have been equipped with a powerful superconducting magnet (0.865 T) operating at 1.8 K thanks to helium evaporative cooling which should have been efficient for three years. By then, thanks to its various particle detectors (electromagnetic calorimeter, silicon tracker, transition radiation detector, time-of-flight counters, and ring-imaging Čerenkov detector) AMS-02 would have accumulated more precise data than any other cosmic ray detector before.

However, because of recent technical issues on the ISS the superconducting magnet is to be replaced by a permanent magnet with a field 6 times lower. The bright side of this situation is that AMS-02 should be able to stay in operation for ten years instead of three, hence have much better statistics and cover various Sun activity periods.

As it can be seen in Table 3.1, AMS-02 should get an insight to cosmic rays of a completely unexplored energy range which may be critical in our understanding of cosmic ray propagation and sources. One should note however, that AMS-02 will operate on the ISS at an altitude of 336–346 km, hence much lower than Fermi and PAMELA then its efficiency at low energy might be less good because of atmospheric pollution and Earth's magnetic field. This table however corresponds to the former design of the apparatus, it is not clear yet how the recent modifications will affect the performance.

### 3.2.2.4 CALET

The CALorimetric Electron Telescope [33] is an experiment which should be installed on the Japanese Experiment Module of the International Space Station around 2013. Its large calorimeters (1,760 kg) will be designed to measure electrons from 1 GeV to 10 TeV and nuclei from 10 GeV to 1,000 TeV. CALET should be able to look at energies extremely interesting for sources and cosmic ray propagation understanding. A smaller version has already successfully been tested on a balloon in the previous years. However, unlike AMS, CALET will not have a magnet and hence will not be able to distinguish antimatter from matter. Smaller prototypes of CALET (1/32 and 1/16 of the final size) have already been tested during balloon flights but they have not published any result yet.

### 3.2.3 Ground-based detectors

At very high energies, the detection of cosmic rays is challenged by the very low flux. An experiment in space cannot be much larger than a few  $\text{m}^2$  hence it is not helpful for energies higher than a few TeV. Indeed as it can be seen in figure 3.1, at this energy, the flux becomes so low that the statistics are too poor to give reliable data. This is why another technique has to be used : instead of looking for the cosmic ray itself, one looks at the shower created by its interaction with the atmosphere. Just like in a calorimeter, incoming particles are interacting with the matter and produce smaller ions, kaons and pions, which in turn decay into muons, electrons and photons. Photons can then be converted in electron pairs and electrons radiate high energy photons. All this process is called an Extensive Air Shower (EAS). Of course if the incoming particle is a photon or an electron, only the second part of the process takes place: it is an electromagnetic shower. Because these showers are extremely large, the probability to detect it is much higher than to detect the particle itself in space. Moreover the size limitations are much less stringent on the ground and collection areas of  $\text{km}^2$  are possible. Various techniques are used to detect these showers.

Pierre Auger was the first to discover these showers in 1939, and ever since, our understanding of the phenomenon has done incredible progresses. More or less refined analytical models exist that describe quite well electromagnetic showers but are much less precise for hadronic showers (those initiated by an incoming hadron). The techniques have really improved in the recent years and precise description are now necessary, this is why, new numerical simulations, which rely on the methods developed by particle collider physicists, have been proposed. Obviously describing the Earth atmosphere over a few kilometres is much more complex and much less under control than describing a man-made calorimeter. Moreover, the atmosphere is always changing and it becomes now crucial to be able to adapt the simulations to atmospheric conditions as they are monitored during data taking. A few simulations are now on the market (SYBILL, FLUKA...) but it is impossible today to state which one is better than the others and systematic errors will always dim the results relying on these methods.

#### 3.2.3.1 HESS

The High Energy Stereoscopic System [19] is made of four 12 m diameter Čerenkov telescopes installed in Namibia. These instruments actually use the Earth atmosphere as a calorimeter and observe the Čerenkov light emitted by relativistic particles produced by the interaction of cosmic rays with the atmosphere. HESS has been designed to measure gamma rays from 100 GeV to 100 TeV. Though it is extremely difficult to distinguish atmospheric showers originating from gamma rays and electrons (as they both are electromagnetic showers), the collaboration has been able to evaluate the electron cosmic ray flux up to 5 TeV. Unlike the gamma rays which usually come from the same direction as their source, the electron flux is believed to be isotropic, hence, by pointing the instrument far away from the galactic plane and from known sources, it is possible to estimate the electron flux. However, this analysis is not able to eliminate the diffuse gamma emission, hence has a 50% systematic error. Moreover, the hypothesis that the electron cosmic ray flux is isotropic at energies as high as a few TeV is clearly open to debate so the confidence one can put in such results is weakened.

Soon, HESS should be improved into a second stage (HESS2 [25]). It consists in adding one

much bigger telescope (28 m of diameter) in the middle of the four other ones. This should lower the energy threshold from 100 to 10 GeV, allowing HESS to reach the region covered by Fermi, allowing cross-calibration. Hence one can hope that this new stage may allow electron cosmic ray measurement at energies lower by one order of magnitude.

### 3.2.3.2 KASCADE Grande

The Karlsruhe Shower Core Array DETector [9] in Germany is a  $200\text{ m} \times 200\text{ m}$  array made of 252 detectors each of which consists of an electron/gamma detector and a muon detector. KASCADE is also equipped with a large central detector (no longer in use) designed to detect the hadronic part of the Extended Air Shower (EAS), and with a muon-tracking detector that aims to triangulate the height of the formation of the shower. After five years of data taking (and good measurement of the knee as can be seen on Fig. 3.1), KASCADE has been extended to KASCADE-Grande [12] by reassembling 37 detectors of the former EAS-TOP experiment from Gran Sasso Laboratories, Italy. Though the resolution in energy is now lower, the new size of the array ( $700\text{ m} \times 700\text{ m}$ ) allows the experiment to look at much higher energies. A small scintillator array called Piccolo has been added to trigger both arrays together. The principle of functioning of KASCADE is quite different from that of HESS as the former one aims to directly detect the particles of the extended air-shower (and not their Čerenkov light). By counting the number of electrons and muons (and eventually their energy) thanks to simulations of the interactions of cosmic rays with the atmosphere (CORSIKA), it is possible to reconstruct the mass and the energy of the incoming particle responsible for the shower. KASCADE Grande is actually the first experiment trying to measure at the chemical composition of cosmic rays at the energy of the knee and to see whether or not the knee is at the same energy for each cosmic component.

KASCADE is also hosting an experiment called a LOFAR PrototypE Station (LOPES) [21] which proved the feasibility of studying extended air-shower through the radio emission of the electrons produced by the electro-magnetic shower which are deviated by the Earth magnetic field.

During my Ph.D., I had the opportunity to spend a few weeks in Karlsruhe among the KASCADE Grande team which was extremely kind and patient to me. It was a very pleasant stay and I am really thankful for the time they spent to teach me the basics of experimental cosmic ray detection and data analysis.

### 3.2.3.3 Pierre Auger

The Pierre Auger cosmic ray observatory [14], in Malargüe, Argentina, relies on the same principle as KASCADE except that it is much larger ( $3,000\text{ km}^2$ ). To detect the electrons and the muons of the extended air shower, the 1,600 detectors of Pierre Auger, instead of scintillating like for KASCADE, watch at the Čerenkov light that each of these particles is creating inside the water tank the detector is made of. Moreover, four atmospheric fluorescence detectors, which, unlike the rest of the array, can work only during the night, are monitoring the deexcitation of di-nitrogen molecules that have interacted with the extensive air shower. The combination of these two methods and the size of the collection area, allows Pierre Auger observatory to monitor cosmic rays of energies higher than  $10^{18}\text{ eV}$  and to precisely measure

their incoming direction. Hopefully, in a few years, Pierre Auger should be completed with a second observatory in the northern hemisphere. It should be built in the Colorado and have a surface of approximately 21,000 km<sup>2</sup>. The interest of such an observatory is to cover the full extent of the sky and to look at even higher energies.

### 3.2.3.4 LOFAR

LOW Frequency ARray for radio astronomy [24] is a huge array of radio antennas spanning over the Netherlands, The United Kingdom, Sweden, Germany, and France. Some extensions to Poland and Ukraine are also under consideration. This instrument is simply a radio interferometer that will watch the 10–240 MHz frequency band. Though its main mission will be to monitor radio emission from very distant objects (redshifts from 1.5 to 10), as it has been demonstrated by LOPES, it will also be able to measure cosmic rays. Though it is larger than Pierre Auger, its effective collecting area will only be 1 km<sup>2</sup>. Hence it will cover the energy gap between KASCADE-Grande and Pierre Auger. However it is not possible yet to trigger LOPES without KASCADE hence it is not sure that LOFAR will actually be able to measure cosmic rays by itself. A smaller array built on the souther Pierre Auger site is under consideration and may help future development of the technique.

## 3.3 Current understanding of Cosmic Rays

After more than a century of study, Cosmic Rays still have many secrets to reveal. However since Wilson first looked at cosmic rays, our understanding of the phenomenon has evolved a lot.

### 3.3.1 Energy spectrum

The energy spectrum of Cosmic Rays is maybe their most striking feature: as it can be seen from fig. 3.1 space is rich in particles which can reach energies as high as  $\sim 10^{21}$ eV which is billions of times higher than the energy at which protons are accelerated in the LHC. At first glance, this spectrum looks like a power law which implies that a scale invariant process should be the origin of this phenomenon. However, when looking more carefully, a few features appear: the knee at  $\sim 10^{15.5}$ eV, the second knee at  $\sim 10^{17.5}$ eV, the ankle at  $\sim 10^{18.5}$ eV and a cut-off around  $\sim 10^{19.5}$ eV. The ankle can be understood as a faint but with softer spectrum population of cosmic rays that becomes more important than the other one at this energy. The Cosmic Rays above the ankle cannot be confined in the Milky Way hence they are believed to be of extragalactic origin. Indeed the gyroradius of a relativistic particle in a magnetic field  $B$  being  $R \sim \frac{E}{qB}$ , the maximal energy a confined proton can have for a magnetic field of  $1\mu G$  in galaxy of 20 kpc is  $\sim 2 \times 10^{18}$ eV. The two knees are more puzzling, indeed the spectrum gets softer there. Hence, these knees cannot be explained by the transition from one population to another as for the ankle, unless a very surprising coincidence is invoked. This feature should probably find its explanation either in a phenomenon taking place during the acceleration in the source, or in the propagation of the cosmic rays in the Galactic halo. The last feature will

be discussed in paragraph 3.3.4

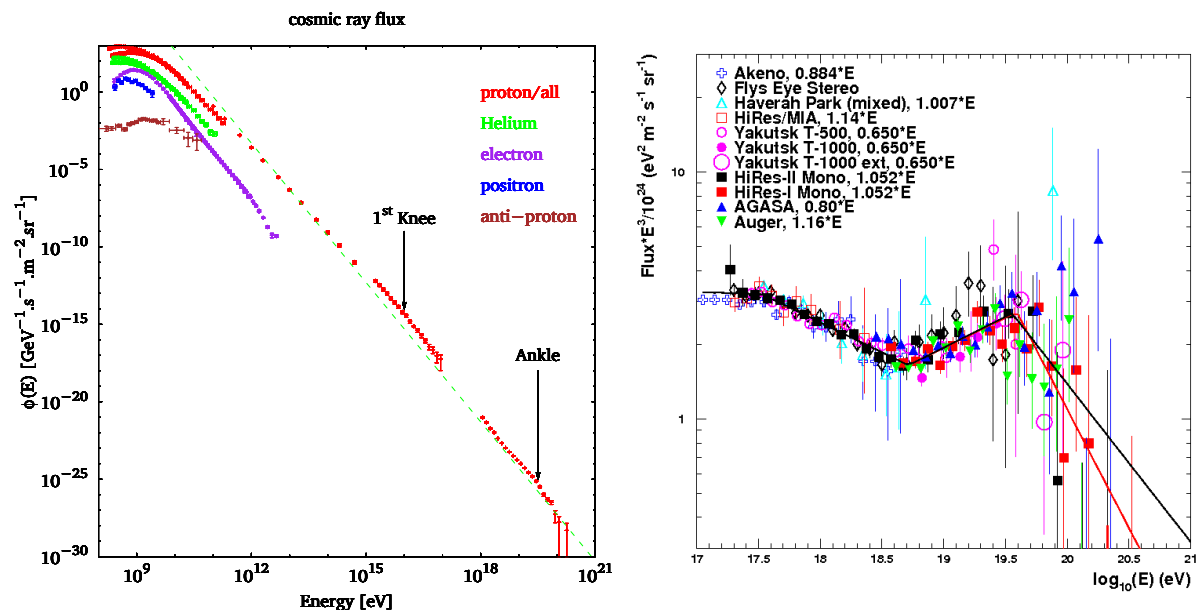


Figure 3.1: Left panel: Cosmic ray spectrum observed at the Earth. The red points correspond to protons or all cosmic ray data taken by BESS[28], IMAX[26], Cascade [8], and Pierre Auger [32] experiments plus an extrapolation from Ishimura *et alii* [22]. The green points are the Helium fluxes as measured by BESS[28] and IMAX[26]. Purple points correspond to electron (or electron plus positron) fluxes measured by AMS-01[5], Fermi[1, 27], and HESS[3, 4]. Blue points are for positron spectrum measured by AMS-01[5] and brown points show the anti-proton fluxes measured by BESS[13] and Caprice[15]. Right panel: Cosmic ray spectrum above  $10^{17}$  eV multiplied by  $E^3$  to make the second knee, the ankle and the GZK cut-off clearer. Plot taken from [11].

### 3.3.2 Composition

Quite surprisingly, the composition of cosmic rays is extremely rich. Though it is mainly made of protons, the cosmic rays also contain ions which can be as heavy as iron or nickel, and anti-matter (positrons and anti-proton). The study of the chemical composition of the cosmic rays shows that it is quite similar to that of the Solar system. This means that most cosmic rays are particles, of the Galactical medium or of stars, that have been accelerated by some process and not created ab nihilo at these high energies. However, as it can be seen if Fig. 3.2 some elements seem to contradict this analysis. For instance boron can be found quite copiously in cosmic rays but not in stars, indeed nuclear processes at high density do not favour creation of boron in large quantity as it is immediately transformed into heavier and more stable elements. The most reasonable explanation to this is that the cosmic ray borons are created by the interaction (spallation) of heavy cosmic rays (mainly carbon and oxygen) with the interstellar matter (hydrogen and helium).

Hence we have two populations of cosmic rays: one which is made of galactic matter accelerated by some astrophysical phenomena and injected at high energy in the interstellar medium that we will call primary cosmic rays and the other, which is produced by nuclear interaction of the primary population with the interstellar gas and that we call secondary cosmic rays. Moreover, there is also a tertiary population which is the result of the interaction of the secondary population with the interstellar gas. But this third population can be safely neglected in most cases (except for anti-protons) as it is usually extremely faint. Because of propagation and nuclear processes, these three populations do not have the same flux and this is why it is important to take them into account separately when doing predictions, even though experiments are not able to distinguish them.

One should pay attention to the fact that these names apply only when speaking of interstellar cosmic rays, indeed, unfortunately, the same names are used to distinguish cosmic rays coming from outer space (primaries) and the high energy particles of the extensive air shower (secondaries).

Another interesting species one can find in cosmic rays are anti-particles like positrons and anti-protons. Of course these are secondary cosmic rays only, as regular stars do not produce such particles in great amount. It seems quite unlikely, but it is possible that anti-stars, completely made of anti-matter, exist in the Universe and hence produce primary anti-cosmic rays. However, if they can produce anti-protons and positrons, they should also produce anti-nuclei which have never been detected in cosmic rays yet. By looking for anti-helium, AMS-02 should answer at this question and definitely close the hypothesis of anti-stars. Finally, the last interesting species, which does not appear in Fig. 3.2, are radio-isotopes. The presence of some of them (like  $^{10}\text{Be}$ ,  $^{36}\text{Al}$ ...) and the absence of short-lived radio elements, gives us an idea of how much time cosmic rays propagate in space: millions of years. This means that cosmic radiation is not an episodic phenomenon but is really a component of our Galaxy.

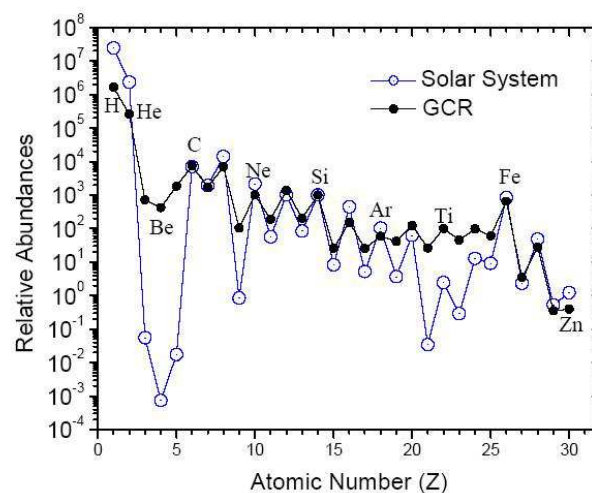


Figure 3.2: Elemental composition of cosmic rays (in black) compared to the one of the Solar system (in blue). This figure has been made by Prof. Israel for the Advanced Composition Explorer experiment's webpage<sup>f</sup>.

### 3.3.3 Isotropy

Until 2008, no experiment recorded any hint of anisotropies in the directions of the incoming cosmic rays at the Earth. Of course at very low energies, Solar wind contributes to the cosmic ray flux hence making it anisotropic. In the same way, the magnetic field of our planet deviates positive and negative charges in opposite directions creating an East-West anisotropy. However, at energies above a few 100 MeV, no anisotropy has been recorded yet. This is consistent with the fact that cosmic rays are trapped in the Milky Way by its magnetic field and that they diffuse a lot (see Chapter 5) and completely loose memory of their origin.

However ultra high energy cosmic rays ( $E \geq 10^{19}$  eV) cannot be confined by the Galactic magnetic field and should not be deflected much by intergalactic magnetic fields which are even weaker, this is why anisotropies are expected above the ankle. Of course a complete isotropy analysis requires a reliable statistics which is quite challenging with so low fluxes (around one particle per year and per km<sup>2</sup>). The first experiment to look for this was AGASA but did not see much. More recently Pierre Auger observatory published some results which seem to indicate that the directions of ultra high energy cosmic rays are correlated with the ones of the Active Galactic Nuclei [30], some not fully understood extremely violent phenomena which take place in the center of very heavy galaxies. However it is strange that since, with the accumulation of statistics, evidence for anisotropy became less pronounced [16].

### 3.3.4 Greisen-Zatsepin-Kuzmin cut-off

The energy of the cosmic microwave background is so low that it does not interact with heavy particles (but it does with electrons as we will see in Chapter 5), but this should not be true any more if one considers extremely energetic particles. This is why Greisen [18], Zatsepin and Kuzmin [34] predicted that at energies above  $10^{22}$  eV protons should interact with CMB photons through inverse Compton scattering and lose energy. It was then expected to see a drop in the flux at these high energies. This question was still under debate in the previous decade as the non existence of this cut-off could be a hint for new physics. However, recent and precise measurements from Pierre Auger observatory clearly closed the debate [31] in favour of the GZK cut-off as one can see in Fig. 3.1.

## Bibliography

- [1] Abdo, A. A., Ackermann, M., Ajello, M., *et alii* . 2009, Physical Review Letters, 102, 181101 47
- [2] Adriani, O. & et al. 1997, in International Cosmic Ray Conference, Vol. 5, International Cosmic Ray Conference, 49–+ 42
- [3] Aharonian, F., Akhperjanian, A. G., Anton, G., *et alii* . 2009, A&A, 508, 561 47
- [4] Aharonian, F., Akhperjanian, A. G., Barres de Almeida, U., *et alii* . 2008, Physical Review Letters, 101, 261104 47

---

<sup>f</sup><http://tinyurl.com/348uwzh>

- 
- [5] Alcaraz, J., Alpat, B., Ambrosi, G., *et alii* . 2000, Physics Letters B, 484, 10 47
- [6] AMS Collaboration, Aguilar, M., Alcaraz, J., *et alii* . 2002, Phys. Rep., 366, 331 43
- [7] Anderson, C. 1965, Nobel Lectures, Physics 1922-1941, Elsevier, Amsterdam 40
- [8] Antoni, T., Apel, W. D., Badea, A. F., *et alii* . 2005, Astroparticle Physics, 24, 1 47
- [9] Antoni, T., Apel, W. D., Badea, F., *et alii* . 2003, Nuclear Instruments and Methods in Physics Research A, 513, 490 45
- [10] Beatty, J. 1999, in International Cosmic Ray Conference, Vol. 5, International Cosmic Ray Conference, 61–+ 41
- [11] Bergman, D. R. & Belz, J. W. 2007, Journal of Physics G Nuclear Physics, 34, 359 47
- [12] Bertaina, M. & The KASCADE-Grande Collaboration. 2001, in International Cosmic Ray Conference, Vol. 2, International Cosmic Ray Conference, 792–+ 45
- [13] BESS Collaboration, Abe, K., Fuke, H., *et alii* . 2008, Physics Letters B, 670, 103 47
- [14] Bluemer, J. & Pierre AUGER Collaboration. 2003, in International Cosmic Ray Conference, Vol. 1, International Cosmic Ray Conference, 445–+ 45
- [15] Boezio, M., Bonvicini, V., Schiavon, P., *et alii* . 2001, ApJ, 561, 787 47
- [16] Giorgio Matthiae. 2009, TAUP Conference 49
- [17] Godfrey, G. L. & The GLAST Working Group. 1993, in Towards a Major Atmospheric Cherenkov Detector – II for TeV Astro/Particle Physics, ed. R. C. Lamb, 145–+ 42
- [18] Greisen, K. 1966, Physical Review Letters, 16, 748 49
- [19] Hermann, G. 1997, in Very High Energy Phenomena in the Universe; Moriond Workshop, ed. Y. Giraud-Heraud & J. Tran Thanh van, 141–+ 44
- [20] Hess, V. 1965, Nobel Lectures, Physics 1922-1941, Elsevier, Amsterdam 40
- [21] Horneffer, A., Falcke, H., & Kampert, K. H. 2002, in Proceedings of the 6th EVN Symposium, ed. E. Ros, R. W. Porcas, A. P. Lobanov, & J. A. Zensus, 23–+ 45
- [22] Ichimura, M., Kogawa, M., Kuramata, S., *et alii* . 1993, Phys. Rev. D, 48, 1949 47
- [23] Isbert, J., Guzik, G. T., & et al. 1995, in International Cosmic Ray Conference, Vol. 3, International Cosmic Ray Conference, 718–+ 41
- [24] Lazio, T. J. W., Kassim, N. E., Weiler, K., & Gross, C. A. 1999, in Bulletin of the American Astronomical Society, Vol. 31, Bulletin of the American Astronomical Society, 1498–+ 46
- [25] Masbou, J., Lamanna, G., & Rosier-Lees, S. 2009, in International Cosmic Ray Conference, Vol. 3, Proceedings of the 31<sup>st</sup> ICRC, Łódź, 1059 44

- 
- [26] Menn, W., Hof, M., Reimer, O., *et alii* . 2000, ApJ, 533, 281 [47](#)
- [27] Pesce-Rollins, M. & for the Fermi-LAT Collaboration. 2009, ArXiv e-prints [0912.3611](#) [47](#)
- [28] Shikaze, Y., Haino, S., Abe, K., *et alii* . 2007, Astroparticle Physics, 28, 154 [47](#)
- [29] Smith, P. D., Hughes, R. E., Winer, B. L., Wood, T. W., & for the Fermi LAT Collaboration. 2009, ArXiv e-prints [0912.3777](#) [43](#)
- [30] The Pierre AUGER Collaboration. 2008, Astroparticle Physics, 29, 188 [49](#)
- [31] The Pierre AUGER Collaboration. 2008, Physical Review Letters, 101, 061101 [49](#)
- [32] The Pierre Auger Collaboration. 2010, ArXiv e-prints [1002.1975](#) [47](#)
- [33] Torii, S., Tateyama, N., Tamura, T., *et alii* . 2000, in American Institute of Physics Conference Series, Vol. 504, Space Technology and Applications International Forum, ed. M. S. El-Genk, 187–192 [43](#)
- [34] Zatsepin, G. T. & Kuz'min, V. A. 1966, Soviet Journal of Experimental and Theoretical Physics Letters, 4, 78 [49](#)



# Chapter 4

## Cosmic Ray sources

La source désapprouve presque toujours l'itinéraire du fleuve.

*Jean Cocteau*

Where do cosmic rays come from? Astrophysical phenomena that can produce high or ultra high ( $\geq 10^{18}$  eV) energy cosmic rays are not so many. In this chapter, I discuss primary cosmic rays (created by violent phenomena in the Galaxy), secondaries (created by the interaction of cosmic rays with the interstellar medium), and finally more putative sources of cosmic rays. For each component it is important to know two things in order to perform predictions: the production energy spectrum of cosmic ray and the spatial distribution of the sources in the Milky Way.

## 4.1 Primary Cosmic Rays

Obviously, the number of processes that can produce high energy particles in such a copious amount is small. Though we cannot have in situ observation, the community is now quite convinced that two classes of objects are responsible for cosmic rays at least up to a few hundreds of TeV: supernova remnants and pulsars. Both these objects come from the explosion of a star, hence there are many of them in the Milky Way (where it is estimated that one star explodes every 20 or 50 years [*exempli gratia* 53, 56, 85]). More over, only a small fraction of the energy released by the explosion is necessary to account for the energy measured in cosmic rays. Finally, as we will see later, the cosmic ray spectral index predicted by Fermi acceleration (see section 4.1.1.1) is consistent with radio observation and coherent with what we know about cosmic ray propagation. Pulsars are a little different as they do not contribute to the cosmic ray ion population but only to electrons and positrons.

The explosion of a star sometimes much heavier than our Sun is an extremely violent phenomenon called a supernova. This crucial event in the life of a Galaxy, allows to enrich the interstellar medium in elements heavier than helium which were not synthesised during the primordial nucleosynthesis (see paragraph 1.2.1.2), this leads to more complex chemistry and eventually at some point of enrichment, to life. The study of this explosion is a very active field of research involving very complex magnetohydrodynamical simulations. Baade & Zwicky [8] were the first ones to suggest supernovæ as cosmic ray sources.

Supernovæ are believed to be of two kinds: thermonuclear or core-collapse. Thermonuclear supernova explosions happen when a white dwarf star accretes mass from a companion, when its mass reaches the Chandrasekhar mass (usually  $\sim 1.44$  Solar mass for most classical stars), the degeneracy pressure of the electrons is not sufficient to oppose the gravitational contraction. The star starts to collapse until the core is stabilised again by the ignition of carbon mainly into neon, sodium and magnesium. This ignition releases so much energy that it blows the star out. For spectroscopy reason this kind of supernova is also called type Ia (no hydrogen line). Because this kind of explosion always starts at the same mass, the light curve is supposed not to depend on the object, which behaves as a standard candle useful to measure Hubble's law<sup>a</sup>.

Core-collapse supernovæ originate from much more massive objects. They happen when the core of the star has completely burnt into nickel and iron which cannot produce any more energy through fusion and to oppose the gravitational contraction. The pressure of the core is then sustained by the degeneracy pressure of the electrons. As previously, when the mass of the core gets higher than the Chandrasekhar mass, gravitational collapse starts until eventually the

---

<sup>a</sup>As said in chapter 1, this is not absolutely true but corrections are under control.

pressure is so high that all the atoms are converted to neutrons which brutally stops the collapse and causes an outgoing shock–wave which pushes away the outer layers of the star. From a spectroscopy point of view, this kind of explosion is called type Ib, Ic or type II (depending on the chemical composition of the outer layers and hence of the initial mass of the star).

Usually after the explosion of a star, a very dense object remains: a neutron star (which if it rotates very fast will be called a pulsar) or, maybe, a black hole. Around this object, the outer layers of the old star will carry on to expand for millions of years creating a vast turbulent structure called a supernova remnant.

Though the explosion is very violent, it cannot transfer much energy to individual particles and hence to accelerate cosmic rays. Indeed the speed of the gas ejected during the explosion is very big but not relativistic, and it diminishes quite fast as the front expands). It is actually the plasma shock of the remnant which accelerates particles.

### 4.1.1 Supernova remnants

A supernova remnant is the shell of gas that is ejected during the explosion of a star. This shell expands for millions of years until its pressure become equal to the one of the interstellar medium. The expansion of a supernova remnant is quite complex and can be decomposed into four phases. First, the shell freely expands at constant speed, because its mass is too small to feel any gravitational effect from the compact object left after the explosion or from itself. Its radius scales then like its age. The second phase, often referred to as Sedov–Taylor phase, starts when the mass of interstellar medium swept off by the shock–wave becomes important, in the absence of energy losses, the radius of the remnant then goes as  $t^{2/5}$ . Later, the shock has less energy and starts to dissipate it through turbulences of the interstellar medium, the expansion slows down, until the last phase takes place: the dissipation of the remnant, the pressure decreases and reaches the one of the interstellar medium, the remnant does not radiate any more light and vanishes. Mainly during the Sedov–Taylor phase, the front shock of the supernova remnant is very strong and, thanks to Fermi mechanism, can accelerate particles up to very high energies.

#### 4.1.1.1 Fermi acceleration mechanism

Enrico Fermi proposed in 1949 an acceleration mechanism of particles in plasma shocks. Many ameliorations to this model have been proposed since, but the main idea is the same: in a plasma shock, each time a particle crosses the shock front, it will gain energy, if, thanks to diffusion, it crosses many times the shock front it can gain a huge amount of energy. Let us see in detail how it works. There are many ways to prove this result as recalled by Jones & Ellison [46], however the most intuitive one is the microscopic approach of Bell [12, 13].

Let us consider a plasma shock that is an infinite plane discontinuity at  $x = 0$  in a flowing plasma. The plasma flows in from  $x = -\infty$  with a supersonic speed  $u_1$  due to the supernova, and flows out to  $x = \infty$  with a subsonic speed  $u_2$  (the interstellar gas pushed away by the shock). It is possible (see Jones & Ellison [46]) to chose a frame where the speed of the plasma flow is parallel to the magnetic field everywhere. If we assume that, to first order in  $v/c$ , the distribution function  $f(x, p)$  in space and scalar momentum of the accelerated particle is isotropic, and one can write that the only change in momentum comes from adiabatic expansion

of the flow (see section B.6). So that:

$$\dot{p} = -\frac{1}{3}p\frac{\partial u}{\partial x}. \quad (4.1)$$

If one follows a particle crossing the shock from region 1 to region 2, the integration gives:

$$\int_1^2 \dot{p} dt = -\frac{1}{3} \int_1^2 p \frac{\partial u}{\partial x} \frac{dx}{v_x} = \frac{1}{3} \frac{p}{v \cos(\theta)} (u_1 - u_2). \quad (4.2)$$

A particle which would cross the shock in the opposite direction would be accelerated by the same quantity as the minus sign coming from the integration would be compensated by another minus sign from the  $\cos(\theta)$  term. The flux of particle crossing the shock being proportional to  $\cos(\theta)$ , the average momentum gained by a particle crossing the shock is  $\langle \delta p \rangle = \frac{2}{3} \frac{p}{v} (u_1 - u_2)$ . The factor 2 comes from the averaging. So a particle with initial momentum  $p_0$ , after crossing the shock  $N$  times will have an average momentum :

$$\langle p \rangle_N = \prod_{i=1}^N \left( 1 + \frac{2}{3} \frac{(u_1 - u_2)}{v_i} \right) p_0. \quad (4.3)$$

As only suprathermic particles may undergo this acceleration process, one can consider that  $u_2 < u_1 \ll v_i$ , so the previous equation becomes:

$$\ln \left( \frac{\langle p \rangle_N}{p_0} \right) \sim \frac{2}{3} (u_1 - u_2) \sum_{i=1}^N \frac{1}{v_i} \sim \frac{4}{3} (u_1 - u_2) \sum_{i=1}^{N/2} \frac{1}{v_i}, \quad (4.4)$$

where the second approximation will actually be useful later. It simply comes from the fact that the speed variation is not very large during one travel forth and back through the shock. To know the distribution of particles, one needs the probability for a particle to cross  $N$  times the shock. Let us consider all the particles going with a given speed  $v$  in the downstream frame (*id est* oriented towards increasing  $x$ ). In this frame, the shock moves with a speed  $-u_2$ , hence for a particle to cross it, it must have a speed which satisfies  $v_x < -u_2$ . The flux of particles passing the shock from downstream to upstream is hence:

$$\left| \int_{-v}^{-u_2} (u_2 + v_x) dv_x \right| = \frac{1}{2} (u_2 - v)^2.$$

In the opposite direction one gets:

$$\left| \int_{-u_2}^v (u_2 + v_x) dv_x \right| = \frac{1}{2} (u_2 + v)^2.$$

The probability for a particle to pass forth and back the shock front is the ratio of fluxes:

$$\mathcal{P} = \left( \frac{1 - u_2/v}{1 + u_2/v} \right)^2.$$

The logarithm of the probability to pass the shock  $N$  times is hence:

$$\ln(\mathcal{P}_N) = 2 \sum_{i=1}^{N/2} \ln \left( \frac{1 - u_2/v_i}{1 + u_2/v_i} \right) \sim -4u_2 \sum_{i=1}^{N/2} \frac{1}{v_i}. \quad (4.5)$$

The logarithm of the probability to get a particle with momentum  $p$  is then obtained combining eq. 4.5 and eq. 4.4:

$$\ln(\mathcal{P}(p)) = -\frac{3u_2}{u_1 - u_2} \ln \left( \frac{p}{p_0} \right).$$

If the upstream particle density is  $N_0$ , the resulting differential spectrum is:

$$f(p) = -N_0 \left( \frac{u_1}{u_2} \right) \frac{\partial \mathcal{P}}{\partial p} = \frac{N_0 u_1}{p_0 u_2} \left( \frac{p}{p_0} \right)^{-(u_1+2u_2)/(u_1-u_2)}.$$

So the accelerated particle spectrum is a power law indeed. The  $u_1/u_2$  term accounts for the compression of the upstream density by the shock. The spectral index  $\sigma = (u_1+2u_2)/(u_1-u_2) = (r+2)/(r-1)$ , in term of the compression factor  $r = u_1/u_2$ , does not depend on the injection spectrum but only on the shock itself. In the case of a monoatomic non-relativistic gas, in such a plasma shock, one expects high Mach-numbers, this leads to a compression factor of 4 and hence to a power index  $\sigma$  of 2. As we will see later, this is in perfect agreement with available observation and this is a great success of this first order Fermi acceleration mechanism theory.

One should however be cautious with the previous calculi, indeed:

- Many approximations done here rely on the fact that  $u_2 < u_1 \ll v_i$  which is true only once the particle has received sufficient energy from the shock.
- The plasma shock has been considered as invariant during the whole process. This is known to be false and actually the increasing pressure from the accelerated particle and local environment imply many non-linear effects which cannot be taken into account analytically.
- A particle can cross the shock many times only if the diffusion coefficients of the medium at both sides of the shock are large enough, this depends on the microscopic magnetic field which is very sensitive to the population of accelerated particles.

However, recent numerical simulations [46, 81] still agree on the fact that the spectrum is a power with an index not very far from -2.

#### 4.1.1.2 Released cosmic ray energy spectrum

As we have seen, the cosmic ray spectrum at the supernova remnant, is a power law of momentum (or equivalently of energy). However, it is important to stress that the Fermi acceleration process cannot accelerate particles up to infinite energies, indeed when the particle is too energetic, its Larmor radius is too large compared to size of the magnetic inhomogeneities, hence the probability of such a particle to be scattered back in the remnant drops dramatically. In the energy spectrum this translates into an exponential cut-off the precise value of which is

not very well constrained by theory. For electrons it is supposed to lie between a few hundreds of GeV and a few hundreds of TeV. Hence an energy dependence of the kind:

$$Q(E) = Q_0 \epsilon^{-\sigma} \exp \left\{ -\frac{E}{E_c} \right\}. \quad (4.6)$$

The problem now is to set the values of the three parameters  $\sigma$  the spectral index,  $Q_0$  the amplitude, and  $E_c$  the cut-off energy.

### The spectral index $\sigma$

In the previous paragraph we did not consider differently electrons and protons, hence one expects rather close indices for protons and electrons. Since protons above a few GeV are barely affected by energy losses and have long range propagation scale, the proton spectrum measured at the Earth can provide information on the mean index at sources. Since  $\phi_p \tilde{\propto} Q(E)/K(E) \propto E^{-\tilde{\sigma}}$  ( $K(E) \sim K_0 E^\delta$  is the diffusion coefficient – see Chapter 5), the index at source is therefore  $\sigma \approx \tilde{\sigma} - \delta$ . With  $\tilde{\sigma} \simeq 2.7$  and  $\delta$  ranging in 0.5-0.7, one finds  $\sigma$  ranging in 2.0-2.2, in rough agreement with theoretical predictions.

We will see in Chapter 7, that the synchrotron emission by a power law spectrum of electrons is a power law as well with index  $\sigma_r = (\sigma - 1)/2$ .

An up-to-date catalogue of supernova remnants can be found in Green [41]; it contains  $\sim 265$  objects, 70 for which the distance to the Earth has been estimated and 207 for which a spectral index for the radio emission has been measured. Observations, however, are not expected to reflect the actual statistical properties of the whole population of Galactic supernova remnants because of observational selection effects favouring the brightest sources as well as sites of fainter background (high longitudes, towards the anticentre). Anyway, disregarding the spatial distribution of these objects which is likely to be strongly biased, such a sample may still be fairly representative of their general spectral properties [40].

A histogram of the measured radio indices done in [28] is presented in the left panel of Fig. 4.1. It clearly appears that the radio indices exhibit a Gaussian distribution. This points towards similar physical grounds for the electron properties at sources, which is obviously not surprising. With these distributions, one can derive mean values and statistical ranges for the parameters. We found  $\langle \sigma_r \rangle = 0.50 \pm 0.15$ . One can therefore infer the electron index  $\langle \sigma \rangle = 2 \langle \sigma_r \rangle + 1 = 2.0 \pm 0.3$  in very good agreement with theoretical expectations. Although this relation between the radio index and the electron index is not completely exact (other radio components, absorption), and although some systematic errors also affect the data, this provides a complementary mean to bracket the uncertainty, which is consistent with theoretical results.

### The amplitude $Q_0$

Sizing the value of the normalisation  $Q_0$  is quite problematic. To describe a distribution of sources in the Galaxy, one usually assumes that the high energy electron injection is connected to the explosion rate of supernovæ, so that we can guess that  $Q_0$  is such that the total energy

carried by electrons is:

$$\int_{E_{\min}}^{\infty} dE' E' Q(E') = f E_{\star} \Gamma_{\star}, \quad (4.7)$$

where  $\Gamma_{\star}$  is the supernova explosion rate,  $E_{\star}$  is the kinetic energy released by the explosion and  $f$  is the fraction of this energy conferred to electrons. Since we are interested in the non-thermal electrons only, we will fix  $E_{\min} = 0.1$  GeV. It is worth mentioning that the spectral index influences the normalisation procedure sketched above.

The question arises of constraining  $\Gamma_{\star}$ ,  $E_{\star}$  and  $f$ . The explosion rate of supernovæ is typically predicted to be a 1-5 per century and per galaxy [*exempli gratia* 53, 85], which is consistent with observations [*exempli gratia* 30, 84]. Nevertheless, supernovæ are of different types, and may thereby lead to different cosmic ray acceleration processes. About 2/3 of supernovæ are expected to be core-collapse supernovæ (CCSNe), the remaining 1/3 being composed of type 1a supernovæ (SNe1a).

Explosions of core-collapse supernovæ with masses  $\lesssim 20 M_{\odot}$  can liberate a huge amount of energy,  $10^{53-54}$  erg typically,  $\sim 99\%$  of which is in the form of neutrinos [*exempli gratia* 22, 45, 86]. They usually lead to quite complex systems characterised by supernova remnants beside (or inside) which one can find active neutron stars like pulsars and associated wind nebulae (PWN) — we will focus on pulsars in the next paragraph 4.1.2. Aside, supernovæ 1a are much more modest systems and release about  $10^{51}$  erg of kinetic energy in the interstellar medium [*exempli gratia* 38, 57, 63]. Since we will only deal with supernova remnants in this part, we will set  $E_{\star} = 10^{51}$  erg in the following.

The fraction of supernova energy conferred to electrons was recently studied by Tatischeff [81], who found about  $f \sim 10^{-5} - 10^{-4}$ . This result turns out to be rather independent from the exact values of the spectral index  $\sigma$  and the cut-off energy  $E_c$ , but the theoretical error is still of about one order of magnitude.

We emphasise that at this stage, the theoretical uncertainty on the product  $f E_{\star} \Gamma_{\star}$  already reaches about 2-3 orders of magnitude in average, which is quite huge and translates linearly in terms of flux.

For known single sources, it is possible to derive better constraints on the individual normalisations  $\mathcal{Q}_0 = f E_{\star}$  from observations in wavelengths for which electrons are the main emitters. This is precisely the case for the non-thermal radio emission due to synchrotron processes, provided the magnetic field is constrained independently. The synchrotron emissivity associated with an electron source of injection rate  $\mathcal{Q}(E)$  can be found in chapter 7. Armed with this expression, one can constrain  $\mathcal{Q}_0$  by means of the source radio brightness  $B_r(\nu)$ , which is usually found in catalogues:

$$B_r(\nu) = \frac{1}{\delta\nu} \int_{\nu}^{\nu+\delta\nu} d\nu' h\nu' \frac{d\phi(\nu')}{d\nu'} \stackrel{\delta\nu \rightarrow 0}{=} \frac{[b(E)]_{\text{sync}}}{4\pi d^2} \mathcal{Q}(E) \frac{dE}{d\nu}.$$

Which leads to:

$$\mathcal{Q}_0 = \frac{4\pi d^2}{[b(E)]_{\text{sync}}} \left( \frac{E}{E_0} \right)^{\sigma} \frac{d\nu}{dE} B_r(\nu).$$

where  $d$  stands for the distance between the Earth and the observed object and  $[b(E)]_{\text{sync}}$  is the electron energy loss term due to synchrotron emission (see paragraphs 5.2.2 and 7.2). For

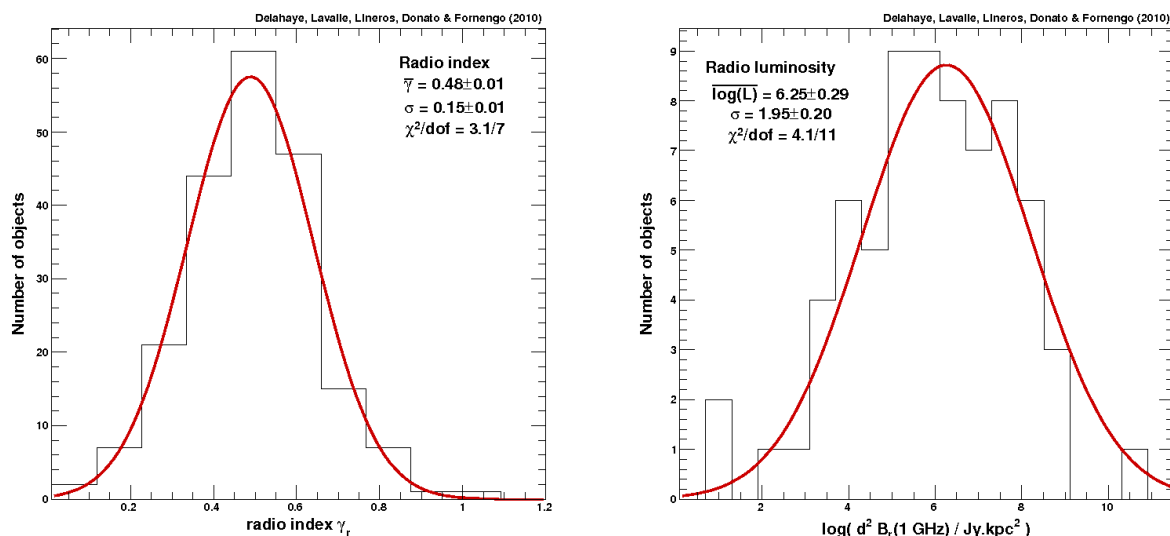


Figure 4.1: Left: histogram of supernova remnant radio spectral indices. Right: histogram of supernova remnant luminosities —  $\mathcal{L}/(4\pi) = d^2 B(1 \text{ GHz})$ . The supernova remnant data are taken from the Green catalogue [41].

the values of interest, this gives:

$$\frac{\mathcal{Q}_0}{\text{GeV}^{-1}} = 1.2 \times 10^{47} \times (0.79)^\sigma \left[ \frac{d}{\text{kpc}} \right]^2 \left[ \frac{\nu}{\text{GHz}} \right]^{\frac{\sigma-1}{2}} \left[ \frac{B}{100 \mu\text{G}} \right]^{-\frac{(\sigma+1)}{2}} \left[ \frac{B_r(\nu)}{\text{Jy}} \right].$$

Note that we have recovered the well-known relation between the radio index and the electron index,  $\sigma_r = (\sigma - 1)/2$ .

As for the radio indices, we have made a histogram of the estimated intrinsic luminosities —  $\mathcal{L}/(4\pi) = d^2 B_r(1 \text{ GHz})$  — which is plotted in the right hand side panel of Fig. 4.1. The luminosities follow a log-normal distribution. Again, it is possible to derive mean values and statistical ranges for the parameters. We found  $\langle d^2 B_r(1 \text{ GHz}) \rangle = \exp\{6.26 \pm 1.95\} \text{ Jy.kpc}^2$ .

We can use this statistical information to constrain directly the single source normalisation  $\mathcal{Q}_0$  from equation (4.8), but we further need an estimate of the magnetic field in supernova remnants. From the observational point of view, information on electron density and magnetic field at sources is degenerate. More insights may come from theoretical studies on the amplification of magnetic fields in sources from numerical simulations, which involve cosmic rays themselves as seeds and amplifiers. The current state-of-the-art [*exempli gratia* 52] gives  $B \sim 100 \mu\text{G}$ , in agreement with observations, and that we will further use. With this value, we finally find  $\langle \mathcal{Q}_0 \rangle = 3.9 \times 10^{49} \text{ GeV}^{-1}$  for an index  $\sigma = 2$ , which translates into  $\langle f E_\star \rangle \simeq 4.3 \times 10^{50} \text{ GeV} \simeq 6.9 \times 10^{47} \text{ erg}$  (with a cut-off  $E_c = 10 \text{ TeV}$ ). This is in rough agreement with the other values derived above, but probably biased, as expected, towards the brightest objects.

### The energy cut-off $E_c$

The cut-off energy is much more difficult to constrain. Indeed electrons having an energy around 1 TeV, in a magnetic field of 100  $\mu\text{G}$ , emit synchrotron radiation at a frequency of  $\nu_s \sim 10^{12}$  Hz (see equation 7.8). At these very high frequencies, the infra-red thermal emission is completely dominating the synchrotron emission and it is impossible to see the cut-off.

Another idea is to look at the gamma emission of the supernova remnant. TeV electrons produce gamma ray through inverse Compton scattering off photons. The issue is that we have little observation of supernovae remnants in the gamma ray range, more over, it is not clear which signal should dominate: the inverse Compton from electrons or the  $\pi^0$  decay coming from the accelerated protons which interact with the interstellar medium.

In the absence of definite answer, the best thing to do is probably to choose  $E_c$  so that the electron flux computed fits the high energy data published by HESS [2, 3] which exhibits a cut-off at an energy of 3 TeV roughly.

## 4.1.2 Pulsars

Independently of the specific pulsar model, like for instance the polar gap [71], the outer gap [25, 26] or the slot gap [42] models, what concerns cosmic ray electrons and positrons can be summarised as follows. Gamma rays can be generated in the pulsar magnetosphere from inverse Compton processes of electrons accelerated along the strong and rotating magnetic field off local synchrotron radiation, which can further produce electron-positron pairs by annihilating with photons from the local radiation fields. Those gamma rays can be observed as a pulsed emission, like those recently discovered with the Fermi satellite [1], which may therefore be used to constrain the pair production. These electron-positron pairs are further accelerated within the surrounding and expanding shocked medium, at least in the phase of pulsar wind nebula, located inside or offset a more extended supernova remnant. Observations of young systems like the Crab nebula tell us that this acceleration can be very efficient and lead to huge Lorentz factors, up to  $\sim 10^8 - 10^9$  [7]. What is important when trying to predict the electron-positron yield from a pulsar is not their energy distribution and density close to the magnetosphere, but instead the final features after acceleration has proceeded and when particles are released in the interstellar medium. This was already noticed and detailed in Malyshev *et alii* [54]. It is therefore rather difficult to provide accurate predictions when disregarding the whole dynamics at stake there, and, in this part, we mostly aim to survey the roles of the main ingredients that characterise pulsars rather than making peremptory predictions. Indeed, we will show in the following that current uncertainties still make it difficult to derive but qualitative predictions.

Following the arguments developed in [54], to which we refer the reader for further details, we define the source term associated to any single pulsar as

$$\mathcal{Q}_p(E, \vec{x}, t) = q_p(E, t_\star) \delta(t - (t_\star + \delta t_\star)) \delta(\vec{x} - \vec{x}_\star), \quad (4.8)$$

where  $t_\star$  and  $\vec{x}_\star$  are the pulsar age and position, respectively, and  $\delta t_\star$  allows for a certain delay in the release of cosmic ray electrons in the interstellar medium after the supernova explosion. Generic pulsars should have ceased their pulsar wind nebula phases after  $\sim 10$ -100 kyr [37]; for simplicity, however, since characterising the pulsar wind nebula evolution is far beyond our purpose here, we will assume that  $\delta t_\star = 0$  in the following. The pulsar age is usually estimated

from the spin-down age [66], only relevant in the spin-down magnetic radiation approximation, which involves the rotation period  $P$  and its first time derivative  $\dot{P}$ :

$$t_{\text{pulsar}} = -\frac{P}{2\dot{P}}. \quad (4.9)$$

Like in the supernova remnant case, it is worth stressing again that such an age estimate relies on current observations, so that the actual age used for cosmic ray calculations should have an additional  $d/c$  term, where  $d$  is the distance of the pulsar to the observer. We emphasise, however, that using the spin-down age for the pulsar age estimate turns out, in many cases, to be erroneous [see *exempli gratia* 36]. Still, for simplicity, we will adopt this method to deal with local pulsars in the following.

For the energy spectrum, we adopt the same general shape as used previously for supernova remnants (see Eq. 4.6), *id est* a power-law of index  $\sigma$  with an exponential cut-off at energy  $E_c$ :

$$q_p(E) = \mathcal{Q}_0 \left( \frac{E}{E_0} \right)^{-\sigma} \exp\left(-\frac{E}{E_c}\right). \quad (4.10)$$

Note that contrarily to the supernova remnant case for which the spectral index can be constrained from radio observation, the spectral index associated with high energy electrons from pulsars can hardly be constrained from radio observations of the pulsed emission. Indeed, this pulsed emission originates from regions close to the pulsar magnetosphere, where the acceleration processes are not yet achieved. An alternative is to use the spectral indices derived from pulsar wind nebula observations, when available. To simplify the discussion, we will use  $\sigma = 2$  in the following, unless other values are specified.

The normalisation  $\mathcal{Q}_0$  is intimately linked to the total rotational energy  $W_0$  of the pulsar, a fraction  $f$  of which is released in the form of electron-positron pairs, such that

$$\int_{E_{\text{min}}}^{\infty} dE E q_p(E) = f W_0. \quad (4.11)$$

$W_0$  can be constrained from measurements assuming that the whole energy lost is carried by the magnetic dipole radiation, such that

$$W_0 = \dot{E} \tau_{\text{dec}} \left( 1 + \frac{t_{\star}}{\tau_{\text{dec}}} \right)^v, \quad (4.12)$$

where  $\dot{E}$  is the spin-down luminosity and  $\tau_{\text{dec}} \equiv E_0/\dot{E}_0$  is the typical pulsar decay time. Notice that the index  $v$  featuring the age dependence is in principle related to the braking index  $k$  which defines the rotation deceleration  $\dot{\Omega} \sim -\Omega^k$ , where  $\Omega$  is the angular velocity, through  $v = (k+1)/(k-1)$ . In the spin-down approximation,  $k = 3$ , and therefore  $v = 2$ . Nevertheless, it turns out that  $k$  can also be computed if the second time derivative of  $\Omega$  is known,  $k = -\Omega\ddot{\Omega}/\dot{\Omega}^2$ . In that case, it is usually found slightly different than 3.

Again, this illustrates the large degree of theoretical uncertainties arising when trying to model pulsars, even in simple approaches. Still, we will use the spin-down approximation, and will therefore fix  $v = 2$  in the following.

Since accounting for the details in the pulsar modelling is beyond the scope of this paper, we will adopt the source model defined by Eqs. (4.8-4.12), and assume a universal decay time of  $\tau_{\text{dec}} = 1$  kyr. Using this latter input together with the ATNF data for the rotation period and its derivative, Malyshev *et alii* [54] found typical values of  $W_0 \sim 10^{49}$  erg, *id est* one or two orders of magnitude below the characteristic supernova energy release, in agreement with the picture of a pulsar as a subdominant energy supply beside its companion supernova remnant. In the following, we will further assume by default that a fraction  $f = 0.1$  of this energy is converted into electron-positron pairs.

### 4.1.3 Distribution in the Milky Way

Although GeV-TeV electrons have a short range propagation scale, the injection rate of energy discussed above is not sufficient to describe the Galactic cosmic ray electrons. We further need to specify the spatial distribution of sources. For nearby sources, we can use available catalogues since observational biases are less prominent, so that they may provide a rather good description of the local injection. Nevertheless, for more distant sources, which will have influence in the intermediate energy range  $\sim 1$ -100 GeV, we have to rely on a distribution model.

Since 2/3 of supernovæ are expected to be core collapse supernovæ, one can use pulsars as tracers of the SNR distribution, instead of SNRs themselves whose observed population is much more modest. Indeed, as an illustration, the ATNF catalogue<sup>b</sup> [55] lists more than 1800 pulsars compared to the  $\sim 265$  SNRs contained in Green [41]. Nevertheless, a too naive use of the statistics would lead to errors since it is well known that data do not reflect reality faithfully because of detection biases [*exempli gratia* 51].

There are few distribution models in the literature that we can compare. Since the energetics associated with the source injection (birth) rate has been discussed above, we are only interested in the normalised source distribution. Consequently, the normalisation coefficient in front of each model will be fixed such that it normalises the spatial distribution within the diffusion halo characterised by its radius  $R$  and half-thickness  $L$ . Moreover, in the following, we will set the position of the Sun at  $r_{\odot} = 8$  kpc from the Galactic centre<sup>c</sup>.

Most of models exhibit radial and vertical dependences in the form

$$\rho(r, z) = \rho_0 r^a \exp\left\{-\frac{r}{r_0}\right\} \exp\left\{-\frac{|z|}{z_0}\right\}, \quad (4.13)$$

where  $\rho_0$  ensures the normalisation to unity so that the explosion rate is taken into account in  $Q(E)$ . For simplicity, we will only discuss differences in the radial distributions in the following, since the vertical distribution is rather consensual among studies. Consequently, we will keep fixed the vertical dependence like in the above equation, with  $z_0 = h = 0.1$  kpc, throughout the rest of this work.

Different sets of values can be found in the literature for the pair  $(a, r_0)$ . Lorimer [51], hereafter L04, found (2.35, 1.528 kpc); Yusifov & Küçük [87], hereafter YK04, derived (4, 1.25 kpc);

<sup>b</sup><http://www.atnf.csiro.au/research/pulsar/psrcat>

<sup>c</sup>Some of the distributions listed in this paragraph are actually derived assuming 8.5 kpc, but I will disregard this small change to make the discussion easier.

while Paczynski [67], hereafter P90, early determined (1, 4.5 kpc). Finally, at variance with the parametrisation sketched above, let us mention the distribution proposed by Case & Bhattacharya [23], hereafter CB98, though it was obtained from a fit on a poor statistics of 36 supernova remnants:

$$\rho(r, z) = \rho_0 \sin\left(\pi \frac{r}{r_s} + \theta\right) \exp\left\{-\frac{r}{r_0}\right\} \exp\left\{-\frac{|z|}{z_0}\right\}, \quad (4.14)$$

where I have added the same vertical term as in equation (4.13). The authors found  $r_0 = 7.7 \pm 4.7$  kpc,  $r_s = 17.2 \pm 1.9$  kpc and  $\theta = 0.08 \pm 0.33$ . This relation is only valid for  $r < r_s(1 - \theta/\pi)$ , *id est* within 16.8 kpc, and null beyond. More recently, Sasaki & Breitschwerdt [72], Sasaki *et alii* [73] using the same function found  $r_0 = 13.4 \pm 0.55$  kpc,  $r_s = 4.02 \pm 0.83$  kpc and  $\theta = -0.2 \pm 0.4$ . Note however that Brogan *et alii* [20] recently reported the detection of 35 new remnants in the inner Galaxy, and suggest that former radial distribution estimations should be revised.

## 4.2 Secondary Cosmic Rays

Secondary electrons and positrons are mainly produced by the interaction of cosmic protons and  $\alpha$  particles with interstellar hydrogen and helium. This process is hadronic hence the cross-sections cannot be computed analytically but require measurements. Most of the data available concern  $p + p$  processes. The direct production of electrons is negligible at the energies we consider here, the production mainly comes from the decay of charged pions and kaons. These latter processes are electroweak and can be computed analytically. This simple computation is performed in the next paragraph, before looking at the measurements of the kaon and pion production cross-sections. One needs to compute  $q_e(\mathbf{x}, \epsilon_e)$ , the number of electron (or positron) of energy  $\epsilon_e$  created per unit volume at position  $\mathbf{x}$ , per unit time and per GeV. The positron source term reads:

$$q_e(\mathbf{x}, \epsilon_e) = 4\pi \sum_{\text{targ}=\text{H,He}} \sum_{\text{proj}=\text{p},\alpha} n_{\text{targ}}(\mathbf{x}) \times \int \Phi_{\text{proj}}(\mathbf{x}, \epsilon_{\text{proj}}) \times d\epsilon_{\text{proj}} \times \frac{d\sigma}{d\epsilon_e}(\epsilon_{\text{proj}} \rightarrow \epsilon_e), \quad (4.15)$$

where  $\Phi_{\text{proj}}(\mathbf{x}, \epsilon_{\text{proj}})$  denotes the cosmic ray nucleon flux at position  $\mathbf{x}$ ,  $n_{\text{targ}}(\mathbf{x})$  the number density of target nuclei, and  $d\sigma/d\epsilon_e$  the cross-section for the reactions creating electrons (or positrons). These quantities are detailed in this section, following the work previously developed in [29].

### 4.2.1 Production cross-sections

Let us first focus on the differential cross-section for the production of electrons and positrons. This production occurs by means of a nuclear reaction between two colliding nuclei, yielding mainly charged pions  $\pi^\pm$  and other mesons, for which electrons or positrons are one of the final products of the decay chain. There are four main possible collisions: cosmic ray proton on interstellar hydrogen or helium; cosmic ray alpha particle on interstellar proton or

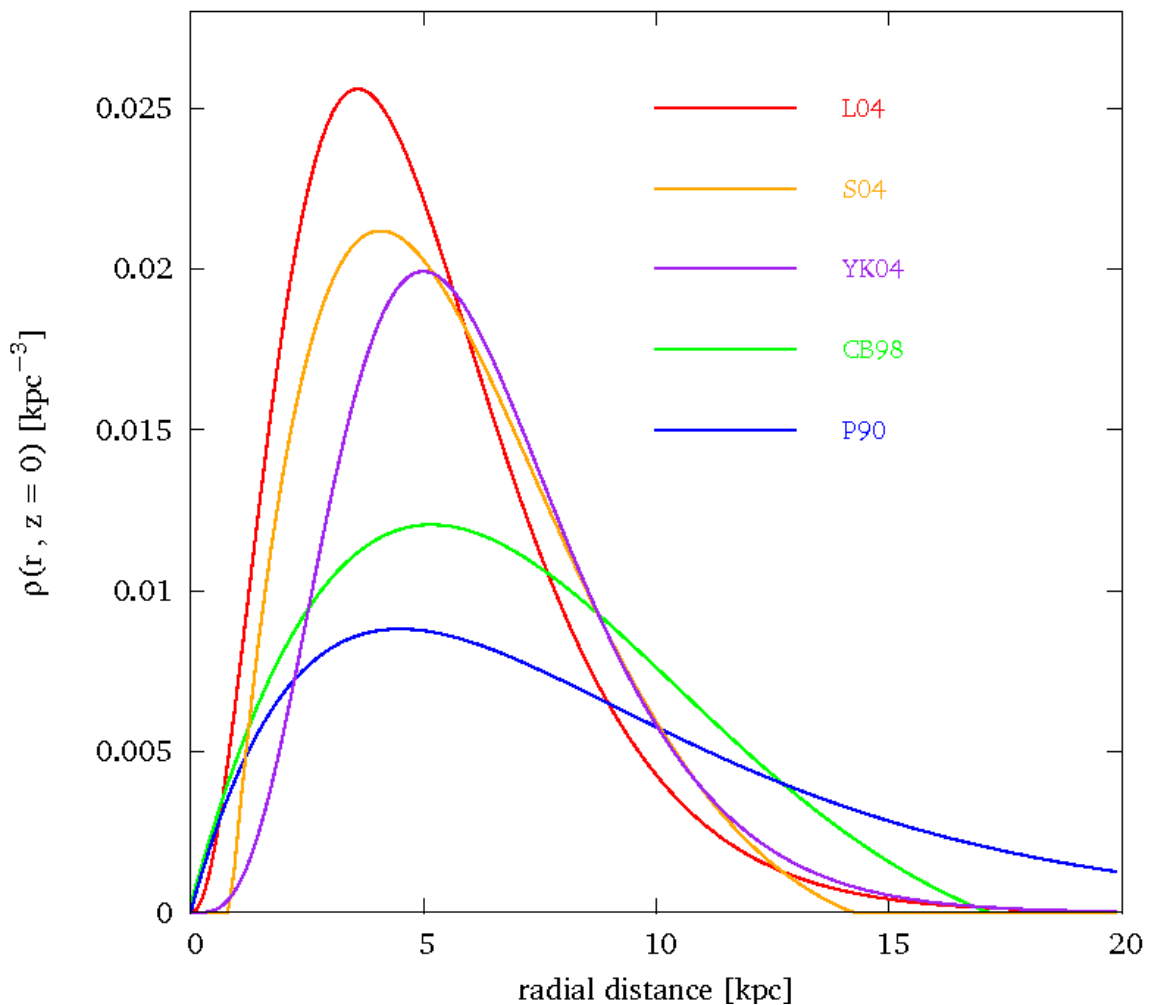


Figure 4.2: Spatial distribution models for supernova remnants and pulsars. The references corresponding to the label are in the text. Here, all the distributions have been renormalised so as to give the same number of sources in the Galaxy.

helium. For the sake of clarity, we present only the formulæ for the proton–proton collisions, but include all four processes in our results on the positron spectra.

This spallation, because of charge conservation (both the target and the projectile are positive), produces a little bit more positrons than electrons. At energies below about 3 GeV, the main channel for production of positrons involves the excitation of a Delta resonance, which then decays into pions:

$$p + H \rightarrow p + \Delta^+ \rightarrow \begin{cases} p + \pi^0 \\ n + \pi^+ \end{cases} .$$

The charged pions decay into muons, which subsequently decay into positrons.

At higher energies direct production of charged pions and kaons proceeds with the process:

$$p + H \rightarrow \begin{cases} X + \pi^\pm \\ X + K^\pm \end{cases},$$

and the decay of kaons produces muons (63.44 %) and pions (20.92 %), which then decay into electrons and positrons as final products of their decay chain.

In order to compute the differential cross-section for the pion or kaon-production processes, one needs the probability  $d\sigma(\epsilon_p \rightarrow \epsilon_{\pi/K})/d\epsilon_{\pi/K}$  of a spallation of a proton of energy  $\epsilon_p$  yielding a pion (or a kaon) with energy  $\epsilon_{\pi/K}$  and the probability  $\mathcal{P}(\epsilon_{\pi/K} \rightarrow \epsilon_e)$  of such a pion (kaon) to lead to an electron of energy  $\epsilon_e$ .

#### 4.2.1.1 Pion to muon

A charged pion created by the collision of a cosmic ray with interstellar gas mainly decays into muon (more than 99% probability) and not into an electron. Let us consider a negative<sup>d</sup> pion  $\pi^-$  decaying in his rest-frame into a fermion  $f^-$  and an antineutrino  $\bar{\nu}_f$ . The antineutrino  $\bar{\nu}_f$  being almost massless, it must have right-handed helicity. By conservation of kinetic momentum, the decay happening in  $s$  wave, the charged fermion has to have right-handed helicity as well. One can show that the life time of a pion through a decay channel is inversely proportional to the mass of the fermion squared. The muon  $\mu^-$  being one hundred times heavier than the electron  $e^-$ , the pion has ten thousand times more probability to decay into a muon rather than into an electron. All other channels are excluded because the  $\tau$  fermion is heavier than the pion.

Writing down the energy-momentum 4-vector of each particle involved in the decay in the rest-frame of the pion gives:  $\pi_\rho = (m_\pi, \vec{0})$ ,  $\mu_\rho = (E_\mu, \vec{k})$  and  $\bar{\nu}_\rho = (E_\nu, -\vec{k})$ . By energy and momentum conservations, one easily gets the energy of the muon:

$$\begin{aligned} E_\mu + E_\nu &= E_\pi = m_\pi \\ E_\mu^2 - k^2 &= E_\mu^2 - \{E_\nu - (m_\nu = 0)\}^2 = m_\mu^2 \end{aligned}$$

which, noticing that  $m_\pi \sim m_\mu$ , gives:

$$E_\mu = \frac{m_\pi^2 + m_\mu^2}{2m_\pi} \simeq m_\mu.$$

In the rest-frame  $R'$  of the pion, the muon is hence mono-chromatic and polarised. In the laboratory frame  $R$ , the pion goes at velocity  $\beta_\pi$  (expressed in units of  $c$ ) associated with a Lorentz coefficient  $\gamma_\pi$  and an energy  $\epsilon_\pi$ . The energy  $\epsilon_\mu$  of the muon in the laboratory frame is equal to:

$$\epsilon_\mu = \gamma_\pi \gamma'_\mu \left( m_\mu + \vec{\beta}_\pi \cdot m_\mu \vec{\beta}'_\mu \right),$$

<sup>d</sup>The choice of the charge is important only for helicity considerations, all the following is also true for a positive pion but with left-handed fermions.

which takes values between  $m_\mu\gamma_\mu^+$  and  $m_\mu\gamma_\mu^-$  where  $\gamma_\mu^\pm = \gamma_\pi\gamma'_\mu(1 \pm \beta_\pi\beta'_\mu)$ . Moreover,  $\beta'_\mu$  is the velocity of the muon in the rest-frame of the pion (and  $\gamma'_\mu$  the corresponding Lorentz coefficient). The energy distribution of the muon  $\epsilon_\mu$  created by a pion of energy  $\epsilon_\pi$  in the laboratory frame  $R$  is hence:

$$f(\epsilon_\pi, \epsilon_\mu) = \frac{\theta(\epsilon_\mu - m_\mu\gamma_\mu^-) - \theta(\epsilon_\mu - m_\mu\gamma_\mu^+)}{2m_\mu\gamma_\pi\gamma'_\mu\beta_\pi\beta'_\mu},$$

where  $\theta(x)$  is Heaviside's step function.

This result is true regardless of the charge of the muon.

#### 4.2.1.2 Muon to electron

Let us carry on with a negative pion. Muon is an unstable particle which decays according to the following process:  $\mu^-(P) \Rightarrow e^-(p) + \bar{\nu}_e(k) + \nu_\mu(\bar{k})$ . Doing Fermi's approximation for the description of weak interaction, one gets the following matrix element:

$$M = G \{ \bar{u}(k)\gamma^\mu(1 - \gamma_5)(1 + \gamma_5 s)u(P) \} \{ \bar{u}(p)\gamma_\mu(1 - \gamma_5)v(\bar{k}) \}$$

where the term  $(1 + \gamma_5 s)$  comes from the fact that the muon is fully polarised. By summing over electron spin, one finally gets, in the rest-frame  $R^*$  of the muon, the distribution probability to get an electron with energy  $\epsilon_e^*$  and a trajectory which makes an angle  $\theta^*$  with the spin of the muon, to be:

$$f_\xi^*(\epsilon_e^*, \cos(\theta^*)) = \frac{8\epsilon_e^{*2}}{m_\mu^3} \left\{ 3 - 4\frac{\epsilon_e^*}{m_\mu} - \xi \cos(\theta^*) \left( 1 - 4\frac{\epsilon_e^*}{m_\mu} \right) \right\},$$

where  $\xi$  is 1 for a positron and  $-1$  for an electron. Probability being a Lorentz invariant quantity one gets:

$$f_\xi(\epsilon_\mu, \epsilon_e)d\cos(\theta)d\epsilon_e = f_\xi^*(\epsilon_e^*, \cos(\theta^*))d\cos(\theta^*)d\epsilon_e^*,$$

where  $f_\xi$  is the probability function in the laboratory frame. With a Lorentz boost, one can go from the muon rest-frame  $R^*$  to the laboratory frame  $R$  and get:

$$\begin{aligned} \epsilon_e^* &= \epsilon_e\gamma_\mu(1 - \beta_\mu\cos(\theta)) \\ \vec{k}_e^* &= \gamma_\mu(\vec{k}_{e\parallel} - \epsilon_e\vec{\beta}_\mu) + \vec{k}_{e\perp} \end{aligned} \quad (4.16)$$

Performing a projection of the second equation over the direction of the muon spin, one gets:  $\epsilon_e^*\cos(\theta^*) = \epsilon_e\gamma_\mu(\cos(\theta) - \beta_\mu)$  and, making use of the first equation, one has:

$$\cos(\theta^*) = \frac{\cos(\theta) - \beta_\mu}{1 - \cos(\theta)\beta_\mu},$$

which allows the change of variables.

#### 4.2.1.3 Pion to electron

We have now everything required to compute the distribution function of electrons/positrons as a function of the pion energy in the laboratory frame  $R$ . A short discussion is nevertheless required before proceeding. In the muon frame  $R^*$ , the momentum of the electron is maximal

when both neutrinos go in the same direction, then the electron will take away the energy  $\epsilon_e^* = m_\mu/2$ . If one puts this result in equation 4.16 one gets :  $\cos(\theta) \geq \eta_1 = \frac{1}{\beta_\mu} \left(1 - \frac{m_\mu}{2\epsilon_e\gamma_\mu}\right)$ . Depending on the value of  $\epsilon_e$  one sees that the allowed values for  $\gamma_\mu$  and  $\cos(\theta)$  are different. Formally, the distribution function of electrons/positrons with respect to pion energy in the laboratory frame  $R$ ,  $F_\xi(\epsilon_e, \epsilon_\pi)$  reads:

$$F_\xi(\epsilon_e, \epsilon_\pi) = \int_{m_\mu\gamma^-}^{m_\mu\gamma^+} d(m_\mu\gamma_\mu) f(\epsilon_\pi, \epsilon_\mu) \int_{\eta_{min}}^1 d\cos(\theta) f_\xi(\epsilon_\mu, \epsilon_e),$$

with  $\eta_{min} = \max(-1, \eta_1)$ . Let us introduce  $\gamma_1 = \frac{\epsilon_e}{m_\mu} + \frac{m_\mu}{4\epsilon_e}$ , the solution of the equation  $\eta_1 = -1$ . Depending on the value of  $\epsilon_e$ ,  $\gamma_1$  may be smaller than  $\gamma_\mu^-$  or greater than  $\gamma_\mu^+$ . In a practical way, one can decompose the variation domain of  $\epsilon_e$  into five regions depending on the value of  $\eta_{min}$ .

$$F_\xi(\epsilon_e, \epsilon_\pi) = A \times \begin{cases} X_\xi(\gamma^+) - X_\xi(\gamma^-) & \epsilon_e \leq \frac{m_\mu}{2\gamma_\mu^+(1 + \beta_\mu^+)} \\ X_\xi(\gamma_1) - X_\xi(\gamma^-) + Y_\xi(\gamma^+) - Y_\xi(\gamma_1) & \frac{m_\mu}{2\gamma_\mu^+(1 + \beta_\mu^+)} \leq \epsilon_e \leq \frac{m_\mu}{2\gamma_\mu^-(1 + \beta_\mu^-)} \\ Y_\xi(\gamma^+) - Y_\xi(\gamma_\mu) & \frac{m_\mu}{2\gamma_\mu^-(1 + \beta_\mu^-)} \leq \epsilon_e \leq \frac{m_\mu}{2\gamma_\mu^-(1 - \beta_\mu^-)} \\ Y_\xi(\gamma^+) - Y_\xi(\gamma_1) & \frac{m_\mu}{2\gamma_\mu^-(1 - \beta_\mu^-)} \leq \epsilon_e \leq \frac{m_\mu}{2\gamma_\mu^+(1 - \beta_\mu^+)} \\ 0 & \frac{m_\mu}{2\gamma_\mu^+(1 - \beta_\mu^+)} \leq \epsilon_e \end{cases}$$

where  $A$  stands for  $\frac{1}{m_\mu\gamma_\pi\beta_\pi\gamma'_\mu\beta'_\mu}$ . The value of coefficient  $\xi$  is  $\xi = \pm 1$  depending on one considers positron or electrons or  $\xi = 0$  if one does not care about polarisation (obviously not in the frame of a pion decay); functions  $X_\xi$  and  $Y_\xi$  are defined as follows:

$$X_\xi(\gamma) = \frac{m_\mu}{2} \int_{-1}^{\gamma} \int_{-1}^1 d(\gamma_\mu) d\cos(\theta) f_\xi(\epsilon_\mu, \epsilon_e)$$

$$X_\xi(\gamma) = \frac{4}{9} \left(\frac{\epsilon_e}{m_\mu}\right)^2 \left\{ (27 + 9\xi\beta)\gamma^2 - 9\xi \ln(\gamma(1 + \beta)) + \frac{\epsilon_e}{m_\mu} [-32\gamma^3(1 + \xi\beta) + \gamma(24 + 32\xi\beta)] \right\}.$$

and

$$Y_\xi(\gamma) = \frac{m_\mu}{2} \int_{\eta_1}^{\gamma} \int_{-1}^1 d(\gamma_\mu) d\cos(\theta) f_\xi(\epsilon_\mu, \epsilon_e)$$

$$Y_+(\gamma) = \frac{1}{12} \left\{ \left(\frac{\epsilon_e}{m_\mu}\right)^3 \left[ 16 \ln\left(\frac{\gamma+1}{\gamma-1}\right) - 64\gamma(1-\beta) \right] + \left(\frac{\epsilon_e}{m_\mu}\right)^2 \left[ 48\gamma^2(1-\beta) + 24 \ln\left(\frac{\beta}{\beta+1}\right) \right] - 2 \ln(\gamma\beta) + 10 \ln(\gamma(\beta+1)) \right\}$$

$$Y_-(\gamma) = \frac{1}{36} \left\{ \left( \frac{\epsilon_e}{m_\mu} \right)^3 \left[ -48 \ln \left( \frac{\gamma+1}{\gamma-1} \right) - 512\gamma^3(1-\beta) + \gamma(576 - 320\beta) \right] \right. \\ \left. + \left( \frac{\epsilon_e}{m_\mu} \right)^2 \left[ 288\gamma^2(1-\beta) - 72 \ln \left( \frac{\beta}{\beta+1} \right) \right] + 6 \ln(\gamma\beta) + 30 \ln(\gamma(\beta+1)) \right\}$$

$$Y_0(\gamma) = \frac{1}{18} \left\{ \left( \frac{\epsilon_e}{m_\mu} \right)^3 \left[ -128\gamma^3(1-\beta) + \gamma(96 - 32\beta) \right] + \left( \frac{\epsilon_e}{m_\mu} \right)^2 \left[ 108\gamma^2(1-\beta) \right] + 15 \ln(\gamma(\beta+1)) \right\}$$

Or, in a more generic way:

$$Y_\xi(\gamma) = \frac{1}{36} \left\{ \left( \frac{\epsilon_e}{m_\mu} \right)^3 \left[ -256\gamma^3(1-\beta)(1-\xi) + \gamma(192 - 384\xi - (64 - 256\xi)\beta) + 48\xi \ln \left( \frac{\gamma+1}{\gamma-1} \right) \right] \right. \\ \left. + \left( \frac{\epsilon_e}{m_\mu} \right)^2 \left[ 72\xi \ln \left( \frac{\beta}{1+\beta} \right) + (216 - 72\xi)(1-\beta)\gamma^2 \right] + 30 \ln(\gamma(\beta+1)) - 6\xi \ln(\gamma\beta) \right\}$$

At first sight, one can think that functions  $Y$  may diverge for  $\gamma = 1$ . However one should also notice that this value of  $\gamma$  is reached only if  $\epsilon_e = m_\mu/2$  which allows all the divergences to cancel each other so the result is always finite.

#### 4.2.1.4 Kaon to electron

The high energy interaction of two protons does not only lead to pions but can also produce unstable charged kaons which will finally also give high energy electrons and positrons. Kaons have two main decay channels.

##### Muonic decay

Preferably, (in 63.5 % of the cases), a kaon decays exactly like a pion: into a neutrino and a muon, which itself decays into an electron and two neutrinos. All the formulæ written above are hence valid to describe this decay as long as all the subscripts  $\pi$  are replaced by  $K$ .

##### Pionic decay

In 21.2 % of the cases, the kaon decays into a neutral pion and a charged one. As it is a two-body decay, energy and momentum of the outgoing particle are fully determined. In the rest-frame of the kaon, energy-momentum conservation leads to:

$$\gamma'_{\pi^\pm} = \frac{1}{m_{\pi^\pm}} \frac{m_{K^\pm}^2 + m_{\pi^\pm}^2 - m_{\pi^0}^2}{2m_{K^\pm}}$$

and

$$\beta'_{\pi^\pm} = \frac{\sqrt{m_{K^\pm}^4 + m_{\pi^\pm}^4 + m_{\pi^0}^4 - 2m_{K^\pm}^2 m_{\pi^\pm}^2 - 2m_{K^\pm}^2 m_{\pi^0}^2 - 2m_{\pi^\pm}^2 m_{\pi^0}^2}}{m_{K^\pm}^2 + m_{\pi^\pm}^2 - m_{\pi^0}^2}$$

Using values given by the Particle Data Group<sup>e</sup>:  $m_{K^\pm} = 493.677$  MeV,  $m_{\pi^\pm} = 139.57018$  MeV and  $m_{\pi^0} = 134.9766$  MeV one gets the following numerical values:

$$\gamma'_{\pi^\pm} \simeq 1.78 \quad \text{and} \quad \beta'_{\pi^\pm} \simeq 0.827$$

<sup>e</sup><http://pdg.lbl.gov>

In the laboratory rest-frame, one gets a homogeneous pion distribution:

$$f(\epsilon_K, \epsilon_\pi) = \frac{\theta(\epsilon_\pi - m_\pi \gamma_\pi^-) - \theta(\epsilon_\pi - m_\pi \gamma_\pi^+)}{2m_\pi \gamma_K \gamma'_\pi \beta_K \beta'_\pi},$$

where  $\theta(x)$  is Heaviside's step function, and, similarly to what has been done concerning pion decay,  $\gamma_\pi^\pm = \gamma_K \gamma'_\pi (1 \pm \beta_K \beta'_\pi)$ .

In the sake of clarity, let us precise our notations: functions ( $F, f, \gamma, \beta \dots$ ) without superscript correspond to values in the laboratory frame  $R$ , those with a prime ' to values in the kaon rest-frame  $R'$ , those with '' to the pion rest-frame  $R''$  and finally the star \* corresponds to the muon rest-frame  $R^*$ . I noted  $\cos(\theta^*)$  the angle between electron momentum and muon spin in frame  $R^*$ . The distribution of electrons (or positrons) of energy  $\epsilon_e$  created by the decay of a kaon  $K^-$  ( $K^+$ ) with energy  $\epsilon_K$  is hence:

$$\begin{aligned} f_\xi(\epsilon_K, \epsilon_e) &= \frac{1}{2m_\pi \gamma_K \gamma'_\pi \beta_K \beta'_\pi} \int_{m_\pi \gamma_\pi^-}^{m_\pi \gamma_\pi^+} F_\xi(\epsilon_e, \epsilon_\pi) d\epsilon_\pi \\ &= \frac{1}{2m_\pi m_\mu \gamma_K \gamma'_\pi \gamma''_\mu \beta_K \beta'_\pi \beta''_\mu} \int_{m_\pi \gamma_\pi^-}^{m_\pi \gamma_\pi^+} \frac{d\epsilon_\pi}{\gamma_\pi \beta_\pi} \Delta_\xi(\gamma_\mu^+, \gamma_\mu^-), \end{aligned}$$

where  $\gamma_\mu^\pm = \gamma_\pi \gamma''_\mu (1 \pm \beta_\pi \beta''_\mu)$  and  $\Delta_\xi$  corresponds to the difference between  $X_\xi$  and  $Y_\xi$  correctly chosen (see definition of  $F_\xi$ ). An analytical integration could be performed but it would require to cut the definition domain of  $\epsilon_e$  in so many zones that it would be too tedious to gain time compared with a numerical computation

Indeed, though

$$\begin{aligned} \int^{\gamma_\pi} \frac{X_\xi(\gamma_1)}{\gamma_\pi \beta_\pi} d\gamma_\pi &= X_\xi(\gamma_1) \ln(\gamma_\pi(1 + \beta_\pi)) \\ \int^{\gamma_\pi} \frac{Y_\xi(\gamma_1)}{\gamma_\pi \beta_\pi} d\gamma_\pi &= Y_\xi(\gamma_1) \ln(\gamma_\pi(1 + \beta_\pi)) \end{aligned}$$

are easy to compute,

$$\begin{aligned} \int^{\gamma_\pi} \frac{4}{9} \left( \frac{\epsilon_e}{m_\mu} \right)^2 \left\{ (27 + 9\xi\beta_\mu^+) \gamma_\mu^{+2} - 9\xi \ln(\gamma_\mu^+(1 + \beta_\mu^+)) + \right. \\ \left. \frac{\epsilon_e}{m_\mu} [-32\gamma_\mu^{+3}(1 + \xi\beta_\mu^+) + \gamma_\mu^+(24 + 32\xi\beta_\mu^+)] \right\} \frac{d\gamma_\pi}{\gamma_\pi \beta_\pi} \end{aligned}$$

are much more of a challenge.

#### 4.2.1.5 Proton to pion (or kaon)

Proton proton collisions imply quantum chromodynamics processes which forbid simple analytical computation, hence for the kaon and pion production we need to rely on models. Several parametrisations of the first quantity can be found in Badhwar *et alii* [9] and Tan &

Ng [80]. Though we are interested in the differential cross-section  $\frac{d\sigma}{dE}$  of production of pion or kaon, parametrisations give the Lorentz invariant cross-section  $E\frac{d^3\sigma}{d\vec{p}^3}$ . Their relation is:

$$\frac{d\sigma}{dE} = \frac{\pi}{p_{\parallel}} \int E \frac{d^3\sigma}{d\vec{p}^3} dp_{\perp}^2,$$

where the  $\pi$  coefficient comes from the integration over the angles and the change of variable from  $p_{\perp} dp_{\perp}$  to  $dp_{\perp}^2$  makes the 2 disappear.

### Parametrisation of Badhwar, Stephens and Golden [9]

Making use of various colliders results, the authors have been able to parametrise charged pions and kaons production section in proton proton collisions. They found for pions:

$$E \frac{d^3\sigma_{\pi}}{d\vec{p}^3} = \frac{A}{1 + 4m_p^2/s)^r} (1 - \tilde{x})^q \exp \left[ -\frac{Bp_{\perp}}{1 + 4m_p^2/s} \right], \quad (4.17)$$

where  $q = \frac{C_1 + C_2 p_{\perp} + C_3 p_{\perp}^2}{\sqrt{1 + 4m_p^2/s}}$  and  $\tilde{x} = \sqrt{x_{\parallel}^{*2} + \frac{4}{s} (p_{\perp}^2 + m_{\pi/K}^2)}$ . Coefficient  $x_{\parallel}^*$  is the ratio of the

parallel component of the centre-of-mass momentum to the maximum transferable momentum and  $\sqrt{s}$  is the total energy in the centre-of-mass system. The values of parameter  $A$ ,  $B$ ,  $C_1$ ,  $C_2$ ,  $C_3$  and  $r$  can be found in table 4.1. Concerning kaons, the parametrisation is simpler:

$$E \frac{d^3\sigma_K}{d\vec{p}^3} = A(1 - \tilde{x})^C \exp[-Bp_{\perp}]. \quad (4.18)$$

According to Norbury and Townsend [64], this parametrisation is in good agreement with quite recent data from the NA49 collaboration [82].

Particle	$A$ [mb/(GeV <sup>2</sup> /c <sup>3</sup> )]	$B$ [(GeV/c) <sup>-1</sup> ]	$r$	$C$ [(GeV/c) <sup>-1</sup> ]	$C_1$	$C_2$ [(GeV/c) <sup>-1</sup> ]	$C_3$ [(GeV/c) <sup>-2</sup> ]
$\pi^+$	153	5.55	1	$\emptyset$	5.3667	-3.5	0.8334
$\pi^-$	127	5.3	3	$\emptyset$	7.0334	-4.5	1.667
$K^+$	8.85	4.05	$\emptyset$	2.5	$\emptyset$	$\emptyset$	$\emptyset$
$K^-$	9.3	3.8	$\emptyset$	8.3	$\emptyset$	$\emptyset$	$\emptyset$

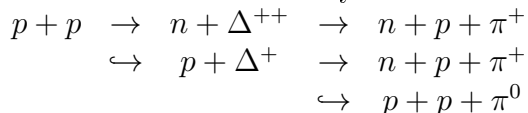
Table 4.1: Parameters for the invariant cross-sections of pion and kaon production.

The newer parametrisation by Tan & Ng [80] intended to be more precise at low energies. However it is too complex (it has 24 parameters) to be understood easily so I chose not to copy it here.

Once one have these parametrisation, the production cross-section of positrons is then given by:

$$\frac{d\sigma}{d\epsilon_e}(\epsilon_p \rightarrow \pi^{\pm}/K^{\pm} \rightarrow \epsilon_e) = \int \frac{d\sigma}{d\epsilon_{\pi/K}}(\epsilon_p \rightarrow \epsilon_{\pi/K}) \times d\epsilon_{\pi/K} \times \mathcal{P}(\epsilon_{\pi/K} \rightarrow \epsilon_e).$$

Kamae *et alii* [47, 48] also provided a direct parametrisation of the  $p + p \rightarrow e^\pm$  reaction. Taking advantage of the recent development of Monte Carlo methods in particle physics (see for instance the Pythia code [76]), these authors have been able to perform new parametrisations which give better results at low transverse momentum of the outgoing species. Indeed, they have been able to take into account resonances which were neglected until then. Proton proton collisions can produce hadrons in an excited state:  $\Delta^+$  and  $\Delta^{++}$ . These particles are unstable and their mass is not very well defined. The reactions we have to consider are:



To know their distribution functions, one can use Breit–Wigner theory. These processes can increase quite importantly the production cross-section of electrons and positrons and should not be neglected. However, this parametrisation is different from the previous ones, in that it does not give the pion or kaon production cross-sections but directly the electrons and positrons (neutrinos and gammas as well) ones. Their conclusion is that the power spectrum index of the secondaries is 0.05 harder than the one of the incoming primaries.

All the afore mentioned parametrisations differ from each other and have been calibrated with different nuclear data sets. The default choice in the following calculations, unless stated otherwise, is the [47, 48] parametrisation, which includes additional processes (especially resonances other than the Delta at low interaction energies) and has been calibrated with recent data. As stated in the original paper, one should be nevertheless warned that this parametrisation relies on fits to Monte–Carlo simulations and may be easily affected by some uncertainties. Actually there are other parametrisations in the literature, however, most of them, like Blattnig *et alii* [16], considered only pions or only kaons but never both of them in the same framework.

#### 4.2.1.6 Dealing with other particles

The interstellar medium is not only made of hydrogen but also of helium. Likewise, the projectile producing electrons and positrons are not only cosmic protons but also  $\alpha$  particles (and to lesser extent other heavier ions). Almost no data exists for these processes but some models have been successful to parametrise the pion production cross-section of the reaction where a projectile of mass number  $A_P$  spallates off a target of mass number  $A_T$ . Quite an old work from Orth & Buffington [65] proposed the following scaling:

$$\sigma_{PT} = \left( A_P^{3/8} + A_T^{3/8} - 1 \right)^2 \sigma_{pp}. \quad (4.19)$$

However at that time little data was available and this parametrisation seems a little out-dated. The more recent parametrisations from Norbury & Townsend [64] using data from Nagamiya *et alii* [60] and Schwalb *et alii* [74] suggest a more refined parametrisation which differs for each pion charge:

$$\begin{aligned} \sigma_{AA \rightarrow \pi^+ X} &= (A_P A_T)^{N_\pm} \sigma_{pp \rightarrow \pi^+ X}, \\ \sigma_{AA \rightarrow \pi^- X} &= \frac{(A_P A_T)^{N_\pm} \sigma_{pp \rightarrow \pi^+ X}}{\frac{Z_P}{A_P} \frac{Z_T}{A_T} \frac{\sigma_{pp \rightarrow \pi^+ X}}{\sigma_{pp \rightarrow \pi^- X}} + \left( \frac{A_P - Z_P}{A_P} \right) \left( \frac{A_T - Z_T}{A_T} \right) \frac{\sigma_{pp \rightarrow \pi^- X}}{\sigma_{pp \rightarrow \pi^+ X}}}, \end{aligned}$$

and

$$\sigma_{AA \rightarrow \pi^0 X} = (A_P A_T)^{N_0} \sigma_{pp \rightarrow \pi^0 X}. \quad (4.20)$$

A fit over various sets of data led to  $N_{\pm} = 2.2/3$  and  $N_0 = 2.4/3$ . However one should stress that most data have only one point in energy for each  $P, T$  couple and sometimes with very large error bars.

It is not clear that this parametrisation can be used for kaon production as well. However, the electron/positron production cross-section being largely dominated by pions, the error one can introduce by using this parametrisation for kaons is not larger than a few percent.

#### 4.2.1.7 Comparison

In figure 4.3, one can see the different parametrisations of electron and positron cross-sections. It appears from it that

- Electrons are produced in less copious amount than positrons, especially at low proton energy and high electron energy. This is due to charge conservation: electrons can be produced only if at the same time a positive extra particle is produced, so the energy threshold is higher.
- At high proton energy, the cross-section depends less on the proton energy. Tan & Ng predict more particles than the others in this regime.
- At low proton energy Badhwar *et alii* [9] exhibits large differences with the other two.

### 4.2.2 Projectile cosmic ray fluxes

The secondary cosmic ray production does not only depend on the production cross-section but also on the projectile particle flux. As far as electrons and positrons are concerned, only protons and to a lesser extent  $\alpha$  particles relevantly contribute. It is hence of importance to know how much this flux is. The only place where we can measure it is at the Earth. We will see later (section B.2) how to deduce the primary flux anywhere in the Galaxy from this, though it is not so important for secondary electrons and positrons. The problem is the data we have are limited at high energy. Hopefully new measurement will come soon. However for the moment, using the up-to-date data, there are three different fits to these data available. Based on AMS data, Donato *et alii* [34] gives

$$\begin{aligned} \Phi_{\odot}^p(T) &= 1.3249 \left( \frac{T}{1\text{GeV}} \right)^{-2.72} \text{cm}^{-2}\text{s}^{-1}\text{sr}^{-1}\text{GeV}^{-1} \\ \Phi_{\odot}^{\alpha}(T) &= 0.0721 \left( \frac{T}{1\text{GeV/n}} \right)^{-2.74} \text{cm}^{-2}\text{s}^{-1}\text{sr}^{-1}(\text{GeV/n})^{-1}. \end{aligned} \quad (4.21)$$

Here  $T$  stands for the kinetic energy per nucleon of the cosmic rays. I will call it (D01). More recent BESS measurement lead Shikaze *et alii* [75] to suggest the form:

$$\begin{aligned} \Phi_{\odot}^p(T) &= 1.94\beta^{0.7}\mathcal{R}^{-2.76}\text{cm}^{-2}\text{s}^{-1}\text{sr}^{-1}\text{GeV}^{-1} \\ \Phi_{\odot}^{\alpha}(T) &= 0.71\beta^{0.5}\mathcal{R}^{-2.78}\text{cm}^{-2}\text{s}^{-1}\text{sr}^{-1}(\text{GeV/n})^{-1}. \end{aligned} \quad (4.22)$$

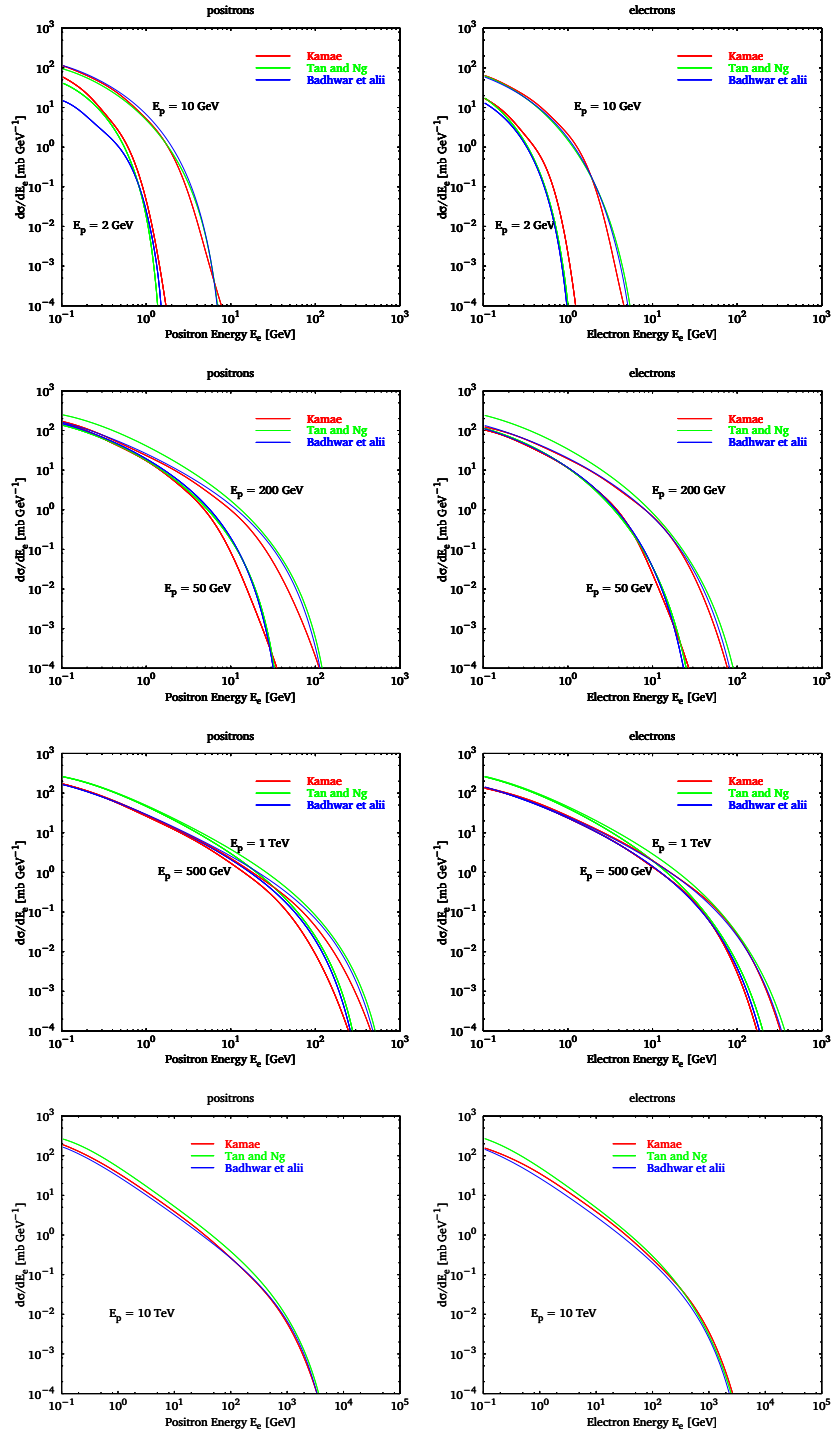


Figure 4.3: Comparison between various parametrisations of the proton proton to electron and positron production cross-sections at different incident proton kinetic energies. Left panels concern positrons and right panels electrons. Red lines are for Kamae, green for Tan & Ng and blue for Badhwar. Notice that the scale has been changed for the last line.

Combining both data Donato *et alii* [33] suggested a correction to the Shikaze function for  $T \geq 20$  GeV:

$$\begin{aligned}\Phi_{\odot}^p(T) &= 2.4132\mathcal{R}^{-2.84}\text{cm}^{-2}\text{s}^{-1}\text{sr}^{-1}\text{GeV}^{-1} \\ \Phi_{\odot}^{\alpha}(T) &= 0.8866\mathcal{R}^{-2.85}\text{cm}^{-2}\text{s}^{-1}\text{sr}^{-1}(\text{GeV}/n)^{-1}.\end{aligned}\quad (4.23)$$

In figure 4.4, one can see the different parametrisations of the incoming cosmic ray proton and helium fluxes measured at the Earth. At low energy, the last two (Shikaze and D09) are of course the same. However at high energy the difference is sizeable but actually less important than the uncertainty due to the cross-sections. The discrepancies come from the fact that data are not taken during the same solar activity period and from the large error bars at high energy. Unless stated otherwise, I will use the Donato *et alii* [33] (D09) parametrisation in the figures.

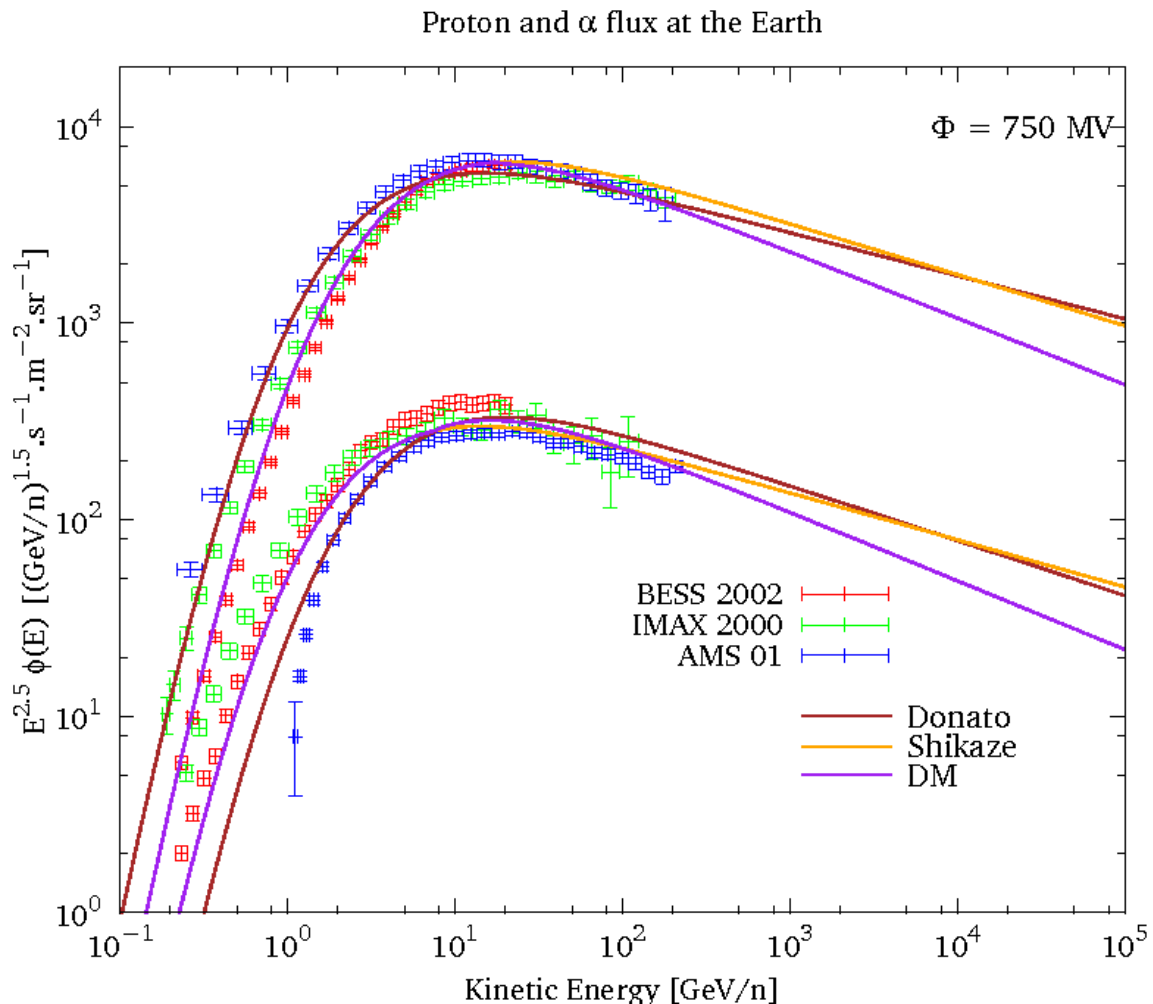


Figure 4.4: Comparison of the effect due to different parametrisations displayed with the data from BESS[75, 75], IMAX[58, 58] and AMS[4, 6]

### 4.2.3 Galactic distribution of targets

The spatial distribution of targets is not very important when dealing with charged cosmic rays. Indeed, as we will see in the next chapter, propagation of cosmic rays smooths all the small spatial scales. Moreover, because we need cylindrical symmetry to solve the propagation with the Bessel method (see section 5.3.1.1), it is impossible to properly take into account such details. In the case of the Green method (see section 5.3.1.2), it is possible but this would imply quite a long resolution time. One spatial feature which is relevant and can easily be counted for, is the local bubble. The Sun lies in a local under-density of gas, probably due to the explosions of some supernovæ a long time ago. Taking into account this void of about 120 pc has an impact for all secondary cosmic ray predictions as it has been shown by Putze *et alii* [70], especially for radio-isotopes (see also reference [35]). The method used to take into account the bubble is detailed in section 6.1.1.3.

Concerning photons, propagation is of course not smoothing any spatial detail and it is hence important to know precisely the gas map of the Galaxy. This will be discussed in chapter 7.

## 4.3 Exotic Cosmic Rays

In the previous sections, I described the standard and well accepted sources of cosmic rays, however some other astrophysical phenomenon can produce cosmic rays in principle. The main debate is whether these new contributions are sizeable and if one can learn anything interesting studying them.

### 4.3.1 Dark matter

If dark matter exists and has something in common with what has been described in Chapters 1 and 2, our Galaxy should contain a lot of it and there is a big chance that the particles it is made of, annihilate or decay and produce high energy standard particles, hence cosmic rays. Of course the exact amount of dark matter originating cosmic rays one should detect at the Earth, strongly depends on both the astrophysical and particle physics properties of the dark matter. However, as we will see in Chapter 8, the spectral features of this cosmic ray component should be quite different from the one of astrophysical origin. This is why, the study of these exotic cosmic rays, may teach us many things about the dark matter properties.

#### 4.3.1.1 Annihilating dark matter

Many models of physics beyond the standard model predict a new stable particle with the good properties to be a dark matter candidate. Being stable does not prevent the particle from annihilating with its anti-particle or with itself (in the case of self-conjugated particles like *exempli gratia* Majorana fermions). The cosmic ray production density term reads:

$$Q(\vec{x}, E, t) = \eta \langle \sigma v \rangle \left\{ \frac{\rho(\vec{x})}{m_\chi} \right\}^2 f(E) . \quad (4.24)$$

The coefficient  $\eta$  is a quantum term which depends on the particle being or not self-conjugate : for instance, for a fermion it equals 1/2 or 1/4 depending on whether the WIMP is a Majorana

or a Dirac particle. In what follows, if not stated otherwise, I will consider a Majorana type species and take  $\eta = 1/2$ .

The annihilation cross section is averaged over the momenta of the incoming dark matter particles to yield  $\langle\sigma v\rangle$ , the value of which depends on the specific beyond the standard model physics model and is constrained by cosmology (see equation 1.14). In what follows I actually have taken a benchmark value of  $3 \times 10^{-26} \text{ cm}^3 \text{ s}^{-1}$  which is a little higher than what we have computed previously but is allowed by the WMAP measurement (taking into account the errors on  $\Omega_m$  and  $\Omega_b$ ). Moreover this value is commonly used by the community and makes comparisons easier.

The dark matter mass  $m_\chi$  is unknown. In the case of neutralinos, theoretical arguments as well as the LEP and WMAP results constrain this mass to range from a few GeV [11, 17, 18, 44] up to a few TeV.

Finally, the energy distribution of the particle species of interest produced in a single annihilation is denoted by  $f(\epsilon) \equiv dN/dE$ . This quantity can for instance be evaluated with the help of a Monte–Carlo. In this work I have used the code `Pythia 6.4` [77].

The only astronomical ingredient in the source term (Eq. 4.24) is the dark matter distribution  $\rho(\vec{x})$  inside the Milky Way halo. This point is discussed in paragraph 4.3.1.4

#### 4.3.1.2 Decaying dark matter

The energy dependence of the cosmic ray production term is fully determined

$$Q(\vec{x}, E, t) = \Gamma \left\{ \frac{\rho(\vec{x})}{m_\chi} \right\} f(E) . \quad (4.25)$$

All the terms have been defined in the previous paragraph, except for  $\Gamma$ , the decay rate of the dark matter particle.

The main difference between annihilating and decaying dark matter is the power of  $\frac{\rho(\vec{x})}{m_\chi}$ . This implies that annihilating dark matter will be easier to detect where the density  $\rho(r)$  is large (at the Galactic centre for instance) whereas decaying dark matter will be easier to detect if the mass of the particle is very heavy.

#### 4.3.1.3 Energy spectra

A priori there is no way to tell how the dark matter particle annihilates (or decays), hence to explicate the function  $f(E)$ . The most generic way to proceed is hence to look for each possible annihilation channel. As it can be seen in figure 4.5, the various annihilation channels give quite different positron/electron spectra. However some of them give similar results, so instead of studying all of them, one can limit oneself to a few channels:  $W^+W^-$ ,  $b\bar{b}$ ,  $\tau^+\tau^-$ , and  $e^+e^-$ . This allows to get a fair idea of the possible scenarios. Generic dark matter candidates, for instance a neutralino or a sneutrino in supersymmetric models, or the lightest Kaluza–Klein particle in models with extra–dimensions (see chapter 2), will entail annihilation processes with specific branching ratios into one or more of these benchmark cases. The positron flux in these more general situations would simply be a superposition of the results for each specific annihilation channel, weighted by the relevant branching ratios and normalised by the actual annihilation

cross section. This is indeed possible, because, as we will see in the next chapter, the observed spectrum depends linearly on the source.

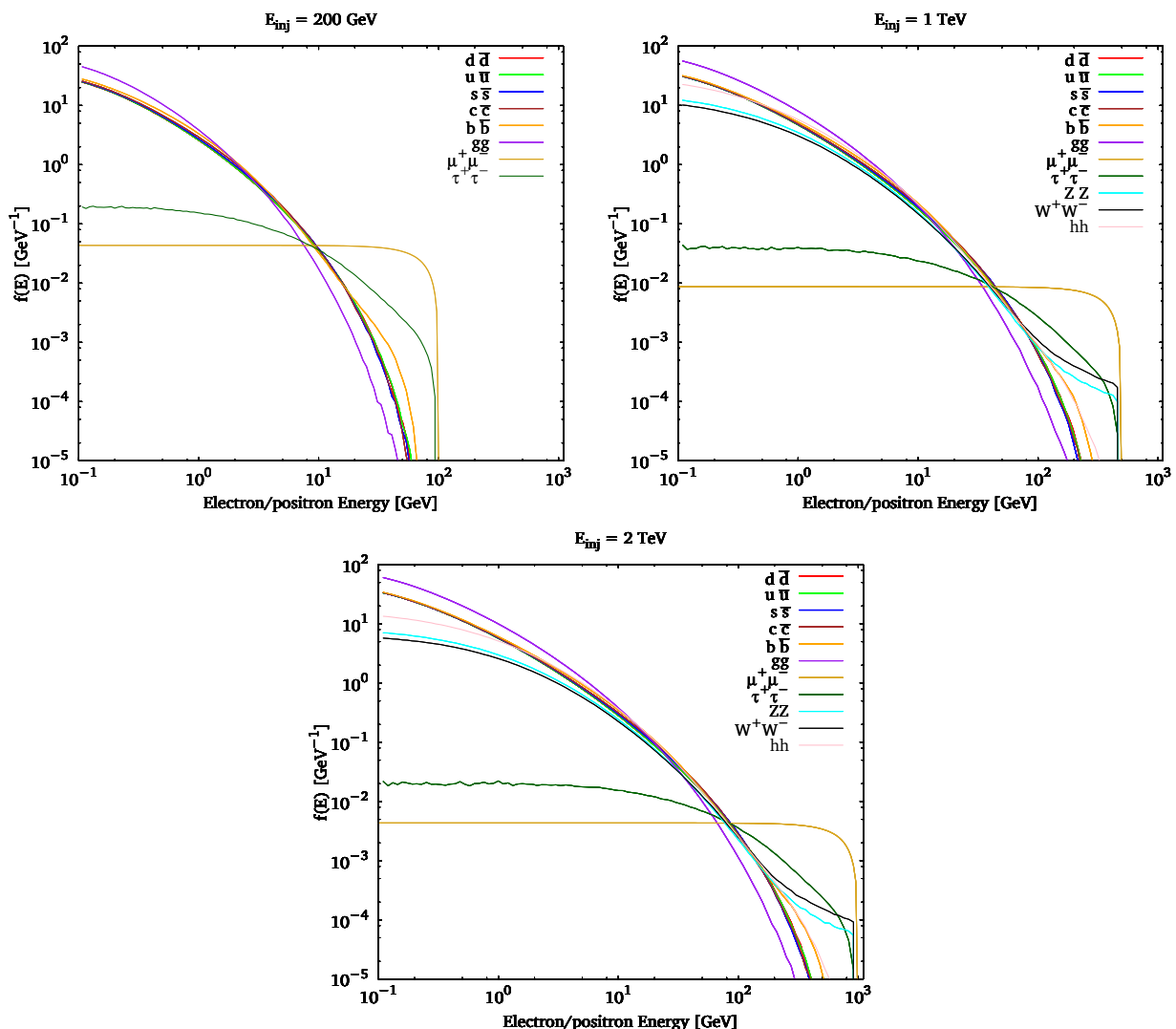


Figure 4.5: Annihilation/decay spectra  $f(E)$  into electrons/positrons for various channels and various injection energies  $E_{inj}$ . The mass of the dark matter particle corresponds to the injection energy in the decaying case and to its half in the annihilating case.

#### 4.3.1.4 Smooth distribution of dark matter

In order to compute the cosmic ray flux due to dark matter, one needs to know its distribution in the Milky Way. This issue is studied by means of large N-body simulations which follow the gravitational evolution of small mass units. In order to reproduce dark matter haloes consistent with the one of our Galaxy, one needs to make evolve the primordial fluctuations of matter density in the proper Universe. Actually the problem is described by five parameters:

the matter density parameter  $\Omega_m$ , the cosmological constant parameter  $\Omega_\Lambda$ , the expansion rate ruled by the Hubble constant  $H_0$ , and two parameters describing the primordial fluctuations,  $\sigma_8$  and  $n_s$ . The first three parameters have already been described in chapter 1. The parameter  $\sigma_8$  is the ratio of the mass variance to the total mass in a sphere of radius 8 Mpc as observed today ; the second parameter,  $n_s$  is  $\frac{d\mathcal{P}}{dk}$ , the power law of the Fourier transform of the fluctuations of matter density  $\mathcal{P}$  as a function of the Fourier space coordinate  $k$ .

Because the precision of the measurement of these five parameters has increased very rapidly in the last few years, as it can be seen in Table 4.2, all the N-body simulations did not use exactly the same values according to what were the best ones at that time. However, as tested by Diemand *et alii* [31] this has little impact on the final results.

Simulation	$\Omega_m$	$\Omega_\Lambda$	$H_0[\text{km.s}^{-1}\text{Mpc}^{-1}]$	$\sigma_8$	$n_s$
Millenium[79] & Aquarius[62]	0.25	0.75	73	0.9	1.0
ViaLactea-II[31]	0.238	0.762	73	0.74	0.951

Table 4.2: Cosmological parameters used by various recent N-body simulations..

Making this kind of large simulations work is already a challenge but analysing their results can be even more difficult. Like any simulation, even the most modern ones, though they sometimes are run on some of the most powerful machines in the world, are limited by resolution in space and mass of the smallest mass units considered. The difficulty is to find a proper function to fit the dark matter distribution profile. The easiest one is the so-called isothermal cored sphere function, which comes from analytical resolution of the linear problem but gives rather poor fits to the N-body simulation results. This is not surprising as one expects to see non linearities to have some importance on structure evolution. Two better fitted functions have been proposed by the authors of some of the numerical simulations: the Navarro-Frenck-White (hereafter NFW) and the Moore (hereafter M99) profiles. Both these functions have two free parameters: a radius  $r_s$  and the corresponding density  $\rho_s^f$ . Depending of the simulation, the definition of parameters is not the same but it is always possible to get one from the other. However it is often more convenient to express these matter density profiles with respect to the local dark matter density  $\rho_\odot$ . This is allowed only because it appears that the matter density function is universal and does not depend on the total mass of the halo. All three functions can be written with the same expression:

$$\rho(r) = \rho_\odot \left(\frac{r_\odot}{r}\right)^\gamma \left(\frac{1 + (r_\odot/r_s)^\alpha}{1 + (r/r_s)^\alpha}\right)^{(\beta-\gamma)/\alpha} \quad (4.26)$$

where the values of  $\alpha$ ,  $\beta$ , and  $\gamma$  are fixed for each profile and  $\rho_\odot$  and  $r_s$  are the free parameters. Another parametrisation which does not exhibit a divergence at the centre of the halo has been suggested by Burkert [21] to fit observations from dwarf Galaxies.

$$\rho(r) = \rho_\odot \frac{(r_\odot + r_s)(r_\odot^2 + r_s^2)}{(r + r_s)(r^2 + r_s^2)} \quad (4.27)$$

<sup>f</sup>Some authors use the radius at which the slope of the logarithm of the density is minus two whereas others prefer the radius inside which the mass is equal to half of the total mass of the halo. Both methods have their pros and cons depending on the resolution.

Recently a new function, which was in use for rotation curves problem for a long time, has been widely used by N-body simulation people: the Einasto function (also known by Vaucouleur's name when  $\alpha = 1/4$  and by Sérsic's for  $\alpha = 1/n$ ).

$$\ln\left(\frac{\rho(r)}{\rho_s}\right) = \frac{2}{\alpha} \left(1 - \left(\frac{r}{r_s}\right)^\alpha\right) \quad (4.28)$$

If one wants to normalise this expression to the local dark matter density, one gets:

$$\rho(r) = \rho_\odot \exp\left\{\frac{2}{\alpha} \left(\frac{r_\odot^\alpha - r^\alpha}{r_s^\alpha}\right)\right\} \quad (4.29)$$

This function gives better fit but has three free parameters. On top on the two previous ones ( $r_s$  and  $\rho_s$ ), the value of  $\alpha$  also has to be fitted.

Model	$\alpha$	$\beta$	$\gamma$	$r_s$ [kpc]
Cored isothermal	2	2	0	5
Navarro Frencck and White (NFW)	1	3	1	20
Moore (M99)	1.5	3	1.3	30
Burkert	$\emptyset$	$\emptyset$	$\emptyset$	10
Einasto	0.15	$\emptyset$	$\emptyset$	15

Table 4.3: Some N-body simulations results. For the first three ones  $\alpha$ ,  $\beta$ , and  $\gamma$  are not fitted on data but fixed by the definition of the functions. Values for  $r_s$  are taken from Bahcall & Soneira [10], Navarro *et alii* [61] and Diemand *et alii* [32] for the first three ones. Concerning the last two parametrisations, an average of the results from Merritt *et alii* [59] and Navarro *et alii* [62] has been used.

Other fitting functions exist in the literature (Prigniel–Simien or  $(1,3,\gamma)$ ) but are less used by the community so I will not consider them.

#### 4.3.1.5 Clumps

Though they disagree on some (important) details, both recent big N-body simulations ViaLactea [31] and Aquarius [78] agree on the broad picture: large scale structures (galaxy clusters and galaxies) form by the merging of smaller structures. Some of the substructures can survive the merging and carry on existing inside the large halo as local dark matter overdensities (the so called clumps). These over-densities can be of great interest for dark matter indirect detection, as the annihilation (or to a lesser extent, decay) rate is amplified in these regions. The correct amount of these subhaloes that can survive inside the main halo, along with their mass and velocity distributions is still under debate. Indeed it seems that the answer depends a lot on the simulation resolution (actually earlier simulations could not see any substructures). However, at most only a few percent of the total mass of the halo lies inside substructures hence the over all effect cannot be extremely large, as shown by Lavalle *et alii* [50] and Pieri *et alii* [69]. As far as we are concerned, because the outer part of the

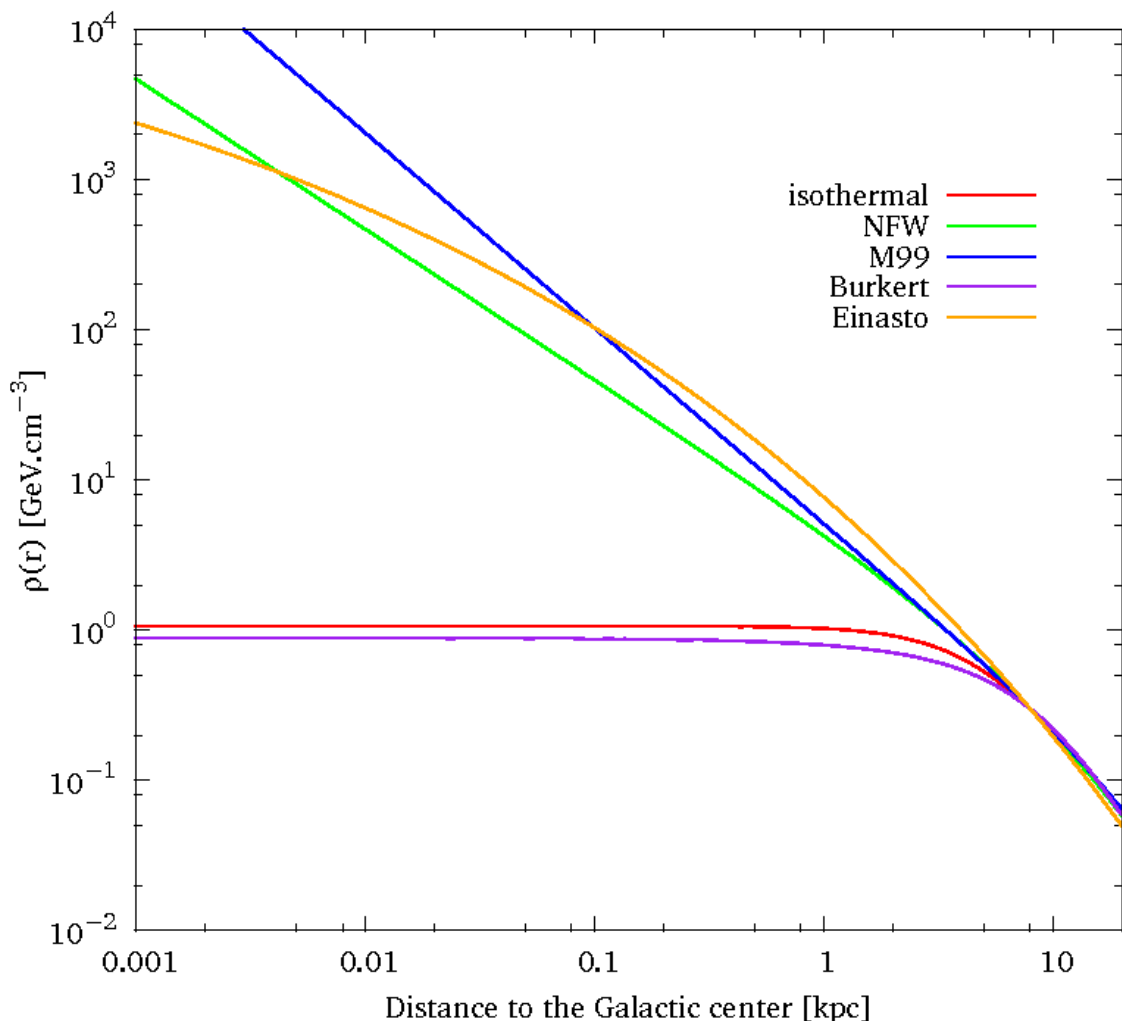


Figure 4.6: Comparison of various dark matter halo density profiles from the literature. Here all the profiles are rescaled to give the same density at the Sun’s position. Except for the central part (which is emphasised here by the logarithmic scale) all profiles agree actually pretty well.

clumps seems to be always stripped of by gravitational tides, we can consider clumps as point like over-densities to which one can associate a luminosity  $\mathcal{L}$  defined as:

$$\mathcal{L} = \int_0^\infty 4\pi\rho_c(r)^2 dr \text{ in } M_\odot^2 \text{pc}^{-3}. \quad (4.30)$$

where  $\rho_c(r)$  is the clump mass-density profile which can be obtained from simulations.

Moreover, because over-densities are older, they are cooler<sup>g</sup>, hence, if the annihilation cross-section depends on the dark matter particle velocity, substructures could be actually much brighter than the halo (see for instance Lattanzi & Silk [49]).

<sup>g</sup>In deed, numerical simulation, see for instance Springel *et alii* [78] relate maximal velocity of the clump  $v_{max}$  to its mass  $M$  by  $v_{max} \propto M^{1/3.5}$ .

### 4.3.1.6 Intermediate Mass Black Holes

Black holes are purely geometrical objects predicted by the theory of General Relativity. By definition they are extremely compact and hence very difficult to detect. However for the past decades many indirect evidences have been accumulated in favour of the existence of black holes. Two categories of black holes have been widely studied: stellar black holes (which are supposed to be created after the explosion of some massive core collapse supernovæ) and super massive black holes. The first ones are predicted to have a mass of order  $10 M_{\odot}$ , a mass range forbidden by theory for neutron stars but in agreement with observations of some binary systems. The second category is supposed to live at the centre of every galaxy. These super massive black holes should have a mass of  $\sim 10^6 - 10^{10} M_{\odot}$ . Their formation mechanism is not completely clear but they are probably due to cosmological over-densities that have accreted a lot of matter during their history. Actually most of them are still accreting and this might be the source of the extremely violent events we call Active Galactic Nuclei (AGN). The study of individual stellar orbits around the centre of our very own Galaxy hints toward a mass of  $\sim 3 \times 10^6 M_{\odot}$ .

A third, maybe more putative, category of black hole has been proposed: intermediate mass black holes (see for instance Coleman Miller & Colbert [27] for a review) are expected to have a mass in the range  $\sim 10^2 - 10^5 M_{\odot}$  and to lie at the centre of stellar clusters. This hypothesis is supported by X-ray observations but also maybe by microlensing surveys such as OGLE [83] and MACHO [5]. If these objects actually exist, one scenario is that they have been created in the very early Universe before primordial nucleosynthesis, for instance during the QCD phase transition, when the equation of state of the Universe was rather soft which would have eased collapse. Another scenario involves the first generation of stars (often referred to as Population III stars), which, thanks to their very low metallicity were much heavier than the present stars. Though most of them could not have core collapsed because of a pair instability process, the most heavy ones ( $M \geq 250 M_{\odot}$ ) could have core collapsed to give birth to these heavy black holes. Finally a third scenario scenario B of Bertone *et alii* [14]) is that small mass black holes ( $\sim 10^5 M_{\odot}$ ) formed during the collapse of the first gas haloes, have accreted so much gas and merged with so many other black holes that it has reach a much larger mass today.

If these objects exist, it is argued [88] that there should be quite numerous in the Galaxy and more important to us, being extremely old, they should have accreted huge amounts of dark matter around them (a mini spike of  $\sim 10^5 M_{\odot}$ ). Though most of these black holes are expected to be in the Galactic centre vicinity, it is possible that some of them are closer to the Sun and could produce a signature in cosmic ray fluxes. However, it has been shown by Bringmann *et alii* [19] that if these objects exist they should have been detected already because of their gamma ray emission.

### 4.3.2 GRB, AGN etc.

Other astrophysical phenomena are suspected of producing cosmic rays such as gamma ray bursts [39], active galactic nuclei [24], Kerr–Newman black wholes through Penrose mechanism [15, 68], or decaying topological defects [43]. However all these phenomena could only produce ultra high energy cosmic rays ( $E \geq 10^{19} \text{eV}$ ) which are not expected to be mixed up

with the dark matter signal we are interested in.

## Bibliography

- [1] Abdo, A. A., Ackermann, M., Ajello, M., *et alii* . 2009, Science, 325, 840 61
- [2] Aharonian, F., Akhperjanian, A. G., Anton, G., *et alii* . 2009, A&A, 508, 561 61
- [3] Aharonian, F., Akhperjanian, A. G., Barres de Almeida, U., *et alii* . 2008, Physical Review Letters, 101, 261104 61
- [4] Alcaraz, J., Alpat, B., Ambrosi, G., *et alii* . 2000, Physics Letters B, 490, 27 75
- [5] Alcock, C., Allsman, R. A., Alves, D. R., *et alii* . 2001, ApJS, 136, 439 82
- [6] AMS Collaboration, Alcaraz, J., Alpat, B., *et alii* . 2000, Physics Letters B, 494, 193 75
- [7] Atoyan, A. M. & Aharonian, F. A. 1996, MNRAS, 278, 525 61
- [8] Baade, W. & Zwicky, F. 1934, Proceedings of the National Academy of Science, 20, 259 54
- [9] Badhwar, G. D., Golden, R. L., & Stephens, S. A. 1977, Phys. Rev. D, 15, 820 70, 71, 73
- [10] Bahcall, J. N. & Soneira, R. M. 1980, ApJS, 44, 73 80
- [11] Belanger, G., Boudjema, F., Cottrant, A., Pukhov, A., & Rosier-Lees, S. 2004, JHEP, 03, 012 77
- [12] Bell, A. R. 1978, MNRAS, 182, 147 55
- [13] Bell, A. R. 1978, MNRAS, 182, 443 55
- [14] Bertone, G., Zentner, A. R., & Silk, J. 2005, Phys. Rev. D, 72, 103517 82
- [15] Bhat, M., Dhurandhar, S., & Dadhich, N. 1985, Journal of Astrophysics and Astronomy, 6, 85 82
- [16] Blattnig, S. R., Swaminathan, S. R., Kruger, A. T., Ngom, M., & Norbury, J. W. 2000, Phys. Rev. D, 62, 094030 72
- [17] Bottino, A., Donato, F., Fornengo, N., & Scopel, S. 2003, Phys. Rev. D, 68, 043506 77
- [18] Bottino, A., Fornengo, N., & Scopel, S. 2003, Phys. Rev. D, 67, 063519 77
- [19] Bringmann, T., Lavalle, J., & Salati, P. 2009, Physical Review Letters, 103, 161301 82
- [20] Brogan, C. L., Gelfand, J. D., Gaensler, B. M., Kassim, N. E., & Lazio, T. J. W. 2006, ApJ, 639, L25 64

- [21] Burkert, A. 1995, ApJ, 447, L25+ 79
- [22] Burrows, A. 2000, Nature, 403, 727 59
- [23] Case, G. L. & Bhattacharya, D. 1998, ApJ, 504, 761 64
- [24] Chechetkin, V. M., D'Yachenko, V. F., Ginzburg, S. L., *et alii* . 2009, Astronomy Reports, 53, 501 82
- [25] Cheng, A., Ruderman, M., & Sutherland, P. 1976, ApJ, 203, 209 61
- [26] Cheng, K. S., Ho, C., & Ruderman, M. 1986, ApJ, 300, 500 61
- [27] Coleman Miller, M. & Colbert, E. J. M. 2004, International Journal of Modern Physics D, 13, 1 82
- [28] Delahaye, T., Lavalle, J., Lineros, R., Donato, F., & Fornengo, N. 2010, ArXiv e-prints 1002.1910 58
- [29] Delahaye, T., Lineros, R., Donato, F., *et alii* . 2009, A&A, 501, 821 64
- [30] Diehl, R., Halloin, H., Kretschmer, K., *et alii* . 2006, Nature, 439, 45 59
- [31] Diemand, J., Kuhlen, M., Madau, P., *et alii* . 2008, Nature, 454, 735 79, 80
- [32] Diemand, J., Moore, B., & Stadel, J. 2004, MNRAS, 353, 624 80
- [33] Donato, F., Maurin, D., Brun, P., Delahaye, T., & Salati, P. 2009, Physical Review Letters, 102, 071301 75
- [34] Donato, F., Maurin, D., Salati, P., *et alii* . 2001, ApJ, 563, 172 73
- [35] Donato, F., Maurin, D., & Taillet, R. 2002, A&A, 381, 539 76
- [36] Gaensler, B. M. & Frail, D. A. 2000, Nature, 406, 158 62
- [37] Gaensler, B. M. & Slane, P. O. 2006, ARA&A, 44, 17 61
- [38] Gamezo, V. N., Khokhlov, A. M., Oran, E. S., Chtchelkanova, A. Y., & Rosenberg, R. O. 2003, Science, 299, 77 59
- [39] Gialis, D. & Pelletier, G. 2005, ApJ, 627, 868 82
- [40] Green, D. A. 2005, Memorie della Societa Astronomica Italiana, 76, 534 58
- [41] Green, D. A. 2009, Bulletin of the Astronomical Society of India, 37, 45 58, 60, 63
- [42] Harding, A. K., Stern, J. V., Dyks, J., & Frackowiak, M. 2008, ApJ, 680, 1378 61
- [43] Hill, C. T. 1983, Nuclear Physics B, 224, 469 82
- [44] Hooper, D. & Plehn, T. 2003, Phys. Lett., B562, 18 77

- [45] Janka, H., Langanke, K., Marek, A., Martínez-Pinedo, G., & Müller, B. 2007, *Phys. Rep.*, 442, 38 59
- [46] Jones, F. C. & Ellison, D. C. 1991, *Space Science Reviews*, 58, 259 55, 57
- [47] Kamae, T., Karlsson, N., Mizuno, T., Abe, T., & Koi, T. 2006, *ApJ*, 647, 692 72
- [48] Kamae, T., Karlsson, N., Mizuno, T., Abe, T., & Koi, T. 2007, *ApJ*, 662, 779 72
- [49] Lattanzi, M. & Silk, J. 2009, *Nuclear Physics B Proceedings Supplements*, 194, 162 81
- [50] Lavalle, J., Yuan, Q., Maurin, D., & Bi, X. 2008, *A&A*, 479, 427 80
- [51] Lorimer, D. R. 2004, in *IAU Symposium*, Vol. 218, *Young Neutron Stars and Their Environments*, ed. F. Camilo & B. M. Gaensler, 105–+ 63
- [52] Lucek, S. G. & Bell, A. R. 2000, *MNRAS*, 314, 65 60
- [53] Madau, P., della Valle, M., & Panagia, N. 1998, *MNRAS*, 297, L17+ 54, 59
- [54] Malyshev, D., Cholis, I., & Gelfand, J. 2009, *Phys. Rev. D*, 80, 063005 61, 63
- [55] Manchester, R. N., Hobbs, G. B., Teoh, A., & Hobbs, M. 2005, *AJ*, 129, 1993 63
- [56] Mannucci, F. 2009, in *American Institute of Physics Conference Series*, Vol. 1111, *American Institute of Physics Conference Series*, ed. G. Giobbi, A. Tornambe, G. Raimondo, M. Limongi, L. A. Antonelli, N. Menci, & E. Brocato, 467–476 54
- [57] Mazzali, P. A., Röpke, F. K., Benetti, S., & Hillebrandt, W. 2007, *Science*, 315, 825 59
- [58] Menn, W., Hof, M., Reimer, O., *et alii* . 2000, *ApJ*, 533, 281 75
- [59] Merritt, D., Graham, A. W., Moore, B., Diemand, J., & Terzić, B. 2006, *AJ*, 132, 2685 80
- [60] Nagamiya, S., Lemaire, M. C., Moeller, E., *et alii* . 1981, *Phys. Rev. C*, 24, 971 72
- [61] Navarro, J. F., Frenk, C. S., & White, S. D. M. 1997, *ApJ*, 490, 493 80
- [62] Navarro, J. F., Ludlow, A., Springel, V., *et alii* . 2010, *MNRAS*, 402, 21 79, 80
- [63] Nomoto, K., Thielemann, F., & Yokoi, K. 1984, *ApJ*, 286, 644 59
- [64] Norbury, J. W. & Townsend, L. W. 2007, *Phys. Rev. D*, 75, 034001 71, 72
- [65] Orth, C. D. & Buffington, A. 1976, *ApJ*, 206, 312 72
- [66] Ostriker, J. P. & Gunn, J. E. 1969, *ApJ*, 157, 1395 62
- [67] Paczynski, B. 1990, *ApJ*, 348, 485 64
- [68] Penrose, R. 1969, *Nuovo Cimento Rivista Serie*, 1, 252 82

- [69] Pieri, L., Lavalle, J., Bertone, G., & Branchini, E. 2009, ArXiv e-prints [0908.0195](#) **80**
- [70] Putze, A., Derome, L., & Maurin, D. 2010, ArXiv e-prints [1001.0551](#) **76**
- [71] Ruderman, M. A. & Sutherland, P. G. 1975, ApJ, 196, 51 **61**
- [72] Sasaki, M. & Breitschwerdt, D. 2003, in International Cosmic Ray Conference, Vol. 5, International Cosmic Ray Conference, 2639–+ **64**
- [73] Sasaki, M., Breitschwerdt, D., & Supper, R. 2004, Ap&SS, 289, 283 **64**
- [74] Schwalb, O., Pfeiffer, M., Berg, F., *et alii* . 1994, Physics Letters B, 321, 20 **72**
- [75] Shikaze, Y., Haino, S., Abe, K., *et alii* . 2007, Astroparticle Physics, 28, 154 **73, 75**
- [76] Sjöstrand, T., Mrenna, S., & Skands, P. 2008, Computer Physics Communications, 178, 852 **72**
- [77] Sjostrand, T., Mrenna, S., & Skands, P. Z. 2006, JHEP, 05, 026 **77**
- [78] Springel, V., Wang, J., Vogelsberger, M., *et alii* . 2008, MNRAS, 391, 1685 **80, 81**
- [79] Springel, V., White, S. D. M., Jenkins, A., *et alii* . 2005, Nature, 435, 629 **79**
- [80] Tan, L. C. & Ng, L. K. 1983, Journal of Physics G Nuclear Physics, 9, 1289 **71**
- [81] Tatischeff, V. 2009, A&A, 499, 191 **57, 59**
- [82] The Na49 Collaboration. 2006, European Physical Journal C, 45, 343 **71**
- [83] Udalski, A., Kubiak, M., & Szymanski, M. 1997, Acta Astronomica, 47, 319 **82**
- [84] Valinia, A. & Marshall, F. E. 1998, ApJ, 505, 134 **59**
- [85] van den Bergh, S. & Tammann, G. A. 1991, ARA&A, 29, 363 **54, 59**
- [86] Woosley, S. & Janka, T. 2005, Nature Physics, 1, 147 **59**
- [87] Yusifov, I. & Küçük, I. 2004, A&A, 422, 545 **63**
- [88] Zhao, H. & Silk, J. 2005, Physical Review Letters, 95, 011301 **82**

## Chapter 5

# Propagation of Cosmic Rays in the Milky Way

An error does not become truth by reason of multiplied propagation, nor does truth become error because nobody sees it.

*Mahatma Gandhi*

Surprisingly, the question of the propagation of Galactic cosmic rays rose quite late in the history of the study of cosmic rays. Indeed, it is only in 1969 that works [19, 30] dedicated to cosmic ray propagation in The Milky Way are presented at the International Cosmic Ray Conference. The very nice work by Parker [31] opened the way to first phenomenological models like the leaky box but already at the same time more refined models were proposed [18]. This work focuses only on the diffusion model proposed by Ginzburg & Syrovatskii and developed by many others after them; see [16, 27, 39, 40] and references therein.

## 5.1 Diffusion model

The radio observation by Ekers and Sancisi [14] of the edge-on spiral galaxy NGC 4631 at 610 and 1412 MHz revealed a non-thermal radio emission coming from a halo much larger than the galaxy itself from an elliptic halo with a minor semi-axis (perpendicular to the galactic plane) a few kpc large; precise measurements were not possible as the precise distance of the galaxy was suffering from large uncertainties. This is naturally interpreted in term of cosmic ray electrons emitting synchrotron radiation because of the ambient magnetic field. This means that cosmic rays are trapped in this rather big halo. Combining this observation with the isotropy of cosmic rays (at least in the energy range we are interested in, that is  $\sim 1$  GeV/n to 10 TeV/n see paragraph 3.3.3), and the measurements of Galactic magnetic field with complex or even chaotic structure, lead to the development of a diffusion theory of cosmic rays.

### 5.1.1 The model

The study of diffusive processes started with phenomenological works by Fourier (1811), Fick (1855), Darcy (1856) in the 19th century, a real and theoretical description of the phenomenon emerged at the beginning of the 20th century with the works of Lorentz (1905), Einstein (1905), Fokker and Planck (1913). Ever since, the study of stochastic processes is a major field of research of utmost importance for many scientists such as nuclear engineers, and of course cosmic ray physicists [2].

In diffusion theories, microscopic and macroscopic scales are deeply related. It is actually possible to show that macroscopic laws such as continuity equations are direct consequences of microscopic laws such as energy and number of particle conservation during each collision of the diffusing particles over diffusing centres. Chapman and Enskog (1916-1917) showed it was possible to relate thermodynamic forces (or affinity), that is the departure from equilibrium of intensive quantities to the response of the flux considered and hence to relate macroscopic diffusion coefficient to microscopic quantities.

However, in the case of charged cosmic ray particles scattering off inhomogeneities of the Galactic magnetic field, it is hopeless to measure the relevant microscopic quantities, *id est* mainly the magnetic field on very small scales  $\sim 1$  pc. Therefore, we have to satisfy with a macroscopic and phenomenological description of the propagation process.

As the measured density of cosmic rays is quite low in space, one can neglect correlations between cosmic rays and consider the continuity equation in a one-body phase space:

$$\partial_t \Psi + \partial_\mu J^\mu = Q - D \quad (5.1)$$

where  $\Psi \equiv \frac{d^4N}{d^3\vec{x}dE}$  is the phase space cosmic ray density, *id est* the number of particles per unit of volume and energy. As the flux is isotropic, we do not need a six–dimension phase space because all momentum directions are equivalent. A priori, this density is a function of time, position and energy but we will see that in some cases, one can simplify the problem. The four–current  $J^\mu$  involves first and second order responses. This term is easier to understand when it is split into energy–like ( $J_E$ ) and space–like ( $\vec{J}$ ) components:

$$\vec{J} = \vec{V}_c\Psi - K\vec{\nabla}\Psi \quad (5.2)$$

which takes into account convection from a stellar wind ( $\vec{V}_c$ ) and scatter off inhomogeneities of the magnetic field that translates into a diffusion coefficient  $K$ .

$$J_E = b_{loss}\Psi - D_{EE}\partial_E\Psi, \quad (5.3)$$

contains also convection and diffusion in momentum space that, in more physical terms, mean energy losses (which will be discussed in paragraph 5.2) and re–acceleration (in case of the inhomogeneities of the magnetic field move and can transfer momentum to cosmic rays). The  $Q$  term being the source term of cosmic rays and  $D$  the one of their destruction, the full diffusive equation is:

$$\partial_t\Psi + \vec{\nabla} \cdot (\vec{V}_c\Psi - K\vec{\nabla}\Psi) + \partial_E(b_{loss}\Psi - D_{EE}\partial_E\Psi) = Q - D, \quad (5.4)$$

where, a priori, everything depends on time  $t$ , energy of the cosmic ray<sup>a</sup>  $E$  and its position  $\vec{r}$ . Moreover, in this model, to reproduce the finite size of the diffusive halo, in agreement with observations like the one from Ekers and Sancisi [14], we will impose the boundary condition that the phase space density of cosmic–rays becomes zero at the edge of our diffusion zone. This condition is obviously wrong, indeed the intergalactic cosmic ray flux is not zero, but we will discuss this approximation later on (see paragraph 5.5).

Some simplifications need now to be made.

To do so, I will follow my predecessors; I am indebted to David Maurin, Fiorenza Donato, Richard Taillet and Pierre Salati [27].

### Time dependence

The global structure of the Galaxy seems quite stable for billions of years, hence one can hope that the phenomenon driving the propagation of cosmic rays does not change over the propagation time–scale of cosmic rays we are interested in (a few million years). Hence, time dependence of all terms of equation 5.4 can be neglected except for the cosmic ray density  $\Psi$  and the source term  $Q$  in specific cases discussed later.

### The diffusion zone

I will consider a cylindrical geometry for the diffusion zone. This is roughly in agreement with observations of NGC 4631 and quite simple to implement. Because the diffusion halo of NGC 4631 seems much thicker than the stellar disc, the thickness of the disc  $2 \times h$  will be considered negligible compared with the thickness of the halo  $2 \times L$ . The radius  $R$  of the halo is not expected to extend much further away than the galactic disc which is  $\sim 20$  kpc. I will make the same cylindricity assumption for all the processes creating, destroying and

---

<sup>a</sup>except of course the convective wind, which is an external phenomenon and does not depend on cosmic rays.

propagating cosmic rays, hence the spatial variation of all quantities depends only of galactic radius  $r$  and orthogonal distance from the galactic disc (height)  $z$ .

### Convection

There are observations that galactic winds exist in outer galaxies, they are probably due to stellar winds, supernova explosions and probably cosmic ray themselves. However its value in our own Galaxy is far from clear [8]. Its structure is even more vague, if it is believed to be caused mainly by stars then it should have a structure similar to the star distribution, but if cosmic rays are the main fuel of this phenomenon, then its structure should be more homogeneous. Lacking conclusive answer, and also to ease the computational difficulty, I will consider a homogeneous convection wind perpendicular to the galactic disc:  $\vec{V}_c(\vec{r}, t) = \frac{z}{|z|} V_c \vec{e}_z$ .

### Diffusion

Because the exact structure of the Galactic magnetic field is very unclear and so are the models relating this structure to the diffusion parameter  $K$ , but also because most cosmic rays travel a lot in the Galaxy and are not sensitive to short-scale variations, diffusion will be considered homogeneous over the complete diffusion halo. Magnetohydrodynamics considerations (see [34]) lead to:  $K(\vec{r}, E, t) = K_0 \beta \mathcal{R}^\delta$  where  $\beta$  is the speed  $v/c$  of the cosmic ray (usually equal to 1 in the energies of interest) and  $\mathcal{R}$  is the particle rigidity (the ratio of momentum to electric charge number  $p/Ze$ ). The normalisation  $K_0$  is expressed in  $\text{kpc}^2 \cdot \text{Myr}^{-1}$ .

### Energy losses

As for the other terms, the energy losses will be considered as constant and homogeneous. This will be discussed in more details in paragraph 5.2.

### Energy diffusion

Random magnetohydrodynamical waves can lead to stochastic acceleration of cosmic rays but the proper microscopic description is not easy. Describing the process requires to know the collision rate (which is related to diffusion) and the speed of the waves: the Alfvén velocity  $\vec{V}_a$ . Magnetohydrodynamical simulations of Ptuskin *et alii* [34] support this expression of  $D_{EE}$ :

$$D_{EE} = \frac{2}{9} V_a^2 \frac{E^2 \beta^4}{K(E)}. \quad (5.5)$$

### Source term

The source term  $Q$  has already been discussed in the previous chapter.

### Destruction term

Cosmic rays may disappear for many reasons: stable nuclei interact with the inter-stellar medium gas and produce secondary cosmic rays, radio-isotopes decay during their cosmic journey, anti-matter particles annihilate with regular matter of the Galactic disc. All these processes can be described and there is no free parameters here. The related uncertainties come from spallation and annihilation cross-sections and gas distribution in the Milky Way. Another very specific destruction term has to be considered: electron capture. This process exists only for nuclei that are unstable under electron capture (*exempli gratia*  $^{41}\text{Ca}$ ,  $^{44}\text{Ti}$ ,  $^{55}\text{Fe}$ ,  $^{57}\text{Co}$ ,  $^{56}\text{Ni}$  and  $^{59}\text{Ni}$ ). Usually these radio-isotopes are very short lived on Earth where the electron density is very high, however in space the electron density is so low (especially outside the disc) that these elements are able to survive for much longer times. This process concerns only species which are not relevant for this study, this is why the interested reader is advised to read David Maurin's Ph.D. thesis [26].

When interested in anti-matter, one should consider matter anti-matter annihilation. However, one can show that for a relativistic positron interacting with an electron of the interstellar medium, the total annihilation cross section is:

$$\sigma_{tot} \sim \frac{\pi\alpha^2}{\gamma m_e^2} (\log(\gamma) - 1)$$

which is negligible in the energies of interest for cosmic rays. Here,  $\gamma$  stands for the boost factor of the cosmic ray with respect to the Galactic rest frame.

### 5.1.2 The propagation parameters

We are hence left with five free parameters:  $K_0$ ,  $\delta$ ,  $L$ ,  $V_c$  and  $V_a$ . Though it is impossible with actual data to relate microscopic quantities to macroscopic propagation parameters, it is nevertheless possible to constrain them. Indeed, all species do not have the same history and their fluxes do not have the same dependence on every parameter.

The thorough work of Maurin *et alii* [13, 27, 28, 29, 35] allowed to constrain the values of the five propagation parameters of this very model.

The principle of these works is to propagate all the cosmic rays nuclei from their sources to the Earth, starting by the heaviest species (iron) down to the lightest ones (anti-protons) taking into account all the processes described above. This huge work requires to find all the spallation cross-sections (which actually is the main source of uncertainties) and, for primary cosmic rays, the composition and spectra at the sources. In a simple leaky-box model, it can be shown that secondary to primary ratios do not depend on the source spectra. This is not true any more in this diffusive model, but the dependence is almost negligible. Moreover, secondary to primary ratios do not depend on  $K_0$  and  $L$  individually but on  $K_0/L$ . To break this degeneracy, it is possible to use some radio-isotopes. Indeed short-lived radio elements are necessarily secondary cosmic rays and they travel so little in the Galaxy that the probability they reach the limit of the diffusion slab is negligible<sup>b</sup>. Because the propagation equations can be solved analytically, computation of fluxes is extremely fast and allows Bayesian approach. Performing this analysis, Putze *et alii* [35] found that present data favour  $K_0 = 8 \times 10^{-3} \text{ kpc}^2 \cdot \text{Myr}^{-1}$ ,  $\delta = 0.86$ ,  $L = 8 \text{ kpc}$ ,  $V_c = 18.7 \text{ km} \cdot \text{s}^{-1}$ ,  $V_a = 55 \text{ km} \cdot \text{s}^{-1}$  and a local gas bubble of radius  $r_b = 120 \text{ pc}$ . However 68 % confidence level envelopes are quite large because the data available at energies higher than a few GeV/nucleon are scarce and have large error bars. Hopefully, Pamela and AMS should help solving this issue soon. As the new data are not available yet, I have used the parameters found by Maurin *et alii* [27], in a previous work. They are in agreement with the new Monte Carlo study and easier to use. The most useful three sets of propagation parameters are defined in Table 5.1. These three sets give a good estimation of the total uncertainty due to the propagation. However they do not exempt us to do a complete scan over the  $\sim 1600$  parameters sets in agreement with the data, that have been selected by Maurin *et alii* [27]. This number of 1600 comes from the way these authors have binned the parameter space, it could be reduced but it is difficult to find a subset that would represent the full impact of the freedom left after boron to carbon ratio constraints.

---

<sup>b</sup>This is true only if  $L$  is quite large

Model	$\delta$	$K_0$ [kpc <sup>2</sup> /Myr]	$L$ [kpc]	$V_c$ [km/s]	$V_a$ [km/s]
<i>min</i>	0.85	0.0016	1	13.5	22.4
<i>Med</i>	0.70	0.0112	4	12	52.9
<i>MAX</i>	0.46	0.0765	15	5	117.6

Table 5.1: Typical combinations of diffusion parameters that are compatible with the B/C analysis [27]. As shown in [12], these propagation models correspond respectively to minimal, medium, and maximal primary antiproton fluxes.

As we will see later (see chapter 7), photons may be extremely helpful in constraining the propagation parameters. Indeed, photons are a good tracer of cosmic rays which produce them in copious amount. Moreover as photons are not charged, they do not suffer solar modulation (see paragraph 5.4) so low energy data is usable, moreover, their propagation being much simpler, they allow us to infer information from far away regions.

## 5.2 Energy losses

The only term of equation 5.4 that has not been discussed yet is the energy loss. One can divide the many loss processes into two categories: those which take place only in the gaseous disc of the Galaxy and those which take place everywhere in the diffusion zone.

### 5.2.1 Energy losses in the disc

#### Ionisation

When a charged relativistic particle (with electric charge  $Ze$ ) crosses a material medium (made of atoms of charge number  $Z'$ ), it interacts with the electrons of this medium because of the Coulomb interaction. If this interaction transfers enough momentum to the target electron, it may escape the atom it was bound to. This interaction is of utmost importance as it is the way most of our particle detectors “see” the cosmic rays. Of course the only material medium cosmic rays cross is not our human-made scintillators, but also the inter stellar gas. Hence ionisation has its importance for propagation too. A classical description of the energy transfer from an incoming charged particle to an electron at rest is an easy exercise. However, the complete relativistic quantum theory approach is a little more complex and conclude with the Bethe-Bloch formula, which is described, for instance in the famous book of M. Longair [24, 25]:

$$-\frac{dE}{dt} = \frac{Z^2 e^4 Z' N}{4\pi \epsilon_0^2 m_e c \beta^2} \left[ \ln \left( \frac{2\gamma^2 m_e c^2 \beta^2}{\bar{I}} \right) - \beta^2 \right], \quad (5.6)$$

where  $\gamma$  and  $\beta$  are the Lorentz coefficient of the incoming cosmic ray in the laboratory rest frame and  $\bar{I}$  is the average potential energy of an electron of the considered atom and  $N$  is its number density in the medium. When the projectile is not a heavy nucleus but a light electron,

some simplifications cannot be made any more and the previous formula should be changed into:

$$-\frac{dE}{dt} = \frac{e^4 Z' N_e v}{8\pi\epsilon_0^2 m_e v^2} \left[ \ln \left( \frac{\gamma^3 m_e^2 c^2 v^2}{2I^2} \right) - \left( \frac{2}{\gamma} - \frac{1}{\gamma^2} \right) \ln 2 + \frac{1}{\gamma^2} + \frac{1}{8} \left( 1 - \frac{2}{\gamma} \right)^2 \right] \quad (5.7)$$

$$\sim 7.62 \times 10^{-18} N (3 \ln \gamma + 18.8) \text{ GeV.s}^{-1}, \quad (5.8)$$

where the numerical result of the second line is valid for target hydrogen (which makes about 90 % of the interstellar gas). The target density  $N$  is expressed in  $\text{cm}^{-3}$ .

Whatever the incoming cosmic ray (electron or nucleus), this loss term is proportional to  $\ln \gamma$  hence at high energies it is negligible compared to the other ones (see next paragraph).

### Bremsstrahlung

When a charged particle crosses a material medium, it also interacts with nuclei. The physical concepts are of course the same as the ones taking place during ionisation, but the difference is that the nucleus is much heavier than an electron therefore very little momentum can be transferred to it. The electrostatic interaction translates hence into a braking radiation, or in German Bremsstrahlung. A full quantum relativistic treatment performed by Bethe and Heitler gives:

$$-\frac{dE}{dt} = \frac{Z(Z+1.13)e^6 N_i E}{16\pi^3 \epsilon_0^3 m_e^2 c^4 \hbar} \left[ \ln \left( \frac{183}{Z^{1/3}} \right) + \frac{1}{8} \right] \quad (5.9)$$

$$\sim 3.66 \times 10^{-16} N E \text{ GeV.s}^{-1} \text{ for electrons on neutral hydrogen.}$$

The number density of interstellar protons  $N$  is measured in  $\text{cm}^{-3}$ .

### Adiabatic losses

It is basic knowledge that an expanding gas cools down, hence as convection expands the volume occupied by cosmic rays, by conservation of density in phase-space, energy has to decrease. The proper expression of this loss term is:

$$-\frac{dE}{dt} = \frac{\vec{\nabla} \cdot \vec{V}_c}{3} E_k \left( \frac{2mc^2 + E_k}{mc^2 + E_k} \right), \quad (5.10)$$

where  $E_k$  stands for the kinetic energy of the cosmic ray (see section B.6 for a demonstration). In our model, the Galactic wind is homogeneous everywhere, except for  $z = 0$  so the previous term simplifies into:

$$-\frac{dE}{dt} = \frac{2V_c \delta(z)}{3} E_k \left( \frac{2mc^2 + E_k}{mc^2 + E_k} \right),$$

with  $2h$  the width of the Galactic disc. However in other models of convective wind, the gradient of  $\vec{V}_c$  maybe non-zero outside the disc and should be considered everywhere in the halo.

## 5.2.2 Energy losses everywhere: radiative losses

### 5.2.2.1 Synchrotron

If one considers a charged particle (with charge  $q$  and mass  $m$ ) moving along the  $x$  axis in presence of a magnetic field  $\vec{B} = B \cos(\theta)\vec{e}_x + B \sin(\theta)\vec{e}_y$ , the particle, in its rest frame  $S'$  will

feel the force  $q\vec{E}'$ , where  $q$  is the electric charge of the considered cosmic ray. The electric field in this rest frame can be deduced by the one in the laboratory rest frame,

$$\begin{aligned} E'_x &= E_x = 0 \\ E'_y &= \gamma(E_y - \beta c B_z) = 0 \\ E'_z &= \gamma(E_z + \beta c B_y) = \beta c \gamma B \sin(\theta). \end{aligned}$$

Hence the acceleration of the particle in its rest-frame is  $\left| \dot{\vec{v}}' \right| = \frac{q\gamma v B \sin(\theta)}{m}$ . We know that an accelerating charged particle radiates with a power:

$$-\frac{dE}{dt} = \frac{q^2 \left| \dot{\vec{v}}' \right|^2}{6\pi\epsilon_0 c^3},$$

recognising Thomson cross-section  $\sigma_T = \frac{e^3}{6\pi\epsilon_0^2 c^4 m_e^2}$  and averaging over all the possible angles  $\theta$ , one gets:

$$-\frac{dE}{dt} = \frac{4Z^2}{3} \sigma_T c \gamma^2 \left( \frac{m_e}{m} \right)^2 \frac{B^2}{8\pi}. \quad (5.11)$$

From this result, it clearly appears that electrons suffer around three millions times more synchrotron emission than a proton, for heavier nuclei, as the mass increases faster than the charge, this ratio is even more extreme. Hence one can safely neglect synchrotron emission from particles other than electrons. The issue is now to have an expression of the Galactic magnetic field  $\vec{B}$ . As said earlier in this thesis, the reason we believe the diffusive halo is much larger than the Galaxy itself is the fact that we observe synchrotron emission from a large zone around far away galaxies. It is then reasonable to state that the magnetic field is non zero in the halo. However measuring this magnetic field is quite a challenge. Some studies rely on the synchrotron emission of electron cosmic rays but obviously one needs to know its flux before measuring anything, hence we cannot use these data. More model independent is the measurement of the Faraday rotation of polarised light. But this is possible in very few directions and generally suffers many uncertainties because of the astrophysical background. If stars are responsible for the Galactic magnetic field, then its morphology should follow the one of the stars (with spiral arms and complex radial distributions) however, it is also claimed that cosmic rays maybe the Galactic dynamo and then the magnetic field would be much more homogeneous. As explained in Beck *et alii* ([5]), there are two different methods of measurement. The first relies on the intensity of the synchrotron radiation from cosmic electrons and gives a value of  $B \sim 4 \pm 1 \mu\text{G}$  (Prouza & Šmída [33]). However, this value depends on the adopted model, particularly in terms of the cosmic ray electron spectrum estimation. The second method uses the Faraday rotation measurements of pulsar polarised emission, and yields  $B \sim 1.8 \pm 0.3 \mu\text{G}$  (Han *et alii* [20]). The two results are inconsistent but Beck *et alii* ([5]) were able to identify further uncertainty in the second method, which, if the thermal electron density is anti-correlated with the magnetic field strength, produces a revised value of  $B \in [1.5; 4] \mu\text{G}$ . But more recently, same authors gave a field of  $6 \mu\text{G}$  in the local neighbourhood and much stronger fields of  $20\text{--}30 \mu\text{G}$  in spiral arms.

### 5.2.2.2 Inverse Compton

The following discussion is mainly based on results submitted to Astronomy and Astrophysics [9].

The calculation of inverse Compton scattering of electrons with photons in the relativistic regime has been derived a long time ago in the astrophysical context by Jones [21]. It was subsequently extensively revisited and complemented by Blumenthal & Gould [7]. The reader interested in more technical details is referred to the latter in which a relativistic version of the inverse Compton energy losses has been studied.

Relativistic electrons are assumed to propagate in an isotropic and homogeneous gas of photons, which exhibits a black body energy distribution. The electron energy loss rate can be expressed in terms of the energies  $\epsilon$  and  $\epsilon_\gamma$  of a photon before and after the collision, respectively, as follows:

$$-\frac{dE}{dt} = \int d\epsilon \int d\epsilon_\gamma (\epsilon_\gamma - \epsilon) \frac{dN_{\text{coll}}}{dt d\epsilon d\epsilon_\gamma}. \quad (5.12)$$

The collision rate is given by

$$\frac{dN_{\text{coll}}}{dt d\epsilon d\epsilon_\gamma} = \frac{3\sigma_T c}{4\gamma^2} \frac{dn(\epsilon)/d\epsilon}{\epsilon} \times \left\{ 1 + 2q \left( \ln q - q + \frac{1}{2} \right) + \frac{(1-q)}{2} \frac{(\Gamma q)^2}{(1+\Gamma q)} \right\}, \quad (5.13)$$

where the Thomson cross section is  $\sigma_T = \frac{8\pi}{3} \left( \frac{\alpha\hbar}{m_e c} \right)^2$ ,  $\gamma$  is the boost of the electron in the laboratory frame, and  $dn(\epsilon)/d\epsilon$  is the initial photon density in the energy range  $d\epsilon$ , which, for a black body radiation of temperature  $T$  has the form (including the two polarisation states):

$$\frac{dn}{d\epsilon} = 2 \times \frac{4\pi\epsilon^2}{(2\pi\hbar c)^3} (e^{\epsilon/(k_B T)} - 1)^{-1}, \quad (5.14)$$

where  $k_B$  is Boltzmann's constant. Moreover,

$$q \equiv \frac{\hat{\epsilon}_\gamma}{\Gamma(1 - \hat{\epsilon}_\gamma)}; \quad \hat{\epsilon}_\gamma \equiv \frac{\epsilon_\gamma}{\gamma m_e c^2}; \quad \Gamma \equiv \frac{4\gamma\epsilon}{m_e c^2}. \quad (5.15)$$

From kinematics, the range for  $\hat{\epsilon}_\gamma$  is readily found to be  $[\hat{\epsilon}, \frac{\Gamma}{(1+\Gamma)}]$ , which translates into  $[\frac{1}{4\gamma^2}, 1]$  for  $q$ . It proves convenient to rewrite the energy loss rate in terms of an integral over  $q$ :

$$-\frac{dE}{dt} = \int d\epsilon \int dq \frac{\Gamma^2 (\gamma m_e c^2)^2}{(1 + \Gamma q)^2} \cdot \left\{ \frac{q}{(1 - \Gamma q)} - \frac{1}{4\gamma^2} \right\} \times \frac{dN_{\text{coll}}}{dt d\epsilon d\epsilon_\gamma}$$

It turns out that the integral over  $q$  is analytical, so that one can easily check the full numerical calculation.

The discussion about which regime is relevant for the energy loss rate relies on a dimensionless parameter defined as:

$$\alpha \equiv \frac{\gamma (k_b T_0)}{m_e c^2},$$

where  $T_0$  is the mean temperature of the radiation field.

The non-relativistic Thomson limit is recovered for inverse Compton processes within a black body radiation field, using  $\Gamma \ll 1$  or equivalently  $\alpha \ll 1$ :

$$-\frac{dE}{dt} = \frac{4}{3}\sigma_T c U_{\text{rad}} \gamma^2, \quad (5.16)$$

where  $U_{\text{rad}} = \int d\epsilon \epsilon dn/d\epsilon$ , whereas the Klein-Nishina regime applies for  $\alpha \gg 1$ :

$$-\frac{dE}{dt} = \frac{\sigma_T (m_e c k_b T_0)^2}{16 \hbar^3} \left\{ \ln \frac{4\gamma k_b T_0}{m_e c^2} - 1.9805 \right\} \quad (5.17)$$

Figure 5.1 displays the comparison of both regimes with the full calculation. From numerical results, one derives a parametrisation valid for any black body radiation field, which is given by:

$$-\frac{dE}{dt} = \begin{cases} \text{Thomson} & \text{for } \mathcal{C}_{\text{n-r}} \\ \frac{E^2 (k_b T_0)^4}{\alpha} \exp \left\{ \sum_{i=0} c_i (\ln \alpha)^i \right\} & \text{for } \mathcal{C}_{\text{int}} \\ \text{Klein - Nishina} & \text{for } \mathcal{C}_{\text{u-r}} \end{cases}, \quad (5.18)$$

where the conditions  $\mathcal{C}$  read:

$$\begin{aligned} \mathcal{C}_{\text{n-r}} &: \alpha < 3.8 \times 10^{-4} \\ \mathcal{C}_{\text{int}} &: 3.8 \times 10^{-4} \leq \alpha \leq 1.8 \times 10^3 \\ \mathcal{C}_{\text{u-r}} &: \alpha > 1.8 \times 10^3 \end{aligned} \quad (5.19)$$

The fitting formula associated with the intermediate regime and provided in equation (5.18) may be used with the following parameters:

$$c_i = \{74.77, -0.1953, -9.97 \times 10^{-2}, 4.352 \times 10^{-3}, 3.546 \times 10^{-4}, -3.01 \times 10^{-5}\}. \quad (5.20)$$

An additional smooth interpolation between these three regimes might improve the calculation by avoiding tiny gaps at connections, which could arise from very small numerical differences in the unit conversions or constants used above. This parametrisation is valid for any black body distribution of photons. If one considers a photon distribution that can be fitted by a black body distribution but with an energy density  $U_{\text{rad}}$  which differs from that in a standard way derived  $U_{\text{rad}}^{\text{bb}}$ , then one has to renormalise equation (5.18) by a factor  $U_{\text{rad}}/U_{\text{rad}}^{\text{bb}} = n_{\text{rad}}/n_{\text{rad}}^{\text{bb}}$  to get the correct energy loss rate. The photon density of a real black body is given by

$$n_{\text{rad}}^{\text{bb}}(T_0) = \frac{2\zeta(3)T_0^3}{\pi^2 \hbar^3 c^3},$$

where  $\zeta(x)$  is Riemann's function and  $\zeta(3) \sim 1.2020569$ .

In the left panel of figure 5.2, one can see the interstellar radiation field (ISRF) data extracted from the analysis made in Porter *et alii* [32], and averaged in boxes of  $500 \times 500$  pc and  $2 \times 2$  kpc around the Earth, on top of which a sum of black-body distributions actually

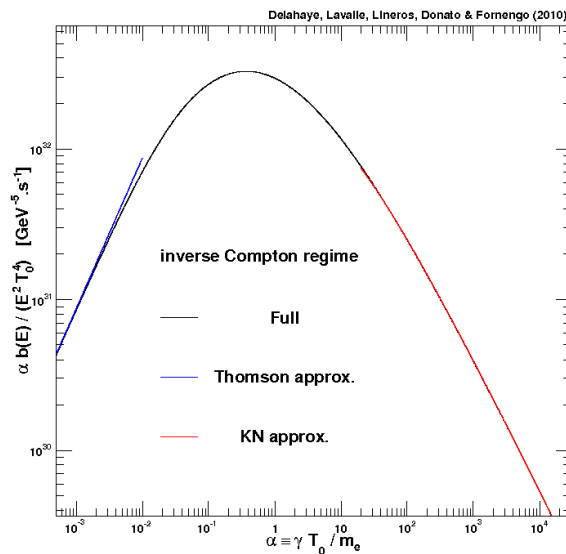


Figure 5.1: Comparison between the different relevant regimes of the inverse Compton energy loss for any black body radiation field.

provides a reasonable fit. These two models, defined with a set of components characterised by their temperatures and energy densities, are summarised in table 5.2. They can be used to size the theoretical error coming from uncertainties in the characterisation of the interstellar radiation field. One can only hope that these uncertainties somehow reflect those affecting the data which are unfortunately not available.

The shape of the interstellar radiation field can be understood as an interplay between the infra-red and ultra-violet components, depending on the averaging volume: a smaller volume gives a larger (smaller) IR (UV) contribution, due to the efficient UV-absorption and IR-emission properties of the dust mostly concentrated in the disk.

### 5.2.3 Comparisons

It clearly appears from figure 5.3 that for energies higher than  $\sim 10$  GeV, the energy losses term is dominated by radiative processes (synchrotron emission and inverse Compton). The other loss terms are relevant at low energies only. Neglecting these latter terms is even justified at low energies because they take place only in the thin Galactic disc whereas the former ones happen everywhere in the diffusion zone in which cosmic electrons and positrons propagate.

## 5.3 Semi-analytical solutions of the diffusion equations

As we have seen in the previous paragraph, for electrons, only the losses that take place in the whole diffusive disc are important. One can therefore safely neglect the other ones. Actually, diffusive re-acceleration and convection also are not important at high energies (see

		$T_0$ [K]	$n_{\text{rad}}$ [ $\text{cm}^{-3}$ ]
M1	CMB	2.725	Planckian
	IR	33.07	33
	Stellar	313.32	0.75
	UV	3 249.3 6 150.4 23 209.0	0.49 0.16 0.022
M2	CMB	2.725	Planckian
	IR	33.653	41
	Stellar	313.32	0.85
	UV	2 901.13 5 570.1 22 048.56	0.5 0.2 0.02

Table 5.2: Parameters used to fit the local interstellar radiation field with blackbodies. **M1** and **M2** correspond to fits done on the data taken from the analysis made in Porter *et alii* [32] averaged over  $2 \times 2$  kpc and  $0.5 \times 0.5$  kpc around the Earth, respectively. **M1** is chosen as the default interstellar radiation field model for the remaining of this work.

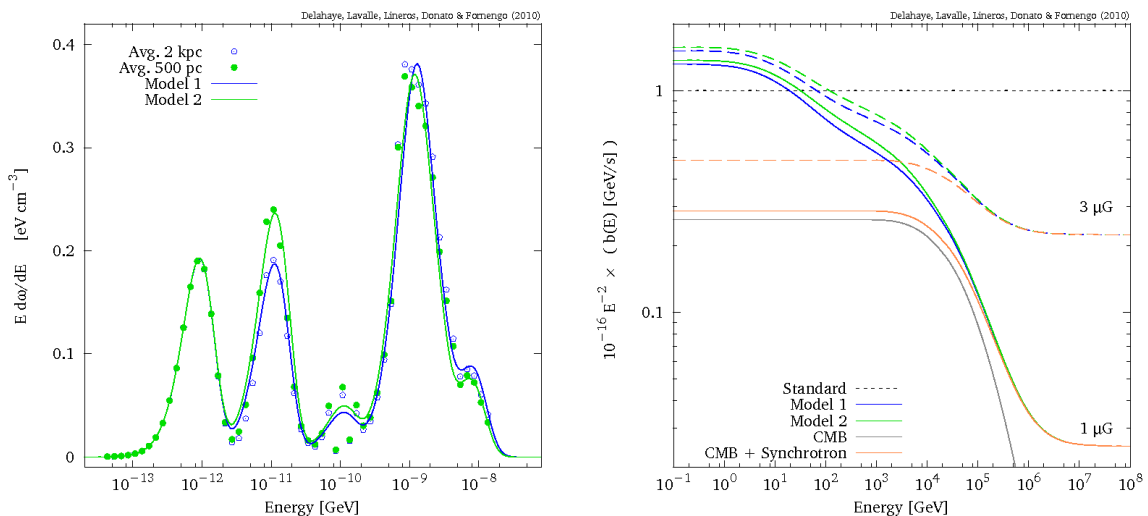


Figure 5.2: *Left*: Energy density distribution of the interstellar radiation fields averaged in two boxes of different volumes, where all components appear (data taken from the analysis by Porter *et alii* [32]). Our models **M1** and **M2**, using both black bodies for all components, are reported against the data. *Right*: Corresponding energy loss rate.

section B.3 in the appendix). Because we are interested in high energy electrons, it is possible to replace  $\beta$  with 1 and the rigidity with the dimensionless energy  $\epsilon = E/E_0$ , where  $E_0$  stands for 1 GeV. For the sake of clarity, it is convenient to note  $b(\epsilon) = -b_{\text{loss}}(E)/E_0$ . The equation

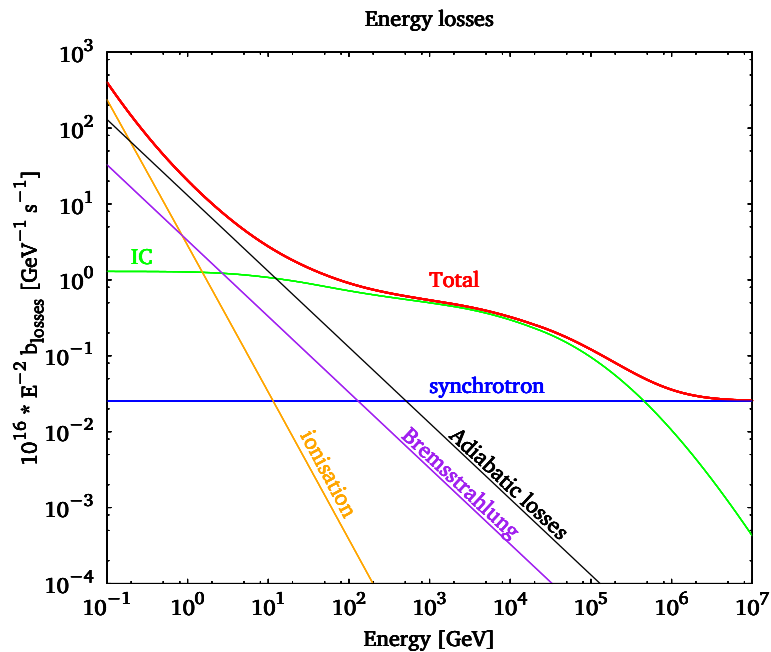


Figure 5.3: Various energy loss rates explained in this paragraph.

of interest is hence:

$$\partial_t \Psi - K_0 \epsilon^\delta \left( \partial_r^2 + \frac{1}{r} \partial_r + \partial_z^2 \right) \Psi - \partial_\epsilon (b\Psi) = Q, \quad (5.21)$$

where another simplification has to be made by stating that energy losses do not vary much on the propagation scales of electrons and can be considered as homogeneous. Depending on the source term  $Q$ , the solutions of equation (5.21) are not the same.

### 5.3.1 Smooth distribution of sources everywhere in the halo

If the source term  $Q(r, z, t, \epsilon)$  is a spatially smooth function which continuously emits cosmic rays, then steady-state approximation can be made. This corresponds for instance, to a dark matter population annihilating or decaying into electrons. This case has been studied in reference [11]. The previous equation simplifies into:

$$- K_0 \epsilon^\delta \left( \partial_r^2 + \frac{1}{r} \partial_r + \partial_z^2 \right) \Psi - \partial_\epsilon (b\Psi) = Q(r, z, \epsilon), \quad (5.22)$$

with  $Q(r, z, \epsilon) = S(r, z)f(\epsilon)$  to distinguish spatial and energy dependence of the source term. For convenience,  $S(r, z)$  is always taken so that its value is 1 at the Sun position. The specific form of the second term,  $f(\epsilon)$ , is of no importance for the propagation. There are (at least) two methods to solve this equation.

### 5.3.1.1 Bessel–Fourier expansion technique

Taking advantage of the cylindrical symmetry of the problem, it is possible to simplify this equation with the help of Bessel expansions. Moreover this allows to automatically take into account the radial boundary condition imposing  $\Psi(r = R) = 0$  at the edge of the diffusive zone. Technical details and a proof of the existence of these expansion can be found in appendix B.1. Each Bessel coefficients  $P_i(z, \epsilon)$  and  $S_i(z)$  of the expansion of  $\Psi(r, z, \epsilon)$  and  $S(r, z)$  respectively satisfies:

$$K_0 \epsilon^\delta \partial_z^2 P_i - K_0 \epsilon^\delta \frac{\alpha_i^2}{R^2} P_i + \partial_\epsilon (b P_i) + S_i f = 0 \quad (5.23)$$

Each Bessel transform  $P_i(z, \epsilon)$  has to vanish at the boundaries  $z = -L$  and  $z = +L$  and may take any value in between. It can be therefore expanded as a Fourier series involving the basis of functions

$$\varphi_n(z) = \sin(n k_0 z') \quad , \quad (5.24)$$

where  $k_0 = \pi/2L$  and  $z' = z + L$ . In most cases, the source distribution is symmetric with respect to the galactic plane and one can restrict oneself to the functions  $\varphi_n(z)$  with odd  $n = 2m + 1$

$$\varphi_n(z) = (-1)^m \cos(n k_0 z) \quad . \quad (5.25)$$

The Bessel transform  $P_i(z, \epsilon)$  is Fourier expanded as

$$P_i(z, \epsilon) = \sum_{n=1}^{\infty} P_{i,n}(\epsilon) \varphi_n(z) \quad ,$$

and the same expression holds for  $S_i(z, \epsilon)$  for which we need to calculate explicitly the Fourier coefficient

$$S_{i,n} = \frac{1}{L} \int_{-L}^{+L} \varphi_n(z) S_i(z) dz \quad . \quad (5.26)$$

The Fourier transform of equation (5.23) involves the energy functions  $P_{i,n}(\epsilon)$  and  $S_{i,n}(\epsilon)$

$$- K n^2 k_0^2 P_{i,n} - K_0 \epsilon^\delta \frac{\alpha_i^2}{R^2} P_{i,n} + \partial_\epsilon (b P_{i,n}) + S_{i,n} f(\epsilon) = 0 \quad . \quad (5.27)$$

At this stage, it is convenient to introduce a new parameter:

$$\tilde{t} = 4 \int_\epsilon^\infty \frac{K(\epsilon)}{b(\epsilon)} d\epsilon$$

This parameter  $\tilde{t}$  has the dimension of a distance squared. It is immediate to deduce:

$$\frac{d}{d\tilde{t}} = - \frac{b(\epsilon)}{4K(\epsilon)} \frac{d}{d\epsilon}$$

By defining the new functions  $\tilde{P}_{i,n} = b P_{i,n}$  and  $\tilde{f} = \frac{b(\epsilon)}{4K(\epsilon)} f$ , we are led to the heat equation

$$\frac{d\tilde{P}_{i,n}}{d\tilde{t}} + \frac{1}{4} \left( n^2 k_0^2 + \frac{\alpha_i^2}{R^2} \right) \tilde{P}_{i,n} = \tilde{f} S_{i,n} \quad .$$

The solution to this linear differential equation is straightforward

$$\tilde{P}_{i,n}(\tilde{t}) = S_{i,n} \int_0^{\tilde{t}} \tilde{f}(\tilde{t}_S) \exp \left\{ -\tilde{C}_{i,n}(\tilde{t} - \tilde{t}_S) \right\} d\tilde{t}_S .$$

The argument of the exponential involves

$$\tilde{C}_{i,n} = \frac{1}{4} \left\{ \left( \frac{n\pi}{2L} \right)^2 + \frac{\alpha_i^2}{R^2} \right\} .$$

This integral is not easy to understand in terms of  $\tilde{t}$ , so it is convenient to introduce the diffusion length:

$$\lambda^2 = \tilde{t} - \tilde{t}_S = 4 \int_{\epsilon}^{\epsilon_S} \frac{K(\epsilon)}{b(\epsilon)} d\epsilon, \quad (5.28)$$

which sizes the distance travelled by an electron created at energy  $\epsilon_S$  and detected at energy  $\epsilon$ . So actually the integral can be re-expressed as:

$$\begin{aligned} \tilde{P}_{i,n}(\epsilon) &= S_{i,n} \int_0^{\sqrt{\tilde{t}}} \tilde{f}(\epsilon_S) \exp \left\{ -\tilde{C}_{i,n}\lambda^2 \right\} \frac{\partial \tilde{t}}{\partial \lambda} d\lambda \\ &= S_{i,n} \int_{\epsilon}^{\infty} \tilde{f}(\epsilon_S) \exp \left\{ -\tilde{C}_{i,n}\lambda^2 \right\} \frac{\partial \tilde{t}}{\partial \epsilon_S} d\epsilon_S . \end{aligned}$$

and understood either as an integral over all the nearby sources or all the sources energies. The cosmic ray electron density is given by the double expansion

$$\psi(r, z, \epsilon) = \sum_{i=1}^{\infty} \sum_{n=1}^{\infty} J_0(\alpha_i r/R) \varphi_n(z) P_{i,n}(\epsilon) ,$$

where

$$P_{i,n}(\epsilon) = \frac{S_{i,n}}{b(\epsilon)} \int_{\epsilon}^{+\infty} f(\epsilon_S) \exp \left\{ -\tilde{C}_{i,n}(\tilde{t} - \tilde{t}_S) \right\} d\epsilon_S. \quad (5.29)$$

We eventually get the electron flux  $\Psi_e = \beta_e \psi(r, z, \epsilon)/4\pi$  where the electron velocity  $\beta_e$  depends on the energy  $\epsilon$ . It is interesting to note that, if one only deals with low energy electrons (less than 100 GeV), then the radiative energy losses are in the Thomson regime  $b_{loss} = -\frac{E_0 \epsilon^2}{\tau_E}$  and the expression of  $\lambda$  is analytical:  $\lambda^2 = 4\tau_E K_0(\epsilon^{\delta-1} - \epsilon_S^{\delta-1})/(1 - \delta)$  and the integral 5.29 is computed extremely rapidly.

It is nice to see that in the expression of the coefficients  $P_{i,n}$  the various physical quantities can be treated separately. Indeed propagation affects only  $\tilde{C}_{i,n}$  and  $\lambda$ , the energy spectrum at the source appears only in the term  $f(\epsilon_S)$  while the space distribution of sources is relegated to  $S_{i,n}$ . This means that during a study it is not necessary to recompute everything but only the ingredients one likes to analyse. This is clearly the most striking advantage of semi-analytical methods such as this one.

### 5.3.1.2 The Green functions technique

The Bessel–Fourier expansion method is quite efficient, however, if the source distribution is very irregular, it can require many Bessel and Fourier orders before convergence is achieved, making the advantage of semi–analytical methods less interesting. This is obviously even more dramatic when one wishes to deal with sources located only in the thin Galactic disc which is very painfully described by Fourier expansions or with point–like sources like dark matter clumps.

The Green formalism consists in solving the equation where the source term is replaced by a Dirac function  $\delta(\vec{x} - \vec{x}_S)\delta(\epsilon - \epsilon_S)$  and then to do the convolution of this Green function with the real source term. Before we do so, let us follow Baltz & Edsjö [3] and do the same changes in variables as before:

$$\tilde{t} = 4 \int_{\epsilon}^{\infty} \frac{K(\epsilon)}{b(\epsilon)} d\epsilon$$

and rescale  $\tilde{\Psi} = b(\epsilon)\Psi$  and  $\tilde{f} = b(\epsilon)f/4K(\epsilon)$ , so that equation 5.22 becomes a usual heat equation:

$$\partial_{\tilde{t}}\tilde{\Psi} - \frac{1}{4}\Delta\tilde{\Psi} = S\tilde{f},$$

where  $S$  and  $f$  are defined as  $Q(r, z, \epsilon) = S(r, z)f(\epsilon)$  as in the previous paragraph. In the absence of boundary conditions, the Green function of this equation is a standard result of this method:

$$\tilde{G}(\vec{x}_{\odot}, \tilde{t} \leftarrow \vec{x}_S, \tilde{t}_S) = \frac{\theta(\lambda)}{(\pi\lambda^2)^{3/2}} \exp\left\{-\frac{\|\vec{x}_S - \vec{x}_{\odot}\|^2}{\lambda^2}\right\},$$

where  $\lambda$ , as previously, sizes the propagation length, and is  $\lambda^2 = \tilde{t} - \tilde{t}_S$ . The cosmic ray density is then given by:

$$\Psi(\vec{x}, \epsilon) = \int_{\epsilon}^{\infty} \left[ f(\epsilon_S) \int_{Diff.Zone} S(\vec{x}_S) G(\vec{x}_{\odot}, \epsilon \leftarrow \vec{x}_S, \epsilon_S) d^3\vec{x}_S \right] d\epsilon_S,$$

where the propagator  $G(\vec{x}_{\odot}, \epsilon \leftarrow \vec{x}_S, \epsilon_S)$  is  $\frac{1}{b(\epsilon)}\tilde{G}(\vec{x}_{\odot}, \tilde{t} \leftarrow \vec{x}_S, \tilde{t}_S)$

Very often we do not know the energy dependence of the source term  $f(\epsilon)$ . This is why, it can be convenient to study the so called *halo function*  $\tilde{I}$ .

$$\begin{aligned} \tilde{I}(\lambda) &= \sum_{i=1}^{\infty} \sum_{n=1}^{\infty} J_0(\alpha_i r/R) \varphi_n(z) S_{i,n} \exp\{-\tilde{C}_{i,n}\lambda^2\} \\ &= \int_{Diff.Zone} S(\vec{x}_S) \tilde{G}(\vec{x}_{\odot}, \epsilon \leftarrow \vec{x}_S, \epsilon_S) d^3\vec{x}_S \end{aligned} \quad (5.30)$$

which correspond respectively to the Bessel (see paragraph 5.3.1.1) and the Green (see paragraph 5.3.1.2) methods. In both cases one simply gets the flux by performing a convolution of  $\tilde{I}$  with the energy dependence term  $f(\epsilon_S)$ :

$$\Psi(\vec{x}_{\odot}, \epsilon) = \frac{\beta_e}{4\pi b(\epsilon)} \int_{\epsilon}^{\infty} f(\epsilon_S) \tilde{I}(\lambda) d\epsilon_S. \quad (5.31)$$

Moreover, in our problem of Galactic cosmic rays, we need to take into account the boundary conditions. The problem is more easily handled if we separate the  $z$  and the  $r$  components.

### The radial bound

If one wants to take into account the radial boundary, it is enough to add a second propagator that will cancel out the first one at  $r = R$ . This image method has been developed for electrostatic problems but is very useful here too. The horizontal 2D-propagator becomes:

$$\tilde{G}_{2D}^r(\vec{r}_\odot, \tilde{t} \leftarrow \vec{r}_S, \tilde{t}_S) = \frac{\theta(\lambda)}{\pi \lambda^2} \left( \exp \left\{ -\frac{(\vec{r}_\odot - \vec{r}_s)^2}{\lambda^2} \right\} - \exp \left\{ -a(r_s) \frac{(\vec{r}_\odot - \vec{r}_{im})^2}{\lambda^2} \right\} \right), \quad (5.32)$$

where the image satisfies  $\vec{r}_{im} = \vec{r}_s/a(r_s)$  with the scale parameter  $a(r) = \frac{r^2}{R^2}$ . This is actually equivalent with replacing  $R_\odot$  by  $\frac{R^2}{R_\odot}$  and  $\lambda$  by  $\lambda \frac{R}{R_\odot}$  (except for the first  $\lambda^2$  that is in factor). A justification of this can be found in appendix B.5.

### The vertical bounds

As for the radial bound, it is possible to use the image method, however, because there are two bounds one image is not enough and one has to take into account an infinite number of images and images of images:

$$\tilde{G}_{1D}^z(z_\odot, \tilde{t} \leftarrow z_S, \tilde{t}_S) = \sum_{n=-\infty}^{+\infty} (-1)^n \frac{\theta(\lambda)}{\sqrt{\pi \lambda^2}} \exp \left\{ -\frac{(z_n - z_\odot)^2}{\lambda^2} \right\}, \quad (5.33)$$

where  $z_n = 2Ln + (-1)^n z_S$ . This methods proves to converge very fast when the extension  $\lambda$  of the electron sphere is smaller than the half-thickness  $L$  of the diffusive halo.

In the opposite situation, a more suitable expression is based on an analogy with the solution to the Schrödinger equation in an infinitely deep square potential: expansion of the solution over the eigenfunctions of the Laplace operator:

$$\tilde{G}_{1D}^z(z_\odot, \tilde{t} \leftarrow z_S, \tilde{t}_S) = \frac{1}{L} \sum_{n=1}^{+\infty} e^{-k_n^2 \lambda^2 / 4} \phi_n(z_\odot) \phi_n(z_S) + e^{-k_n'^2 \lambda^2 / 4} \phi_n'(z_\odot) \phi_n'(z_S) \quad (5.34)$$

where:

$$\begin{aligned} \phi_n(z) &= \sin [k_n(L - |z|)] & ; & \quad k_n = \left( n - \frac{1}{2} \right) \frac{\pi}{L} \quad (\text{even}) \\ \phi_n'(z) &= \sin [k_n'(L - z)] & \text{and} & \quad k_n' = n \frac{\pi}{L} \quad (\text{odd}). \end{aligned}$$

In general, The Green technique is much faster than the Bessel-Fourier one as long as we limit ourselves to values of  $\lambda$  shorter than 3 kpc. The best to have a fast converging result is then to combine all the methods.

## 5.3.2 Smooth distribution of sources in the disc only

As we have said earlier, the Bessel-Fourier method does not work when the sources are located only in the Galactic disc. However the Green functions works perfectly well. Actually

the integral over the diffusion zone can even sometimes be performed analytically. When it is possible, let us consider the radial and the vertical parts separately, and split the function  $S(r, z)$  into  $S_r(r) \times S_z(z)$ . In this case, the halo function defined in equation 5.30 can be split into a radial and a vertical part as well.

### 5.3.2.1 Radial propagators

#### A homogeneous disc

If the sources are homogeneously distributed in the disc,  $S_r(r) = 1$ , which is relevant for secondary cosmic rays for which the retro-propagation of primaries<sup>c</sup> is neglected. Then one has:

$$\begin{aligned} \tilde{I}_{r,\theta}^{\text{hom}} &= \int_0^{2\pi} \int_0^R r \tilde{G}_{2D}^r(\vec{r}, E \leftarrow \vec{r}_s, E_s) dr d\theta \\ &= e^{-\frac{R_\odot^2}{\lambda^2}} \sum_{m=0}^{\infty} \left\{ \left( \frac{R_\odot^2}{\lambda^2} \right)^m \frac{1}{m!} \left( 1 - e^{-\frac{R^2}{\lambda^2}} \sum_{j=0}^m \left( \frac{R^2}{\lambda^2} \right)^j \frac{1}{j!} \right) \right\} \\ &\quad - \frac{e^{-\frac{R^2}{\lambda^2}}}{a(R_\odot)} \sum_{m=0}^{\infty} \left\{ \left( \frac{R^2}{\lambda^2} \right)^m \frac{1}{m!} \left( 1 - e^{-\frac{R_\odot^2}{\lambda^2}} \sum_{j=0}^m \left( \frac{R_\odot^2}{\lambda^2} \right)^j \frac{1}{j!} \right) \right\}. \end{aligned} \quad (5.35)$$

#### A specific kind of source profiles

In the case that the source profile  $S_r(r)$  is described by Eq. 4.13, if the parameter  $a$  is an integer (for instance YK04 and P90 of paragraph 4.1.3), then it is possible to get an analytical solution of the horizontal integral.

$$\begin{aligned} \tilde{I}_{r,\theta}^{\text{smooth}} &= \int_0^{2\pi} \int_0^R r^{a+1} e^{-r/r_0} \tilde{G}_{2D}^r(\vec{r}, E \leftarrow \vec{r}_s, E_s) dr d\theta \\ &= e^{-\frac{R_\odot^2}{\lambda^2}} \sum_{m=0}^{\infty} \left\{ \left( \frac{R_\odot^2}{\lambda^4} \right)^m \frac{1}{(m!)^2} S_m(\tilde{r}, \tilde{R}) \right\}, \end{aligned} \quad (5.36)$$

where  $\tilde{r} = \frac{\lambda^2}{2r_0}$ ,  $\tilde{R} = R + \frac{\lambda^2}{2r_0}$  and

$$S_m(a, b) = e^{\frac{\lambda^2}{4r_0^2}} \sum_{j=0}^N \binom{N}{j} \left( \frac{-\lambda^2}{2r_0} \right)^{N-j} U_j(\tilde{r}, \tilde{R}). \quad (5.37)$$

For convenience I have noted  $N = 2m + a + 1$  and the integral  $U_j(\tilde{r}, \tilde{R})$  as follows. If  $j = 2p + 1$  is odd:

$$U_j(\tilde{r}, \tilde{R}) = \sum_{k=0}^p \lambda^{2k} \frac{p!}{(p-k)!} \left[ r^{2p-2k} e^{-r^2/\lambda^2} \right]_{r=\tilde{R}}^{r=\tilde{r}}, \quad (5.38)$$

---

<sup>c</sup>What I call retro-propagation is taking into account the full spatial distribution of spallating cosmic rays and not their local value. The way to do so is detailed in the appendix B.2.

and if  $j = 2p$  is even:

$$\begin{aligned}
U_j(\tilde{r}, \tilde{R}) &= \lambda^{2p-1} \Gamma(p+1/2) \left[ \operatorname{erf} \left( \frac{r}{\lambda} \right) \right]_{r=\tilde{r}}^{r=\tilde{R}} \\
&\quad - \sum_{k=0}^{p-1} \lambda^{2k} \frac{\Gamma(p+1/2)}{\Gamma(p-k+1/2)} \left[ r^{2p-2k-1} e^{-r^2/\lambda^2} \right]_{r=\tilde{r}}^{r=\tilde{R}}.
\end{aligned} \tag{5.39}$$

To take into account the radial boundary condition it is enough to subtract the same term where each  $R_\odot$  has been replaced with  $\frac{R^2}{R_\odot}$  and each  $\lambda$  with  $\lambda \frac{R}{R_\odot}$  and to divide this term by  $a(R_\odot)$ . Unfortunately, this solution is not very fast to converge and can be tricky to implement numerically, making its use less interesting.

### 5.3.2.2 Vertical propagators

#### A homogeneous disc

Here, I just quote the result already obtained in reference [10] for secondary positrons. We have:

$$\begin{aligned}
\tilde{I}_z^{\text{hom}} &= \int_{-z_{\max}}^{z_{\max}} dz_s \tilde{G}_{1D}^z(\lambda, z = 0 \leftarrow z_s) \\
&= \begin{cases} \frac{1}{2} \sum_{n=-\infty}^{\infty} \left\{ \operatorname{erf} \left( \frac{z_n^{\max}}{\lambda} \right) - \operatorname{erf} \left( \frac{z_n^{\min}}{\lambda} \right) \right\}, \\ \frac{2}{L} \sum_{n=1}^{\infty} (-1)^{n+1} \frac{\cos(k_n(L - z_{\max}))}{k_n} \times e^{-k_n^2 \lambda^2 / 4}. \end{cases}
\end{aligned} \tag{5.40}$$

The latter case corresponds to the Helmholtz solution, while the former one is the image solution, for which we have  $z_n^{\max} \equiv 2nL + (-1)^n z_{\max}$  and  $z_n^{\min} \equiv 2nL - (-1)^n z_{\max}$ . Throughout this thesis, I have used a disk of half-thickness  $z_{\max} = h = 0.1$  kpc. This approximation is discussed in appendix D.1.4.

#### An exponential disc

If we consider sources which exhibit an exponential vertical profile, the integral has to be performed over the complete diffusion zone:

$$\begin{aligned}
\tilde{I}_z^{\text{exp}} &= \int_{-L}^L dz_s \tilde{G}_{1D}^z(\lambda, z = 0 \leftarrow z_s) e^{(-|z|/z_0)} = \\
&\quad \begin{cases} \sum_{n=-\infty}^{\infty} (-1)^n e^{b_n^2 - (\frac{2nL}{\lambda})^2} \left\{ \operatorname{erf} \left( \frac{L}{\lambda} + b_n \right) - \operatorname{erf} (b_n) \right\}, \\ \frac{2}{L} \sum_{n=1}^{\infty} ((-1)^{n+1} z_0 k_n e^{-L/z_0} + 1) \times \frac{z_0 e^{-k_n^2 \lambda^2 / 4}}{1 + z_0^2 k_n^2}. \end{cases}
\end{aligned} \tag{5.41}$$

The first case corresponds to the image solution and  $b_n$  stands for  $\frac{\lambda}{2z_0} + (-1)^n \frac{2nL}{\lambda}$ . The second case corresponds to the Helmholtz solution.

### 5.3.3 Time dependent solution

The steady-state solutions derived above are safe approximations for a continuous injection of cosmic rays in the interstellar medium, as it is the case for secondaries. In opposition, primary cosmic rays are released after violent and localised events like supernova explosions, the remnants and sometimes pulsars of which are thought to be the most common Galactic cosmic ray accelerators. Since the supernova explosion rate  $\Gamma_\star$  is approximately a few per century, the cosmic ray injection rate could exhibit significant local variations over the cosmic ray lifetime (confinement time, or energy loss time, depending on the species) provided this latter is much larger than the individual source lifetime. Since electrons lose energy very efficiently, there is a spatial scale (an energy scale, equivalently), below (above) which these local variations will have a significant effect on the local electron density. To get a rough estimate of this scale, one can compare the energy loss rate  $b(E)$  with the local injection rate. Assuming that source events are all identical and homogeneously distributed in an infinitely thin disk of radius  $R = 20$  kpc, local fluctuations are expected to be smoothed when integrated over an electron horizon  $\lambda$  such that  $\Gamma_\star(\lambda/R)^2 \gg b(E)/E$ . Using  $K_0 \approx 0.01$  kpc<sup>2</sup>/Myr,  $b(E) \approx (\text{GeV}/\text{Myr}/315)\epsilon^2$  and  $\Gamma_\star \approx 1/100$  yr, we find  $E \ll 80$  GeV, which means that local fluctuations of the flux are likely important above a few tens of GeV. A similar reasoning was in fact emphasised a few decades ago by Shen [37]. Anyway, it is worth recalling that a significant number of supernova remnants and pulsars is actually observed within a few kpc from the Earth. We can therefore hope that current measurements will help to feature them as electron sources, and thereby provide grounds to predict the local electron density.

To estimate the contribution of local transient sources, we need to solve the full time-dependent transport equation (5.4), and we will further show that the method used for the steady-state case can also be used, though partly, for the transient case. The time-dependent Green function,  $\tilde{G}_t$ , is again defined by means of the transport operator, asking that  $\widehat{\mathcal{D}} \tilde{G}_t = \delta^3(\vec{x} - \vec{x}_s)\delta(E - E_s)\delta(t - t_s)$ . The general procedure to solve this equation is to work in Fourier space [*exempli gratia* 1, 4, 6, 17, 23], using

$$\tilde{G}_t(t, E, \vec{x}) = \frac{1}{(2\pi)^2} \iint d^3k d\omega \times \exp \left\{ i(\vec{k} \cdot \vec{x} + \omega t) \right\} \phi(\omega, E, k). \quad (5.42)$$

In Fourier space, we now get an ordinary differential equation on  $E$  for each pair  $(\omega, k)$ ,

$$\{i\omega + k^2 K(E)\} \phi - \partial_E (b(E)\phi) = \delta(E - E_s) \times \frac{1}{(2\pi)^2} \exp \left\{ -i(\vec{k} \cdot \vec{x}_s + \omega t_s) \right\},$$

that is solved by:

$$\phi(\omega, E, k) = \frac{1}{b(E)} \frac{1}{(2\pi)^2} \exp \left\{ -\frac{1}{4} k^2 \lambda^2 - i\vec{k} \cdot \vec{x}_s \right\} \times \exp \left\{ -i\omega(t_s + \Delta\tau) \right\}.$$

This solution is only valid for  $E \leq E_s$  because it describes processes ruled by energy losses. It contains the propagation scale  $\lambda$  previously defined in equation (5.28) and the loss time defined as

$$\Delta\tau(E, E_s) \equiv \int_E^{E_s} \frac{dE'}{b(E')}. \quad (5.43)$$

This loss time corresponds to the average time that a particle needs to see its energy decreased from  $E_s$  to  $E$  because of losses. The inverse Fourier transformation is straightforward from equation (5.42), and we eventually obtain:

$$\tilde{G}_t(t, E, \vec{x} \leftarrow t_s, E_s, \vec{x}_s) = \frac{\delta(\Delta t - \Delta\tau)}{b(E)} \frac{\exp\left\{-\frac{(\vec{x}-\vec{x}_s)^2}{\lambda^2}\right\}}{(\pi\lambda^2)^{3/2}}, \quad (5.44)$$

where  $\Delta t = t - t_s$ , and where one recognises the steady-state solution times a delta function mixing real time and loss time. Like in the steady-state case, we can further account for the vertical boundary condition by expanding this 3D solution by means of the image method or in the basis of Helmholtz eigen-functions. The final result can therefore be expressed in terms of the full steady-state solution

$$\tilde{G}_t(t, E, \vec{x} \leftarrow t_s, E_s, \vec{x}_s) = \delta(\Delta t - \Delta\tau) \tilde{G}(E, \vec{x} \leftarrow E_s, \vec{x}_s) \quad (5.45)$$

A complementary interpretation of the time dependence emerges when the temporal delta function is converted into an energy delta function, which is shown convenient for bursting sources for which  $\Delta t$  is fixed. In this case, the Green function reads instead:

$$\tilde{G}_t(t, E, \vec{x} \leftarrow t_s, E_s, \vec{x}_s) = \delta(E_s - E^*) b(E^*) \times \tilde{G}(E, \vec{x} \leftarrow E_s, \vec{x}_s), \quad (5.46)$$

where the energy  $E^*$  satisfies:

$$\Delta\tau(E, E^*) = \Delta t. \quad (5.47)$$

Thus,  $E^*$  corresponds to the injection energy needed to observe a particle with energy  $E$  after a time  $\Delta t = t - t_s$ . Although there is no analytical solution to this equation in the full relativistic treatment of the energy losses (see section 5.2.2), it is still worth working it out in the Thomson approximation:

$$E^* \stackrel{\text{Th.}}{\underset{\text{approx.}}{=}} \frac{E}{1 - E/E_{\max}^{\text{Th}}} \quad (5.48)$$

with  $E_{\max}^{\text{Th}} \equiv [b_0 \Delta t]^{-1} = \frac{\tau_l}{\Delta t} E_0,$

where we have used the energy loss term from equation (5.16). We see that while the energy loss time-scale  $\tau_l \gg \Delta t$ , we have  $E^* \approx E$ . We see also that there is a maximal energy set by the ratio  $\tau_l/\Delta t$ : in the Thomson approximation, a particle injected with energy  $\geq E_{\max}^{\text{Th}}$  will have already lost all its energy by  $\Delta t$ . We stress that  $E_{\max} \geq E_{\max}^{\text{Th}}$  in the general relativistic case (see section 5.2.2).

It is worth mentioning that as a further consequence of this energy  $E^*$  arising here, the propagation scale  $\lambda$  is no longer set by energy losses, but instead by the injection time  $\Delta t$ . Indeed, in the simplified case of a constant diffusion coefficient  $K$ , we would have found  $\lambda^2 = 4K\Delta t$ . Of course, the energy dependence of the diffusion coefficient slightly modifies this

relation, but this remark can help to make a rough prediction of the observed spectrum for a bursting source (see reference [9]).

Finally, we stress that solutions to the time-dependent transport equation do not guarantee causality, which is important to account for to avoid irrelevant predictions when playing with the source age and distance. To ensure causality at zeroth order and for the sake of definitiveness, we will use

$$\tilde{G}_t(t, E, \vec{x} \leftarrow t_s, E_s, \vec{x}_s) = \theta(c\Delta t - \|\vec{x} - \vec{x}_s\|) \delta(E_s - E^*) \times b(E^*) \tilde{G}(E, \vec{x} \leftarrow E_s, \vec{x}_s), \quad (5.49)$$

as our time-dependent propagator. A more accurate causal solution would need more specific methods inferred from *exempli gratia* more detailed studies of the relativistic heat conduction.

## 5.4 Solar modulation

Propagation of cosmic rays inside the Solar system has been under study for a much longer time than the Galactic propagation. However the lack of knowledge of the exact structure of the magnetic field around the Sun makes this work extremely difficult. Moreover, only little data concerning cosmic ray fluxes in the Solar system at positions different from the one of the Earth are available. The only probes to have measured cosmic ray fluxes far away from us are Voyager 1 & 2 and Pioneer 10 & 11.

The most striking evidence of the existence of such a modulation is the anti-correlation of the number of Sun spots (which quantifies the Sun activity) and the quantity of low energy cosmic rays arriving at the Earth (quantified by neutron monitoring) as it can be seen on the left panel of figure 5.4. It is believed that the Sun vicinity (the Heliosphere) is made of an inner part where the solar wind is fast ( $\sim$  one million kilometre per hour) and is delimited by a termination shock situated at 75~90 astronomical units from the Sun. This shock corresponds to the place where the solar wind becomes subsonic. It seems that both Voyager probes have crossed this region in 2005 and 2007 respectively. The outer heliosphere has a radius of about 230 astronomical units. It is delimited by the bow shock due to the velocity of the heliosphere with respect to the interstellar medium. Moreover, between the bow shock and the termination shock, there is a heliopause: a region where pressure of the solar wind is equal to the pressure of the interstellar medium. In the outer-heliosphere (or heliosheath), due to its interaction with the interstellar medium, the magnetic field becomes turbulent. The places where temporal variations of the magnetic field occur are called merged interaction regions and are believed to be localised and of three kinds: global, co-rotating or localised. These names refer to the size of the merged interaction regions. All these regions, as well as the three frontiers (bow shock, heliopause, termination shock) have a dramatic impact on cosmic ray propagation in the Sun vicinity.

Cosmic ray particles interact with waves and discontinuities embedded in heliosphere plasma. Four main physical processes result from this:

- Pitch-angle scattering of particles at magnetohydrodynamics waves which results in a random walk of the cosmic rays in the heliosphere.
- Convection of particles with the solar wind and adiabatic deceleration in the expanding solar wind plasma, just as cosmic rays do with the galactic wind.

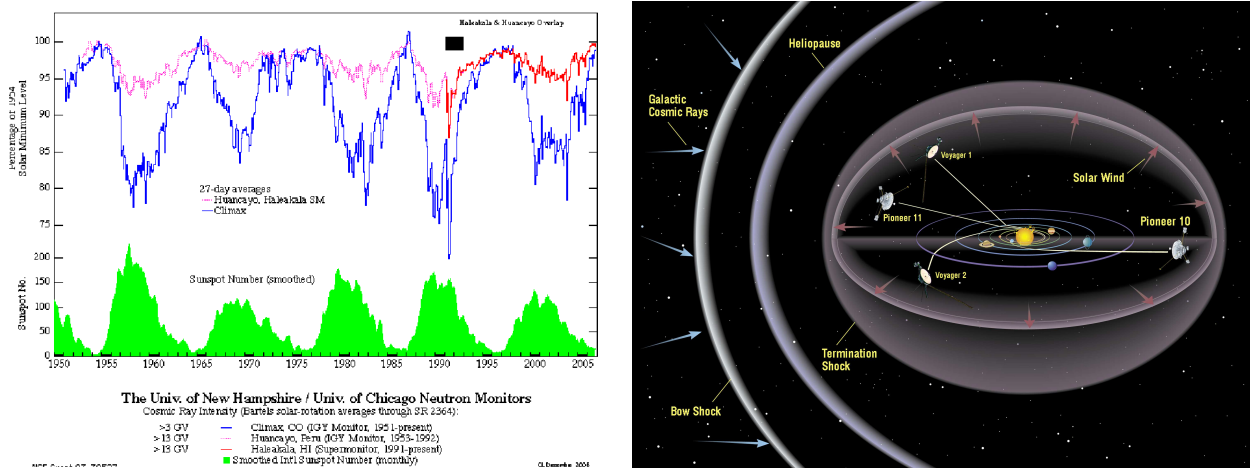


Figure 5.4: *Left panel:* number of sunspots observed every month and measured cosmic ray flux since 1951. *Right panel:* The Solar system and its magnetic environment.

- Drifts due to changes of the Larmor radius during a gyro-period of the particles. Indeed, if the magnetic field changes brutally or if the speed of the cosmic ray varies during one rotation around a field line, the particle will drift from one field line to another. Positive and negative particles drift in opposite directions.
- Blocking and reflection at inhomogeneities such as magnetic clouds.

All these processes can be modelled with a diffusion equation similar to Eq. 5.1 however, because of the very little number of data, large uncertainties remain and the relative importance of each phenomenon is unknown. Moreover, because of the dependence on Solar activity and polarity, it is impossible to make predictions. One can read [22] and references therein for a more complete introduction to the Solar modulation problem.

It seems however that a good approximation, called the force field approximation, reproduces the data correctly. It has no solid theoretical justification but because it is convenient, it became extremely popular among the cosmic ray community. It states:

$$\Psi_{TOA}(\mathcal{R}_{TOA}) = \left( \frac{\mathcal{R}_{TOA}^2}{\mathcal{R}_{IS}^2} \right) \Psi_{IS}(\mathcal{R}_{IS}) \quad (5.50)$$

where  $\mathcal{R}_{TOA} = \mathcal{R}_{IS} - \Phi_{Fisk}$ . The <sup>TOA</sup> and <sup>IS</sup> superscripts correspond to Top Of the Atmosphere (solar modulated) and Interstellar quantities respectively. This notation will be kept in the following chapters. As in the beginning of this chapter,  $\mathcal{R}$  is the particle rigidity (the ratio of momentum to electric charge number  $p/Z$ ), for relativistic electrons, it can be considered as equivalent to the energy. Finally, the Fisk potential,  $\Phi_{Fisk}$ , measured in MegaVolt, characterises the solar modulation effect. Obviously this parameter has to be changed for each measurement as it depends on solar activity and cosmic ray species (which are not affected by drift in the same way). Usually  $\Phi_{Fisk}$  is of the order of a few hundreds of MV.

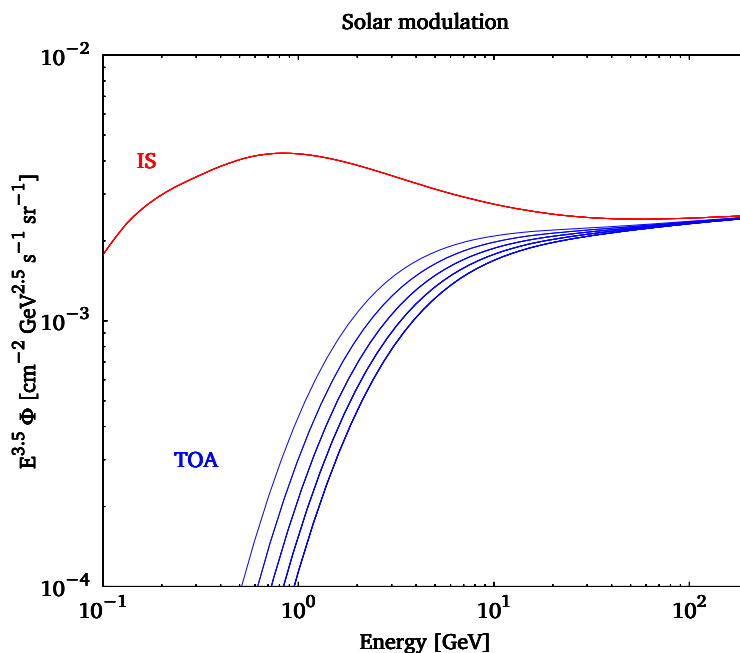


Figure 5.5: This plot shows the influence of Solar modulation by comparing interstellar and top of the atmosphere fluxes. The Fisk potential is increased from 500 MV to 900 MV by steps of 100 MV. The conclusion is clearly that Solar modulation washes out all the spectral features below  $\sim 10$  GeV. This will justify neglecting diffusive re-acceleration, convection and energy losses that happen in the Galactic disk only in the next chapters.

## 5.5 Improving the model

### 5.5.1 Boundary conditions

Imposing the phase-space density to vanish at  $r = R_{Gal}$  and at  $|z| = L$  does not have a strong theoretical motivation. The only reason is that it seems to reproduce rather well the synchrotron emission of the outer galaxies. However the shape usually observed is not the one of a slab as it has been considered here but rather of an ellipsoid, thicker above the Galactic bulge (where stellar population is denser hence the cosmic rays fluxes and the magnetic fields are more intense). This is not possible to do with an analytical resolution scheme, but it should be possible for a numerical one. However, this would increase the uncertainties and make comparisons among models more difficult which would not be very satisfactory. A way to get around this issue is to consider anisotropic diffusion.

### 5.5.2 Anisotropic propagation

Up to this point, the diffusion coefficients have all been considered homogeneous. However, as the physical phenomena responsible for these propagation coefficients are not homogeneous throughout the Galactic halo, it seems logical to try to take into account these spatial variation.

A first step in this direction has been performed by Gebauer & de Boer [15] in the fully numerical scheme of GALPROP [38], a public code for cosmic ray propagation. Of course, analytical models cannot handle all kinds of spatial dependence, but may give an interesting insight to the problem nevertheless.

In the most generic case, if we discard isotropy, the phase-space density cannot be considered as a scalar anymore as the projection of the momentum of the cosmic rays may be different in each direction. Instead one needs now to deal with a vector:

$$\vec{\Psi} \equiv \begin{pmatrix} \frac{d^4 N}{d^3 \vec{x} d p_x} \\ \frac{d^4 N}{d^3 \vec{x} d p_y} \\ \frac{d^4 N}{d^3 \vec{x} d p_z} \end{pmatrix}. \quad (5.51)$$

For the same reason the diffusion coefficients  $K$  and  $D_{EE}$  should be considered as a three by three matrix. Because of continuity reason, it has to be diagonal. Hence instead of one diffusion equation, one actually has to deal with three. Keeping cylindrical symmetry (which is not possible if one wishes to take into account the impact of spiral arms), decreases this number to two. This would be justified by the fact that magnetic processes are anisotropic but would be too tedious to handle and would make recovering the observed anisotropy quite difficult.

A first step is then to keep the previous isotropic equation 5.4 but to include a space variation to the scalar propagation coefficients. Following Gebauer & de Boer [15], one can modify only the diffusion coefficient as follows:

$$K = \begin{cases} K_0 \beta \mathcal{R}^\delta & \text{if } |z| \leq z_d \\ K_0 \beta \frac{|z|}{z_d} \mathcal{R}^\delta & \text{if } |z| \geq z_d. \end{cases} \quad (5.52)$$

This allows to get rid of the vertical boundary condition and the conceptual difficulties it rises (see previous paragraph) as it is the increase of the diffusion which kills the cosmic ray density instead of an ad hoc boundary condition. The consequence of this new diffusion coefficient is that it will create a new convection-like term ( $\propto \partial_z \Psi$ ). Solving the new diffusion equation is trivial for  $|z| \leq z_d$  as it is the one already solved in this chapter. For larger values of  $z$ , the equation can be solved analytically if the source term is localised in the disk or if its  $z$  variation can be expanded as a power series.

In the same way, a linear variation of the convective wind with  $z$  can be implemented as it would only add a new term proportional to  $P_i$  in equation 5.23 and hence will rescale  $\tilde{C}_{i,n}$ .

Radial variation of the parameters is more complex and cannot be taken care of in any analytical way that I know. One should however ask if adding more and more parameters in the problem is not increasing the uncertainties in such a way that it prevents any prediction.

### 5.5.3 Time dependence

On one hand, the data we have about cosmic rays are only a few decades old on the other hand cosmic ray propagation time-scale is of the order of millions of years hence stating steady state is not well motivated. Actually, study of meteorites and polar ices teaches us that the cosmic ray flux at the Earth has varied with time. A nice review which considers all the time variation reasons can be found in Scherer *et alii* [36] from which figure 5.6 is taken. However, a

complete description of all the time dependences of the Sun and various sources position would be far too complex to be implemented.

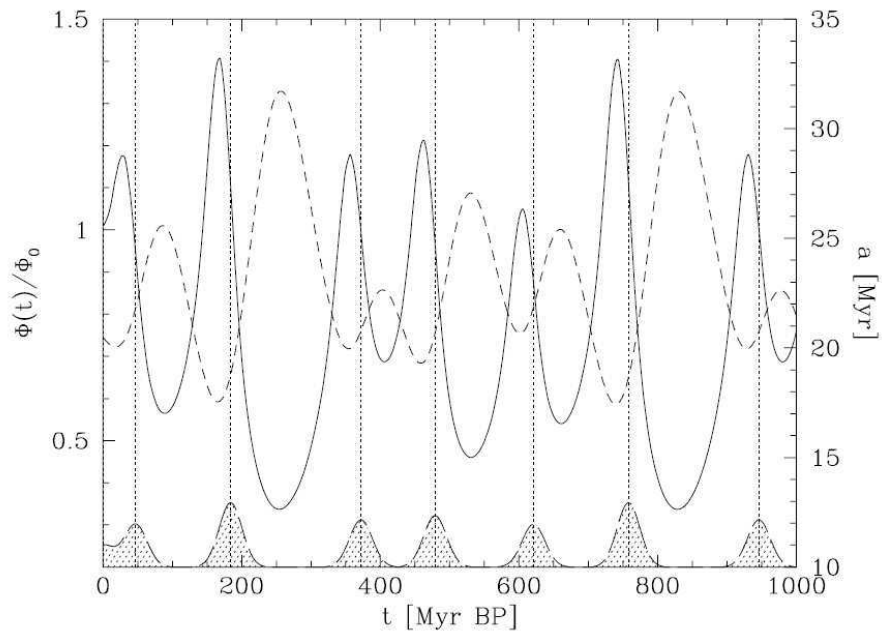


Figure 5.6: Variation time scales of cosmic ray fluxes measured or estimated by Scherer *et alii* [36].

We now have everything we need to compute the propagation of Galactic cosmic rays. Next chapters will use these results to estimate the electron/positron cosmic ray fluxes at the Earth and everywhere in the Milky Way.

## Bibliography

- [1] Atoyan, A. M., Aharonian, F. A., & Völk, H. J. 1995, *Phys. Rev. D*, 52, 3265 [106](#)
- [2] Balian, R. 1983, *Du Microscopique au Macroscopique*, ed. Ellipses [88](#)
- [3] Baltz, E. A. & Edsjö, J. 1999, *Phys. Rev. D*, 59, 023511 [102](#)
- [4] Baltz, E. A. & Wai, L. 2004, *Phys. Rev. D*, 70, 023512 [106](#)
- [5] Beck, R., Shukurov, A., Sokoloff, D., & Wielebinski, R. 2003, *A&A*, 411, 99 [94](#)
- [6] Berezhinskii, V. S., Bulanov, S. V., Dogiel, V. A., & Ptuskin, V. S. 1990, *Astrophysics of cosmic rays*, ed. Berezhinskii, V. S., Bulanov, S. V., Dogiel, V. A., & Ptuskin, V. S. [106](#)
- [7] Blumenthal, G. R. & Gould, R. J. 1970, *Reviews of Modern Physics*, 42, 237 [95](#)
- [8] Cox, D. P. 2005, *ARA&A*, 43, 337 [90](#)
- [9] Delahaye, T., Lavalle, J., Lineros, R., Donato, F., & Fornengo, N. 2010, *ArXiv e-prints* [1002.1910](#) [95](#), [108](#)
- [10] Delahaye, T., Lineros, R., Donato, F., *et alii* . 2009, *A&A*, 501, 821 [105](#)
- [11] Delahaye, T., Lineros, R., Donato, F., Fornengo, N., & Salati, P. 2008, *Phys. Rev. D*, 77, 063527 [99](#)
- [12] Donato, F., Fornengo, N., Maurin, D., Salati, P., & Taillet, R. 2004, *Phys. Rev. D*, 69, 063501 [92](#)
- [13] Donato, F., Maurin, D., & Taillet, R. 2002, *A&A*, 381, 539 [91](#)
- [14] Ekers, R. D. & Sancisi, R. 1977, *A&A*, 54, 973 [88](#), [89](#)
- [15] Gebauer, I. & de Boer, W. 2009, *ArXiv e-prints* [0910.2027](#) [111](#)
- [16] Ginzburg, V. L. & Ptuskin, V. S. 1976, *Reviews of Modern Physics*, 48, 161 [88](#)
- [17] Ginzburg, V. L. & Syrovatskii, S. I. 1964, *The Origin of Cosmic Rays*, ed. Ginzburg, V. L. & Syrovatskii, S. I. [106](#)
- [18] Ginzburg, V. L. & Syrovatskii, S. I. 1969, *The origin of cosmic rays*, ed. Ginzburg, V. L. & Syrovatskii, S. I. [88](#)
- [19] Gloeckler, G. & Jokipii, J. R. 1970, in *International Cosmic Ray Conference*, Vol. 1, *International Cosmic Ray Conference*, 541–+ [88](#)
- [20] Han, J. L., Manchester, R. N., Lyne, A. G., Qiao, G. J., & van Straten, W. 2006, *ApJ*, 642, 868 [94](#)
- [21] Jones, F. C. 1965, *Physical Review*, 137, 1306 [95](#)

- [22] Kallenrode, M. 2000, in *The Outer Heliosphere: Beyond the Planets*, ed. K. Scherer, H. Fichtner, & E. Marsch, 165–190 [109](#)
- [23] Kobayashi, T., Komori, Y., Yoshida, K., & Nishimura, J. 2004, *ApJ*, 601, 340 [106](#)
- [24] Longair, M. S. 1992, *High energy astrophysics. Vol.1: Particles, photons and their detection*, ed. Willcox, P. J. [92](#)
- [25] Longair, M. S. 1994, *High energy astrophysics. Vol.2: Stars, the galaxy and the interstellar medium*, ed. Longair, M. S. [92](#)
- [26] Maurin, D. 2001, PhD thesis, Université de Savoie [90](#)
- [27] Maurin, D., Donato, F., Taillet, R., & Salati, P. 2001, *ApJ*, 555, 585 [88](#), [89](#), [91](#), [92](#)
- [28] Maurin, D., Putze, A., & Derome, L. 2010, *ArXiv e-prints* [1001.0553](#) [91](#)
- [29] Maurin, D., Taillet, R., & Donato, F. 2002, *A&A*, 394, 1039 [91](#)
- [30] Mewaldt, R. A., Turner, R. E., Friedlander, M. W., & Israel, M. H. 1970, in *International Cosmic Ray Conference, Vol. 1, International Cosmic Ray Conference*, 433–+ [88](#)
- [31] Parker, E. N. 1969, *Space Science Reviews*, 9, 651 [88](#)
- [32] Porter, T. A., Moskalenko, I. V., Strong, A. W., Orlando, E., & Bouchet, L. 2008, *ApJ*, 682, 400 [96](#), [98](#)
- [33] Prouza, M. & Šmída, R. 2003, *A&A*, 410, 1 [94](#)
- [34] Ptuskin, V. S., Voelk, H. J., Zirakashvili, V. N., & Breitschwerdt, D. 1997, *A&A*, 321, 434 [90](#)
- [35] Putze, A., Derome, L., & Maurin, D. 2010, *ArXiv e-prints* [1001.0551](#) [91](#)
- [36] Scherer, K., Fichtner, H., Borrmann, T., *et alii* . 2006, *Space Science Reviews*, 127, 327 [111](#), [112](#)
- [37] Shen, C. S. 1970, *ApJ*, 162, L181+ [106](#)
- [38] Strong, A. W. & Moskalenko, I. V. 1998, *ApJ*, 509, 212 [111](#)
- [39] Strong, A. W., Moskalenko, I. V., & Ptuskin, V. S. 2007, *Annual Review of Nuclear and Particle Science*, 57, 285 [88](#)
- [40] Webber, W. R., Lee, M. A., & Gupta, M. 1992, *ApJ*, 390, 96 [88](#)

# Chapter 6

## Positrons and electrons

Knowledge would be fatal, it is the uncertainty that charms one. A mist makes things beautiful.

*Oscar Wilde in The picture of Dorian Gray*

Now that we know how to estimate the amount of cosmic rays the sources are producing and the effect of interstellar propagation, all we have to do is to convolute these two quantities to get estimations of the fluxes at the Sun position. I will first focus on secondary cosmic rays and then on primaries. The aim is not only to give a prediction (this has been done already by Moskalenko & Strong [33]) but to take advantage of the speed of analytical methods to size and understand the various uncertainties affecting our predictions.

## 6.1 Secondaries

This section is mainly inspired by reference [13]. The discussion is more or less the same, the main difference is that the figures have been updated to take into account the full expression of the energy losses, indeed, in the earlier work, we had considered only the Thomson regime. A discussion of the effect of a local bubble has also been added (see paragraph 6.1.1.3).

In the sake of clarity, the various sources of uncertainties will be varied one by one. This means that for each of them we need to choose a reference value. These choices are only meant for discussion and do not imply I put more faith in one model rather than in another. The reference propagation parameter is *Med* as in Table 5.1, but without convection and reacceleration (which will be added only in paragraph 6.1.1.5). Concerning energy losses, I will make use of model M1 from Table 5.2 and disregard the losses taking place in the disc only. The production cross-section parametrisations will be the ones from Kamae *et alii* [23] corrected as in reference [24]. The projectile fluxes considered for protons and  $\alpha$  particles are the one from Donato *et alii* [16] (denoted D09 see section 4.2.2). Finally, for the target density, I will take the reference value of 0.9 hydrogen atom per  $\text{cm}^3$  and 0.1 helium atom per  $\text{cm}^3$  (see discussion in Appendix D.1). Being dominated by primaries, secondary electrons are less interesting than secondary positrons. So sometimes the discussion will focus only on positrons.

### 6.1.1 The electron and positron fluxes and their uncertainties

#### 6.1.1.1 Propagation

Figure 6.1 displays the calculated secondary positron flux modulated at solar minimum along with recent experimental data. A Fisk potential of  $\phi = 600$  MV has been applied as explained in section 5.4. The *min*, *Med* and *MAX* cases are illustrated by the red solid, long-dashed and short-dashed lines, respectively, while the yellow area denotes the uncertainty in the propagated flux caused by the uncertainty in the astrophysical parameters. In the same figure, one can also see the interstellar flux. The upper long-dashed curve corresponds to the *Med* case whereas the slanted band indicates the uncertainty in the Galactic propagation parameters. The solid line shows the interstellar flux from Moskalenko & Strong [33].

Below  $\sim 100$  GeV, the yellow uncertainty band is delineated by the *min* and *MAX* models. The *min* (*MAX*) set of parameters yields the highest (lowest respectively) values for the secondary positron flux. Since we considered more than about 1600 different configurations compatible with the boron to carbon ratio [29], other propagation models become important in determining the extremes of the uncertainty band at higher energies. The maximal flux at energies above 100 GeV does not correspond to any specific set of propagation parameters

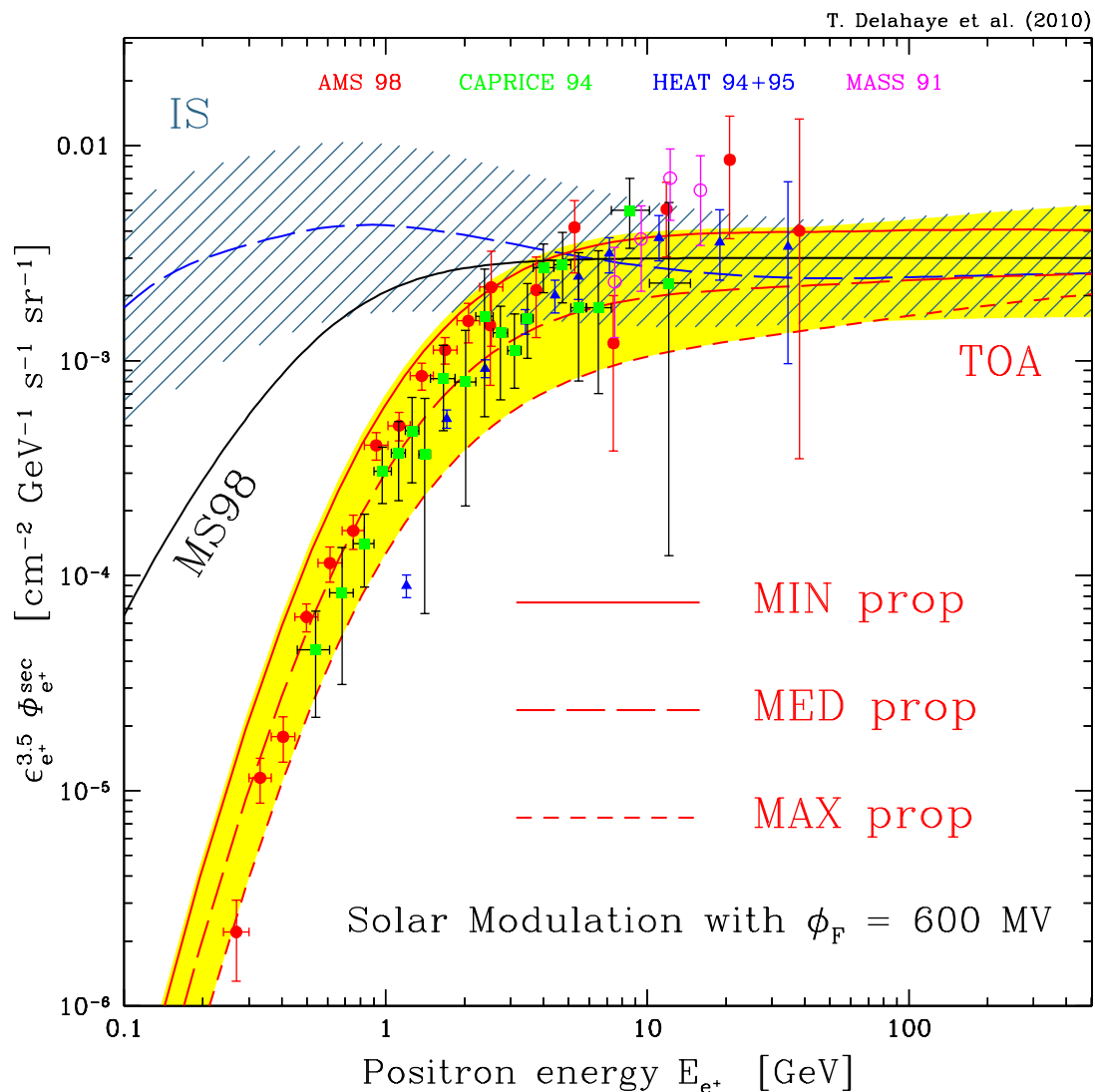


Figure 6.1: Secondary positron flux as a function of the positron energy. The blue hatched band corresponds to the cosmic ray propagation uncertainty in the interstellar prediction (*id est* without solar modulation), whereas the yellow strip refers to top of the atmosphere fluxes. The long-dashed curves feature our reference model with the Kamae *et alii* [23, 24] parametrisation of nuclear cross-sections, the Shikaze *et alii* [36] injection proton and helium spectra and the *Med* set of propagation parameters. The *min*, *Med* and *MAX* propagation parameters are displayed in Tab. 5.1. Data are taken from CAPRICE [9], HEAT [7], AMS [2, 4] and MASS [20]. This figure is similar to figure 5 in reference [13], except that the full expression of the energy losses has been taken into account here and not the Thomson regime approximation. The black line labeled MS98 corresponds to the unmodulated flux predicted by Moskalenko & Strong [33] and parametrised by Baltz & Edsjö [6].

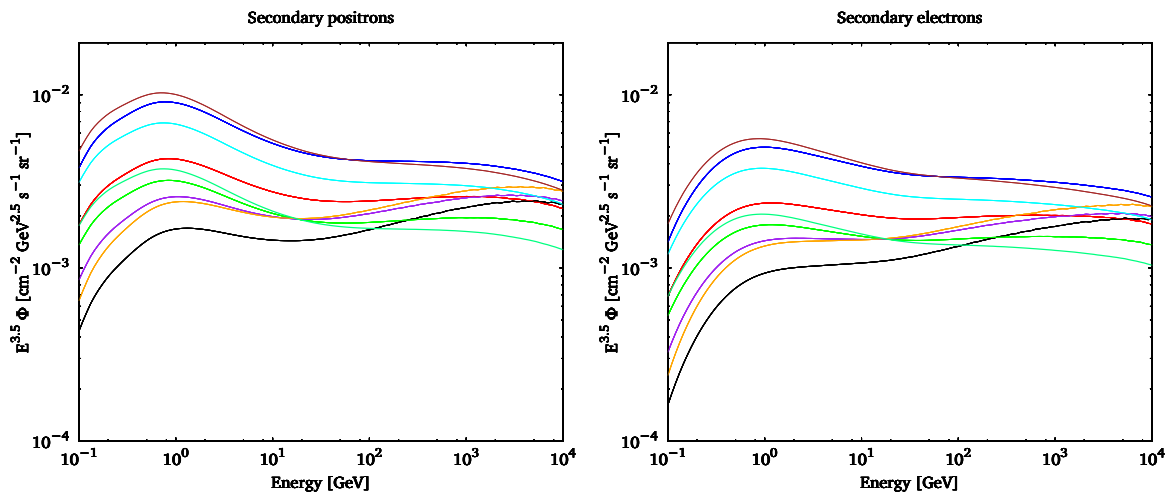


Figure 6.2: *Left*: This figure is similar to figure 6.1, except it shows only the interstellar flux and more propagation parameters sets that are also compatible with boron to carbon ratio analysis. *Right*: Same as left panel but for electrons. The three parameter sets *min*, *Med*, and *MAX* are in blue, red and black respectively.

over the whole range of energies. This is also true when dealing with primary positrons and is explained in more details in paragraph 6.2.2.

From Fig. 6.1, we see that the variation in the propagation parameters induces an uncertainty in the positron flux, which reaches about one order of magnitude over the entire energy range considered here. It is a factor of 6 at 1 GeV, and smoothly decreases down to a factor of 4 or less for energies higher than 100 GeV.

Figure 6.2 shows the interstellar flux for various propagation parameter sets, all of them compatible with boron to carbon ratio data. It clearly exhibits that changing the propagation parameters does not only change the normalisation (as one can believe in comparing only the *min*, *Med* and *MAX* cases) but also the shape. Actually some predictions even cross each other. This stresses the importance of not only considering the three *min*, *Med* and *MAX* configurations when wishing to perform a fit on data for example. This illustrates quite well the advantage of analytical methods over numerical, as a full scan of the parameter space is not too time costly.

The effect from propagation are similar for electrons and positrons, the only difference comes from the source term. As explained before, the secondary electron flux is a little lower than the positron one, especially at low energy because most of the resonances producing positrons do not produce electrons.

### 6.1.1.2 Source

The effects induced by different parametrisations of the nuclear production cross-sections and by the variation in the proton injection spectrum are shown in Fig. 6.3. In the left panel, the top of the atmosphere positron fluxes calculated from the Tan & Ng [38] (dotted-dashed),

Badhwar *et alii* [5] (short-dashed), and Kamae *et alii* [23, 24] (solid) cross-section models for the *Med* propagation scheme and the D09 [16] proton and helium injection spectra are presented. The Kamae *et alii* [23, 24] model leads systematically to the lowest flux. For positron energies  $\lesssim 1$  GeV, the three cross-section parametrisations differ by just a few percent, while the differences are significantly larger at higher energies. Figure 6.3 translates the uncertainties in the source  $q_{e^+}$  featured in Fig. 4.3. Consequently, the flux obtained at 10 GeV with the Tan & Ng [38] or Badhwar *et alii* [5] parametrisation is a factor of 2 or 1.6, respectively, higher than the reference case [23, 24]. This trend is confirmed at higher energies, although the differences between the various models are smaller above 200 GeV.

In reference [13], we had concluded that the uncertainties caused by the proton and helium spectrum parametrisations are the least relevant to this analysis and that the differences are at most 10–15% around 10 GeV, and are negligible in the lower and higher energy tails. In fact if one considers the parametrisation D09 (see equation 4.23), which is quite different at high proton energy than the two others, one gets a large uncertainty for secondary positrons (almost a factor of 2 at 1 TeV).

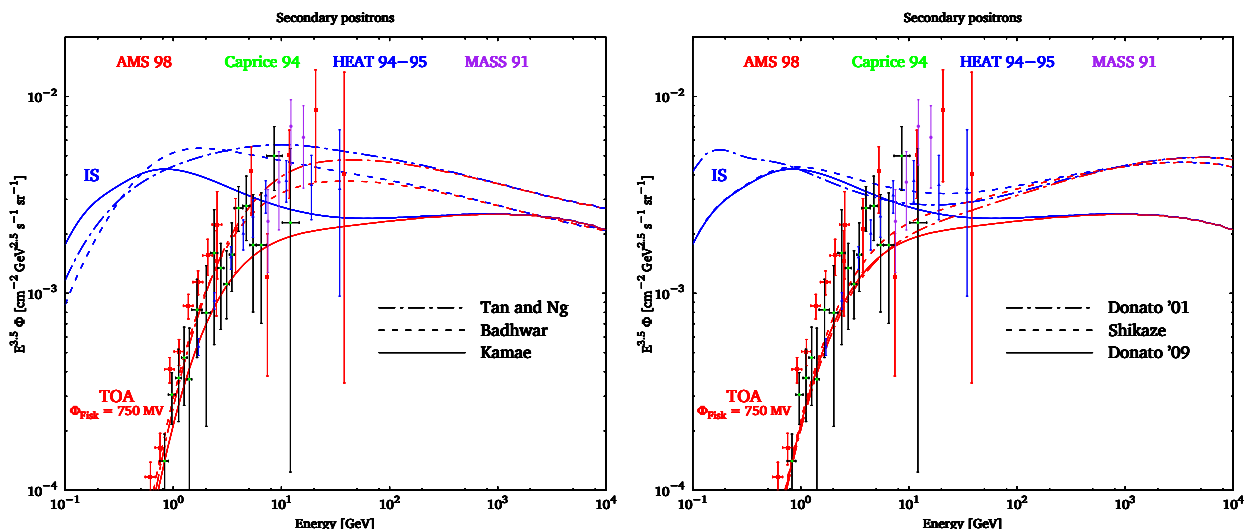


Figure 6.3: *Left*: top of the atmosphere and interstellar positron spectra for three different nuclear cross-section parametrisations: Kamae (solid), Badhwar (dashed) and Tan & Ng (dotted-dashed), which are described in section 4.2.1.5 *Right*: top of the atmosphere and interstellar positron spectra for three different proton fluxes: D01 (dotted-dashed), Shikaze (dashed), and D09 (solid). They respectively correspond to equations 4.21, 4.22 and 4.23. In all cases, diffusion parameters are set to the *Med* case of Tab. 5.1. These figures are similar to those of figure 6 in reference [13], except that the full expression of the energy losses has been taken into account here. Moreover the D09 proton flux parametrisation has been added.

Concerning electrons, as one can see from figure 6.4, the discussion is pretty much the same concerning projectile flux parametrisations. However for the cross sections, the discrepancy among the models is more important here than what it is for positrons. Indeed at high energy, the parametrisations of Tan & Ng [38] or Badhwar *et alii* [5] are a factor of 2 lower than the

reference case [23, 24]. The spectral index also exhibits large variations.

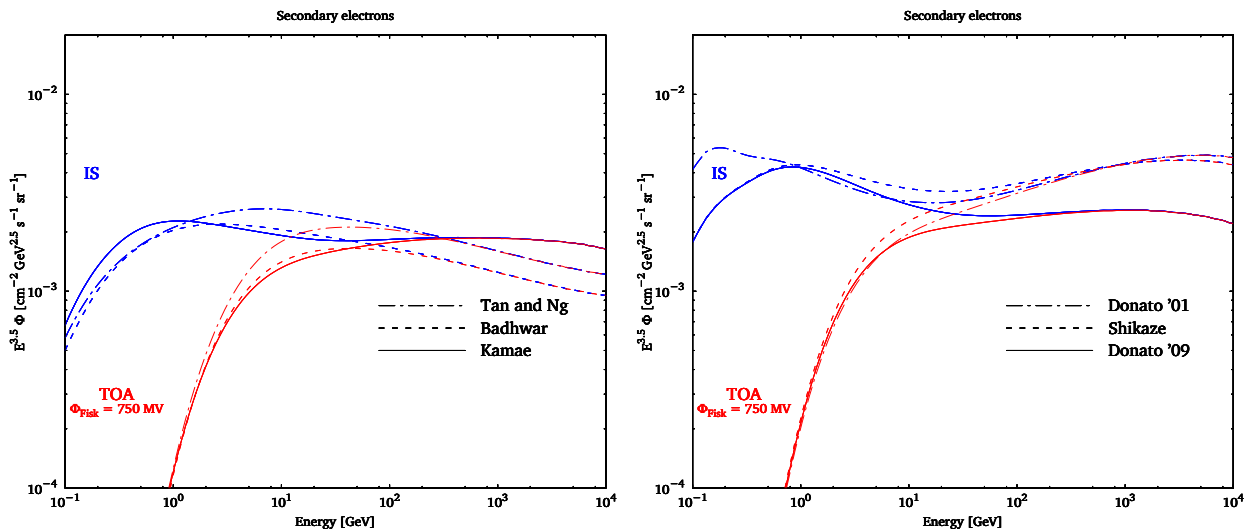


Figure 6.4: Same as Figure 6.3 but for electrons instead of positrons.

Moreover, one should consider the uncertainty due to the average matter density of the interstellar medium. As discussed in appendix D.1 the local average density is one atom per  $\text{cm}^3$ . However the uncertainties on this value are difficult to size and can be estimated of order 50%. This would directly translate into an uncertainty of the same size in the predicted fluxes' normalisation. Ideally one should not take an average value but consider a realistic matter distribution. Though such maps exist, it would be far too difficult to implement them and as we will see in paragraph 6.1.1.4 its impact would be quite irrelevant. Furthermore, it would be inconsistent to use a gas density different than the one used by Maurin *et alii* [29] to constrain the propagation parameters because the latter are very sensitive to this gas density.

### 6.1.1.3 Local bubble

As it has been shown by Combet *et alii* [11], Donato *et alii* [17], and Putze *et alii* [35] a local underdensity of interstellar gas could have an important impact on the secondary heavy nuclei cosmic ray fluxes at the Earth. The method to take into account a void around the Sun is detailed in appendix B.4. The reason for considering such an underdensity is simply that astronomers have observed that the nearby 100 pc are extremely under-dense. It is believed that ancient supernova explosions have pushed away the interstellar gas of the region leaving it almost completely void. The exact position of the Sun in this void is not very clear so I will always consider the Sun at the center of this void.

As it can be seen in Figure 6.5, the impact of a local void of a few hundred of parsecs is not very important. Its effect starts to be relevant at quite high energies only. This is exactly the opposite of what has been observed for boron and other heavy nuclei. The reason for this is that only cosmic rays propagating on short distances will be affected by a depletion of the local environment, now low energy nuclei travel very little whereas high energy electrons/positrons

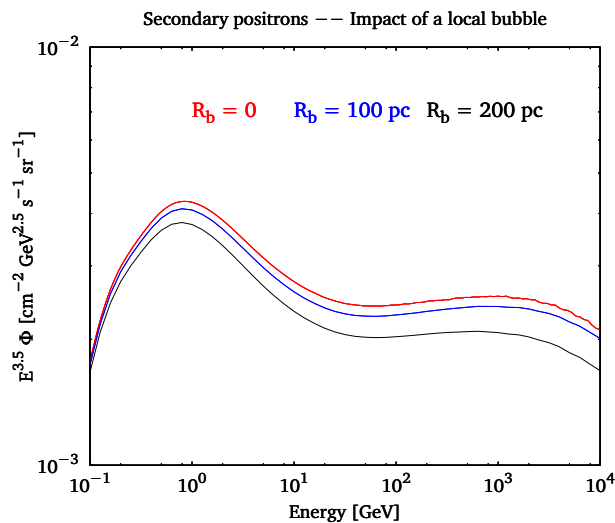


Figure 6.5: Impact of a local void on the secondary positron flux.

are the ones to be local (see paragraph 6.1.2), from which it follows that they are not affected in the same way.

#### 6.1.1.4 Proton retro-propagation

At every location in the Galaxy, the positron production by spallation is determined by the local flux of cosmic ray proton and helium projectiles. Their spatial distribution  $\Phi(\mathbf{x}, E)$  was assumed to be constant and set equal to the value  $\Phi_{\odot}(E)$  measured at the Solar System location. However, one can note that these primary cosmic rays also diffuse in the Milky Way, so that their flux should exhibit a spatial dependence. This will be discussed in more details in chapter 7. The positron source term  $q_{e^+}$  should vary accordingly inside the Galactic disk. The behaviour of the proton and helium fluxes with radius  $r$  can be inferred readily from their measured values  $\Phi_{\odot}(E)$  once the propagation parameters are selected. This so-called retro-propagation was implemented in the original boron to carbon analysis by Maurin *et alii* [29]. The method to do so is detailed in section B.2. The radial variation in the proton flux is presented in the left panel of Fig. 6.6 for two quite different proton energies, and is found to be significant. This is why one should question the hypothesis of a homogeneous positron production throughout the disk. Actually taking the retro-propagation of projectile spectra into account has little effect on the positron flux, as is clear in the right panel of Fig. 6.6. Indeed, for most configurations, the error is always smaller than 5%. Even for the *MAX* propagation set, though the error may get as large as 15% at low energy, at energies relevant for our study ( $\gtrsim 10$  GeV), the error is negligible.

#### 6.1.1.5 Diffusive reacceleration and full energy losses

Up to this point, space diffusion and energy losses through inverse Compton scattering and synchrotron emission were the only processes considered. As it is explained in paragraph B.3,

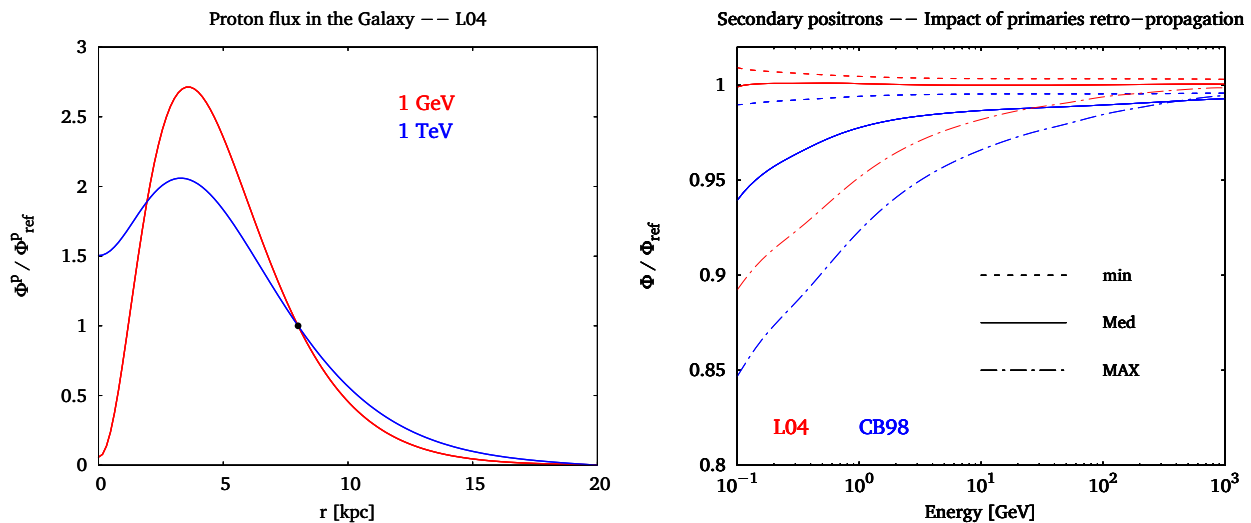


Figure 6.6: *Left*: Ratio of the proton flux at radius  $r$  to the Solar value. In this plot, retro-propagation has been taken into account, and all propagation effects of the *Med* configuration (*id est*, convective wind, spallation, and diffusion) have been included. The dot refers to the Solar System position in the Galaxy. *Right*: Ratio of the positron flux computed with and without retro-propagation, as a function of positron energy. The three propagation models of table 5.1 and different source distribution have been used. These plots are similar to figures 7 and 9 of reference [13], except that the source distributions have been updated accordingly to section 4.1.3 and the full energy loss expression has been used here (and not only the Thomson approximation).

when one wants to take into account all the effects described in chapter 5, there is no longer an analytical solution to the diffusion equation, at least none that I know.

The solid line of Fig. 6.7 considers only space diffusion and energy losses by inverse Compton scattering and synchrotron emission. When these processes are supplemented by diffusive reacceleration, we derive the long-dashed curve with a noticeable bump at  $\sim 3$  GeV. Below that value, positrons are reaccelerated and their energy spectrum is shifted to higher energies. Above a few GeV, inverse Compton scattering and synchrotron emission dominate over diffusive reacceleration, inducing a shift in the spectrum towards lower energies. Positrons accumulate in an energy region where energy losses and diffusive reacceleration compensate each other, hence a visible bump which is already present in the analysis by Moskalenko & Strong [33]. The short-dashed line is obtained by replacing diffusive reacceleration by Galactic convection. The wind is active at low energies, where space diffusion is slow. Positrons are drifted away from the Galaxy and their flux at the Earth is depleted. One should note that diffusive reacceleration and Galactic convection were included separately by Lionetto *et alii* [27] in their prediction of the positron spectrum, with the net result of either overshooting (diffusive reacceleration) or undershooting (galactic convection) the data. If we now incorporate both processes and add the various energy-loss mechanisms, we derive the dotted curve, which also contains a bump, although of far smaller amplitude. The bump cannot be distinguished from the solid line for

energies above a few GeV. Below a few GeV, the situation becomes more complicated, several effects are at stake, modifying the blue hatched interstellar and yellow top of the atmosphere uncertainty intervals in Fig. 6.1 as displayed in the right panel of Fig. 6.7. Reducing the GeV bump of the interstellar flux in agreement with the data now requires a higher Fisk potential of 850 MV. The agreement seems reasonable below a few GeV, although a more detailed investigation would require a refined solar modulation model.

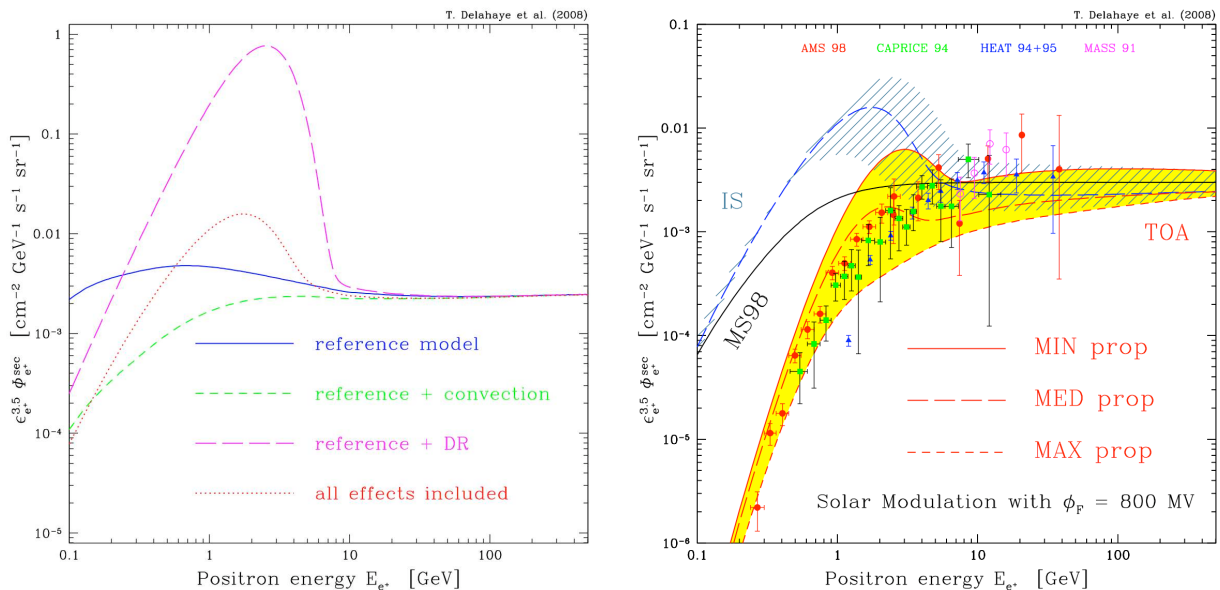


Figure 6.7: *Left*: The reference model is featured here with various effects turned on or off. Space diffusion and energy losses from inverse Compton and synchrotron emission lead to the solid curve. When diffusive reacceleration is added, we get the long-dashed line and its spectacular bump around 3 GeV. The short-dashed curve is obtained by replacing diffusive reacceleration by galactic convection. The spectrum becomes depleted at low energies. Including all the processes yield the dotted line. Diffusive reacceleration and convection are both relevant below a few GeV and induce opposite effects. *Right*: The hatched blue (interstellar) and yellow (top of the atmosphere) regions of Fig. 6.1 delineated by the *MAX* and *min* curves are featured here with all the effects included. Beware that these bands are not the result of a full scan of the parameters sets as in the previous figures, but only the region bracketed by *min* and *MAX*. Above a few GeV, we get the same results as before. Data are taken from CAPRICE [9], HEAT [7], AMS [2, 3] and MASS [20].

Because of solar modulation, these effects cannot be tested, and however we see that they do not come into play for energies higher than  $\sim 10$  GeV. Hence we can safely neglect them in the remaining of this work.

### 6.1.2 Discussion

Let us evaluate the contribution to the total signal from a disk of radius  $r_{\text{source}}$  surrounding the Earth, modelled with the source term

$$q_{\text{source}}(r, E) = q_{e^+}(r, E) \times \theta(r_{\text{source}} - r), \quad (6.1)$$

where  $\theta(x)$  is Heaviside's function and  $r$  measures the radial distance from the Solar System. The positron flux yielded by  $q_{\text{source}}$  is  $\phi_{e^+}^{\odot}(r_{\text{source}}, E)$ , the contribution of which to the total signal  $\phi_{e^+}^{\odot}(E)$  is plotted in Fig. 6.8 as a function of  $r_{\text{source}}$ , for several values of the positron energy  $E$ . Most of the positron signal originates at short distances, especially at high energy. At 1 TeV, more than 80% of the positrons are created within 1 kpc while more than half of the 1 GeV positrons come from less than 1.5 kpc. Energy losses are indeed quite efficient. They reduce the positron horizon strongly as the energy increases. This clearly shows that electrons and positrons are mainly created in the local environment of the Sun. This is why the cosmic proton and  $\alpha$  fluxes are close to their solar values when averaged over the positron horizon scale. This conclusion also holds for the interstellar gas distribution as well.

Obviously it is difficult to say whether or not convection and diffusive reacceleration are relevant phenomena just by looking at the positron flux. Indeed they affect the predictions at an energy range where they are completely smeared out by solar modulation. An interesting way to study this aspect, would be to analyse the radio emission such a low energy bump would produce in the Galaxy. This is one of my next projects.

Concerning positrons, as one can see from figure 6.1, the agreement with experimental data is quite good at all energies within the uncertainty band. The Moskalenko & Strong [33] prediction of the interstellar secondary positron flux as parametrised by Baltz & Edsjö [6] is indicated by the black solid curve, and hardly differs from our reference model (long-dashed curve and *Med* propagation) above a few GeV. The HEAT data points are in good statistical agreement with this *Med* model. This confirms the idea that cosmic ray positrons are mainly secondary. At least up to  $\sim 10$  GeV.

For electrons, the discrepancy is huge because the main population of cosmic electrons is the primary one.

## 6.2 Primaries

The first two paragraphs of this section are mainly inspired by reference [12]. The last paragraph about dark matter is an update of references [14] and [10] with the full expression of the energy losses and not only the Thomson regime. For the annihilation spectra of reference [14], a newer version of the Pythia code has been used (no major difference).

### 6.2.1 Astrophysical sources

As detailed in chapter 4, supernova remnants are not expected to produce positrons as neither the stars which gave birth to the supernovæ, nor the interstellar medium, do contain positrons, they cannot accelerate them. It has been recently suggested [1, 8, 32] that protons

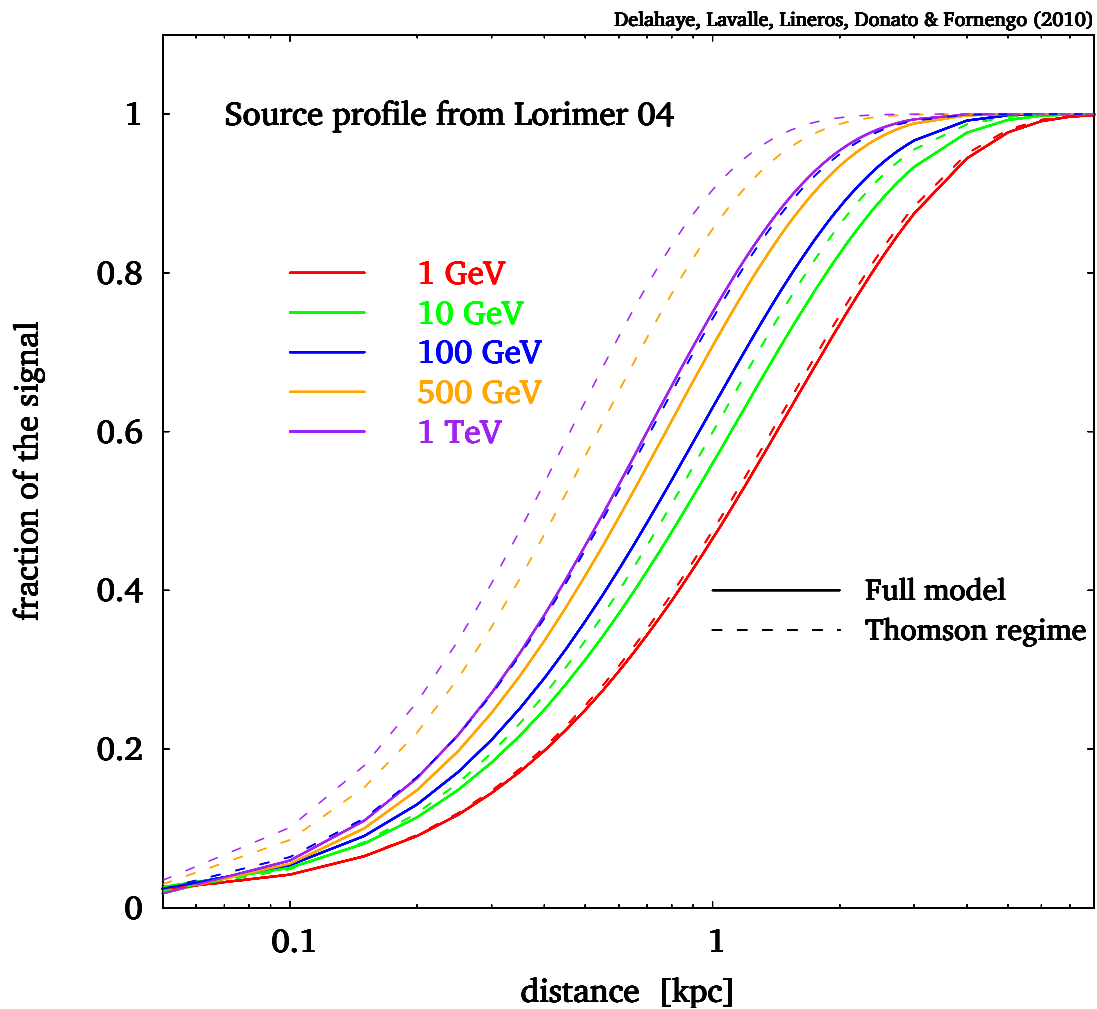


Figure 6.8: Fraction of the signal reaching the Earth as a function of the integrated radius, for different energies, using full relativistic energy losses. The Thomson approximation result is reported in dashed line. This plot actually corresponds to primary electrons coming from a source distribution of L04 ([28]), but the equivalent plot for secondaries is extremely similar (differences are at the percent level).

accelerated by the supernova remnant could produce secondary positrons directly inside the remnant during the acceleration process. I will not consider this mechanism here.

On the other hand pulsars produce electrons and positrons. Concerning electrons, supernova remnants and pulsars are rather similar: they have the same spatial distribution and the same injection spectrum:

$$Q(E) = Q_0 \epsilon^{-\sigma} \exp \left\{ -\frac{E}{E_c} \right\} .$$

except that the three parameters  $Q_0$ ,  $\sigma$ , and  $E_c$  are probably different for each kind of sources.

So I will here present some results valid both for supernova remnants and pulsars. I will

consider separately the distant sources and the local ones (less than 2 kpc away). This will be justified in the next paragraph.

### 6.2.1.1 Smooth distribution of sources

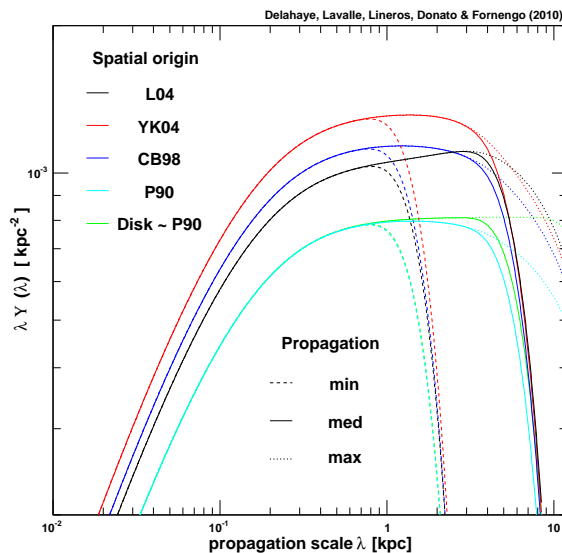


Figure 6.9: Various halo functions defined in section 4.1.3 and that size the transport probability as a function of the propagation scale  $\lambda$ , which decreases with energy.

In order to understand the deviations induced in the electron flux prediction when using these different distributions, it is convenient in term of the rescaled halo function  $\tilde{\Upsilon} = \rho_0 \tilde{I}$ , where  $\tilde{I}$ , defined in equation (5.30), sizes the probability for an electron to reach the Earth given its propagation scale  $\lambda$  and  $\rho_0$  is the normalisation of the spatial distribution of source (see equation 4.13). The electron flux is merely the energy integral of this probability times the source spectrum, so that the shape of this probability function gives a preliminary taste of the final result. More important, it allows to connect the spatial origin of the signal with energy, through the propagation scale  $\lambda$ .

As one can see from Fig. 4.2, the spatial distribution listed above are plotted as a function of the galactocentric radius  $r$ , and in the galactic plane  $z = 0$ . We see that except in the solar neighbourhood, where relative amplitudes can vary by a factor of  $\sim 2$  at maximum, they are quite different in the direction of the Galactic centre as well as towards the anti-centre. Nevertheless, these differences are significantly smoothed when calculating  $\tilde{\Upsilon}(\lambda)$ , because of the spatial average — see equation (5.30). This is shown in Fig. 6.9, where  $\lambda \times \tilde{\Upsilon}(\lambda)$  is plotted as a function of  $\lambda$  for the different spatial distributions and for the *min*, *Med*, and *MAX* propagation set-ups. We see that the probability is maximal and constant —  $\lambda \tilde{\Upsilon}$  grows linearly with  $\lambda$  — for short propagation scales up to  $\lambda \sim h = 0.1$  kpc. Then, the probability decreases linearly with  $\lambda$  —  $\lambda \tilde{\Upsilon}$  exhibits a plateau — before shrinking exponentially when  $\lambda \sim L$ , which naturally

occurs farther and farther when going from *min* to *MAX*. Notice that each spatial distribution model is characterised by a very similar curve that mostly differs in terms of amplitude. This can be understood in the following manner: when  $\lambda < h$ , the source can be considered as homogeneous in 3D space, then  $\tilde{\Upsilon} \propto \int dr r^2 \lambda^{-3} \exp\{-r^2/\lambda^2\} = \text{cst}$ ; when  $h < \lambda < L$ , since the source distributions do not exhibit strong radial variations at the kpc scale, they can be considered as thin disks, and one recovers the solution  $\tilde{\Upsilon} \propto \lambda^{-1}$  which translates the fact that the number of sources increases as  $\lambda^2$  whereas the diffusion volume goes as  $\lambda^3$ ; for  $\lambda > L$ , electrons escape the diffusion zone.

One could perform the exercise consisting in checking the cumulative fraction of the interstellar signal received at the Earth as a function of the radial integration distance, as done for the secondaries (see Fig. 6.8). The result would not be much different except for some very small variations from one source distribution to another.

Another important information that we can get from Fig. 6.8 is that the cumulative signal fraction is  $\gtrsim 95\%$  (80%) for  $r \gtrsim 2$  kpc and  $E \gtrsim 100$  (10) GeV. This will help us to define how to include local sources in our predictions, as we will discuss later in the next paragraph. Indeed, we know at present that if we replace the smooth spatial distribution within 2 kpc with discrete sources, the latter will affect the whole available energy range quite significantly: if powerful enough, local sources will dominate above a few tens of GeV, otherwise, flux predictions will be significantly depleted compared with a smooth-only description of sources, for a given normalisation pattern.

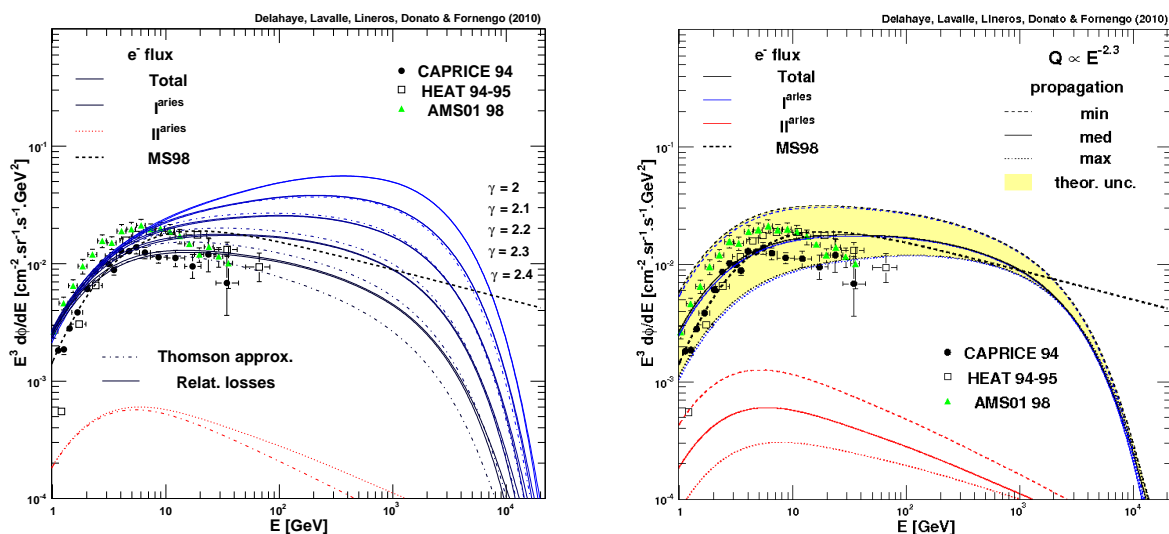


Figure 6.10: primary electron flux from a smooth distribution of supernova remnants. *Left*: fluxes associated with injection indices  $\sigma$  from 2.0 to 2.4. *Right*: propagation effect for  $\sigma = 2.3$ . A renormalisation factor of 5 has been applied to  $fE_*\Gamma_*$  in both panels and a cut-off energy of 3 TeV has been considered.

Let us now have a look at the uncertainties due to the injection spectrum. I will consider here the spatial distribution from Lorimer [28] (see section 4.1.3) as a reference. The freedom

comes here from three parameters: the amplitude  $Q_0$ , the spectral index  $\sigma$  and the energy cut-off  $E_c$ . They directly translate in the amplitude, the spectral index and shape of the received flux at the Earth. This is far too much freedom to be predictive. However, because the smooth distribution dominates only at low energy, the value of the cut-off is not relevant. I will here keep it at 3 TeV. So we need to constrain the injection normalisation necessary for a model to fit, at least roughly, the data and the spectral index. As a reference normalisation, I will take a supernova explosion rate  $\Gamma_\star$  of 4/century, a supernova remnant total energy of  $E_\star = 10^{51}$  erg, of which a fraction of  $f = 2 \times 10^{-4}$  is carried by electrons, giving therefore  $fE_\star\Gamma_\star = 8 \times 10^{47}$  erg/century (see equation (4.7)).

Such a study cannot be performed on pulsars as they are not expected to dominate the signal neither for electrons nor for positrons, at least in the energy range where data is available. We are hence left free to chose the three source parameters as we wish.

In figure 6.10, various flux calculations are plotted, for which a solar modulation correction with a Fisk potential of 600 MV has been applied. In the left panel, one can see the effect of varying the injected spectral index from 2 to 2.4 for the *Med* propagation set-up. In this plot, I had to renormalised  $fE_\star\Gamma_\star$  by a factor of 5 for all indices, so that we see that reasonable fits to the data can be obtained within the expected normalisation range discussed in section 4.1.1.2. This means that the expected energy budget available for electrons is in rough agreement with what is needed to explain the current observations. From the same plot, we could also conclude that the injection spectral index should be slightly softer than 2. Nevertheless, this also depends on the logarithmic slope  $\delta$  of the diffusion coefficient — note that complementary constraints on  $\sigma + \delta$  could also be derived from high energy proton data, under the assumption that the proton index is the same as the electron index after their acceleration at sources and that proton propagation is simply described by diffusion (*id est* no reacceleration nor convection). This is illustrated in the right panel of figure 6.10, where is shown the effect of the theoretical uncertainties on the propagation parameters, using the same spectrum normalisation and the same spectral index for all models. We see that the *min* model gives the largest amplitude because of its smaller value of  $K_0$  and the softer observed index due to its larger diffusion slope  $\delta$  — the analysis is reversed in the *MAX* configuration. For a given normalisation, the amplitude uncertainty is therefore proportional to  $\sqrt{K_0}$ , which gives a factor of  $\sim 7$  from the *min* to the *MAX* configurations. In both panels of figure 6.10, we have also reported the prediction obtained in Moskalenko & Strong [33], as fitted in Baltz & Edsjö [6], where the authors used an injection index of 2.1 below 10 GeV, steepening to 2.4 above. This model, very often quoted as the reference model, does not include relativistic losses, but is shown for comparison.

It should be noted that since the data have a quite limited statistics and range up to  $\sim 40$  GeV only, they are likely insufficient to provide strong constraints on the electron cosmic ray component. Moreover, such a smooth description of the supernova remnant contribution is probably not valid locally, *id est* for energies above a few tens of GeV, where we expect discrete effects to become important. Nevertheless, such a preliminary analysis is still useful to delineate the relevant ranges for the spectral index and for the injected energy. Likewise, it will help to better size the influence of distant sources with respect to local ones.

### 6.2.1.2 Local supernova remnants

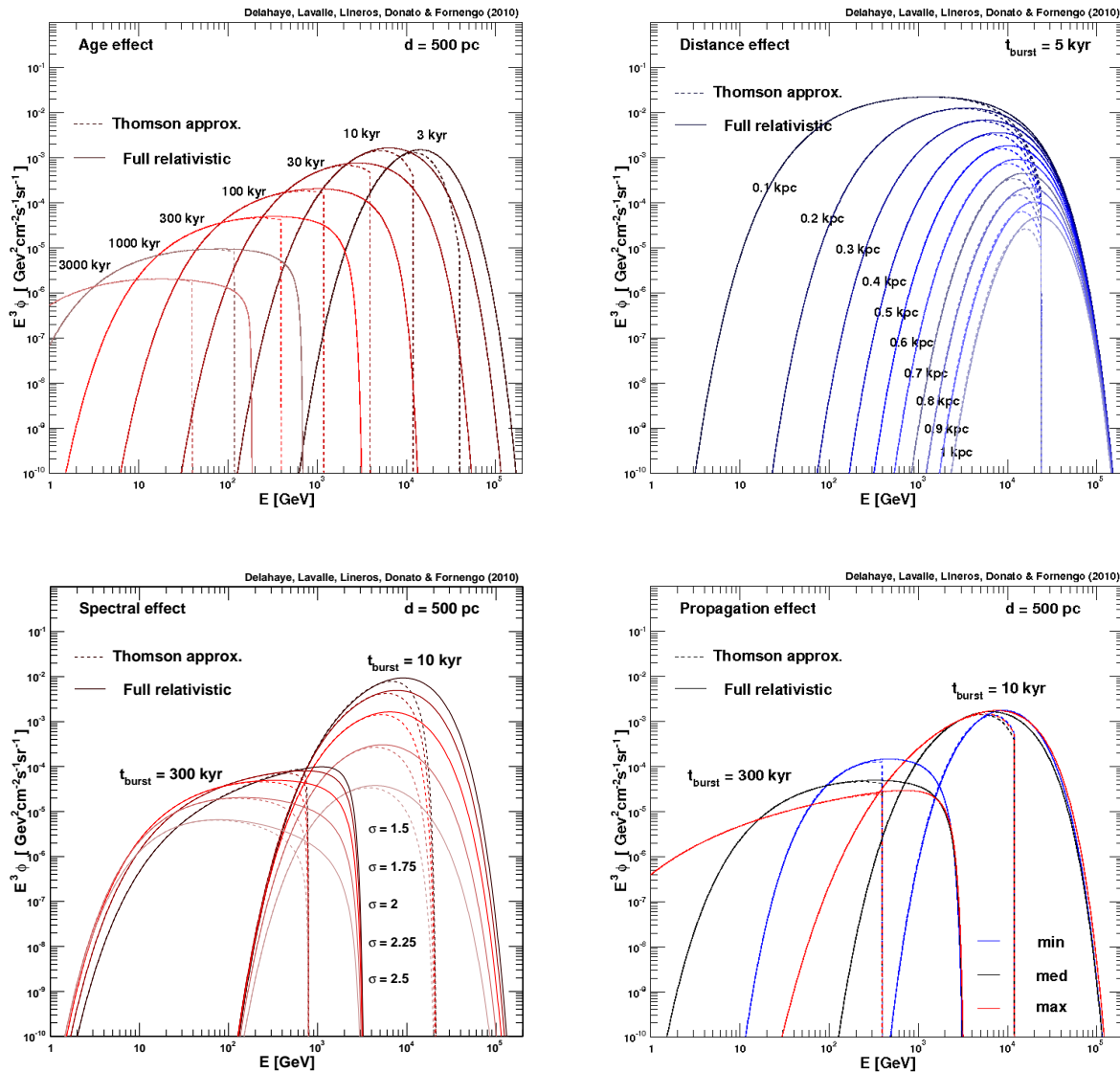


Figure 6.11: Main uncertainties associated with the flux of primary electrons injected from a single bursting source. Top left: varying the age at a fixed distance of 500 pc — notice that taking 1 kpc would have suppressed the 3 kyr source for causality reasons. Top right: varying the distance for a fixed age of 5 kyr. Bottom left: varying the spectral index  $\sigma$  for fixed age of 10 kyr and 300 kyr at a fixed distance of 500 pc. Bottom right: varying propagation parameters, with the *min*, *Med* and *MAX* set-ups.

Before discussing the contribution of local known supernova remnants to the cosmic ray electron flux, it is essential to review the impact of uncertainties in the main parameters that describe the source. They are only a few, but their mixed effects on the flux will be shown to

be important.

Aside from the propagation modelling and related parameters, theoretical errors may originate from uncertainties

- (i) in the spectral shape and normalisation at the source,
- (ii) in the distance estimate and
- (iii) in the age estimate.

The first point was discussed in section 4.1.1.2, and is featured by two main parameters: the spectral index at source  $\sigma$  and the energy released in the form of high energy electrons  $f E_\star$ , both related in the normalisation procedure given equation (4.7) that allows to derive  $\mathcal{Q}_l$ . Points (ii) and (iii) have some impact that can be understood from section 5.3.3. Although the consequences of varying these parameters can be understood from equations only, it is more pedagogical to illustrate them. To do so, let us consider a template event-like source located in the Galactic plane ( $z = 0$ ) at a distance  $d$  from the Earth and bursting a population of electrons a time (age)  $t_\star$  ago:

$$\mathcal{Q}_\star(t_s, E_s, \vec{x}_s) = \delta(t_s - t_\star) \delta(z_s) \delta^2(r_s - d) \mathcal{Q}(E_s), \quad (6.2)$$

where the spectrum  $\mathcal{Q}(E_s)$  is given by equation (4.6). Let us assume here that  $f E_\star = 2 \times 10^{47}$  erg.

In Fig. 6.11, the electron flux for different configurations of the parameters is plotted, the default configuration being defined by:  $Med$ ,  $\sigma = 2$ ,  $E_c = 10$  TeV.

In the top left panel (a), the source age effect; in the top right panel (b), the distance effect; in the bottom left panel (c), the spectral index effect; and finally in the bottom right panel (d), the propagation model effect are displayed.

All these effects can be understood from equations 5.44 to 5.48. For instance the linear dependance of the maximum energy detected is linear with the age of the source (until the cut-off is reached). However the other effects are less straightforward and looking to the figure is easier.

First of all, it clearly appears that the electron flux detected at the Earth from a young far away source is not a power law.

The important comment to make is that it is actually quite difficult to relate the observed spectral index to the source spectral index, because of the complex and degenerate effects coming from all parameters: distance, age, source index, energy cut-off, normalisation and diffusion coefficient. For instance, we see that a large diffusion coefficient (*min* model) can make a source of 300 kyr (c) look like a source of 30 kyr (a) associated with a larger diffusion coefficient and a lower energy cut-off. In any case, a mere overlook at the four panels Fig. 6.11 is striking enough.

This exhaustive analysis of the impact of the main parameters characterising individual sources already points towards the difficulties that we will encounter in the interpretation of the data. Nonetheless, although this part might look depressing at first sight in the perspective of making predictions, it will still be very useful to size the theoretical confidence level of our forthcoming attempts.

Let us see how these uncertainties translate into the expected flux when we consider all the known local supernova remnants and constrain them as described in section 4.1.1.2.

A detailed summary of the observations of the local supernova remnants located within 2 kpc from the Sun can be found in the appendix of reference [12]. Everything is summed up in Table 6.1. As we have seen previously, most of the signal comes from this region so this is the place where one should focus one's efforts.

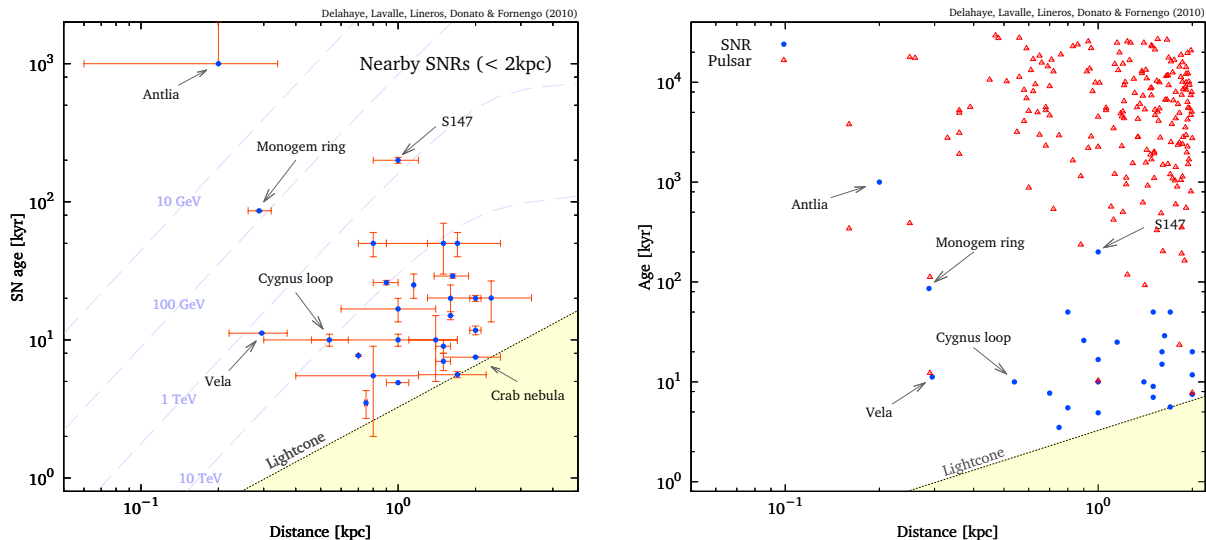


Figure 6.12: Left: Plot of the age versus distance to the Earth for our sample of local supernova remnants (and associated uncertainties, see table 6.1). The dashed lines correspond to limits beneath which a local source cannot contribute significantly to the signal at the corresponding energy (valid only in the *Med* propagation model). Indeed the age sets an upper limit, while the distance sets a lower limit to the energy range. Right: Same plot for our complete sample of local supernova remnants and pulsars.

As discussed earlier, contributions from local sources are expected to be significant above a few tens of GeV. Following the method proposed in Kobayashi *et alii* [25], we wish to take a census of all known sources of primary electrons located within 2 kpc from the Earth in order to compute their associated flux explicitly.

To proceed so, let us first take advantage of the information provided in the supernova remnant catalogue of Green [19], beside which an extensive synthesis of all published properties and associated errors (mostly from radio data) has been made (see appendix of reference [12]). We have found 26 supernova remnants within 2 kpc in this catalogue, to which we have added an extra-object, Antlia [31, 37]. A full description of these sources including information on distance, age, spectral index, radio flux, associated objects are summarised in table 6.1.

As regards the injection spectrum, one can use equation (4.6) and set the spectral index  $\sigma$  from the observed radio index  $\sigma_r$ :  $-\sigma = 2\sigma_r + 1$  and then further constrain the spectrum normalisation with the observed radio flux by means of equation (4.8).

An additional important remark concerns the non-observed local sources of primary electrons that should exist. So far, we have listed 27 supernova remnants and about 200 pulsars. Nevertheless, it is worth recalling, as it will be delved into more details in the next paragraph,

#	SNR G+long+lat	other name	distance [kpc]	radio index $\sigma_r$	Brightness [Jy]	age [kyr]	Pulsar
1	18.95-1.1		$2. \pm \mathbf{0.1}$	0.28	40	$11.75 \pm 0.85$	?
2	65.3+5.7		$0.9 \pm 0.1$	$0.58 \pm 0.07$	52	$26 \pm \mathbf{1}$	$\emptyset$
3	65.7+1.2	DA 495	$1.0 \pm 0.4$	$0.45 \pm 0.1$	5	$16.75 \pm 3.25$	unknown
4	69.0+2.7	CTB 80	$2.0 \pm \mathbf{0.1}$	$0.20 \pm 0.10$	$60 \pm 10$	$20 \pm \mathbf{1}$	J1952+3252
5	74.0-8.5	Cygnus Loop	$0.54^{+0.10}_{-0.08}$	$0.4 \pm 0.06$	$175 \pm 30$	$10 \pm \mathbf{1}$	$\emptyset$
6	78.2+2.1	$\gamma$ Cygni	$1.5 \pm \mathbf{0.1}$	$0.75 \pm 0.03$	$275 \pm 25$	$7 \pm \mathbf{1}$	$\emptyset$
7	82.2+5.3	W63	$2.3 \pm 1.0$	$0.36 \pm 0.08$	$105 \pm 10$	$20.1 \pm 6.6$	$\emptyset$
8	89.0+4.7	HB 21	$1.7 \pm 0.5$	$0.27 \pm 0.07$	$200 \pm 15$	$5.60 \pm 0.28$	$\emptyset$
9	93.7-0.2	CTB 104A or DA 551	$1.5 \pm 0.2$	$0.52 \pm 0.12$	$42 \pm 7$	$50 \pm 20$	$\emptyset$
10	114.3+0.3		0.7	$0.49 \pm 0.25$	$6.4 \pm 1.4$	$7.7 \pm \mathbf{0.1}$	$\emptyset$
11	116.5+1.1		1.6	$0.16 \pm 0.11$	$10.9 \pm 1.2$	$20 \pm 5$	B2334+61 ?
12	116.9+0.2	CTB 1	1.6	$0.33 \pm 0.13$	$6.4 \pm 1.4$	$20 \pm 5$	B2334+61 ?
13	119.5+10.2	CTA 1	$1.4 \pm 0.3$	$0.57 \pm 0.06$	$42.5 \pm 2.5$	$10 \pm 5$	J0010+7309
14	127.1+0.5	R5	$1. \pm 0.1$	$0.43 \pm 0.1$	$12 \pm 1$	$25 \pm 5$	$\emptyset$
15	156.2+5.7		$0.8 \pm 0.5$	$2.0^{+1.1}_{-0.7}$	$4.2 \pm 0.1$	$10 \pm \mathbf{1}$	B0450+55 ?
16	160.9+2.6	HB 9	$0.8 \pm 0.4$	$0.48 \pm 0.03$	$\sim 75$	$5.5 \pm 1.5$	B0458+46
17	180.0-1.7	S147	$1.2 \pm 0.4$	0.75	$74 \pm 12$	$600 \pm \mathbf{10}$	J0538+2817
18	184.6-5.8	Crab nebula or 3C144 or SN1054	$2.0 \pm 0.5$	0.3	1,040	$7.5 \star$	B0521+31
19	189.1+3.0	IC 443	$1.5 \pm \mathbf{0.1}$	$0.36 \pm 0.04$	$160 \pm 5$	30 or 4	$\emptyset$
20	203.0+12.0	Monogem ring	$0.288^{+0.033}_{-0.027}$			$86 \pm \mathbf{1}$	B0656+14
21	205.5+0.5	Monoceros Nebula	$1.63 \pm 0.25$	$0.66 \pm 0.2$	$156.1 \pm 19.9$	$29 \pm \mathbf{1}$	$\emptyset$
22	263.9-3.3	Vela(XYZ)	$0.295 \pm 0.075$	variable	$2,000 \pm 700$	$11.2 \pm \mathbf{0.1}$	B0833-45
23	266.2-1.2	RX J0852.0-4622 or Vela Jr or SN1300	$0.75 \pm \mathbf{0.01}$			$3.5 \pm 0.8 \star?$	J0855-4644 ?
24	276.5+19.0	Antlia	$0.2 \pm 0.14$			$\geq 1,000$	B0950+08
25	315.1+2.7		$1.7 \pm 0.8$	0.7		$\mathbf{50} \pm \mathbf{10}$	J1423-56
26	330.0+15.0	Lupus Loop	$1.2 \pm 0.3$			$50 \pm \mathbf{10}$	B1507-44 ?
27	347.3-0.5	SN393	$1. \pm 0.3$			$4.9 \star$	$\emptyset$

Table 6.1: Characteristics of nearby supernova remnants. Spectral index and Brightness are inferred from measurements made at 1 GHz. Uncertainties in bold are not taken from bibliographic references, but just correspond to a rough uncertainty on the last relevant digit; hence they can be underestimated. An age is flagged with a  $\star$  for a historical remnant; in this case, the age uncertainty is set from the distance uncertainty. Note that, except for the historical supernovæ the ages are the observed ages, which differ from the actual ages by  $d/c$ .

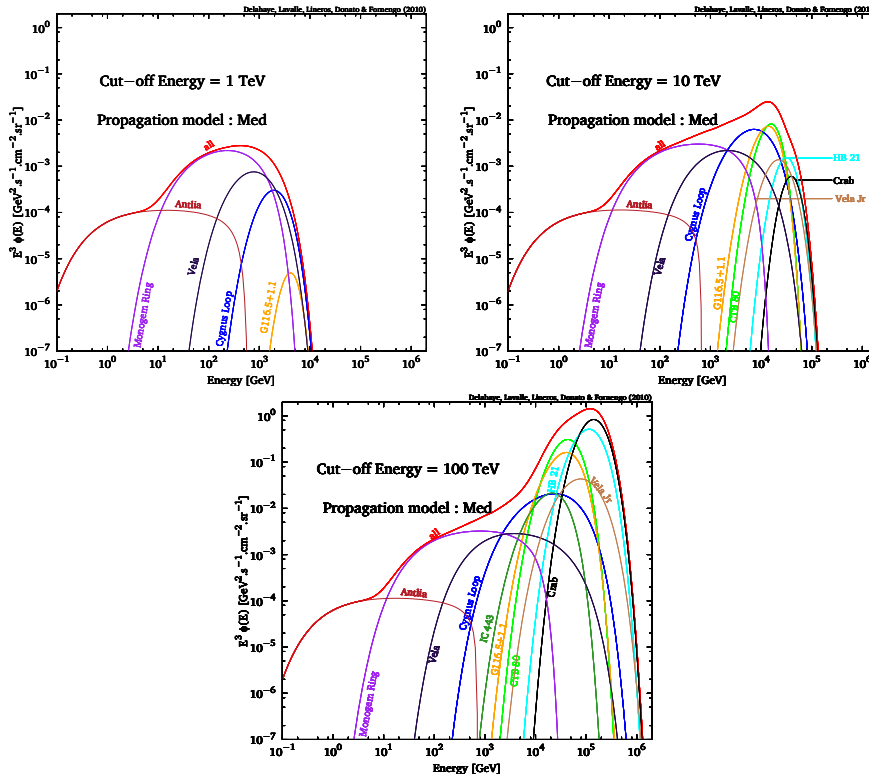


Figure 6.13: Primary electron flux from local supernova remnants in the *Med* propagation model and using radio observation constraints. *Left*: energy cut-off at  $E_c = 1$  TeV. *Right*:  $E_c = 10$  TeV. *Bottom*:  $E_c = 100$  TeV.

	$E_c$	1 TeV	10 TeV	100 TeV
<i>min</i>	$\sigma = 2.0$	5, 20, 22, 24	+ 23	+ 8, 18, 19, 26
	$\sigma = 2.2$	5, 20, 22, 24	+ 8, 18	+ 17, 19
	$\sigma = 2.4$	5, 20, 22, 24	+ 8, 17, 18	+ 19
<i>Med</i>	$\sigma = 2.0$	5, 20, 22, 24, 26	+ 4, 11, 19	+ 8, 18, 23
	$\sigma = 2.2$	5, 11, 20, 22, 24	+ 4, 8, 18, 23	+ 19
	$\sigma = 2.4$	5, 11, 20, 22, 24	+ 4, 18, 19, 23	+ 8, 17
<i>MAX</i>	$\sigma = 2.0$	5, 20, 22, 24, 26	+ 8, 11, 19, 23	+ 4, 18
	$\sigma = 2.2$	5, 20, 22, 24	+ 8, 11, 18, 19	+ 4, 23, 26
	$\sigma = 2.4$	5, 20, 22, 24	+ 8, 11, 18, 19	+ 4, 23, 24

Table 6.2: Ranked id numbers (see table 6.1) of those supernova remnants which contribute more than 10% of the signal for various propagation models, cut-off energies  $\epsilon_c$  and spectral index  $\sigma$ . Index  $\sigma$  is only used for sources that are not constrained by radio data. The dominant sources are Cygnus Loop (5), Monogem Ring (20), Vela (22) and Antlia (24).

that pulsars are rotating neutron stars originating from core collapse supernova explosions. Therefore, each pulsar should be accompanied by a supernova remnant. Such a systematic

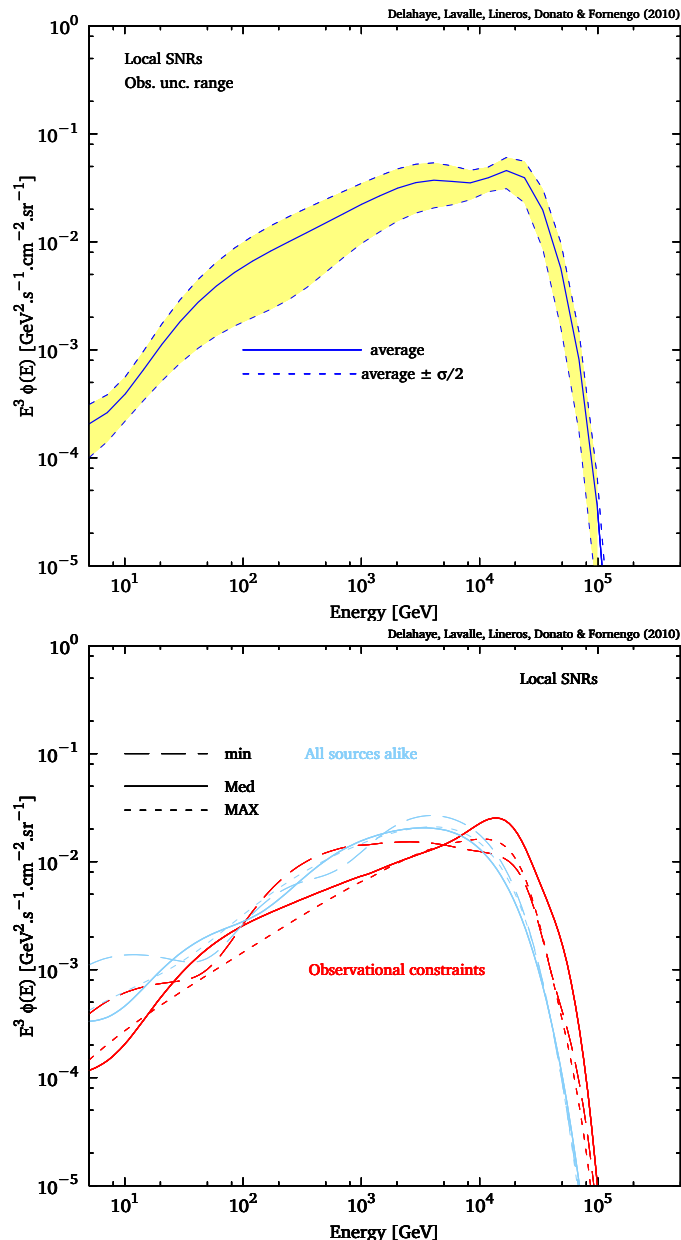


Figure 6.14: *Top*: Electron flux from observed local supernova remnants, with associated uncertainty band (due to observational uncertainties on ages, distances, radio fluxes and spectral indices). *Bottom*: Propagation effects on the electron flux originating from local supernova remnants, using either the observational constraints or the average flux and index from figure 4.1. In both panels, we have assumed a source cut-off energy of 10 TeV.

association is obviously not supported by observations. This is already illustrated in our object list, in which we find only 27 supernova remnants for 200 pulsars. Moreover, among these 27 local supernova remnants, only 10 have a known pulsar counterpart (very often with differences in the distance and age estimates). Yet, this certainly does not mean that the theoretical expecta-

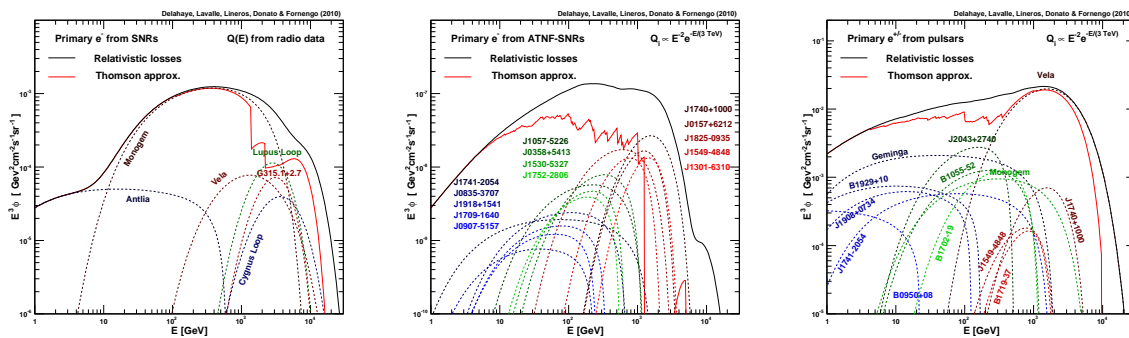


Figure 6.15: Primary electron flux from local sources located within 2 kpc from the Earth. *Left*: from known supernova remnants (radio constraints). *Middle*: from unknown supernova remnants that should accompany unassociated local pulsars (generic spectrum for each, age and distance from the pulsar companion). *Right*: from known pulsars (generic spectrum, observational constraints on age and distance). Here, all generic spectra refer to a spectral index of 2 and an energy cut-off of 3 TeV.

tion is wrong, but instead that the counterparts are probably not bright enough to be observed. Therefore, again for theoretical consistency reasons, we choose here to add a supernova remnant counterpart to each non-associated pulsar, but with a brightness such that it could not be observed with current telescopes. We have adopted  $B(1 \text{ GHz}) \lesssim 1 \text{ Jy}$  as a general criterion for non-observed supernova remnants. Note finally that this local statistics can be tested against predictions of the supernova explosion rate  $\Gamma_\star$ . If we assume at zeroth order that sources are distributed homogeneously inside a flat disk of radius  $R = 20 \text{ kpc}$ , then the local explosion rate within a radius of  $r = 2 \text{ kpc}$  around the observer merely reads  $\Gamma_\star(r/R)^2 = 0.01 \times \Gamma_\star$ , leading to  $\sim 0.01 \text{ SN/century}$  for usual values of  $\Gamma_\star$ . This can be compared to the observed local explosion rate, which we can estimate from the number of sources in our sample divided by the oldest age, *id est*  $\sim 200/30 \text{ Myr} \simeq 0.7 \times 10^{-3}/\text{century}$ . This rough calculation leads to a difference of only a few, which would tend to tell us that using only the observed sources translates into a slight under-estimate of the actual local electron budget. This makes sense, since observations favour the brightest objects. Our samples of local supernova remnants and pulsars are shown in the age–distance plane in figure 6.12.

In figure 6.13, we show the electron flux obtained in the *Med* propagation set-up, using the local supernova remnant properties summarised in table 6.1 and assuming different cut-off energies. The first important comment to make is that the whole flux is far from being described from a mere smoothly power law, since many spectral wave-like features show up. Moreover, because of the interplay between the age and the maximal energy, we see that varying the energy cut-off from 1 to 100 TeV, though the latter value is probably not realistic and too high, leads to considerable effects. Not only do new contributions arise at high energy when the cut-off value increases, but also the hierarchy among other sources is altered. This illustrates an additional source of theoretical uncertainty, beside those we discussed above. Figure 6.14 further illustrates the theoretical and observational uncertainties affecting both the source modelling and the propagation modelling. The upper panel allows to bracket the impact

of the observational uncertainties on the ages, distances, radio fluxes and spectral indices. This plot was made from 1000 Monte Carlo realisations in which we drew each parameter according to a flat distribution within the observational errors. The lower panel exhibits (i) the impact of varying the propagation parameters on the overall local supernova remnant contribution and (ii) the difference arising from different injection spectrum prescription. For the latter point, we actually compared the flux obtained with generic spectral properties, namely a spectral index of 2 and a fixed normalisation of  $\mathcal{Q}_0 = 3.9 \times 10^{49} \text{GeV}^{-1}$  (see end of section 4.1.1.2), with the observationally constrained predictions. Again, we see that the global spectral shape is much more complex than a mere power law, and that the overall flux can vary within a factor of 2-5 depending on the energy.

We plot the results obtained with a template calculation for all local electron primaries in figure 6.15, where we have used the *Med* propagation set-up together with the M1 interstellar radiation field model. The three panels from left to right show the contributions of local known supernova remnants, from non-observed supernova remnants associated with observed pulsars, and from observed pulsars, respectively. For the non-observed supernova remnants, we have taken the distances and ages of the associated pulsars, and we have assumed an injection spectrum with an index of 2 and a non-observable radio flux of  $B(1 \text{GHz}) = 1 \text{Jy}$ . While the contribution from the non-observed supernova remnants is shown negligible with respect to the two others (notice that the scales are different for each plot), it is interesting to note that our local pulsar modelling leads to a larger primary electron flux than local supernova remnants. For pulsars, we actually assumed that 10% of the spin-down energy was converted into electron-positron pairs to set the individual normalisations (see section 4.1.2). Although the injection mechanism is subject to large theoretical uncertainties, it is still rather surprising to find that even when accounting for observational constraints for pulsars, their local population can contribute as many primary electrons as the local known supernova remnants. We stress, however, that these calculations are subject to very large theoretical uncertainties, so no strong conclusions should be drawn: by no means should they be considered as predictions, only indications. The main conclusion at this stage is that nearby sources dominate the flux above few tens of GeV, the spectral imprints of which are very difficult to predict, due to large theoretical uncertainties in their modelling.

### 6.2.1.3 Local pulsars

Selecting the local pulsars from the ATNF catalogue requires imposing few constraints. First, one should apply a radial cut-off of 2 kpc, like for the supernova remnant treatment. Moreover, considering energies above the GeV scale implies an upper limit of the pulsar age  $\lesssim 30 \text{Myr}$ , which shrinks down to 1 Myr above 100 GeV (see figure 6.11). Consequently, we will restrict our sample by requiring ages  $\lesssim 30 \text{Myr}$ . The final sample contains a bit more than 200 objects located at less than 2 kpc from the Earth, which is quite large compared to the number observed supernova remnants, *id est* 27, discussed in section 6.2.1.2.

The positron flux derived from this pulsar selection is actually the same as the pulsar contribution to the electron flux discussed in section 6.2.1.2, because of the pair production mechanism. This local contribution is shown in the right panel of figure 6.15.

J2000	other name	distance [kpc]	spin-down age [kyr]	spin-down energy [ $10^{49}$ erg]	Rank @ 5/100/1000 GeV
J0633+1746	Geminga	0.16	342	1.25	1/2/4
J1932+1059	B1929+10	0.36	3,100	11.9	2/ $\emptyset$ / $\emptyset$
J1908+0734		0.58	4,080	17.9	3/ $\emptyset$ / $\emptyset$
J1741-2054		0.25	387	0.47	4/5/ $\emptyset$
J0953+0755	B0950+08	0.26	17,500	54.2	5/ $\emptyset$ / $\emptyset$
J2043+2740		1.13	1,200	25.9	$\emptyset$ /1/ $\emptyset$
J1057-5226	B1055-52	0.72	535	2.8	$\emptyset$ /3/ $\emptyset$
J0659+1414	B0656+14	0.29	111	0.18	$\emptyset$ /4/2
J0835-4510	B0833-45	0.29	11.3	0.99	$\emptyset$ / $\emptyset$ /1
J1740+1000		1.24	114	1.1	$\emptyset$ / $\emptyset$ /3
J0742-2822	B0740-28	1.89	157	1.23	$\emptyset$ / $\emptyset$ /5
J1549-4848		1.54	324	0.8	$\emptyset$ / $\emptyset$ /6

Table 6.3: Main positron sources among the ATNF nearby pulsars. The pulsars are ranked from the largest contribution to the flux in different energy bins, assuming a spectral index of  $\gamma = 2$  and a cut-off energy of 1 TeV. All other parameters are derived from the ATNF catalogue. J0659+1414 is the counterpart of the supernova remnant Monogem and J0835-4510 the one of Vela.

As shortly mentioned in the previous paragraph, one should note that using the magnetic radiation approximation to constrain the energy released in the form of electron–positron pairs makes pulsars important sources of local high energy electrons and positrons, as intense as the observed local supernova remnants. A pair conversion efficiency of  $f = 0.1$  has been used in this calculation, which might be optimistic, but still, decreasing this efficiency down to a few percent would still lead to a quite significant contribution to the local electron and positron budget. It is noteworthy that only the local positron flux is dominated by a few objects only among our  $\sim 200$  selected objects. The main sources and their properties are listed in table 6.3. Although pulsar modelling is subject to many and large theoretical uncertainties, and despite the simplistic model we have employed to set the individual normalisations, our results suggest that supernova remnants might not be the only prominent sources of electron cosmic rays.

### 6.2.2 Dark matter

In this section I will very often speak about positrons. The only reason for this is that dark matter signals are expected to be more visible in positron fluxes because the background is lower. However, whatever the dark matter candidate we consider, it always produces as many positrons as electrons and always with the same spectrum<sup>a</sup>.

We are now equipped with a rapid enough method to scan the  $\sim 1600$  different cosmic ray propagation models that have been found compatible [29] with the boron to carbon measurements. The most interesting ones for anti–protons and boron to carbon ratios are recalled in Table 5.1.

---

<sup>a</sup>This is not completely true when polarisation is involved like in section 4.2, however the effect is quite small (a few %) and will be neglected.

Do these configurations play the same role for positrons? Can we single out a few propagation models which could be used later on to derive the minimal or the maximal positron flux without performing an entire scan over the parameter space? These questions have not been addressed in the pioneering investigation of Hooper & Silk [22] where the cosmic ray propagation parameters have indeed been varied but independently of each other and without any connection to the boron to carbon ratio.

Let us first study the Galactic dark matter halo and the possible impact of substructures or clumps.

### 6.2.2.1 The Galactic halo

In figure 6.16, we have set the positron detection energy  $E$  at a fixed value of 10 GeV and varied the injection energy  $E_S$  from 10 GeV up to 1 TeV. The three panels correspond to the dark matter halo profiles of table 4.3. For each value of the injection energy  $E_S$ , we have performed a complete scan over the 1600 different configurations mentioned above and have found the maximal and minimal values of the halo integral  $\tilde{I}$  with the corresponding sets of propagation parameters. In each panel, the resulting uncertainty band corresponds to the yellow region extending between the two solid red lines. The lighter yellow domain is demarcated by the long-dashed black curves labelled *min* and *MAX* and has a smaller spread. The *Med* configuration is featured by the long-dashed blue line. In the bottom right panel of figure 6.16, the Moore profile has been chosen with four different values of the detection energy  $E$ . The corresponding uncertainty bands are coded with different colours and encompass each other as  $E$  increases.

As  $E_S$  gets close to  $E$ , we observe that each uncertainty domain shrinks. In that regime, the diffusion length  $\lambda$  is very small and the positron horizon probes only the solar neighbourhood where the dark matter density is given by  $\rho_\odot$ . Hence the flagellate structure of figure 6.16 and a halo integral  $\tilde{I}$  of order unity whatever the propagation model. As is clear in figure 6.17, a small half-thickness  $L$  of the diffusion slab combined with a large diffusion length  $\lambda$  implies a small positron halo integral  $\tilde{I}$ . The lower boundaries of the various uncertainty bands in figure 6.16 correspond therefore to parameter sets with  $L = 1$  kpc. Large values of  $\lambda$  are obtained when both the normalisation  $K_0$  and the spectral index  $\delta$  are large. However both conditions cannot be satisfied together once the boron to carbon constraints are applied. For a large normalisation  $K_0$ , only small values of  $\delta$  are allowed and vice versa. For small values of the detection energy  $E$ , the spectral index  $\delta$  has little influence on  $\lambda$  and the configuration which minimises the halo integral  $\tilde{I}$  corresponds to the large normalisation  $K_0 = 5.95 \times 10^{-3} \text{ kpc}^2 \text{ Myr}^{-1}$  and the rather small  $\delta = 0.55$ . For large values of  $E$ , the spectral index  $\delta$  becomes more important than  $K_0$  in the control of  $\lambda$ . That is why in the bottom right panel of figure 6.16, the lower bound of the red uncertainty domain corresponds now to the small normalisation  $K_0 = 1.65 \times 10^{-3} \text{ kpc}^2 \text{ Myr}^{-1}$  and the large spectral index  $\delta = 0.85$ . Notice that this set of parameters is very close to the *min* configuration. For intermediate values of  $E$ , the situation becomes more complex. We find in particular that for  $E = 30$  GeV, the halo integral  $\tilde{I}$  is minimal for the former set of parameters as long as  $E_S \leq 200$  GeV and for the later set as soon as  $E_S \geq 230$  GeV. In between, a third propagation model comes into play with the intermediate values  $K_0 = 2.55 \times 10^{-3} \text{ kpc}^2 \text{ Myr}^{-1}$  and  $\delta = 0.75$ . It is not possible therefore to single out one particular combination of  $K_0$  and  $\delta$  which would lead to the minimal value of the halo integral and of the positron dark matter

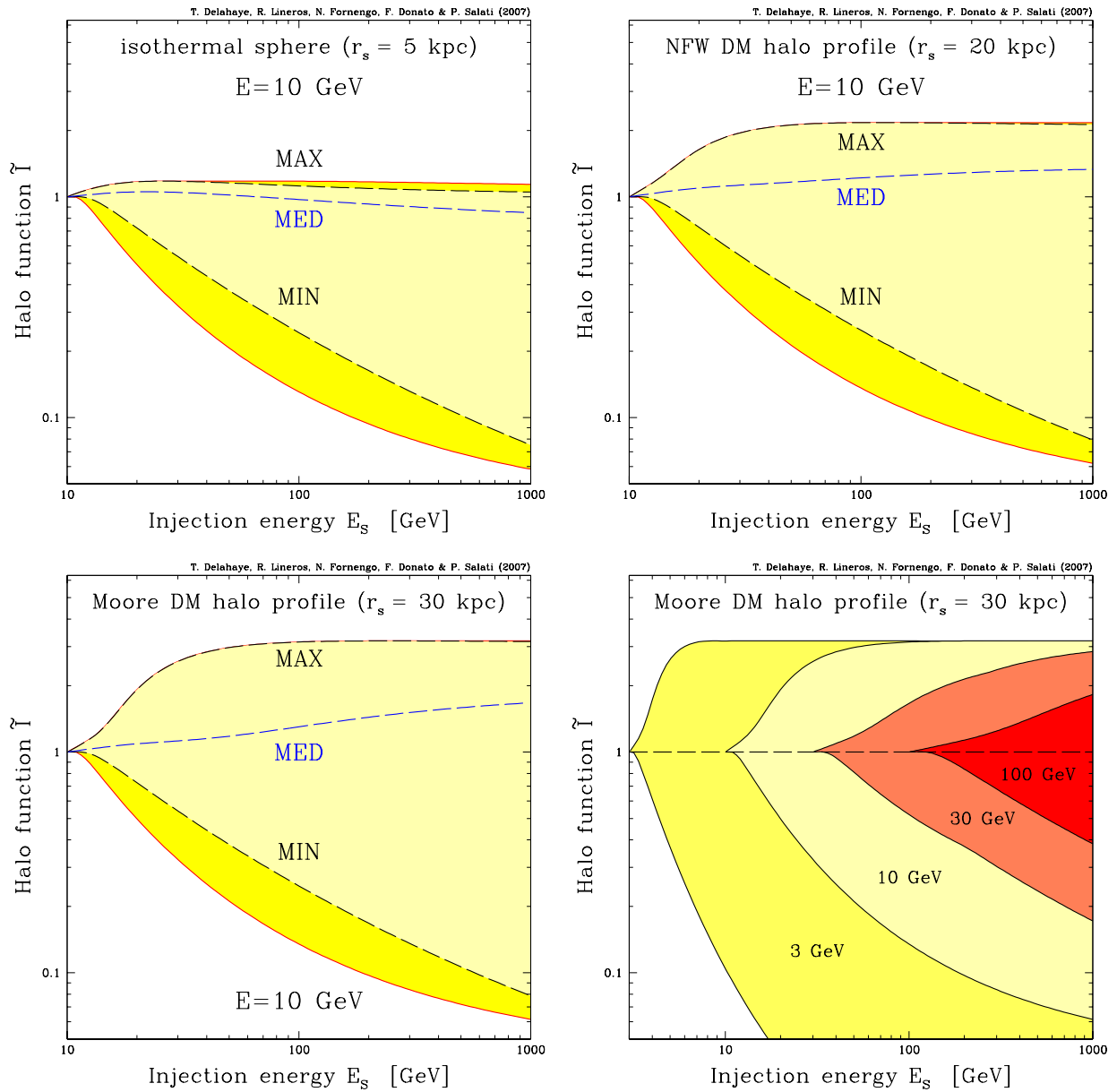


Figure 6.16: In each panel, the halo integral  $\tilde{I}$  is plotted as a function of the positron injection energy  $E_s$  whereas the energy  $E$  at the Earth is fixed at 10 GeV. Various galactic DM halo profiles (see section 4.3.1.4) are featured. The curves labelled as *Med* correspond to the choice of cosmic ray propagation parameters which best-fit the B/C ratio [29]. The *MAX* and *min* configurations correspond to the cases which were identified to produce the maximal and minimal dark matter antiproton fluxes [15], while the entire coloured band corresponds to the complete set of propagation models compatible with the B/C analysis [29]. *Bottom right*: Same plot as before where the Moore dark matter profile has been selected. Four values of the positron detection energy  $E$  have been assumed. The flagella structure of this figure results from the widening of the uncertainty band as the detection energy  $E$  is decreased.

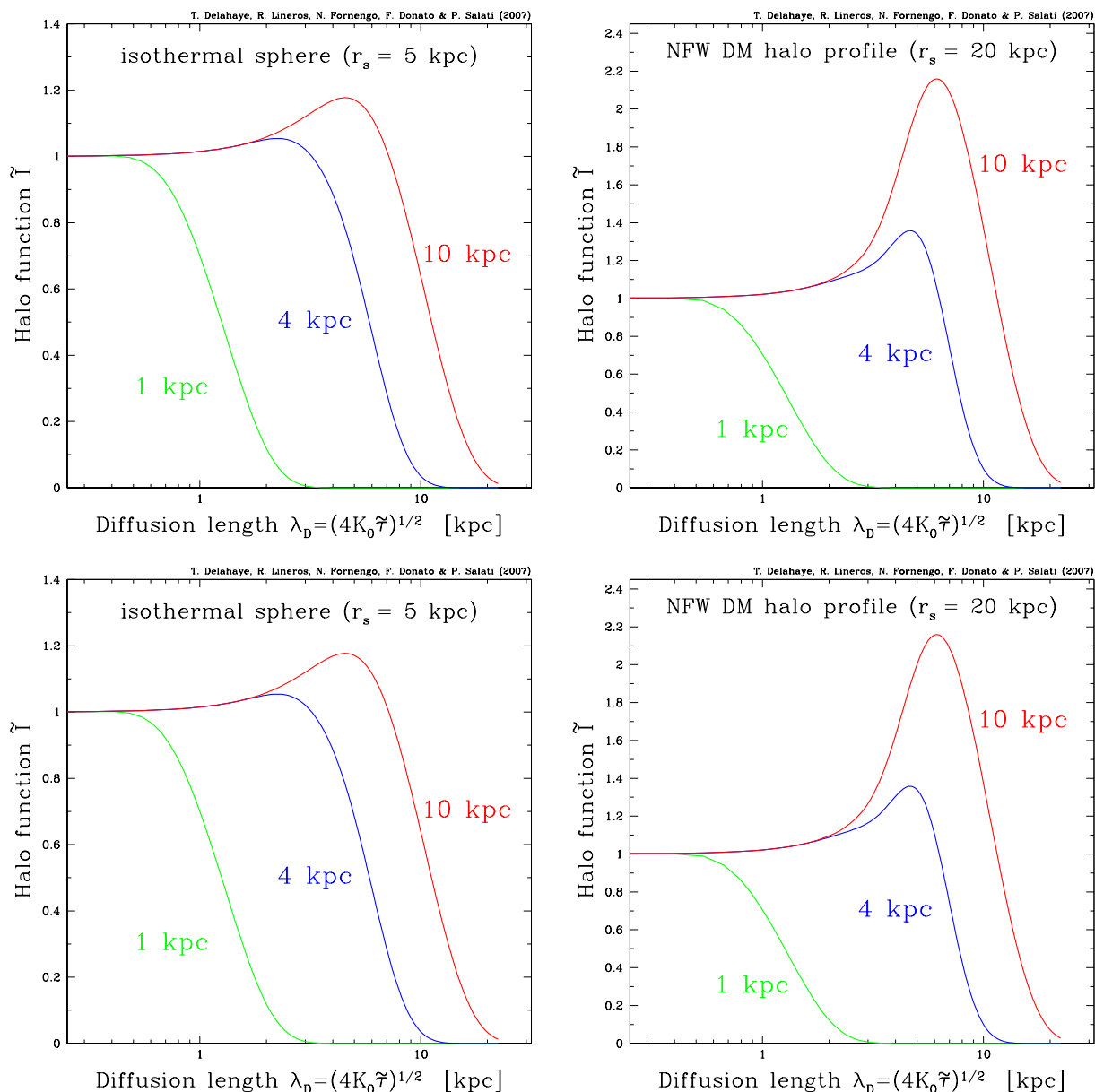


Figure 6.17: *Upper panels:* The halo convolution  $\tilde{\Gamma}$  is plotted as a function of the diffusion length  $\lambda$  for various values of the slab half-thickness  $L$ . The left panel features the case of an isothermal dark matter distribution whereas a NFW profile has been assumed in the right panel. When  $L$  is large enough for the positron horizon to reach the galactic centre and its denser dark matter distribution, a maximum appears in the curves for  $\lambda \sim r_\odot$ . *Lower panels:* same as above but for decaying dark matter.

signal. The *min* configuration which appeared in the antiproton analysis has no equivalent for positrons.

The same conclusion holds, even more strongly, in the case of the upper boundaries of the uncertainty bands. Whatever the dark matter halo profile, the panels of figure 6.17 feature a

peak in the halo function  $\tilde{I}$  for large values of  $L$  and for a specific diffusion length  $\lambda^{\max} \sim 7$  kpc. At fixed  $E$  and  $E_S$ , we anticipate that the maximal value for  $\tilde{I}$  will be reached for  $L = 15$  kpc and for a diffusion length  $\lambda$  as close as possible to the peak value  $\lambda^{\max}$ . Two regimes can be considered at this stage.

(i) To commence, the diffusion length  $\lambda$  is below the critical value  $\lambda^{\max}$  whenever the difference  $\tilde{t} - \tilde{t}_S$  (see equation 5.28), is small enough. This condition is met in general when  $E$  and  $E_S$  are close to each other or when  $E$  is large. The largest possible value of  $\lambda$  maximises  $\tilde{I}$  and once again, we find two propagation models. For small  $E$ , the large normalisation  $K_0 = 7.65 \times 10^{-2}$  kpc<sup>2</sup> Myr<sup>-1</sup> is preferred with  $\delta = 0.46$ . We recognise the *MAX* configuration and understand why the long-dashed black curves labelled *MAX* in the panels of figure 6.16 are superimposed on the solid red upper boundaries. For large  $E$ , the spectral index  $\delta$  dominates the diffusion length  $\lambda$  and takes over the normalisation  $K_0$  of the diffusion coefficient. The best model which maximises  $\tilde{I}$  becomes then  $\delta = 0.75$  and  $K_0 = 2.175 \times 10^{-2}$  kpc<sup>2</sup> Myr<sup>-1</sup>.

(ii) When the difference  $\tilde{t} - \tilde{t}_S$  is large enough, the diffusion length  $\lambda$  may reach the critical value  $\lambda^{\max}$  for at least one propagation model which therefore maximises the halo integral. As  $E$  and  $E_S$  are varied, the peak value of  $\tilde{I}$  is always reached when a scan through the space of parameters is performed. This peak value corresponds to the maximum of the halo integral, hence a horizontal upper boundary for each of the uncertainty bands of figure 6.16. The set that leads to  $\lambda = \lambda^{\max}$  is different for each combination of  $E$  and  $E_S$  and is not unique. In the case of the NFW dark matter profile of figure 6.16, the halo integral  $\tilde{I}$  is maximised by more than 30 models above  $E_S = 120$  GeV.

The complexity of this analysis confirms that the propagation configurations selected by boron to carbon do not play the same role for primary antiprotons and positrons. The two species experience the propagation phenomena, and in particular energy losses, with different intensities. As pointed out in Ref. [30], the average distance travelled by a positron is sensibly lower than the one experienced by an antiproton produced in the halo.

Now that we have discussed in detail the solution of the propagation equation, and have identified and quantified the astrophysical uncertainties on the halo integral  $\tilde{I}$ , we are ready to apply our analysis to the theoretical predictions for the positron signal at the Earth position. The positron flux is obtained through Eq. (5.31). As stated in chapter 4, I will not adopt specific dark matter candidates, but will instead discuss the signals arising from a dark matter particle which annihilates into a pure final state. I consider four different specific dark matter annihilation channels: direct  $e^+e^-$  production as well as  $W^+W^-$ ,  $b\bar{b}$  and  $\tau^+\tau^-$ . The dark matter annihilation cross section is fixed at the value  $3 \times 10^{-26}$  cm<sup>3</sup> s<sup>-1</sup> and we will consider the cases of a dark matter species with mass of 100 GeV and of 500 GeV.

In Fig. 6.18, the propagated positron flux  $\Phi_{e^+}$  – multiplied by the square of the positron energy  $E$  for convenience – is featured as a function of  $E$  for a 100 GeV dark matter particle and a NFW density profile.

The coloured [yellow] area corresponds to the total uncertainty band arising from positron propagation. In all panels, it enlarges at low positron energy. This may be understood as a consequence of the behaviour of the halo integral  $\tilde{I}$  which was analysed before. Positrons produced at energy  $E_S$  and detected at energy  $E$  originate on average from a sphere whose radius is  $\lambda$ . That positron sphere enlarges as  $E$  decreases and so does the uncertainty band. As positrons originate further from the Earth, the details of galactic propagation become more

Model	$\delta$	$K_0$ [kpc <sup>2</sup> /Myr]	$L$ [kpc]
MED	0.70	0.0112	4
M1	0.46	0.0765	15
M2	0.55	0.00595	1

Table 6.4: Typical combinations of cosmic ray propagation parameters that are compatible with the boron to carbon analysis [29]. The model *Med* is the same as usual. Models M1 and M2 respectively maximise and minimise the positron flux over some energy range – roughly above 10 GeV – the precise extent of which depends on the mass of the dark matter particle, on the annihilation channel and also on the dark matter profile. Note that M1 is the same as *MAX* but this is coincidental.

important in the determination of the positron flux. On the contrary, high-energy positrons are produced locally and the halo integral  $\tilde{I}$  becomes unity whatever the astrophysical parameters. Notice also that the uncertainty band can be sizeable and depends significantly on the positron spectrum at production. In the case of the  $e^+e^-$  line of the upper left panel, the positron flux  $\Phi_{e^+}$  exhibits a strongly increasing uncertainty as  $E$  is decreased from  $m_\chi$  down to 1 GeV. That uncertainty is one order of magnitude at  $E = 10$  GeV, and becomes larger than 2 orders of magnitude below 1 GeV. Once again, the positron sphere argument may be invoked. At fixed detected energy  $E$ , the radius  $\lambda$  increases with the injected energy  $E_S$ . We therefore anticipate a wider uncertainty band as the source spectrum gets harder. This trend is clearly present in the panels of Fig. 6.18. Actually direct production is affected by the largest uncertainty, followed by the  $\tau^+\tau^-$  and  $W^+W^-$  channels where a positron is produced either directly from the  $W^+$  or from the leptonic decays. In the  $b\bar{b}$  case, which is here representative of all quark channels, a softer spectrum is produced since positrons arise mostly from the decays of charged pions originating from the hadronisation of quarks. Most of the positrons have already a low energy  $E_S$  at injection and since they are detected at an energy  $E \sim E_S$ , they tend to have been produced not too far from the Earth, hence a lesser dependence to the propagation uncertainties. The astrophysical configuration M2 – see Tab. 6.4 – provides the minimal positron flux. It corresponds to the lower boundaries of the yellow uncertainty bands of Fig. 6.18. The M1 configuration maximises the flux at high energies. For direct production and to a lesser extent for the  $\tau^+\tau^-$  channel, that configuration does not reproduce the upper envelope of the uncertainty band in the low energy tail of the flux. The response of  $\Phi_{e^+}$  to the propagation parameters depends on the detected energy  $E$  in such a way that the maximal value cannot be reached for a single astrophysical configuration. Finally, taking as a reference the median flux, the uncertainty bands extend more towards small values of the flux. In all channels, the maximal flux is typically a factor of  $\sim 1.5$ –2 times larger than the median prediction. The minimal flux features larger deviations with a factor of 5 for the  $b\bar{b}$  channel at  $E = 1$  GeV, of 10 for  $W^+W^-$  and of 30 for  $\tau^+\tau^-$ .

Fig. 6.19 is similar to Fig. 6.18 but with a heavier dark matter species of 500 GeV instead of 100 GeV. Since the mass  $m_\chi$  is larger, so is on average the injected energy  $E_S$ . Notice that at fixed positron energy  $E$  at the Earth, the radius  $\lambda$  of the positron sphere increases with  $E_S$ . We therefore anticipate that the propagated fluxes are affected by larger uncertainties for heavy dark matter particles. Again, the maximal flux does not exceed twice the median flux, while

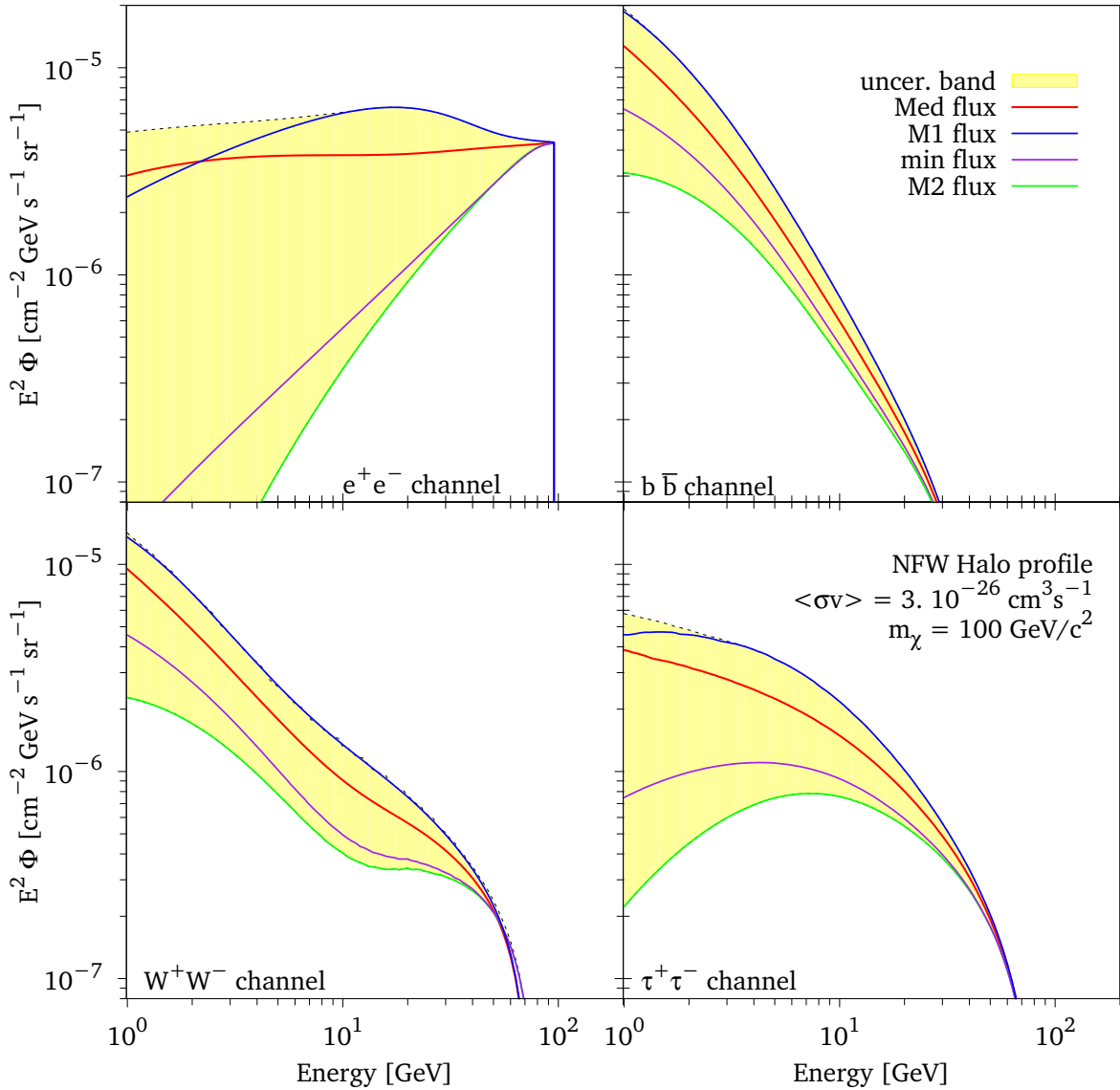


Figure 6.18: Positron flux  $E^2\Phi_{e^+}$  versus the positron energy  $E$ , for a dark matter particle with a mass of 100 GeV and for a NFW profile. The four panels refer to different annihilation final states : direct  $e^+e^-$  production (top left),  $b\bar{b}$  (top right),  $W^+W^-$  (bottom left) and  $\tau^+\tau^-$  (bottom right). In each panel, the thick solid [red] curve refers to the best-fit choice (*Med*) of the astrophysical parameters. The upper [blue] and lower [green] thin solid lines correspond respectively to the astrophysical configurations which provide here the maximal (M1) and minimal (M2) flux – though only for energies above a few GeV in the case of (M1). The coloured [yellow] area features the total uncertainty band arising from positron propagation.

the minimal configurations are significantly depressed. At the reference energy  $E = 1$  GeV, reductions by a factor of 10 between the median and minimal predictions are obtained for the  $b\bar{b}$  channel and amount to a factor of 20 in the  $W^+W^-$  case. They reach up to 2 orders

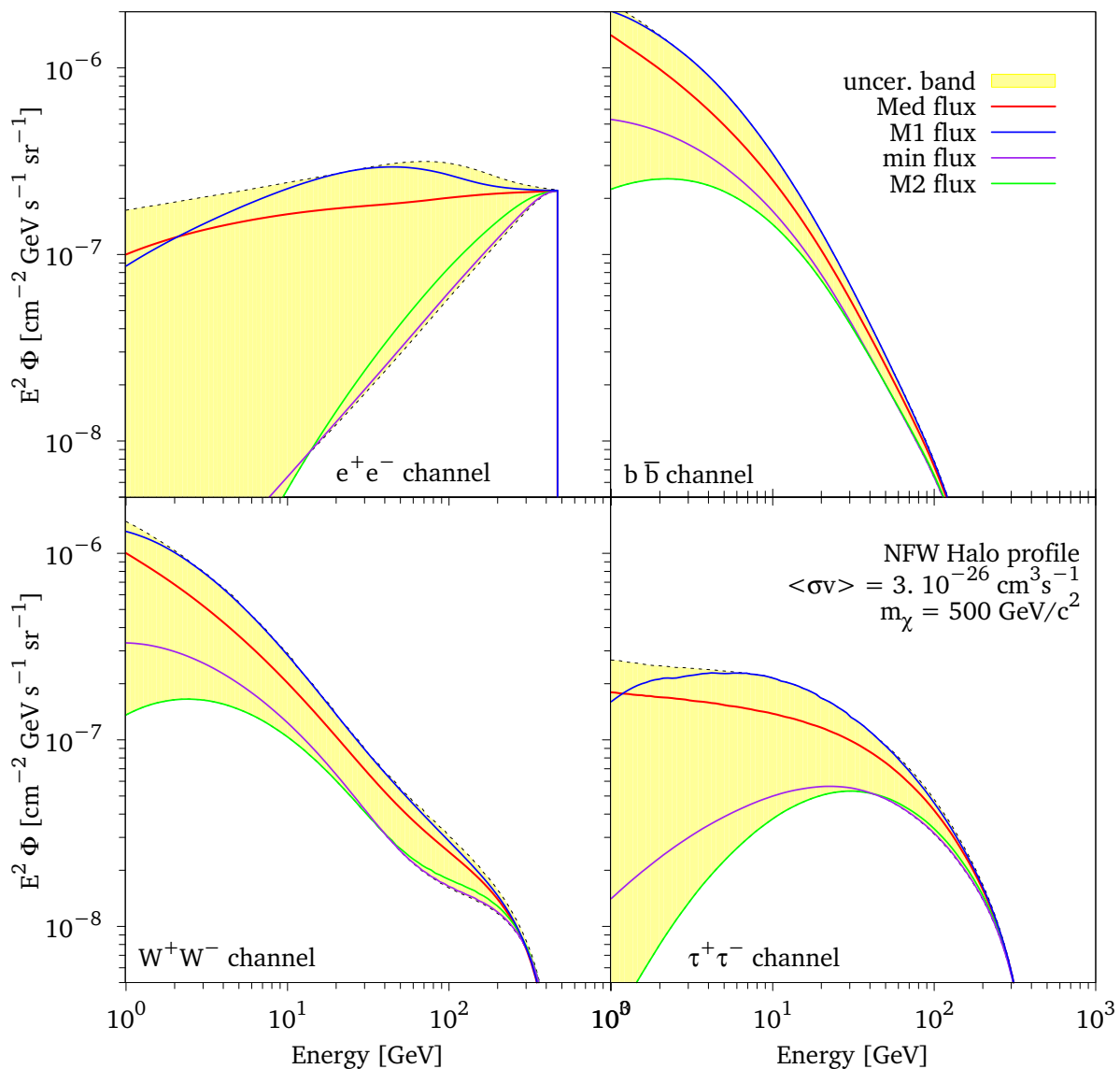


Figure 6.19: Same plot as in Fig. 6.18 but with a dark matter particle mass of 500 GeV.

of magnitude for the direct positron production. In this large dark matter mass regime, the astrophysical configuration M2 does not reproduce by far the lower bound of the uncertainty band as it did for the 100 GeV case. The message is therefore twofold.

- (i) Once the positron spectrum at the source is chosen – and the corresponding branching ratios have been defined – the correct determination of the uncertainty which affects the flux at the Earth requires a full scan of the propagation parameter space for each energy  $E$ . The use of representative astrophysical configurations such as M1 and M2 would not provide the correct uncertainty over the entire range of positron energy  $E$ .
- (ii) However, specific predictions have to be performed for a given model of dark matter

particle and a fixed set of astrophysical parameters. This is why fits to the experimental data should be performed for each propagation configuration over the entire range of the measured positron energies  $E$ . The best fit should correspond to a unique set of astrophysical parameters. This procedure is the only way to reproduce properly the correct and specific spectral shape of the flux.

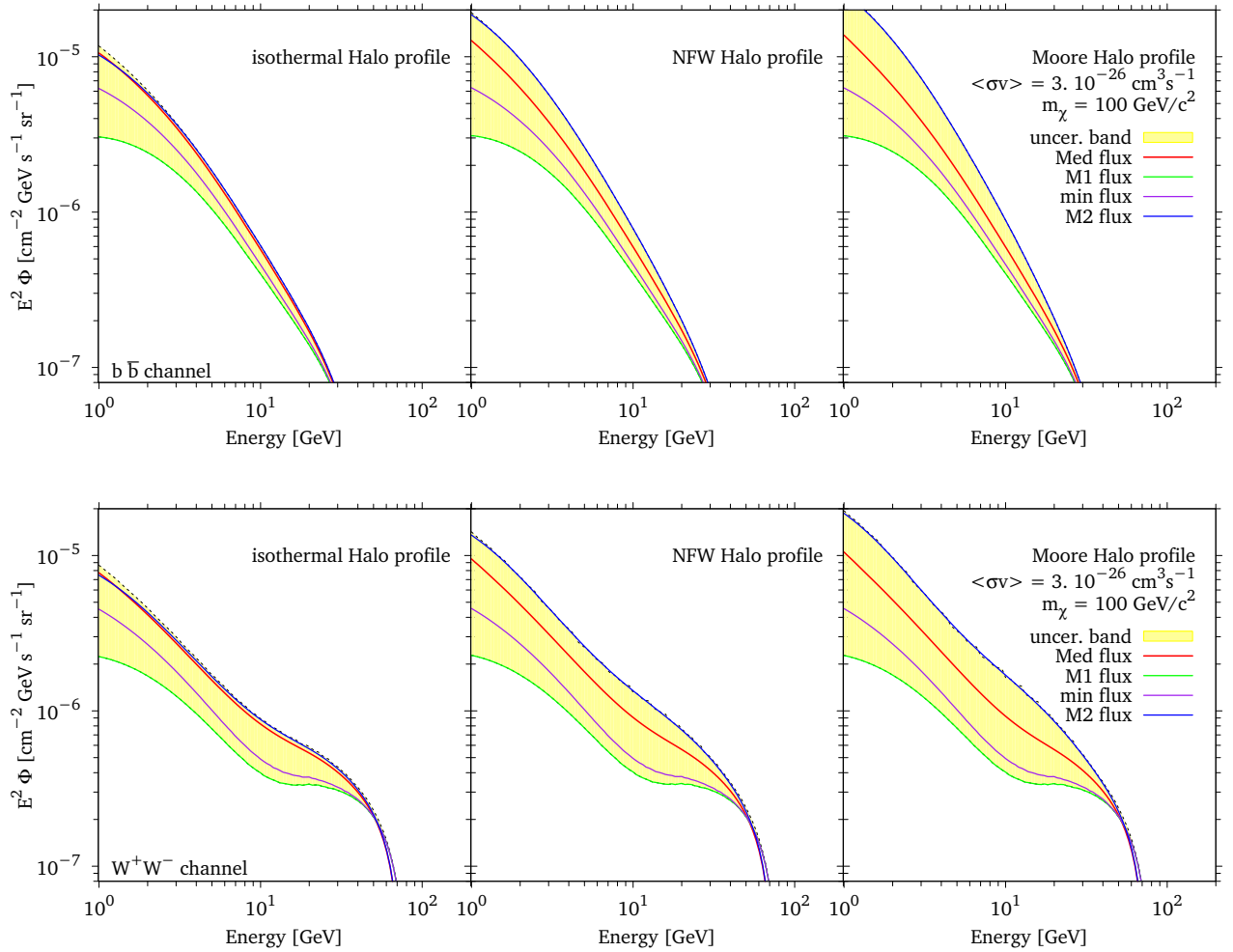


Figure 6.20: Positron flux  $E^2\Phi_{e^+}$  versus the positron energy  $E$ , for a dark matter particle mass of 100 GeV and for different halo density profiles : cored isothermal sphere (left panels), NFW (central panels) and Moore (right panels) – see section 4.3.1.4. The upper and lower rows correspond respectively to a  $b\bar{b}$  and  $W^+W^-$  annihilation channel. In each panel, the thick solid [red] curve refers to the best-fit choice (*Med*) of the astrophysical parameters. The upper [blue] and lower [green] thin solid lines stand for the astrophysical configurations M1 and M2 of Tab. 6.4. The coloured [yellow] area indicates the total uncertainty band arising from positron propagation.

The effect induced by different dark matter profiles is presented in Fig. 6.20, where the positron fluxes for the  $b\bar{b}$  and  $W^+W^-$  channels are reproduced for various dark matter dis-

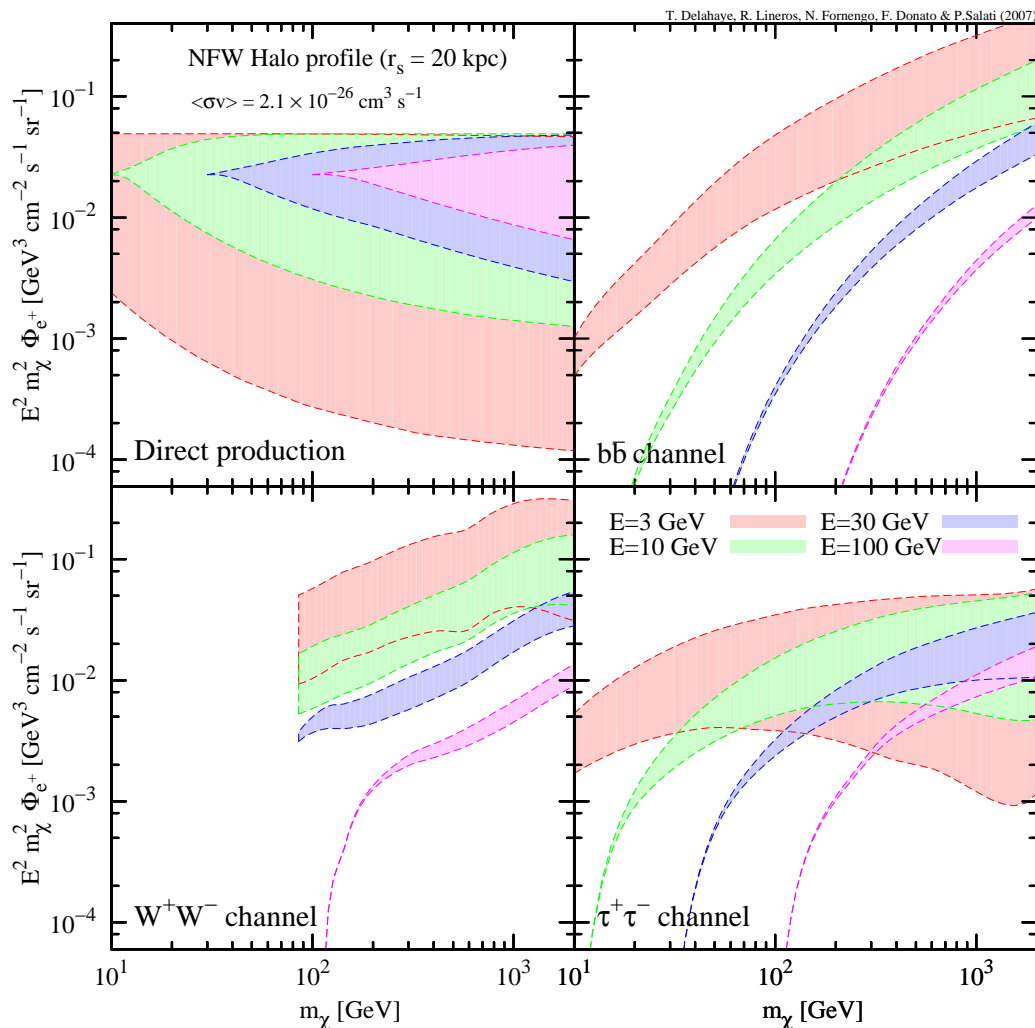


Figure 6.21: For fixed values of the detected energy  $E$ , the uncertainty bands on the positron flux  $E^2 m_\chi^2 \Phi_{e^+}$  are shown as a function of the mass  $m_\chi$  of the dark matter particle. The energies considered in the figure are  $E = 3, 10, 30$  and  $100$  GeV. Each band refers to one of those values and starts at  $m_\chi = E$ .

tributions. The mass of the dark matter particle is fixed at  $m_\chi = 100$  GeV. Notice how steeper profiles entail larger uncertainties, especially for the upper bound. This is mostly due to the fact that for large values of  $L$  – for which larger fluxes are obtained – the positron flux is more sensitive to the central region of the Galaxy, where singular profiles like the NFW and Moore distributions have larger densities and therefore induce larger annihilation rates. On the contrary, the lower envelope of the uncertainty band is not affected by the variation of the halo profile. In this case, with typically small heights  $L$ , positrons reach the solar system from closer regions, where the three halo distributions are very similar and do not allow to probe

the central part of the Milky Way.

Fig. 6.21 depicts the information on the positron flux uncertainty from a different perspective. The flux  $\Phi_{e^+}$  and its uncertainty band are featured for fixed values of the detected energy  $E$  whereas the dark matter particle mass is now varied. The flux  $\Phi_{e^+}$  is actually rescaled by the product  $E^2 m_\chi^2 \Phi_{e^+}$  for visual convenience. Each band corresponds to a specific detected energy  $E$  and consequently starts at  $m_\chi = E$ . In the case of the  $W^+W^-$  channel, the bands start at  $m_\chi = m_W$  because this channel is closed for dark matter masses below that threshold. The behaviour of these bands can be understood from Fig. 6.16, where the halo function  $\tilde{I}$  is plotted for the same detected energies, as a function of the injection energy  $E_S$ . In the case of direct positron production, there is a simple link between the two figures, because the source spectrum in this case is just a line at  $E_S = m_\chi$ . For the other channels, the situation is more involved since we have a continuous injection spectrum with specific features as discussed above. The main information which can be withdrawn from Fig. 6.21 is that at fixed detection energy, the larger the dark matter mass, the larger the uncertainty. Let us take for instance a detection energy of  $E = 3$  GeV. For direct production, where  $E_S = m_\chi$ , increasing the dark matter mass translates into a larger radius  $\lambda$  of the positron sphere. As a consequence, the uncertainty band enlarges for increasing masses. This occurs for all the annihilation channels, but is less pronounced for soft spectra as in the  $b\bar{b}$  case. Similar conclusions hold for all the other values of  $E$ .

Before getting any further, let us consider the case of decaying dark matter.

### 6.2.2.2 Decaying dark matter

As explained in section 4.3.1.2, the cosmic ray production by decaying dark matter is proportional to the dark matter density  $\rho$  and the maximal energy of the produced cosmic ray is  $E_M = m_\chi/2$  whereas it was respectively  $\rho^2$  and  $E_M = m_\chi$  in the annihilating case. Let us consider the case of direct  $e^+/e^-$  production with  $E_M = 200$  GeV. In order to make things comparable, one needs the annihilation rate  $\Gamma$  to be:

$$\Gamma = \langle\sigma v\rangle \frac{\rho_\odot}{E_M} \sim 4.25 \times 10^{-29} \text{ s}^{-1} \left( \frac{\langle\sigma v\rangle}{3 \times 10^{-26} \text{ cm}^3\text{s}^{-1}} \right) \left( \frac{200\text{GeV}}{E_M} \right) \quad (6.3)$$

so that the local production is the same in both cases.

As one can see from figure 6.22, the positron flux due to decaying dark matter is not much different than the one due to annihilating dark matter. However the first is always lower than the second whatever the propagation model. This is more salient when the thickness of the diffusive halo  $2L$  is large. Indeed, in that case, the positrons propagate further and the local flux becomes sensitive to the Galactic centre where the difference between  $\rho$  and  $\rho^2$  becomes important.

However it is clear that annihilating and decaying dark matter give very similar local positron flux so, in case of detection, one would need another method to distinguish the two cases. This will be looked at more into details in chapter 7.

Comparing the predictions from these last two paragraphs and the previous ones, it clearly appears that most of the time the dark matter signal is much lower than the standard one. However it has been proposed that there are some ways to boost the dark matter signal. One

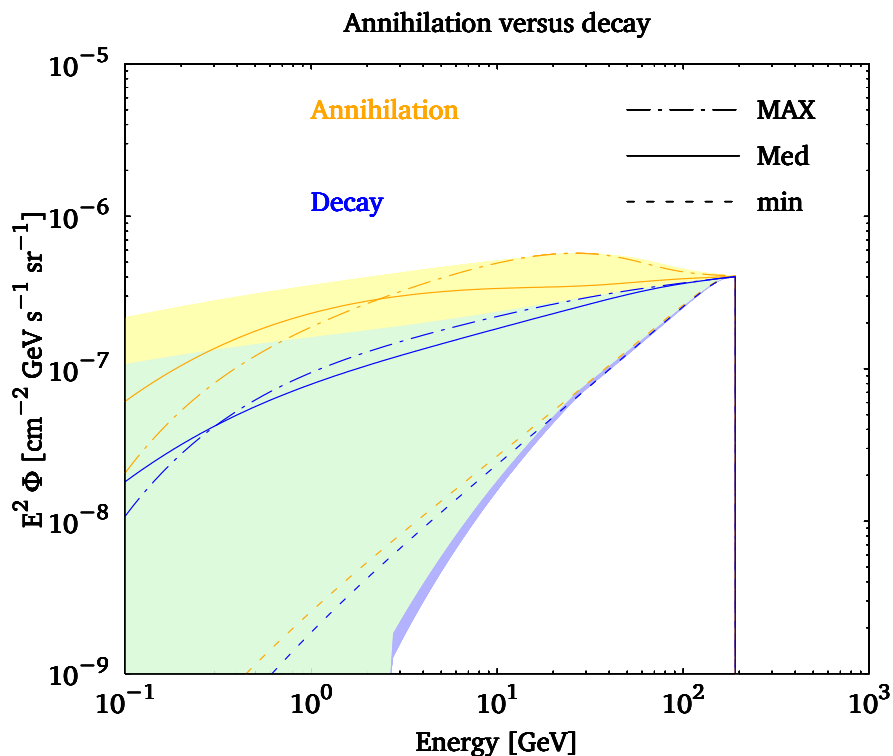


Figure 6.22: Positron flux at the Earth from decaying and annihilating dark matter. The decay rate is set according to equation 6.3. The yellow band corresponds to the uncertainty due to propagation for annihilating dark matter. The blue band is for decaying dark matter. The green band corresponds to the overlap of the two previous ones. The halo profile chosen here is NFW. The results corresponding to *min*, *Med* and *MAX* propagation models are also displayed.

of these ways is to invoke the substructures seen in N-body simulations (see section 4.3.1.5) where the dark matter density is much higher which can hence increase the annihilation (or decay) rate. Lavallo *et alii* [26], Pieri *et alii* [34] have already shown that on average, one cannot expect very large boost factors from clumps.

### 6.2.2.3 The clumps

I will not consider the case of decaying dark matter which is much less enhanced by the presence of substructures in the halo, but most of the phenomenology is the same. Indeed, may the clumps exist or not, the number of dark matter particles in the Galaxy is the same, so is the number of decay. However considering positrons, we are sensitive only to the nearby region, so the presence of a clump would translate into an increase of dark matter particle number in the vicinity. Concerning annihilating dark matter, the existence of clumps implies a larger number of annihilation in the Galaxy. But again, we are sensitive only to the Sun vicinity for positrons, so only nearby clumps could boost the signal.

As explained in section 4.3.1.5, the contribution of a nearby clump located at  $\mathbf{x}_c$  can be

expressed as

$$q_{\text{DM}}^c(\mathbf{x}, E) = \eta \langle \sigma v \rangle \frac{L}{m_\chi^2} \delta^3(\mathbf{x} - \mathbf{x}_c) f(E) ,$$

where  $L = \int_{\text{clump}} \rho_c^2(\mathbf{x}) d^3\mathbf{x}$  is defined as the subhalo luminosity (or without the square on  $\rho_c$  and  $m_\chi$  in the case of decaying dark matter). Furthermore, as clumps are treated here as point-like objects<sup>b</sup>, but unlike supernova remnants and pulsar, they continuously emit electrons and positrons. We can hence use the same propagators as for the smooth distribution and the  $\delta^3(\mathbf{x} - \mathbf{x}_c)$  term makes the integral over the diffusion zone trivial.

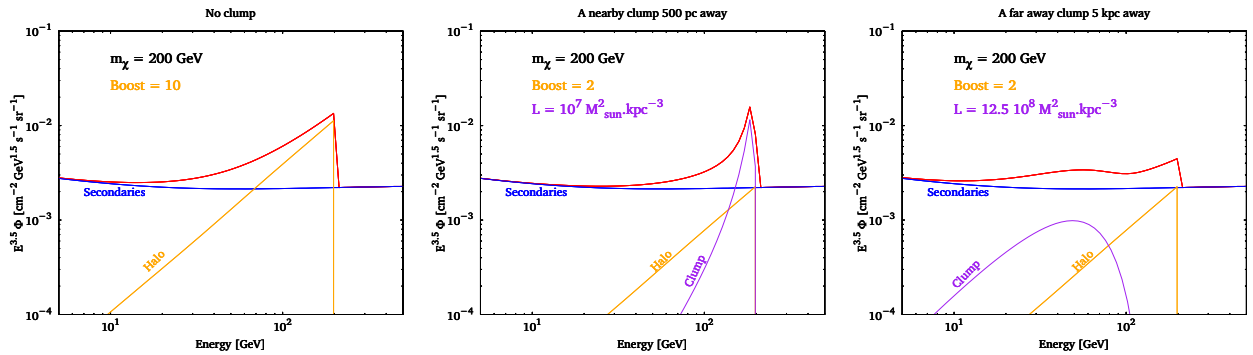


Figure 6.23: Positron flux at the Earth. This flux contains both the secondary positrons and the one coming from a 200 GeV dark matter particle which annihilates into  $e^+e^-$  pair. *Left*: halo with a boost of 10. *Middle*: halo with a boost of 2 plus a nearby clump (500 pc). *Right*: halo with a boost of 2 plus a far away (5 kpc) and very bright clump.

As one can see from figure 6.23, the flux received at the Earth from a nearby clump, depends, on the propagation parameters and the position of the clump (in 3D space). Moreover the presence of clumps does not enhance globally the signal but actually tends to distort it. This is clearly an issue for the goal of analysing the different channels of dark matter annihilation.

### 6.3 Discussion

In figures 6.24 and 6.25 all the previous terms are displayed together. I have not considered dark matter clumps. The solar modulation is taken into account with a Fisk potential of 600 MV and comparisons are made to various recent data. In the first case, the pulsar scenario, the raise in the positron fraction is explained by high electron/positron pair production efficiency in pulsars whereas in the second case, the dark matter scenario, it is due to large dark matter boost. Some conclusions can be drawn immediately:

- Without boost factor, the dark matter component never dominates.
- The uncertainties in the astrophysical background are large enough to have a rather good agreement with the data without over tuning the parameters.

<sup>b</sup>The scale radii of the clumps are always much smaller than the typical lepton diffusion length.

		L04 SNRs	local SNRs (Green)	local SNRs (ATNF)	L04 pulsars	local pulsars (ATNF)	dark matter NFW
Pulsar scen.	Spectral index	2.4	†	2.4	2.0	2.0	∅
	$fE_*\Gamma_*$	7	$1.5 \times \dagger$	★	2.0	†	∅
	Efficiency [%]	∅	∅	∅	6	6	∅
	$E_c$ [TeV]	2.0	2.0	2.0	1.5	1.5	∅
	Boost	∅	∅	∅	∅	∅	1.
DM scenario	Spectral index	2.4	†	2.4	2.0	2.0	∅
	$fE_*\Gamma_*$	7	$1. \times \dagger$	★	2.0	†	∅
	Efficiency [%]	∅	∅	∅	1	1	∅
	$E_c$ [TeV]	2.0	2.0	2.0	1.5	1.5	∅
	Boost	∅	∅	∅	∅	∅	30.

Table 6.5: Injected energy, converted fraction, spectral indices and cut-off energies used for the overall template electron and positron flux calculation. The symbol † indicates that we used observational constraints. The symbol ★ indicates that we have normalised the flux in order to have a brightness of 1 jansky at 1 GHz. For local supernova remnants, we have used a global extra-factor of 1.5, which corresponds to assuming a magnetic field of  $\sim 75$  instead of  $100 \mu\text{G}$  in equation (4.8).

- Both scenarios are possible.
- Unfortunately there are far too many uncertainties to allow liable predictions.

There are a few ways to better the situation:

## Better understanding of the sources

Concerning the electron spectrum predictions, we clearly lack precision because of the poor knowledge of the sources. However we are in fact at a time where the number of data is rapidly increasing. Indeed the radio observations and their analysis are getting more and more numerous. More important, thanks to instruments like HESS [21] or Fermi [18] the cosmic ray sources are now observed in a brand new spectrum.  $\gamma$ -ray observations of supernova remnants could actually teach us a lot about cosmic rays. For instance concerning the normalisation of the injection spectrum  $Q_0$  cross correlating radio emission from synchrotron (which depends on the local magnetic field) with  $\gamma$  emission from inverse Compton (which depends on the radiation field) could help us to get more precise values. Moreover, at high energies, it could be possible to probe the energy cut-off  $E_c$ . This is not possible with radio emission because it corresponds to frequencies where the thermal emission dominates.

## More data

Obviously one important issue we are faced with, is the fact that there is very little data concerning electron and positron fluxes (not the sum). This is why it is difficult to put strong constraints on the model. However, data at high energy with a good energy resolution could

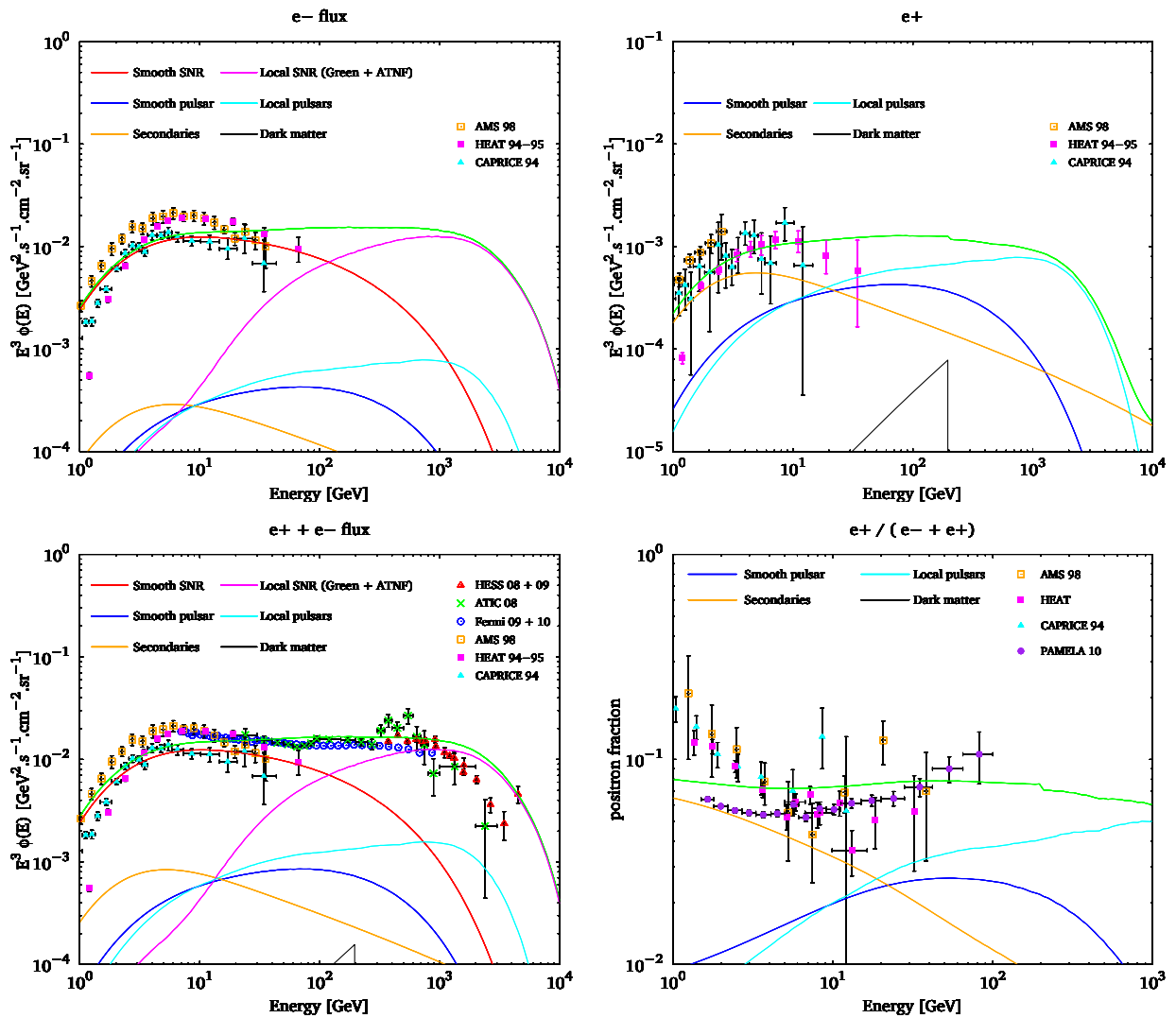


Figure 6.24: *Top left:* electron flux at the Earth with all the various contributions. *Top right:* the same but for positrons. *Bottom left:* sum of the two previous ones. *Bottom right:* positron fraction.

help us distinguishing among the different scenarios. Indeed some spectral features could hint for one model or an other.

## Multi-messenger analysis

Finally, the best way to test the scenarios is to look to other messengers than electrons and positrons. Indeed, with these cosmic rays we are only probing the local environment and it would be difficult to rule out a locality effect. Moreover dark matter is not expected to produce only electrons and positrons (unlike pulsars) so relating many hints, which taken individually are not proofs, could be a good way to achieve dark matter detection. This is what I will start to do in the next two chapters.

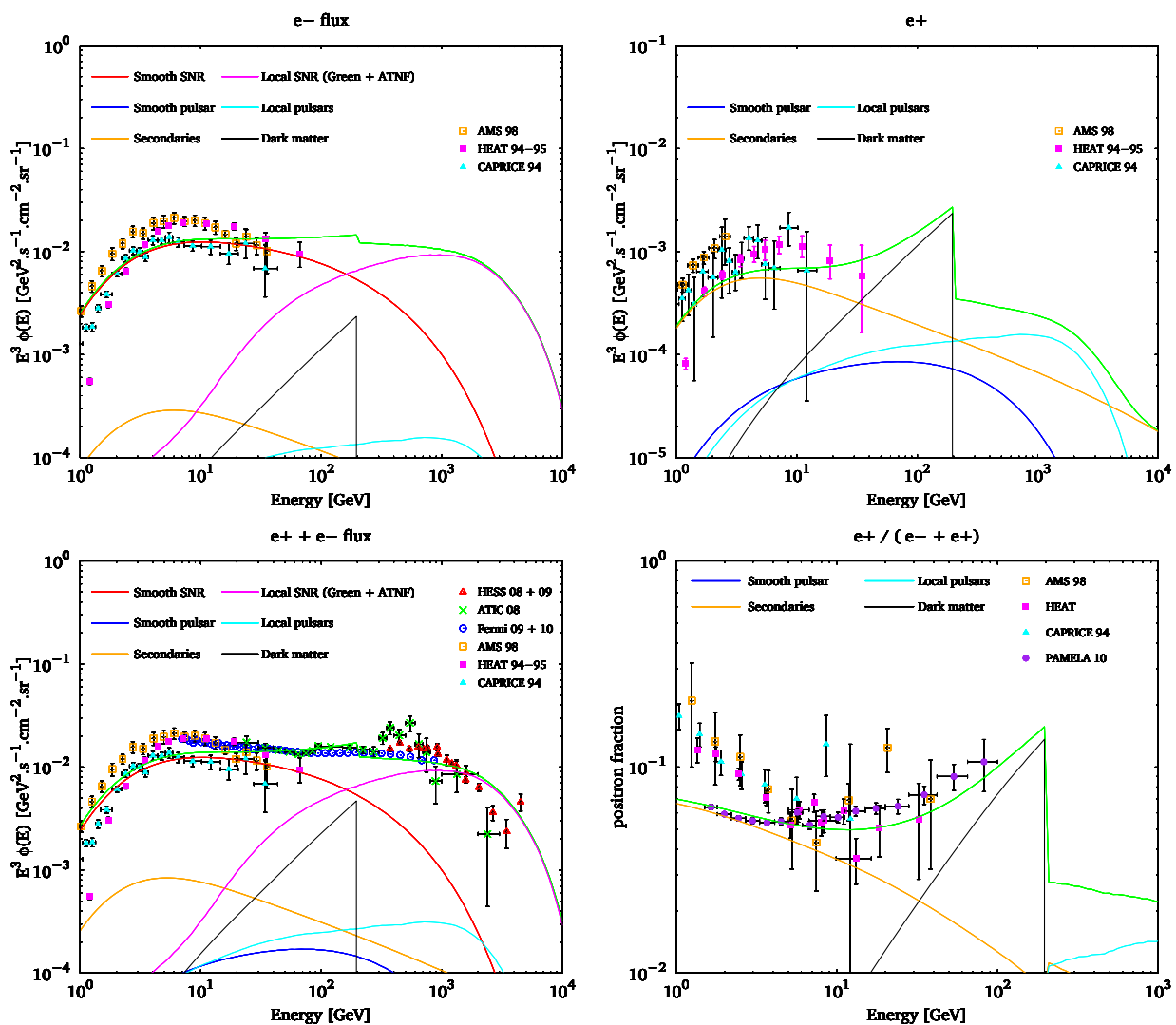


Figure 6.25: Same as figure 6.24 but with a large boost factor for the dark matter and a low electron positron injection efficiency for pulsars.

## Bibliography

- [1] Ahlers, M., Mertsch, P., & Sarkar, S. 2009, Phys. Rev. D, 80, 123017 [124](#)
- [2] Alcaraz, J., Alpat, B., Ambrosi, G., *et alii* . 2000, Physics Letters B, 484, 10 [117](#), [123](#)
- [3] AMS-01 Collaboration, Aguilar, M., Alcaraz, J., *et alii* . 2007, Physics Letters B, 646, 145 [123](#)
- [4] AMS Collaboration, Aguilar, M., Alcaraz, J., *et alii* . 2002, Phys. Rep., 366, 331 [117](#)
- [5] Badhwar, G. D., Golden, R. L., & Stephens, S. A. 1977, Phys. Rev. D, 15, 820 [119](#)
- [6] Baltz, E. A. & Edsjö, J. 1999, Phys. Rev. D, 59, 023511 [117](#), [124](#), [128](#)

- [7] Barwick, S. W., Beatty, J. J., Bhattacharyya, A., *et alii* . 1997, ApJ, 482, L191+ [117](#), [123](#)
- [8] Blasi, P. 2009, Physical Review Letters, 103, 051104 [124](#)
- [9] Boezio, M., Carlson, P., Francke, T., *et alii* . 2000, ApJ, 532, 653 [117](#), [123](#)
- [10] Brun, P., Delahaye, T., Diemand, J., Profumo, S., & Salati, P. 2009, Phys. Rev. D, 80, 035023 [124](#)
- [11] Combet, C., Maurin, D., Donnelly, J., O’C. Drury, L., & Vangioni-Flam, E. 2005, A&A, 435, 151 [120](#)
- [12] Delahaye, T., Lavalley, J., Lineros, R., Donato, F., & Fornengo, N. 2010, ArXiv e-prints [1002.1910](#) [124](#), [131](#)
- [13] Delahaye, T., Lineros, R., Donato, F., *et alii* . 2009, A&A, 501, 821 [116](#), [117](#), [119](#), [122](#)
- [14] Delahaye, T., Lineros, R., Donato, F., Fornengo, N., & Salati, P. 2008, Phys. Rev. D, 77, 063527 [124](#)
- [15] Donato, F., Fornengo, N., Maurin, D., Salati, P., & Taillet, R. 2004, Phys. Rev. D, 69, 063501 [139](#)
- [16] Donato, F., Maurin, D., Brun, P., Delahaye, T., & Salati, P. 2009, Physical Review Letters, 102, 071301 [116](#), [119](#)
- [17] Donato, F., Maurin, D., & Taillet, R. 2002, A&A, 381, 539 [120](#)
- [18] Godfrey, G. L. & The GLAST Working Group. 1993, in Towards a Major Atmospheric Cherenkov Detector – II for TeV Astro/Particle Physics, ed. R. C. Lamb, 145–+ [150](#)
- [19] Green, D. A. 2009, Bulletin of the Astronomical Society of India, 37, 45 [131](#)
- [20] Grimani, C., Stephens, S. A., Cafagna, F. S., *et alii* . 2002, A&A, 392, 287 [117](#), [123](#)
- [21] Hermann, G. 1997, in Very High Energy Phenomena in the Universe; Moriond Workshop, ed. Y. Giraud-Heraud & J. Tran Thanh van, 141–+ [150](#)
- [22] Hooper, D. & Silk, J. 2005, Phys. Rev. D, 71, 083503 [138](#)
- [23] Kamae, T., Karlsson, N., Mizuno, T., Abe, T., & Koi, T. 2006, ApJ, 647, 692 [116](#), [117](#), [119](#), [120](#)
- [24] Kamae, T., Karlsson, N., Mizuno, T., Abe, T., & Koi, T. 2007, ApJ, 662, 779 [116](#), [117](#), [119](#), [120](#)
- [25] Kobayashi, T., Komori, Y., Yoshida, K., & Nishimura, J. 2004, ApJ, 601, 340 [131](#)
- [26] Lavalley, J., Yuan, Q., Maurin, D., & Bi, X. 2008, A&A, 479, 427 [148](#)

- 
- [27] Lionetto, A. M., Morselli, A., & Zdravkovic, V. 2005, *Journal of Cosmology and Astroparticle Physics*, 9, 10 [122](#)
- [28] Lorimer, D. R. 2004, in *IAU Symposium*, Vol. 218, *Young Neutron Stars and Their Environments*, ed. F. Camilo & B. M. Gaensler, 105–+ [125](#), [127](#)
- [29] Maurin, D., Donato, F., Taillet, R., & Salati, P. 2001, *ApJ*, 555, 585 [116](#), [120](#), [121](#), [137](#), [139](#), [142](#)
- [30] Maurin, D. & Taillet, R. 2003, *A&A*, 404, 949 [141](#)
- [31] McCullough, P. R., Fields, B. D., & Pavlidou, V. 2002, *ApJ*, 576, L41 [131](#)
- [32] Mertsch, P. & Sarkar, S. 2009, *Physical Review Letters*, 103, 081104 [124](#)
- [33] Moskalenko, I. V. & Strong, A. W. 1998, *ApJ*, 493, 694 [116](#), [117](#), [122](#), [124](#), [128](#)
- [34] Pieri, L., Lavalle, J., Bertone, G., & Branchini, E. 2009, *ArXiv e-prints* [0908.0195](#) [148](#)
- [35] Putze, A., Derome, L., & Maurin, D. 2010, *ArXiv e-prints* [1001.0551](#) [120](#)
- [36] Shikaze, Y., Haino, S., Abe, K., *et alii* . 2007, *Astroparticle Physics*, 28, 154 [117](#)
- [37] Shinn, J.-H., Min, K. W., Sankrit, R., *et alii* . 2007, *ApJ*, 670, 1132 [131](#)
- [38] Tan, L. C. & Ng, L. K. 1983, *Journal of Physics G Nuclear Physics*, 9, 1289 [118](#), [119](#)

# Chapter 7

## Photons

The true mystery of the world is the visible, not the invisible.

*Oscar Wilde*

When measuring the electron/positron cosmic ray fluxes, for obvious reasons we are limited to get only their local values. Our predictions do not have such a limitation, so it would be nice to be able to infer these fluxes anywhere in the Galaxy. As we have seen in chapter 5, while they propagate in the Galactic diffusive halo, electrons and positrons lose energy, mainly through radiative processes. The idea is to measure these photons emitted by propagating cosmic rays and to study their fluxes anywhere in the Galaxy. This emission does not originate from point-like sources but rather from the whole halo and is therefore called the diffuse emission.

In the point of view of dark matter research, the diffuse emission is interesting for two reasons: as explained above, it allows to probe the electron/positron production but also, more straightforwardly, it reveals the photon production of annihilating or decaying dark matter.

There are actually two energy ranges which are interesting for our study: the gamma ray band and the radio one. The first one leads to electrons through their inverse Compton scattering and to dark matter. The second one only probes the electrons through their synchrotron emission, so in fact both are complementary.

However, as for electrons, it is important to know as good as possibly the background, in order to infer anything interesting.

## 7.1 Gamma rays

One difficulty in measuring the diffuse  $\gamma$  emission is to remove the so called unresolved sources. Because instruments are limited in angular resolution sometime they cannot distinguish a cluster of sources (for instance a cluster of Galactic pulsars or of extra-galactic quasars) from a large zone actually producing a diffuse  $\gamma$  emission. Fortunately, Fermi [10] which is now in flight and has an angular resolution much more acute than any other experiment before, should be able reduce considerably this problem.

The real diffuse emission, however, is made of many ingredients we need to evaluate one by one.

### 7.1.1 Gamma rays from $\pi^0$ decay

This paragraph retraces preliminary results of an ongoing work in collaboration with Armand Fiasson, Pierre Salati, and Martin Pohl.

The main contribution to the  $\gamma$  diffuse emission comes from the spallation of cosmic ray protons and  $\alpha$  particles with the interstellar hydrogen and helium. Exactly like secondary electrons and positrons. Similarly to equation 4.15 the production rate reads:

$$q_\gamma(\vec{x}, \epsilon_\gamma) = 4\pi \sum_{\text{targ}=\text{H,He}} \sum_{\text{proj}=\text{p},\alpha} n_{\text{targ}}(\vec{x}) \times \int \Phi_{\text{proj}}(\vec{x}, \epsilon_{\text{proj}}) \frac{d\sigma}{d\epsilon_\gamma}(\epsilon_{\text{proj}} \rightarrow \epsilon_\gamma) d\epsilon_{\text{proj}}, \quad (7.1)$$

where  $\Phi_{\text{proj}}(\vec{x}, \epsilon_{\text{proj}})$  denotes the cosmic ray nucleon flux at position  $\vec{x}$ ,  $n_{\text{targ}}(\vec{x})$  the number density of target nuclei, and  $d\sigma/d\epsilon_\gamma$  the  $\gamma$  creation cross-section. This reaction mainly goes through the production of  $\pi^0$  particles which in most cases ( $98.823 \pm 0.034$  % according to the Particle Data Group [21]) decays into a pair of photons. All the ingredients have to be known in order to compute this production rate.

### 7.1.1.1 Production cross-section

#### Pion to photon

A neutral pion created by the collision of a cosmic ray with interstellar gas mainly decays into two photons  $p_1$  and  $p_2$ . Writing down the energy-momentum 4-vector of each particle involved in the decay in the rest-frame of the pion gives:  $\pi_\rho = (m_\pi, \vec{0})$ ,  $p_{1\rho} = (E_1, \vec{k}_1)$  and  $p_{2\rho} = (E_2, \vec{k}_2)$ . By energy and momentum conservations, one easily gets the energies of the photons:

$$\begin{aligned} E_1 + E_2 &= E_\pi = m_\pi \\ E_1^2 - k_1^2 &= E_2^2 - \{E_2 - (m_p = 0)\}^2 = m_p^2 = 0 \end{aligned}$$

so

$$E_1 = E_2 = \frac{m_\pi}{2}.$$

In the rest-frame of the pion  $R'$ , photons are hence mono-chromatic. In the laboratory frame  $R$ , the pion goes at velocity  $\beta_\pi$  (expressed in units of  $c$ ) associated with a Lorentz coefficient  $\gamma_\pi$  and an energy  $\epsilon_\pi$ . The energy  $\epsilon_1$  of the photon  $p_1$  in the laboratory frame is equal to:

$$\epsilon_1 = \gamma_\pi \left( m_\pi/2 + \vec{\beta}_\pi \cdot \vec{p}_1 \right).$$

which takes values between  $m_\pi\gamma_\pi(1 + \beta_\pi)/2$  and  $m_\pi\gamma_\pi(1 - \beta_\pi)/2$ . The energy distribution of the photon  $p_1$   $\epsilon_1$  created by a pion of energy  $\epsilon_\pi$  in the laboratory frame  $R$  is hence:

$$f(\epsilon_\pi, \epsilon_1) = \frac{\theta(\epsilon_1 - m_\pi\gamma_\pi(1 - \beta_\pi)/2) - \theta(\epsilon_1 - m_\pi\gamma_\pi(1 + \beta_\pi)/2)}{m_\pi\gamma_\pi\beta_\pi},$$

where  $\theta(x)$  is Heaviside's step function.

This result is true also for photon  $p_2$  so the energy distribution of the outgoing photon is twice the previous one.

#### Proton to pion

All we need now is the  $\pi^0$  production cross-section of the proton-proton collision. Like for charged pions, few parametrisations are available in the literature. For instance, Stephens & Badhwar [25] proposed a parametrisation quite similar to equation 4.17 for charged pions:

$$E \frac{d^3\sigma_\pi}{dp^3} = \frac{1}{1 + 23E_p^{-2.6}} \frac{A}{1 + 4m_p^2/s)^r} (1 - \tilde{x})^q \exp \left[ -\frac{Bp_\perp}{1 + 4m_p^2/s} \right], \quad (7.2)$$

with  $A = 140\text{mb}/(\text{GeV}^2/c^3)$ ,  $B = 5.43(\text{GeV}/c)^{-1}$ ,  $r = 2$ ,  $C1 = 6.1$ ,  $C2 = 3.3(\text{GeV}/c)^{-1}$ , and  $C3 = 0.6(\text{GeV}/c)^{-2}$ . Moreover, as we have seen in paragraph 4.2.1.5,  $\Delta^+$  resonance produces  $\pi^+\pi^0$  pairs. Their production has been parametrised by Stecker [24] so that this process, quite important at low energy, can be implemented as well.

#### Kaon decay

As in paragraph 4.2.1.5, the production of charged kaon has also to be considered. Indeed, in %20.92 of cases, a charged kaon decays into a charged pion and a neutral pion. Using the parametrisation from table 4.1 it is possible to compute the gamma ray production due to both

$K^+$  and  $K^-$ . Actually a three body decay  $K^\pm \implies \pi^\pm + 2\pi^0$  also exists but it contributes very little ( $\sim 8.22\%$ ) so I have neglected it.

Unfortunately, Tan and Ng, who provided us with parametrisations for charged pions, did not publish anything about neutral pions (as far as I know). However Kamae *et alii* [14, 15] did so and Huang *et alii* [13] using both a parametrisation and an event generator obtained tables available online<sup>a</sup> which directly give the  $\gamma$  ray production spectrum.

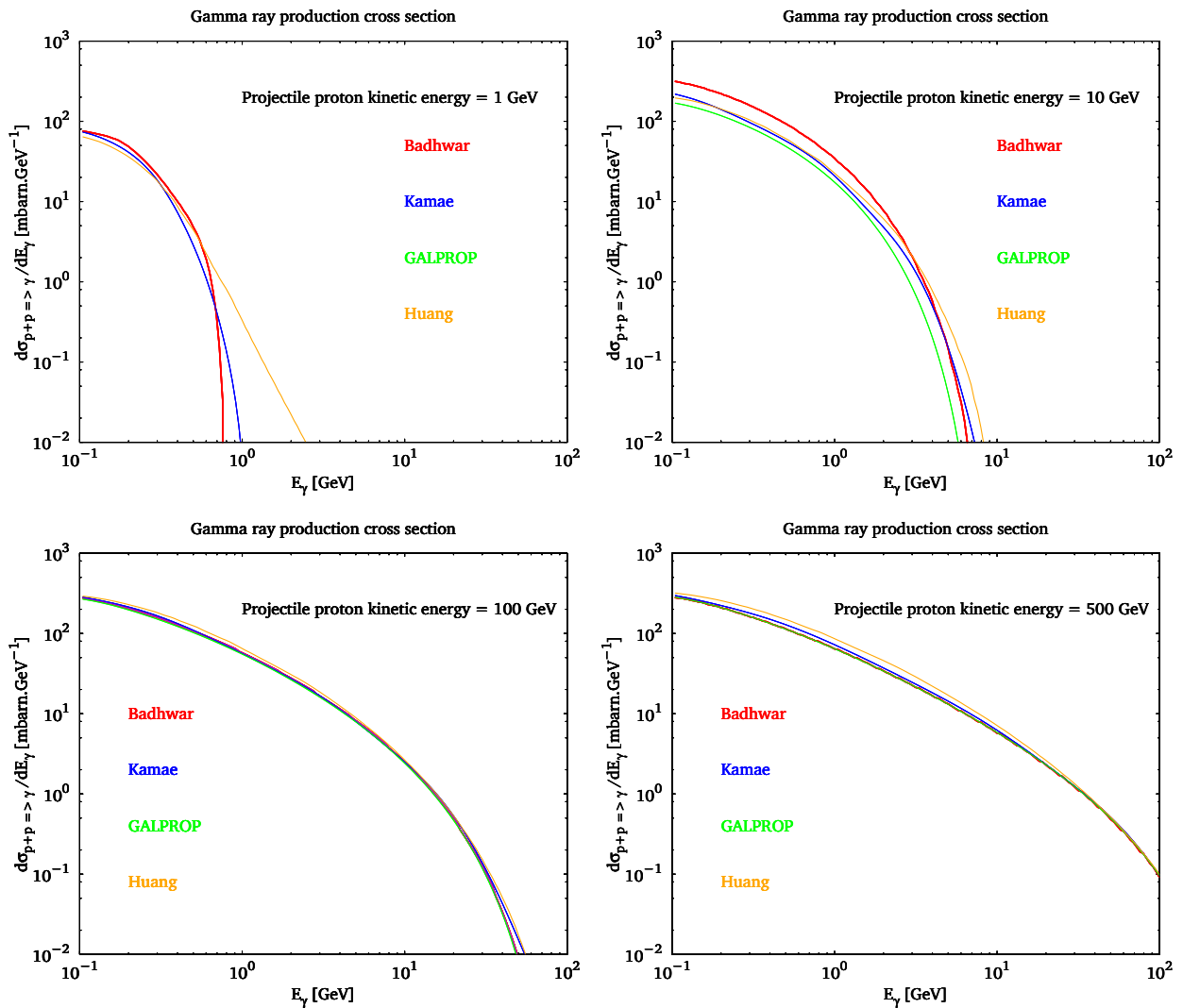


Figure 7.1: Comparison between various parametrisations of the proton cosmic ray plus interstellar gas (and not only hydrogen) to photon production cross-sections at different incident proton kinetic energies (from top to bottom and from left to right, respectively, 1 GeV, 10 GeV, 100 GeV, and 500 GeV). Blue lines are for Kamae *et alii* [14, 15], orange for Huang *et alii* [13], red for Stephens & Badhwar [25], and green line is the result obtained from the GALPROP routine.

<sup>a</sup><http://cherenkov.physics.iastate.edu/gamma-prod/>

As one can see from figure 7.1, the parametrisations of Stephens & Badhwar [25], Kamae *et alii* [14, 15] and Huang *et alii* [13] are in fairly good agreement. The GALPROP routine uses the same references for pion and kaon production as those explained above but did not include  $\Delta$  resonance, this is why for 1 GeV proton energy, there is no photon in the first panel. Moreover, the rescale formula used in GALPROP for nucleon collision is not the one of equation 4.20 by Schwalb *et alii* [23]. This explains why the results are not the same for a proton energy of 10 GeV. At very high proton energies ( $\gtrsim$  few TeV), Kamae *et alii* [14, 15] exhibits a cut-off which is not physical but due to the functions the authors have used. This problem is solved by Huang *et alii* [13], which for the other energy ranges is in quite good agreement with the previous one. Unless stated otherwise, I will always make use of the tables of Huang *et alii* [13] which actually also take into account proton + helium,  $\alpha$ + hydrogen and  $\alpha$ + helium processes as well.

### 7.1.1.2 Primary cosmic ray flux

The argument I used in section 6.1.1.4 showing that spatial variation of the projectile cosmic ray flux were negligible because averaged over the electron sphere is obviously not valid anymore. This means that we need to carefully compute the proton (and  $\alpha$ ) flux anywhere is the Galaxy. Indeed unlike electrons, photons do not lose energy as they propagate in the interstellar medium, they do not diffuse either so we are actually detecting photons coming from everywhere in the Galaxy.

The method to compute such an information is developed in the appendix B.2. The ingredients we need are

- A propagation model. This has already been described at length in section 5.1.2.
- A source distribution, which can be found in section 4.1.3. And finally
- A local measurement of the flux, as parametrised in section 4.2.2.

As one can see from figure 7.2, the uncertainties on the proton flux are not actually that important in the Solar vicinity. Nevertheless, near the Galactic centre or in the vertical direction, they can reach quite large values (a factor of two or three). Above a few tens of GeV, one always gets results very similar to the ones obtained at 1 TeV. The reason for this is that the propagation affects all energies the same way. Below  $\sim 10$  GeV, convection becomes important and changes the results: its main effect is to populate the high  $z$  region (at least if  $L$  is large). The higher the energy, the more the protons propagate, so their spatial distribution at the origin is smoothed. This clearly appears on the right column of figure 7.2, at 1 TeV all the profiles are much flatter than at 1 GeV. One can also see from this figure, that imposing a vanishing flux at  $r = 20$  kpc, kills almost all the freedom allowed by the propagation parameters for large values of  $r$  ( $r \geq 10$  kpc). This means that the  $\gamma$  ray flux in the anti-centre direction should be quite informative concerning this boundary condition.

One should keep in mind two things considering these results. First, our model only allows us to deal with a Galaxy which has cylindrical symmetry, this is wrong at small scales of course because the cosmic ray sources are discrete events but also on large scales ( $\sim$ kpc) as we know that there are spiral arms. This may mean that some work has to be done to allow to take

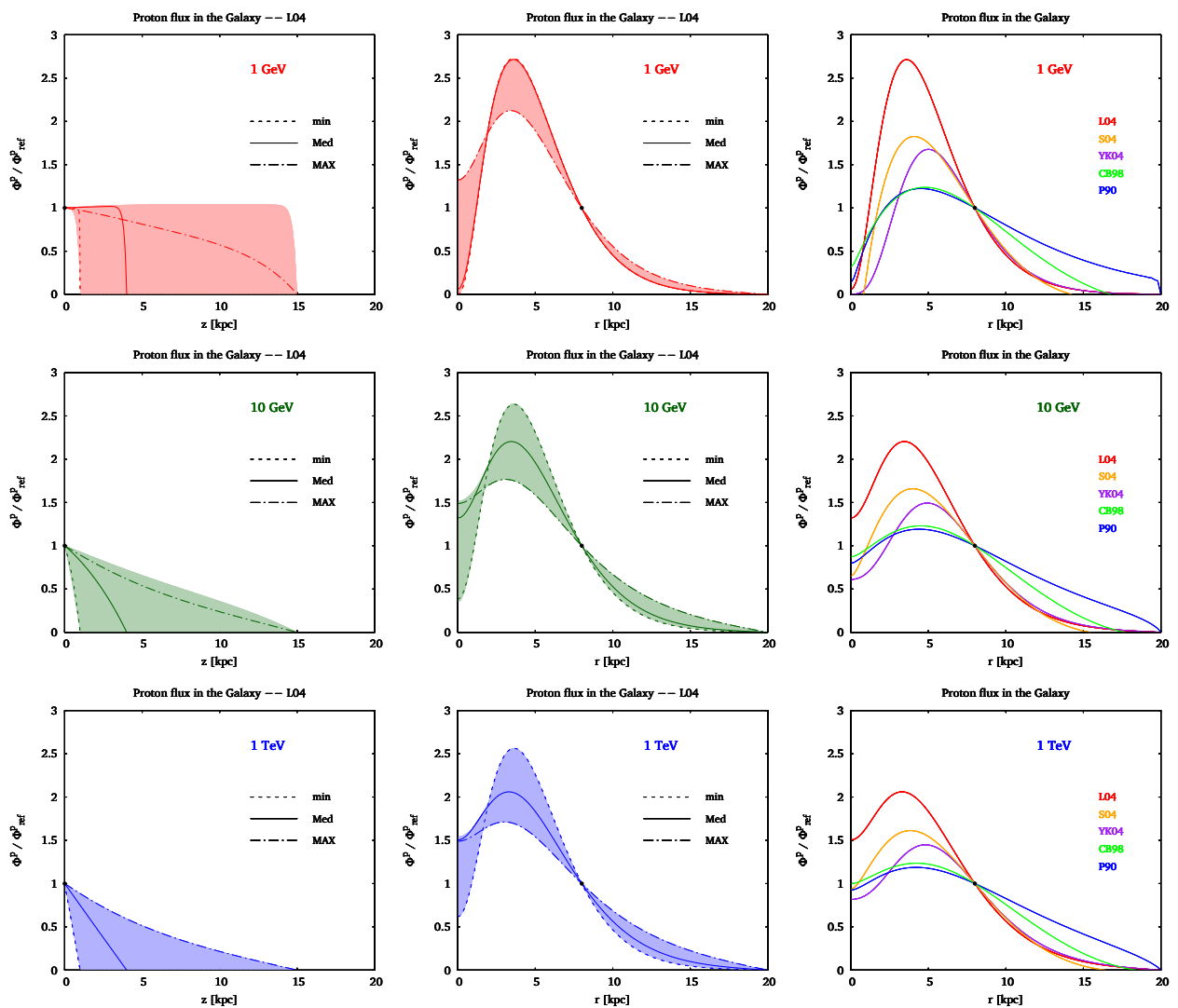


Figure 7.2: Proton flux In the Milky Way, normalised at its local value. *Left*: Proton flux at  $r = r_{\odot}$  as a function of  $z$ . Uncertainties due to propagation are displayed along with the three propagation sets *min*, *Med*, and *MAX*. The source distribution chosen is L04 (see section 4.2.2). *Middle*: same as before but at  $z = 0$  and varying  $r$ . *Right*: comparison among the various source distribution functions of section 4.2.2. Each row corresponds to a different energy from top to bottom, 1, 10, and 1,000 GeV respectively.

into account these effects. Second, the parametrisations for the primary cosmic ray flux at the Earth I use to compute the fluxes are only valid up to a few tens of GeV. New measurements of the proton flux exhibiting any variation from the current parametrisation could dramatically change our results.

### 7.1.1.3 Target distribution

Again, because photon propagation does not allow any spatial averaging, one needs to precisely know the target gas distribution in the Milky Way. Some maps are available in the literature, some of which are described in the appendix D.1.

The GALPROP public code uses a combination of maps and parametrisation by Seth W. Digel which are available online<sup>b</sup>. The level of detail is not the same but both maps are faced with the same issue: our poor knowledge of the  $X_{CO}$  factor. This factor sizes the proportionality between carbon monoxide abundance and molecular hydrogen abundance. The first one is measured thanks to its 2.6 mm line emission and is supposed to trace the second. It has been shown already that this factor depends on the metallicity of the medium considered and actually is different in active places like the Galactic centre and in quiet places like the edges of our Galaxy. However Tibaldo *et alii* [26], thanks to recent Fermi observations has shown that carbon monoxide may be a poor tracer of molecular hydrogen abundance. This is clearly an issue because hydrogen is mainly in its molecular form in the Galaxy and this of course would affect our results.

### 7.1.1.4 Results

The flux received at the Earth is then obtained by integrating the source term of equation 7.1 over the line of sight. If one considers a solid angle define by a width in latitude  $\Delta b$  and one in longitude  $\Delta l$ , then the volume of a bin situated at a distance  $s$  with a thickness  $ds$  is:

$$V(\vec{x}) = \cos(b) \Delta b \Delta l \frac{1}{3} \left\{ \left( s + \frac{ds}{2} \right)^2 - \left( s - \frac{ds}{2} \right)^2 \right\} \sim \cos(b) \Delta b \Delta l \frac{s^2 ds}{3}.$$

The flux of photon coming from this direction is hence:

$$\Psi_{\gamma}^{l,b}(\epsilon_{\gamma}) = \int_{s=0}^{\infty} q_{\gamma}(\vec{x}, \epsilon_{\gamma}) \frac{\cos(b) \Delta l \Delta b}{12\pi} ds \text{ cm}^{-2} \text{ GeV}^{-1} \text{ s}^{-1}.$$

The result is displayed in figure 7.3, for an energy of 1 GeV. The gas maps are those described in the appendix, the cross-sections are those by Huang *et alii* [13], the source distribution is the one from Lorimer [18] (see section 4.1.3) and the propagation model is *Med*. Not very surprisingly this map looks a lot like the carbon monoxide map. I will not detail the calculi here, but I would like to stress that making use of the Bessel functions allows to compute these maps, with a resolution of  $0.5^{\circ} \times 0.5^{\circ}$ , quite rapidly (around ten minutes). Hence sizing the uncertainties and understanding the impact of each parameter is achievable.

As one can see from figure 7.4, though the  $\pi^0$  decay emission mainly follows the gas distribution, some uncertainty remains. Actually the flux is not very dependent on the propagation parameters except the size of the diffusion halo  $2L$ . In this plot,  $L$  has been varied from 1 kpc to 15 kpc, the difference is almost impossible to see at low latitudes, however at  $b = 80^{\circ}$  the uncertainty can be as large as 50% which is quite large but reasonable compared with the other uncertainties.

I will reserve a full discussion of the obtained spectra and comparison to other models and to recent Fermi data to the paper in preparation.

<sup>b</sup>[http://galprop.stanford.edu/FITS/gas\\_maps.tar](http://galprop.stanford.edu/FITS/gas_maps.tar)

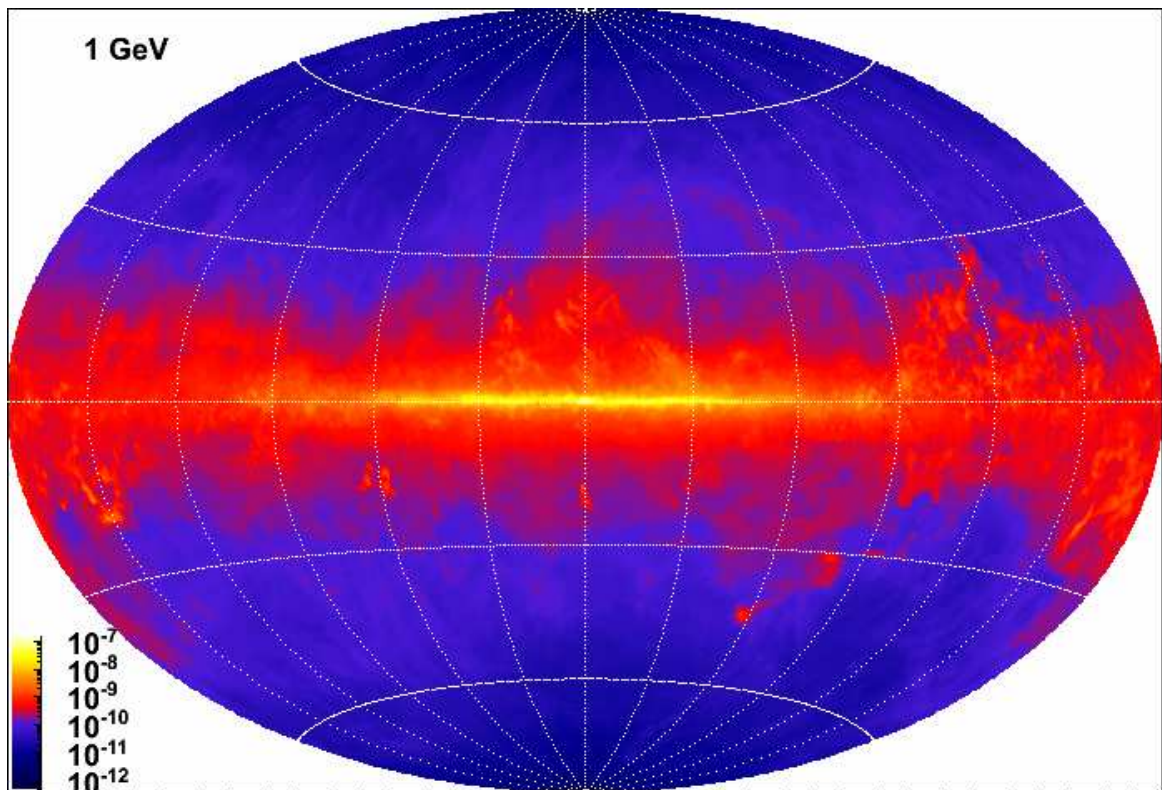


Figure 7.3: Map of the sky displaying the  $\gamma$  emission due to  $\pi^0$  decay at 1 GeV. The computations has been done using the parameters detailed in the text. For all energies, the maps look pretty much the same, it is the intensity that varies. Indeed, the emission always follows the gas distribution.

### 7.1.2 Gamma rays from Bremsstrahlung

Bremsstrahlung or free–free emission is caused by the interaction of a fast electron with a static electric charge during which the fast electron brakes and emits a photon. There are many different types of electrical charges that an electron can encounter during its journey in the Galactic halo. As explained by Blumenthal & Gould [3] most of the processes lead to the same effect: incoming electron or positron scattering off an electron, a positron, or a heavy ion give exactly the same result. However if the target is an atom (with its electronic cloud), because of shielding but also of atomic transitions (including ionisation), the result can be quite different. In theory each atom or molecule should be treated separately but this is far too complex. However when one considers the relative abundances, only a few species have to be considered: hydrogen atom, helium atom and helium ion of charge one. So practically the production of  $\gamma$  rays through Bremsstrahlung is given by:

$$q_\gamma(\vec{x}, \epsilon_\gamma) = 4\pi \sum_{\text{targ}=\text{H,He}} n_{\text{targ}}(\vec{x}) \times \int \Phi_e(\vec{x}, \epsilon_e) \frac{d\sigma}{d\epsilon_\gamma}(\epsilon_\gamma, \epsilon_e) d\epsilon_e, \quad (7.3)$$

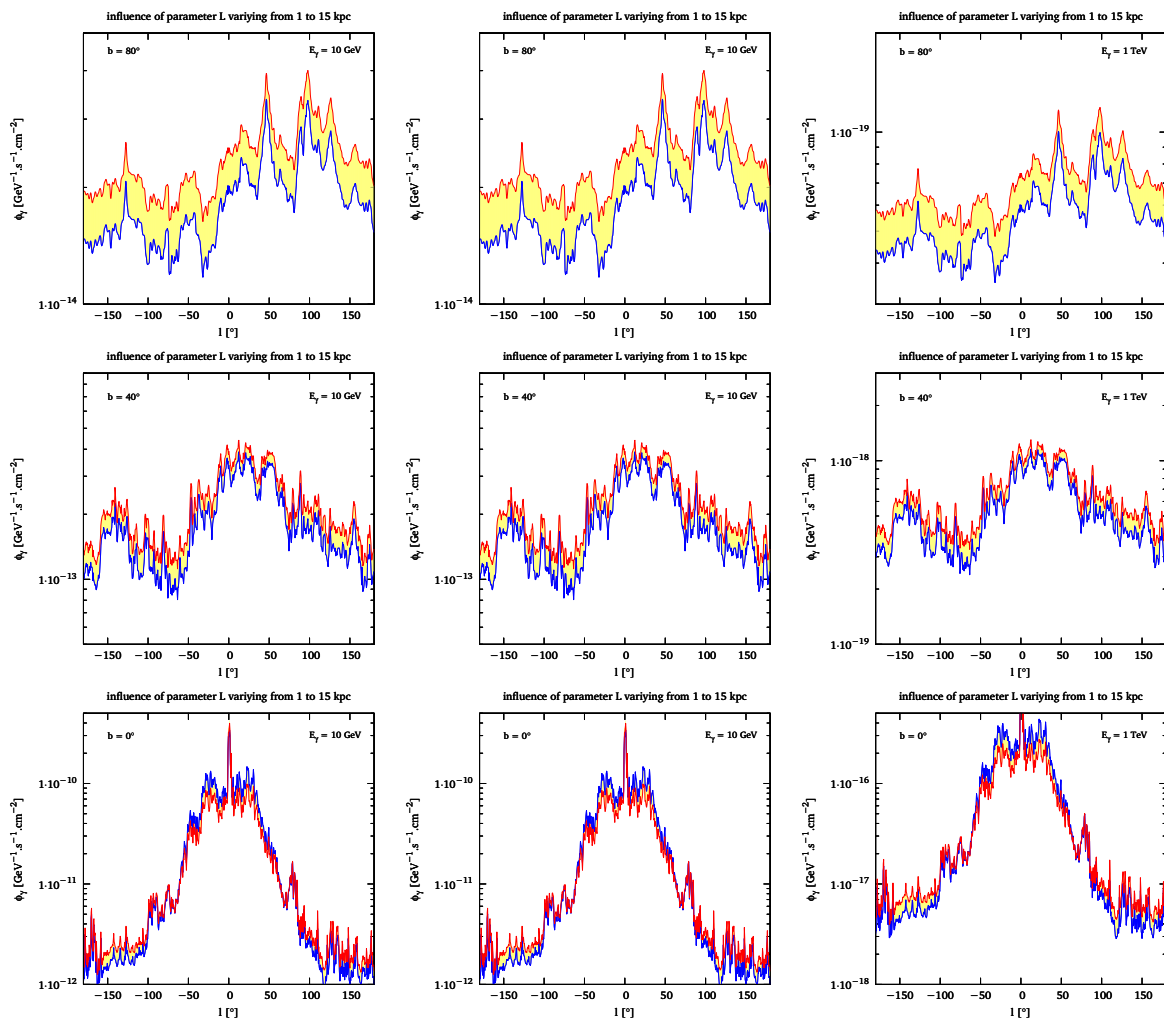


Figure 7.4: Photon flux at the Earth as a function of Galactic longitude  $\ell$  for various values of the Galactic latitude  $b$  and the energy. The value of  $L$  has been varied from 1 kpc to 15 kpc. From left to right  $E_\gamma = 10$  GeV, 100 GeV and 1 TeV. From top to bottom  $b = 80, 40,$  and  $0^\circ$ .

where  $\frac{d\sigma}{d\epsilon_\gamma}(\epsilon_\gamma, \epsilon_e)$  is the differential cross section for emitting a Bremsstrahlung photon of energy  $\epsilon_\gamma$  within  $d\epsilon_\gamma$  in the scattering of an electron of initial energy  $\epsilon_e$  and final energy  $\epsilon_e^f = \epsilon_e - \epsilon_\gamma$ . The fine structure constant is noted  $\alpha$  and the classical electron radius  $r_0 = \alpha\hbar/cm_e$ . In the case of an unshielded charge  $Ze$  one has:

$$\frac{d\sigma}{d\epsilon_\gamma}(\epsilon_\gamma, \epsilon_e) = 4Z^2\alpha r_0^2 \frac{\epsilon_e^2 + \epsilon_e^{f2} - \frac{2}{3}\epsilon_e\epsilon_e^f}{\epsilon_e^2\epsilon_\gamma} \left( \ln \frac{2\epsilon_e\epsilon_e^f}{mc^2\epsilon_\gamma} - \frac{1}{2} \right).$$

In the case of a shielded charge (an atom) one gets:

$$\frac{d\sigma}{d\epsilon_\gamma}(\epsilon_\gamma, \epsilon_e) = \alpha r_0^2 \frac{(\epsilon_e^2 + \epsilon_e^{f2}) \Phi_1 - \frac{2}{3}\epsilon_e\epsilon_e^f \Phi_2}{\epsilon_e^2\epsilon_\gamma},$$

where the  $\Phi$ 's are of the form:

$$\Phi_i = 4 \int f_i(q; \epsilon_e, \epsilon_\gamma) \zeta(q) dq.$$

In this expression  $q$  stands for the momentum transfer  $\vec{q} = \vec{k}_e - \vec{k}_e^f - \vec{k}_\gamma$ . Introducing the parameter  $\delta = \frac{km_e^2 c^4}{2\epsilon_e \epsilon_e^f}$ , the functions  $f_i$  are:

$$f_1(q) = \frac{(q-\delta)^2}{q^3}$$

$$f_2(q) = \frac{q^3 + 3\delta^2 q(1 - 2 \ln \frac{q}{\delta}) - 4\delta^3}{q^4}.$$

The scattering factor  $\zeta(q)$  is different for each species. For hydrogenic species (H or He<sup>+</sup> for instance) with electric charge  $Z$  it reads:

$$\zeta(q) = (Z - 1)^2 + 2Z \left( 1 - \frac{1}{(1 + 4\alpha^2 Z^2 q^2)^2} \right),$$

whereas in the helium-like case it is:

$$\zeta(q) = (Z - 2)^2 + 4Z \left( 1 - \frac{1}{(1 + 4\alpha^2 q^2)^2} \right) - \left( 1 - \frac{1}{(1 + 4\alpha^2 q^2)^4} \right).$$

Moreover, Blumenthal & Gould [3] provide some simplifying formulæ in some cases.

Because this is an electrodynamic process, there is no cross-section uncertainty like for the  $\pi^0$  decay case. The uncertainty concerning the gas distribution is exactly the same but the one concerning the projectile (electrons and positrons) flux is much larger in this case than for protons.

Describing the electron flux everywhere in the Galaxy is not an easy task. Computing it at the Sun's position like I showed in chapter 6 was quite tedious already. But collecting the precise data concerning all the sources in the Galaxy (and not only in the two nearby kpc) cannot seriously be considered. This means that the high energy structures, due to the discreteness of the sources cannot be described. We will need to satisfy ourselves with only a smooth distribution of sources, like for the protons. Not only this, but also the energy loss term, I have considered as homogeneous in the diffusion zone, needs to be described more accurately. This is not even done by full numerical codes so it is clearly far beyond the reach of our semi-analytical methods. This will clearly result in some discrepancy with the data. However the effect may not be that important as the large fluctuations are expected nearby the sources, now these cosmic ray sources are also  $\gamma$  ray sources so they may prevent any measurement of the diffuse emission in their direction. Furthermore, as we have seen, electrons are much more sensitive to propagation parameters than protons, this means that one should expect more striking features in the Bremsstrahlung emission. This conclusion must however be weakened because Bremsstrahlung is expected to dominate over  $\pi^0$  decay only at low energy ( $\lesssim 10$  MeV) where Fermi will not provide data. Even though it is not a dominating contribution, it represents nevertheless around 10% of the total  $\gamma$  emission.

Unfortunately I am not able to present a more precise discussion of this subject for the moment.

### 7.1.3 Gamma rays from inverse Compton scattering

As already explained in section 5.2.2.2, inverse Compton scattering is the interaction between a fast electron and a low energy photon. Hence it does not trace the Galactic gas distribution as the two previously discussed processes, but rather the interstellar radiation field. If one considers a relativistic electron with energy  $\epsilon_e = \gamma m_e c^2$  interacting with a photon of energy  $\epsilon$  (within  $d\epsilon$ ), after averaging over the angles (both electron cosmic ray flux and interstellar radiation field are more or less isotropic), one gets the energy spectrum of the outgoing photon (with energy  $\epsilon_\gamma$ ) already given in equation 5.13:

$$\frac{dN_{\text{coll}}}{dt d\epsilon d\epsilon_\gamma} = \frac{3\sigma_T c}{4\gamma^2} \frac{dn(\epsilon)/d\epsilon}{\epsilon} \times \left\{ 1 + 2q \left( \ln q - q + \frac{1}{2} \right) + \frac{(1-q)}{2} \frac{(\Gamma q)^2}{(1+\Gamma q)} \right\}, \quad (7.4)$$

The used notations are explained in equations 5.15. To get the outgoing photon flux, one has to multiply this quantity by the incoming electron flux and integrate it over the electron energy  $\gamma m_e c^2$  and the initial photon energy  $\epsilon$ . If we consider, as we did in section 5.2.2.2, that  $dn(\epsilon)/d\epsilon$ , the initial photon density in the energy range  $d\epsilon$ , is a sum of black body radiation spectra of the form (including the two polarization states):

$$\frac{dn}{d\epsilon} = 2 \times \frac{4\pi\epsilon^2}{(2\pi\hbar c)^3} (e^{\epsilon/(k_b T)} - 1)^{-1},$$

one gets:

$$q_\gamma(\vec{x}, \epsilon_\gamma) = \frac{3\sigma_T m_e}{\pi\hbar^3} \int d\gamma \frac{\Phi_e(\vec{x}, \gamma)}{\gamma^2} \times \sum_b \int \left\{ 1 + 2q \left( \ln q - q + \frac{1}{2} \right) + \frac{(1-q)}{(1+\Gamma q)} \frac{(\Gamma q)^2}{2} \right\} \frac{\epsilon d\epsilon}{e^{\epsilon/(k_B T_b)} - 1}, \quad (7.5)$$

where we sum over the various black body spectra of temperature  $T_b$  the interstellar radiation field is made of. The integral over  $\epsilon$  goes from  $\epsilon_m = \frac{\epsilon_\gamma}{4\gamma^2} \frac{\gamma m_e c^2}{\gamma m_e c^2 - \epsilon_\gamma}$  to  $\epsilon_\gamma$  and the one over  $\gamma$  goes from  $\epsilon_\gamma m_e c^2$  to  $\infty$ .

The integral over  $\epsilon$  is very small as long as  $\gamma^2 \lesssim 4\epsilon_\gamma/k_B T$ , so this means that, at a given  $\gamma$  ray energy  $\epsilon_\gamma$  each black body of the interstellar radiation field does not necessarily contribute, this would depend of the energy of the electrons present in the Galaxy. Some values are given in table 7.1 for further discussion.

One difficulty arises from the fact that model M1 for the interstellar radiation field is valid only in the Solar vicinity. This is good enough to compute the local electron flux but is it also valid for the rest of the Galaxy? There is a model of the interstellar radiation field of the Galaxy proposed by Porter *et alii* [22] and available online. However implementing it is not possible when computing the energy losses during electron propagation because this would breakdown the cylindrical symmetry we need to solve the propagation equation. It would also destroy any hope of working with a semi-analytic method. How much of a problem is this? Obviously concerning the cosmic microwave background, it is not an issue. The stellar light is expected to vary radially like the stellar population but not too much in the vertical direction.

BB	$\epsilon_\gamma = 1$ GeV	$\epsilon_\gamma = 10$ GeV	$\epsilon_\gamma = 50$ GeV
CMB	527 GeV	1.7 TeV	3.7 TeV
IR	151 GeV	479 GeV	1.1 TeV
Stellar	49 GeV	155 GeV	348 GeV
UV1	15 GeV	48 GeV	107 GeV
UV2	11 GeV	35 GeV	78 GeV
UV3	6 GeV	18 GeV	40 GeV

Table 7.1: Minimal electron energy  $\gamma m_e c^2$  to be responsible for the emission of a photon of energy  $\epsilon_\gamma$  through inverse Compton scattering on each blackbody component of the interstellar radiation field. The various black body here refer to model M1 of table 5.2

The ultra violet light, created by very large stars obviously follows their population, but it is also absorbed by molecular gas so its variation can be quite important. Infra-red light, is due to gas heated by ultra violet light. Hence when one increases, the other one decreases. Integrated over the path of an electron this can be smoothed, but the exact corresponding error remains to be sized.

Concerning the inverse Compton emission itself it would be possible to implement the full description at the cost of CPU time. Of course this would help taking into account a more realistic description of the Galaxy, but in the same time it might emphasise the error due to averaging the interstellar radiation field for the propagation. Indeed, where the photon density increases, electrons lose more energy so they are less numerous, but at the same time the inverse Compton radiation is increased by the same amount, so one error actually partially cancels out the other one. Moreover this choice is also easier and faster to implement, though it is not enough to have reliable predictions, it can already give us some insight to the inverse Compton map of the sky.

I am not able to produce such a map at the moment but hopefully will very soon, in the frame of our project on diffuse emission. Indeed, this component is clearly underdominant at low latitudes but can be relevant at high latitudes, where there is no gas to produce  $\pi^0$  nor Bremsstrahlung. This may reveal an interesting way to size the half height of the diffusive halo  $L$ .

#### 7.1.4 Gamma rays from radio isotopes

When Paul Villard first discovered the  $\gamma$  rays in 1900, it was not in the sky but in his laboratory, where he was studying radioactive decay of radium. Indeed many unstable isotopes, during their decay chain produce  $\gamma$  rays. When a radio-element decays through  $\alpha$  or  $\beta$  decay, for some species, the daughter nucleus appears in an excited nuclear state. It can then pass from this excited state to its ground state by emitting one or more (if there are intermediate excited levels)  $\gamma$  rays. Hence nuclear  $\gamma$  rays are always monochromatic lines, which makes them quite difficult to detect for a telescope, as it requires a very good energy resolution. Of course, unstable radio-elements are not very abundant in the interstellar medium nevertheless some of them are continuously created by the spallation processes of cosmic rays which produce all the

non cosmogenic elements like for instance the cosmic boron. This allowed a nuclear  $\gamma$  ray line astronomy to appear nevertheless, see review by Diehl *et alii* [7] for instance.

The isotopes which are short lived do not have the time to propagate so their gamma emission should trace the position where the spallation process occurs. Actually observations of  $^{56}\text{Co}$ ,  $^{57}\text{Co}$ , and  $^{44}\text{Ti}$  probe recent supernovæ rather than the interstellar gas because during the explosion of the star many nuclear reactions occur. The sensitivity of modern instrument is not good enough yet to detect the same emission from the interstellar gas.

More long lived isotopes like  $^{26}\text{Al}$  and  $^{60}\text{Fe}$  have life times of millions of years so they can propagate in the diffusive halo before they decay. A diffuse emission of  $^{26}\text{Al}$  has indeed been observed and maybe the  $^{60}\text{Fe}$  one as well. One issue however is that propagating cosmic rays would not emit  $\gamma$  ray lines because of Doppler effect, this would lower the signal even more and make the analysis more complex. However the energies at which these decays produce  $\gamma$  rays is of the order of the MeV hence quite lower than the range of interest for dark matter. Finally an other issue is the poor knowledge we have of the very long lived but under-abundant isotopes, indeed their life time is very difficult to measure in a laboratory, so one cannot exclude that some isotopes have been forgotten. This component can hence be neglected.

### 7.1.5 The extra galactic component

Finally there is a last standard component: the so called extra galactic one. Fermi[2], as well as the previous experiments observes an isotropic diffuse  $\gamma$  emission which is generally understood as being of extra galactic origin. This component exhibits a power law spectrum over more than three decades in energy (from a few tens of MeV up to 100 GeV) with a power law index of  $2.41 \pm 0.05$ . It is considered to be the superposition of many unresolved extra galactic sources such as active galactic nuclei, starburst galaxies and  $\gamma$  ray bursts [6]. This view is consistent with the fact that these objects, look larger and larger when one looks at them with increasing energy in X-rays.

However the extra galactic origin of this isotropic component remains to be proven, indeed one cannot exclude yet that this isotropic component is not due to inverse Compton scattering of cosmic rays over Solar photons [19, 20] or is due to the fact that the diffusive halo is very large [16] or produced by dark matter annihilation or decay. A better understanding of these components would be useful to answer the question of the origin of this isotropic emission.

### 7.1.6 Gamma rays from dark matter

This discussion comes from reference [5]. As said before, dark matter can be responsible for two categories of  $\gamma$  rays. On one hand, those we could call primaries, and which are created by the annihilation or the decay of the dark matter particle. The corresponding flux depends on the annihilation (or decay) channel and can vary a lot. One striking signal would be a line emission, for instance if the dark matter particle annihilates directly into a pair of photons. Except for some nuclear decays, no astrophysical process is known to do so, so, unless very unluckily it is at an energy very close to a radioactive line, this would be easy to interpret. The issue lies more in the technical aspects of such a detection, indeed detecting a monochromatic line requires very acute energy resolution. For radioactive lines it is possible to do because we

know exactly at which energy to look for but a blind search is much more challenging. Even worse, this kind of emission would follow the spatial distribution of dark matter, *id est* would be very concentrated in the centre of the Galaxy. This is a problem because many complex phenomena occur in the Galactic centre (accretion around the central black hole, very large stars etc...) and seeing a signal emerge from this crowded region would be extremely difficult.

On the other hand, there are also secondary gamma rays which are produced by the electrons created during the annihilation of the dark matter particle. Of course this *indirect indirect* detection would difficultly be taken as a strong detection evidence by itself, however it can be an interesting hint. Furthermore correlate this with data concerning leptons cosmic rays at the Earth or any other messenger could help a lot.

One way to give strength to this kind of research would be to look at the morphology of the gamma emission. Indeed, though the spectrum can be difficult to disentangle from the astrophysical background, the position of the emission could be quite different. This has been proposed in reference [4]. Moreover, it may be a way to distinguish annihilating dark matter from decaying one.

Let us consider a very simple model for which a dark matter particle annihilates or decays into  $e^+/e^-$  pairs. Because of internal Bremsstrahlung, this kind of dark matter should also directly produce  $\gamma$  rays but I will neglect this and consider that only electrons and positrons are created at an energy  $E_{inj}$ . If the dark matter particle is annihilating,  $E_{inj}$  is the mass of the particle, in the decaying case,  $E_{inj}$  is half the mass. The aim is to see whether the shape of the inverse Compton emission received at the Earth is different in both cases and if it is possible to distinguish them.

Here are some pixelised maps (with a pixel size of 1 square degree) that have been obtained for the different scenarios. Fig. 7.5 illustrates (for both annihilating and decaying dark matter models) the difference between the propagation patterns that arise by fixing  $E_{inj}$  to 100 GeV and considering three gamma ray energies  $E_\gamma = 1, 10, 50$  GeV. As one can see, in both cases, the  $e^+, e^-$  which give rise to 1 GeV photons have propagated further than those giving rise to 50 GeV photons. These features are common to all the maps including those obtained for heavier dark matter candidates. Note that the propagation parameters that have been considered to obtain this map correspond to the *Med* set.

In Fig. 7.6,  $E_\gamma$  has been fixed to 10 GeV and three values of  $E_{inj}$  have been considered (for both annihilating and decaying dark matter). Interpreting the features for the particular case  $E_{inj} = 500$  GeV and  $E_\gamma = 10$  GeV is non-trivial. As it can be seen from Table 7.2, because the interstellar radiation field is made of more than one black body spectra,  $\gamma$ -emission at 10 GeV can actually be due to more than one electron population. Indeed bright emission at 10 GeV could be due either to electrons of  $\gtrsim 20$  GeV interacting with UV light or to  $\gtrsim 500$  GeV electrons interacting with IR light. Hence as seen in Fig. 7.6, the 10 GeV emission is nearly spherical, and could be interpreted either as an injection energy of  $\sim 20$  GeV or of  $\sim 500$  GeV, leading to very different interpretations concerning the mass of the dark matter particle. However this degeneracy can be lifted by looking at higher energies, as electrons injected at 20 GeV cannot produce gamma rays of 50 GeV. This threshold effect stresses how important it is to look at different  $\gamma$ -ray energies and to compare the various morphologies in order to understand the properties of the dark matter.

In the third column, the difference between the two normalised maps (decays – annihila-

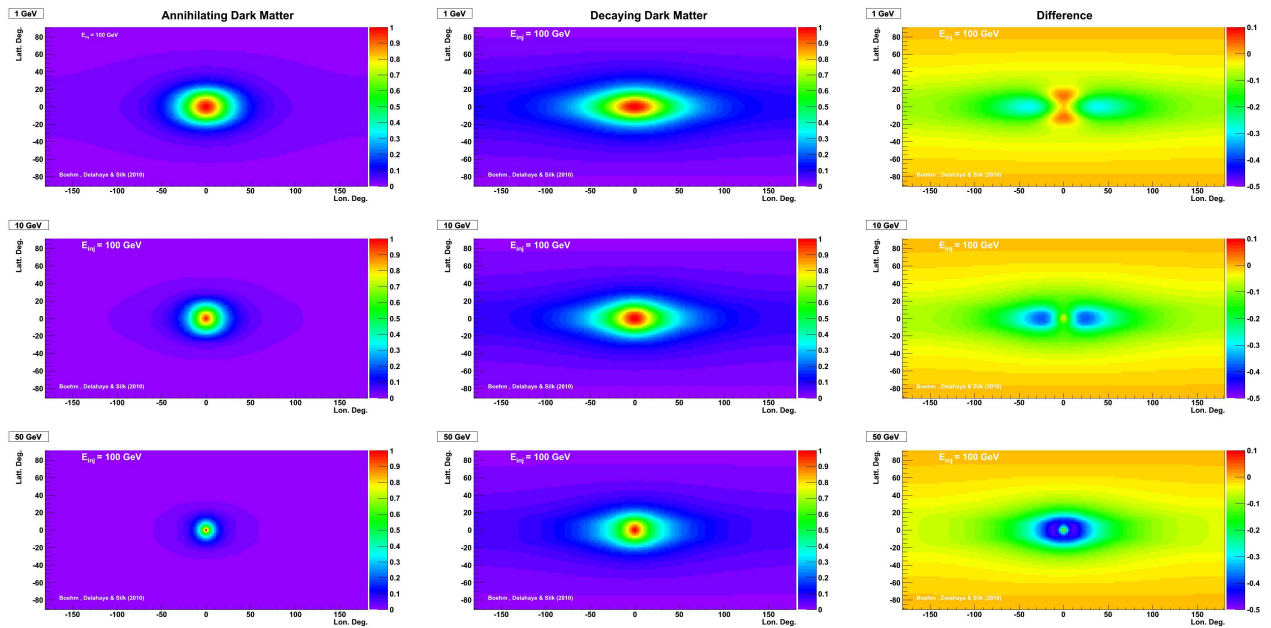


Figure 7.5: Annihilating versus decaying dark matter for  $E_{inj} = 100$  GeV and  $E_\gamma = 1, 10, 50$  GeV. In these figures, fluxes are normalised to the central bin so as to make the comparison of propagation length obvious. Ellipticities at 0.1 of the central bin intensity are equal to  $\epsilon_{10} = 0.46, 0.30, 0.83$  and  $\epsilon_{10} = 0.77, 0.72, 0.67$  for annihilating versus decaying dark matter respectively.

tions) is displayed so as to exhibit the differences of morphology between these two emission models. The negative values at the Galactic Centre confirm that the  $e^+, e^-$  from annihilating dark matter are mainly produced locally and that propagation cannot completely smooth out the contrast with respect to decaying dark matter electrons and positrons.

In Fig. 7.7, we show the effect of the propagation parameters for  $E_{inj} = 1$  TeV. As expected, the  $e^+e^-$  diffuse far more for the set of propagation parameters *MAX* (for which  $L = 15$  kpc) than for *min*. Although it may be possible to constrain decaying versus annihilating dark matter in the *MAX* and *Med* cases, it seems impossible to distinguish these two scenarios in the *min* case. To compare the propagation features between annihilating and decaying scenarios, it is useful to look at the ellipticities  $\epsilon_{10}$  and  $\epsilon_2$  of the  $\gamma$ -emission. To define these quantities, we measure the size of the semi-major axis  $a_{10}$  (or  $a_2$ ) and the semi-minor axis  $b_{10}$  (or  $b_2$ ) of the ellipse that has an intensity of one tenth (or one half) of the maximal intensity. Ellipticity is then defined as  $1 - b/a$ . Hence  $\epsilon$  is equal to zero for a perfect circle and to 1 for a horizontal line. This quantity is a nice way to get rid of the absolute intensity of the signal, which depends on the particle physics model, and to quantify the morphology of the signal. The results are summarised in the caption of Fig. 7.5, 7.6, 7.7 and Table 7.2. Only for larger masses, or in the optimistic case where the sensitivity allows us to measure  $\epsilon_{10}$ , is discrimination possible, especially for the *MAX* propagation model.

Clearly propagation is important for both dark matter scenarios, but although the propagation features differ, they are difficult to distinguish if the propagation parameters correspond to *min* (and perhaps *Med*) rather than to *MAX*. This is, in fact, surprising, as one might have

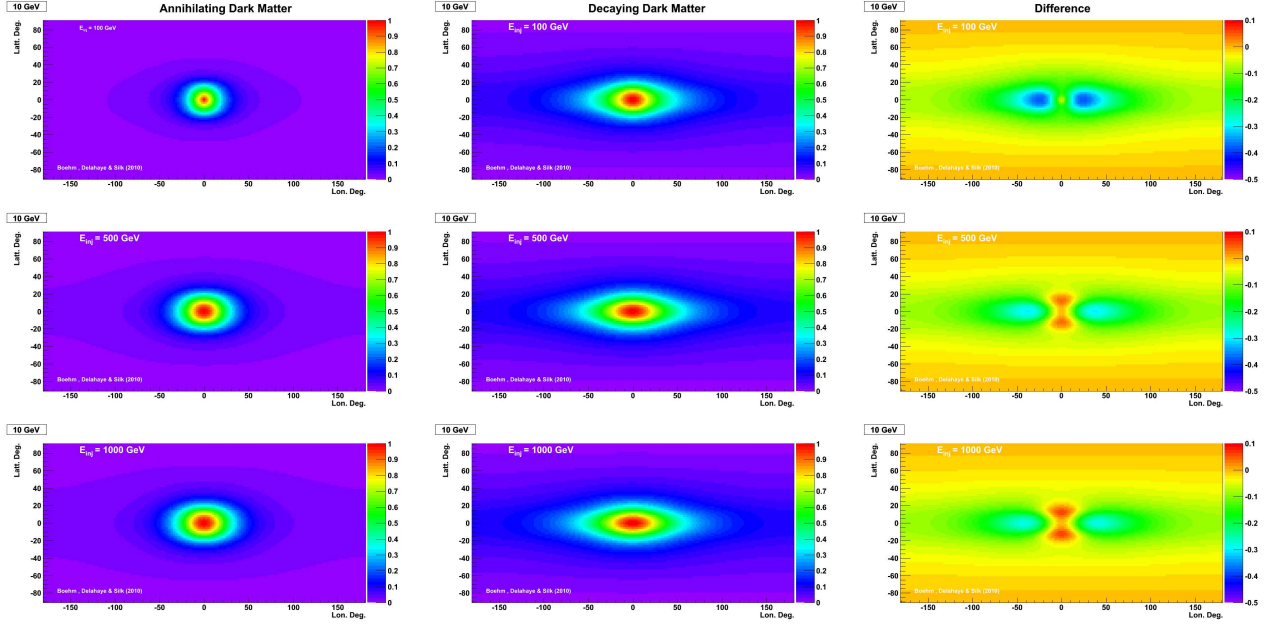


Figure 7.6: Annihilating versus decaying dark matter for  $E_\gamma = 10$  GeV and  $E_{inj} = 100, 500, 1000$  GeV. Ellipticities at 0.1 of the central bin intensity are equal to  $\epsilon_{10} = 0.30, 0.44, 0.47$  and  $\epsilon_{10} = 0.72, 0.76, 0.79$  for annihilating versus decaying dark matter respectively.

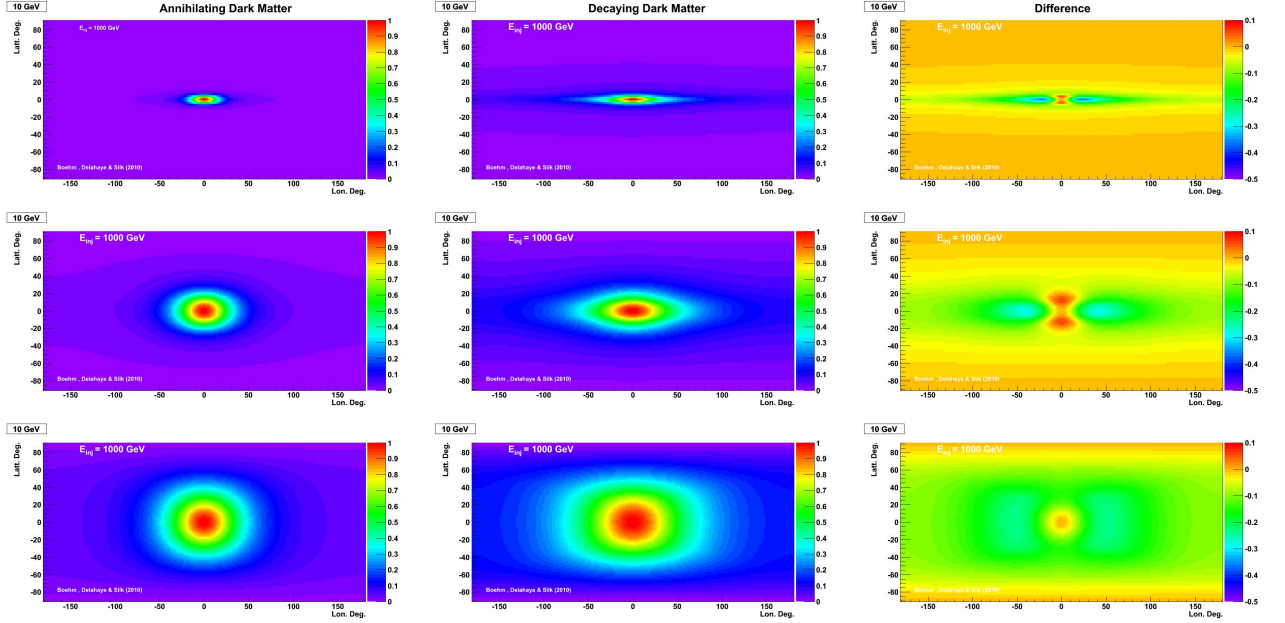


Figure 7.7: Annihilating versus decaying dark matter for  $E_{inj} = 1$  TeV and the *min Med* and *MAX* propagation parameters. Ellipticities at 0.1 of the central bin intensity are equal to  $\epsilon_{10} = 0.76, 0.47, 0.32$  and  $\epsilon_{10} = 0.92, 0.79, 0.60$  for annihilating versus decaying dark matter respectively.

$E_{inj} = 100\text{GeV}$ $E_{\gamma} = 10 \text{ GeV}$	parameter	$a_{10}$	$b_{10}$	$\epsilon_{10}$	$a_2$	$b_2$	$\epsilon_2$
annihilation	<i>min</i>	18.5	6.	0.68	6.5	4	0.38
decay	<i>min</i>	94.5	8	0.92	19	4	0.79
annihilation	<i>Med</i>	36	25	0.30	13.5	12	0.11
decay	<i>Med</i>	128.5	35.5	0.72	31.5	15.5	0.51
annihilation	<i>MAX</i>	55.5	46.5	0.16	19.5	18.5	0.05
decay	<i>MAX</i>	179.5	67.5	0.62	42.5	33.5	0.21

Table 7.2: Ellipticity for  $E_{\gamma} = 10 \text{ GeV}$  and  $E_{inj} = 100 \text{ GeV}$  for 0.1 (subscript 10) and 0.5 (subscript 2) of the intensity.

expected these two scenarios, which involve distinct powers of the dark matter density, to differ significantly. Actually, in the *min* case, detection would be extremely challenging since most of the signal would be hidden by Galactic sources. In some cases, the interstellar radiation field can make the Galactic Centre bright enough to be misinterpreted as  $e^+e^-$  with a lower injection energy.

We have verified that changing the energy density of the interstellar radiation field has little effect as the increase of the  $\gamma$  ray emissivity is partially compensated by the electron density decrease due to increased energy losses. Varying the intensity of the magnetic field within reasonable values has also little impact as synchrotron emission is not the main energy loss term in most cases. In both cases the impact is mainly on the intensity and not on the ellipticity.

One could also think about the  $\pi^0$  production by protons and anti-protons produced by dark matter, but this would clearly be dominated by the astrophysical contribution and very difficult to detect, as it has to follow the gas distribution. Of course, one could imagine a  $\gamma$  bright molecular cloud very far from classical cosmic ray sources, which would be illuminated by a dark matter substructure nearby. But this sounds too unlikely to be considered seriously.

As a conclusion, I would say that clearly a lot of interesting information is to be expected in the  $\gamma$  sky and we are lucky to have the Fermi space telescope giving more and more insight to this interesting problem every day. First observations of the diffuse emission have already been released [1] at intermediate latitudes.

The AMS experiment should also be of great interest in this field as it will have a better energy resolution than Fermi so the search for energy lines should be easier.

## 7.2 Radio emission from synchrotron radiation

As we have seen in section 5.2.2, while propagating in the diffusive halo, electrons do not only lose energy through inverse Compton scattering and Bremsstrahlung but also through synchrotron emission. As we will see later, considering the value of the Galactic magnetic field and the electron energy we are interested in, the corresponding emission is in the radio range. In the radio astronomer's jargon, the diffuse emission is called the continuum. This continuum

is made of four main components: the cosmic microwave background, the thermal emission of the dust of the Galaxy (which includes some lines), the Bremsstrahlung (or free free) already described previously and the synchrotron emission of relativistic electrons. On top of that, of course, many localised sources populate the radio sky, such as supernova remnants, pulsars, stars and extra galactic objects like for instance radio galaxies and active galactic nuclei.

High frequency maps allow to subtract the dust emission (see for instance Finkbeiner *et alii* [8]). This component is sub dominant at the frequencies below 60 GHz but is important above. At the large frequencies the Planck satellite is currently looking (up to 857 GHz), this component will dominate, at least where the dust is.

At high latitude, though the synchrotron is quite weak, it is the most important foreground. Hence its understanding is of utmost importance for Planck data analysis. The method consists in using low frequency maps like the 408 MHz map by Haslam *et alii* [11, 12] and, supposing this map is dominated by synchrotron emission, and that the electrons causing it have a power-law spectrum, in extrapolating it at the observed frequency.

As we have seen in chapter 6, the electron flux is not exactly a power law, especially at low energy. And the importance of Planck for cosmology pleads for a serious estimation of the synchrotron emission and its uncertainties. Not only this, but making use of this new set of data, one may eventually get a new insight in the cosmic ray electron propagation model. Indeed synchrotron emission could be a wonderful tool to probe convection and diffusive reacceleration which solar modulation prevents us to look at.

Let us see how synchrotron emission works. Again I will refer to the very nice work of Blumenthal & Gould [3]. When speaking about synchrotron photon, it is more natural to speak in terms of frequency  $\nu$  rather than in term of energy.

$$q_\gamma(\vec{x}, \nu) = 4\pi \sum_{\text{proj}=p,\alpha} \int \Phi_{\text{proj}}(\vec{x}, \epsilon_{\text{proj}}) J(\vec{x}, \nu, \epsilon_{\text{proj}}) d\epsilon_{\text{proj}}, \quad (7.6)$$

where  $J(\vec{x}, \nu, \epsilon)$ , the emission at frequency  $\nu$  by a photon of energy  $\epsilon$  reads [3, 9, 17]:

$$J(\nu) = \frac{1}{2} \int_0^\pi d\theta \sin(\theta) \int d\nu P_s(\nu, \theta), \quad (7.7)$$

where an average is performed over the pitch angle  $\theta$ , and where the synchrotron radiation power is defined as:

$$P_s(\nu, \theta) = \frac{\sqrt{3} e^3 B_\perp}{4 \pi \epsilon_0 m c} x \int_{x/\sin(\theta)}^\infty dy K_{5/3}(y)$$

$$\text{with } x \equiv \frac{\nu}{\nu_s}; \nu_s \equiv \frac{3}{2} \gamma^2 \nu_c = \frac{3 e B_\perp \gamma^2}{4 \pi m}. \quad (7.8)$$

Actually only the component of the magnetic field which is orthogonal to the line of sight contributes to the received emission. It is far too complex to know the exact direction of the magnetic field everywhere in the Galaxy (see discussion in appendix D.2) and because in most places the random component of the magnetic field is dominating, I will take  $B_\perp \sim B$ .

---

<sup>d</sup><http://lambda.gsfc.nasa.gov/>

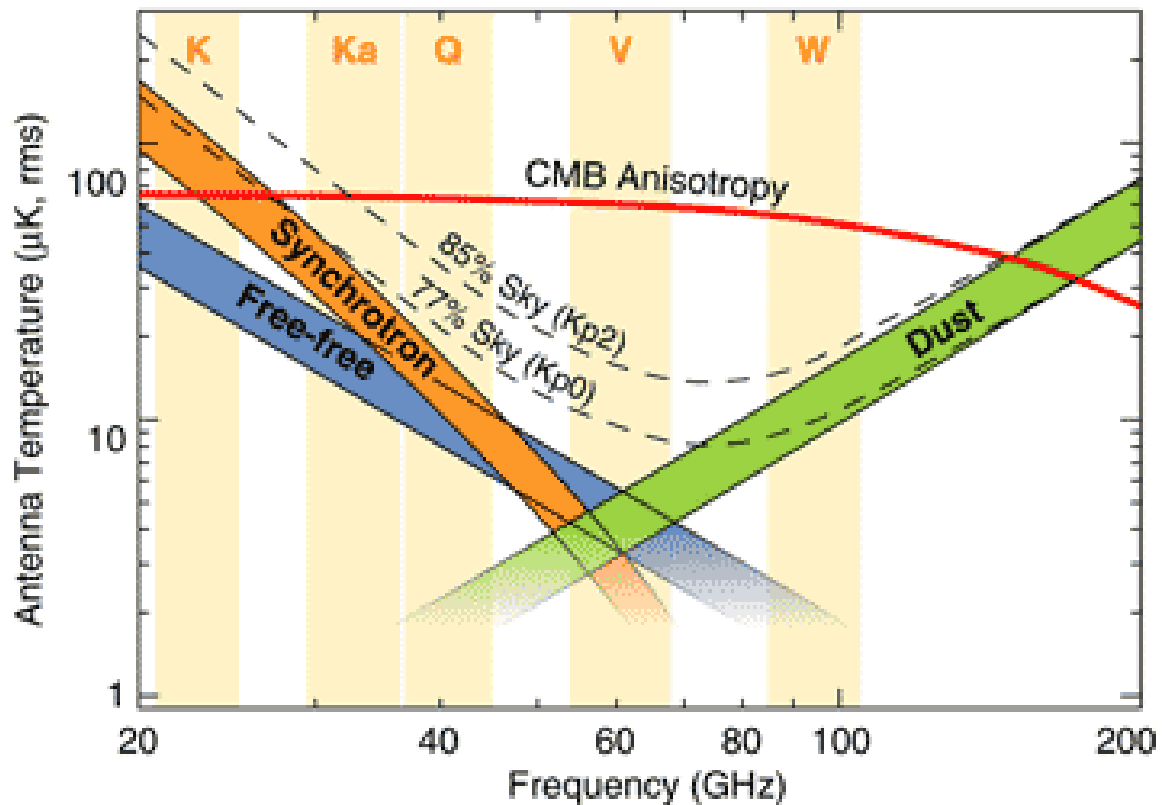


Figure 7.8: The radio sky spectrum. This plot is taken from the Legacy Archive for Microwave Background Data Analysis (LAMBDA)’s website<sup>d</sup>

The parameter  $\nu_s$ , which is called the synchrotron peak frequency, corresponds to the average frequency of the synchrotron emission arising when an electron of Lorentz factor  $\gamma$  interacts with a magnetic field  $B$ , and is  $\propto \gamma^2 \nu_c$ , where  $\nu_c$  is the cyclotron frequency. Indeed, the function  $P_s(\nu)$  happens to be extremely peaked around  $\nu = \nu_s$ . While it is possible to derive the radio flux from the emissivity, it is a bit more striking to work out a more intuitive expression, which actually turns out to provide a fair approximation [17]:

$$q_\gamma(\vec{x}, \nu) = \frac{[b(E_s)]_{\text{sync}}}{ch\nu} \Phi_{\text{proj}}(\vec{x}, E_s) . \quad (7.9)$$

Here, the electron energy  $E_s$  is determined by the relation  $\nu = \nu_s$ . Notice that only the synchrotron part of the electron energy loss rate  $b(E)$  appears and that we also neglect the possible re-absorption of the synchrotron emission. Since  $b(E)$  is the energy lost by an electron, it corresponds to the energy of the emitted photon, so that the factor  $1/(h\nu)$  allows to infer the number of photons.

As for the inverse Compton, it is not possible to take into account the spatial structure of the Galactic magnetic field while propagating the electrons. Nonetheless, it is possible to implement a magnetic map for the synchrotron emission only.

I am not able to present a full estimation of the Galactic synchrotron emission at the moment, with a thorough discussion of the uncertainties due to sources and propagation. This

point notwithstanding, a rapid discussion about the synchrotron emission due to dark matter created electrons, similar to the previous discussion for inverse Compton is not very difficult.

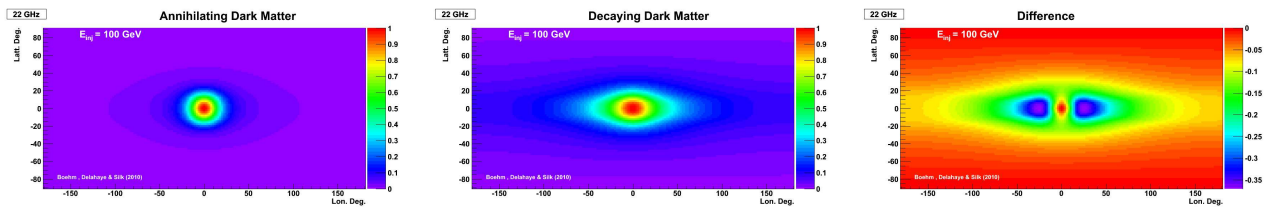


Figure 7.9: Similar to the first line of figure 7.6, but for synchrotron emission observed at 22 GHz.  $\epsilon_{10} = 0.29$  and  $\epsilon_{10} = 71$  for annihilating versus decaying dark matter respectively.

As it can be seen from figure 7.9, synchrotron emission for annihilating and decaying dark matter are not quite the same. Actually, this plot is extremely similar to one of the inverse Compton emission of the same electron population at 10 GeV. However, the signal is much easier to interpret, as there is no threshold effects like for the various black bodies of inverse Compton. Indeed the emission is monochromatic (*id est* for one photon energy, there is one electron energy producing it). Moreover, the Planck satellite has a much better angular resolution than Fermi and it will focus a lot on foreground studies, so synchrotron maybe a more interesting way to go in the future. Note that this plot has been done considering a homogeneous magnetic field in the diffusion zone, structures of the Galactic magnetic field may also enhance the differences between annihilating and decaying dark matter. More details will be soon presented in an on going work [5].

While propagating throughout the Galaxy, cosmic electrons and positrons radiate photons at many different energies. These photons are a unique tool to access the cosmic ray fluxes anywhere in the diffusive halo. As I have shown it is interesting for whom pursues dark matter detection and also for our proper understanding of cosmic rays. For instance the synchrotron emission at large frequencies is a probe for low energy cosmic rays which are inaccessible otherwise because of Solar modulation. Both  $\gamma$  and radio observations offer possibility to look to a broader picture of cosmic ray and to get rid of our poor knowledge of the very local sources.

Though we are really at the limit of the possibilities of analytical methods, it is nevertheless extremely useful to understand acutely the impact of each input, that only a fast analytical method can allow.

## Bibliography

- [1] Abdo, A. A., Ackermann, M., Ajello, M., *et alii* . 2009, Physical Review Letters, 103, 251101 [171](#)
- [2] Abdo, A. A., Ackermann, M., Ajello, M., *et alii* . 2010, Phys. Rev. Lett., 104, 101101 [167](#)
- [3] Blumenthal, G. R. & Gould, R. J. 1970, Reviews of Modern Physics, 42, 237 [162](#), [164](#), [172](#)
- [4] Boehm, C., Delahaye, T., & Silk, J. 2010, ArXiv e-prints [1003.1225](#) [168](#)

- [5] Boehm, C., Delahaye, T., & Silk, J. 2010, in preparation [167](#), [174](#)
- [6] Dermer, C. D. 2007, in American Institute of Physics Conference Series, Vol. 921, The First GLAST Symposium, ed. S. Ritz, P. Michelson, & C. A. Meegan, 122–126 [167](#)
- [7] Diehl, R., Prantzos, N., & von Ballmoos, P. 2006, Nuclear Physics A, 777, 70 [167](#)
- [8] Finkbeiner, D. P., Davis, M., & Schlegel, D. J. 1999, ApJ, 524, 867 [172](#)
- [9] Ginzburg, V. L. & Syrovatskii, S. I. 1965, ARA&A, 3, 297 [172](#)
- [10] Godfrey, G. L. & The GLAST Working Group. 1993, in Towards a Major Atmospheric Cherenkov Detector – II for TeV Astro/Particle Physics, ed. R. C. Lamb, 145–+ [156](#)
- [11] Haslam, C. G. T., Klein, U., Salter, C. J., *et alii* . 1981, A&A, 100, 209 [172](#)
- [12] Haslam, C. G. T., Salter, C. J., Stoffel, H., & Wilson, W. E. 1982, A&AS, 47, 1 [172](#)
- [13] Huang, C., Park, S., Pohl, M., & Daniels, C. D. 2007, Astroparticle Physics, 27, 429 [158](#), [159](#), [161](#)
- [14] Kamae, T., Karlsson, N., Mizuno, T., Abe, T., & Koi, T. 2006, ApJ, 647, 692 [158](#), [159](#)
- [15] Kamae, T., Karlsson, N., Mizuno, T., Abe, T., & Koi, T. 2007, ApJ, 662, 779 [158](#), [159](#)
- [16] Keshet, U., Waxman, E., & Loeb, A. 2004, Journal of Cosmology and Astro-Particle Physics, 4, 6 [167](#)
- [17] Longair, M. S. 1994, High energy astrophysics. Vol.2: Stars, the galaxy and the interstellar medium, ed. Longair, M. S. [172](#), [173](#)
- [18] Lorimer, D. R. 2004, in IAU Symposium, Vol. 218, Young Neutron Stars and Their Environments, ed. F. Camilo & B. M. Gaensler, 105–+ [161](#)
- [19] Moskalenko, I. V., Porter, T. A., & Digel, S. W. 2006, ApJ, 652, L65 [167](#)
- [20] Moskalenko, I. V., Porter, T. A., & Digel, S. W. 2007, ApJ, 664, L143 [167](#)
- [21] Particle Data Group, Amsler, C., Doser, M., *et alii* . 2008, Physics Letters B, 667, 1 [156](#)
- [22] Porter, T. A., Moskalenko, I. V., Strong, A. W., Orlando, E., & Bouchet, L. 2008, ApJ, 682, 400 [165](#)
- [23] Schwalb, O., Pfeiffer, M., Berg, F., *et alii* . 1994, Physics Letters B, 321, 20 [159](#)
- [24] Stecker, F. W. 1970, Ap&SS, 6, 377 [157](#)
- [25] Stephens, S. A. & Badhwar, G. D. 1981, Ap&SS, 76, 213 [157](#), [158](#), [159](#)
- [26] Tibaldo, L., Grenier, I. A., & for the Fermi/LAT collaboration. 2009, ArXiv e-prints [161](#)



# Chapter 8

## Dark matter indirect detection

Si la matière grise était plus rose, le monde aurait moins les idées noires.

*Pierre Dac*

Here I stand, after three years of thesis looking for indirect signals of dark matter annihilation or decay in the cosmic rays. What did we learn in these last three years, rich in new data?

I have shown that most of the data we have can be taken into account by standard astrophysical sources, without any fine tuning of the parameters. But this does not mean that dark matter does not exist, and neither that some of the signal that has been measured does not come from dark matter. The absence of signal itself can also be used to learn something about the dark matter particle properties.

In this chapter, I will hence present the recent data and then discuss them, first with a very arguable a priori in favour of a dark matter interpretation and second with less parti pris.

## 8.1 Recent Data

### 8.1.1 PAMELA

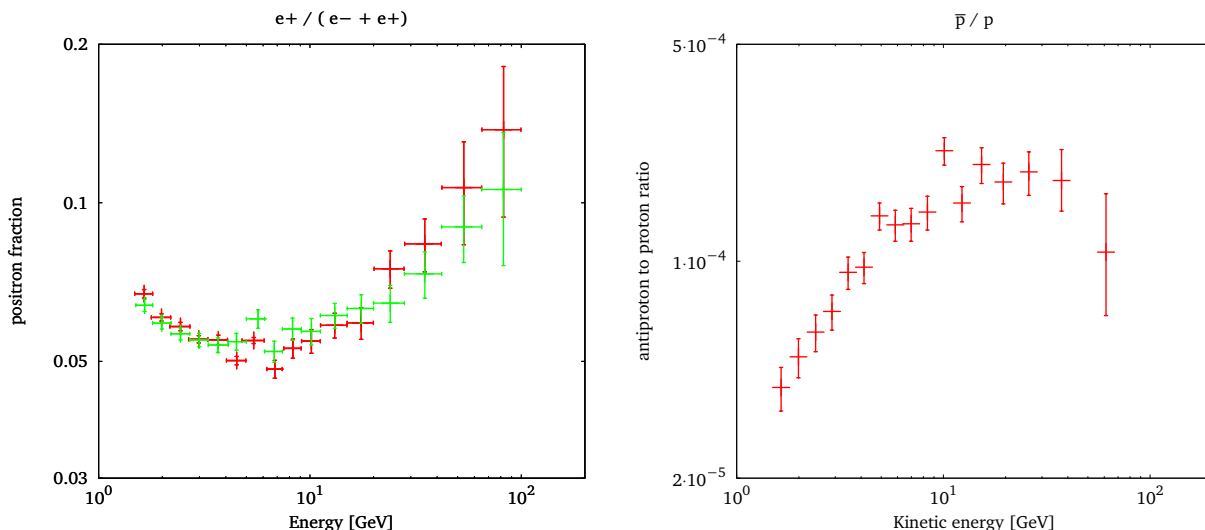


Figure 8.1: *Left*: Positron fraction as measured by the PAMELA experiment in 2008 (ref. [3] in red) and in 2010 (reference [2] in green). *Right*: Anti-proton to proton ratio measured by PAMELA [4].

The Pamela collaboration has released two sets of data of major importance. They are displayed in figure 8.1. The first one (reference [3] which has then been modified according to reference [2]), concerns the positron fraction, that is the positron flux divided by the sum of the electron and positron fluxes; while the second one [4] concerns the anti-proton to proton ratio. The reason the results are given as ratios is that it allows to suppress most of the systematic errors (at least it is hoped so), however this makes the interpretation more delicate as it implies two physical quantities.

In figure 8.1 one can also see the theoretical predictions for both these quantities. Concerning the positron fraction, only secondary positrons have been considered here, this is equivalent to

say that, for one reason or another, pulsars do not contribute. It is striking to see that the theoretical expectations reproduce extremely well the anti-proton to proton ratio but quite poorly the positron fraction, especially at high energy.

### 8.1.2 ATIC

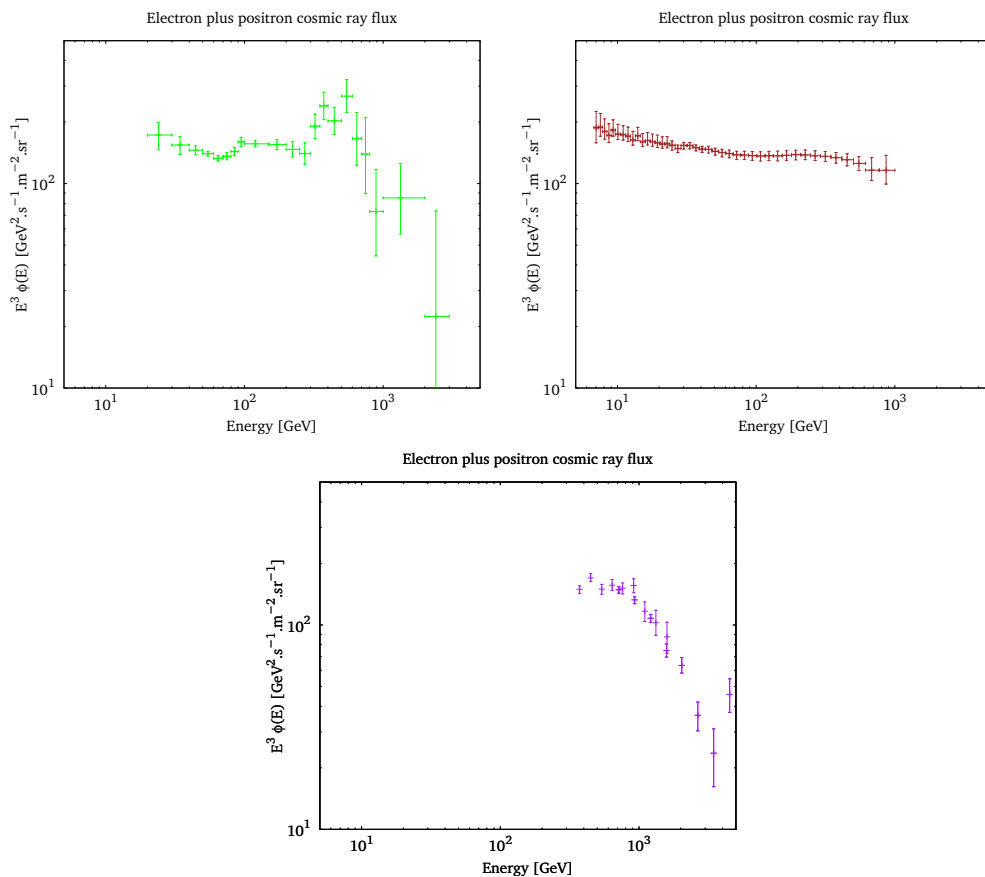


Figure 8.2: Electron plus positron fluxes, as measured by ATIC [17] (top left), Fermi [1, 34] (top right) and HESS [5, 6] (bottom).

Having no magnet, the ATIC experiment cannot distinguish electrons from positrons. The measurement the collaboration provided in 2008 [17], is then the sum of both. As one can see from figure 8.2, the data clearly exhibit a peak around 600 GeV and maybe also another less prominent feature around 150 GeV. As we have seen in chapter 6, local sources could produce some features in the electron flux, however, the ATIC collaboration itself, suggested [17] that this could be interpreted as a dark matter annihilation signal.

### 8.1.3 Fermi

Little time after the ATIC result, Fermi satellite published an equivalent measurement [1] with much better statistics. These results are displayed in the top right panel of figure 8.2. Some month later, new results [34], at lower energies were also published. There clearly is a disagreement between the two experiments. It is not clear however, if this discrepancy comes from a too gross energy resolution of the Fermi apparatus or misidentified protons by the ATIC collaboration. I will consider both interpretations in the following.

Preliminary results shown by the PAMELA collaboration in some conferences seem to indicate that, at least at low energy, PAMELA electron flux is consistent with Fermi electron plus positron flux. However no data being publicly available I will not consider them.

Fermi is not designed for electron cosmic ray study but rather for  $\gamma$  ray observation. According to Dobler *et alii* [21], it seems that Fermi observation of the  $\gamma$  diffuse emission reveals a *haze*, around the Galactic centre, which could not be explained by astrophysical sources. However, one should know that Linden & Profumo [31] have stressed that systematic effects from the method used by the previous authors prevent any firm conclusion concerning the existence of this haze.

### 8.1.4 HESS

A few months before Fermi, the HESS collaboration presented an estimation [6] of the electron plus positron flux at very high energy ( $\geq 714$  GeV), then, the very same day Fermi presented their electron flux, HESS presented an extension [5] to lower energies ( $\geq 373$  GeV). HESS does not see the ATIC feature either, but again has a poor energy resolution. More interesting is the high energy cut-off observed around a few TeV. As explained in chapter 6, this provides us a unique way to estimate the maximal energy at which electrons are accelerated by supernova remnants.

### 8.1.5 WMAP

The Wilkinson Microwave Anisotropy Probe has been designed to measure the cosmic microwave background. In doing so it also offered a very nice map of the radio sky. After subtracting the various foregrounds described in section 7.2, Finkbeiner [25] showed that we were left with an extra component centred around the Galactic centre which could be the synchrotron emission of dark matter originated electron cosmic rays (see for instance Hooper *et alii* [27]).

## 8.2 An optimistic interpretation

What can we learn from these data if we adopt the hypothesis that dark matter is responsible for some or all of the features seen in the data?

As stressed by Cirelli *et alii* [18] and Donato *et alii* [22], it is difficult to understand how dark matter could produce a rise of the positron fraction and not one of the anti-proton to proton ratio. Indeed most annihilation channels produce anti-protons along with the positrons.

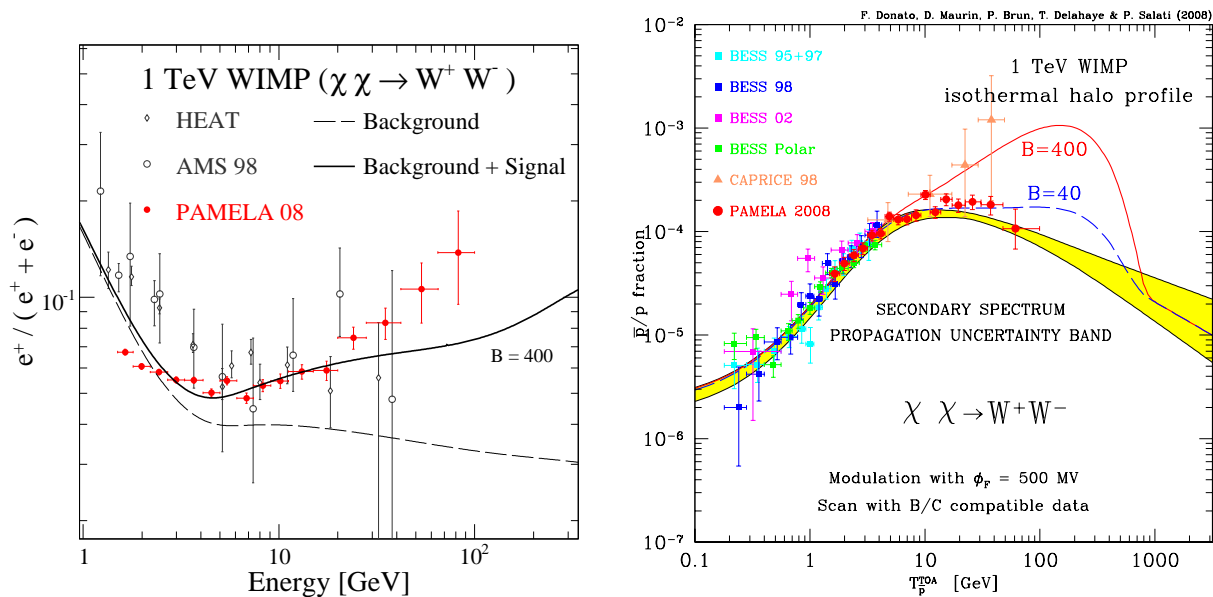


Figure 8.3: The fiducial case of a 1 TeV particle annihilating into a  $W^+W^-$  pair is featured. In the left panel, the positron signal which this dark matter species yields has been increased by a factor of 400, hence the solid curve and a marginal agreement with the PAMELA data. Positron fraction data are from HEAT [9], AMS-01 [7, 8] and PAMELA [2]. If the so-called Sommerfeld effect [26] is invoked to explain such a large enhancement of the annihilation cross section, the same boost applies to antiprotons and leads to an unacceptable distortion of their spectrum as indicated by the red solid line of the right panel.

As it has been showed in section 6.3, with a typical annihilation cross section  $\langle\sigma_{\text{ann}}v\rangle$  of  $3 \times 10^{-26} \text{ cm}^3\text{s}^{-1}$ , a dark matter particle does not produce enough positrons to reproduce the increasing trend observed in  $e^+/(e^+ + e^-)$  data [2], so that a significant enhancement of the annihilation rate is necessary. One can for instance advocate for the Sommerfeld effect [26] as a plausible mechanism to significantly increase the dark matter particle annihilation cross section in the non-relativistic regime prevailing today in galactic haloes.

Let us then consider a generic 1 TeV particle annihilating into  $W^+W^-$  pairs and boost  $\langle\sigma_{\text{ann}}v\rangle$  by a factor of 400 in order to get the solid line in the left panel of Fig. 8.3. Although an annihilation cross section of  $1.2 \times 10^{-23} \text{ cm}^3\text{s}^{-1}$  is possible should non-perturbative effects be involved, the consequences on antiprotons are drastic. The red solid curve in the right panel of Fig. 8.3 features an unacceptable distortion of the  $\bar{p}$  spectrum. The dark matter positron signal cannot be enhanced without playing havoc with the  $\bar{p}$  measurements.

One way out of this issue is to say that the value of 400 assumed for the positron signal of Fig. 8.3 could arise from the combined effects of dark matter clumpiness and  $\langle\sigma_{\text{ann}}v\rangle$  enhancement. If a generous factor of 10 is assumed for the former (a marginally acceptable value [29]) the latter does not exceed 40. Unlike positrons which are produced locally, the antiprotons detected at the Earth originate from a large region of the Milky Way halo over which substructures may not be as important as in our vicinity. The  $\bar{p}$  flux may not be much enhanced by the presence of dark matter clumps so that a value of 40 would apply in that case to the antiproton

boost. The corresponding blue long-dashed line in the right panel of Fig. 8.3 features a fairly acceptable  $\bar{p}$  spectrum.

But how probable is it that a single local clump gives the wanted boost to positrons without over-shooting the  $\bar{p}$  data? This question has been addressed in reference [14].

In this letter, we re-assessed [13, 19, 28] the possibility that a single nearby dark matter clump contributes substantially to the lepton anomalies. Particular attention is paid to cosmic ray propagation. We adjust the clump distance  $D$  and luminosity  $L$  in order to reproduce the PAMELA, ATIC and Fermi data. The probabilities of these clump configurations are calculated based on the cosmological N-body simulation Via Lactea II [20], which allows us to quantify for the first time how unlikely a sufficiently bright nearby cold dark matter subhalo is. We eventually comment about the interplay between the dark matter particle properties and the clump parameters. As an illustration, we point out extreme configurations where these mutual effects lead to subtle, but relevant modulations of the dark matter signal.

The positron flux at the Earth  $\phi_{e^+} = \phi_{e^+}^{\text{sec}} + \phi_{e^+}^{\text{s}} + \phi_{e^+}^{\text{c}}$  results here from three contributions. The astrophysical background  $\phi_{e^+}^{\text{sec}}$  is provided by the secondary species produced by primary cosmic rays impinging on the interstellar material and was computed as in section 6.1. The smooth dark matter halo contribution  $\phi_{e^+}^{\text{s}}$ , was computed as in section 6.2.2.1 and finally the clump contribution as in section 4.3.1.5 The Galactic dark matter halo density  $\rho_{\text{s}}$  has been borrowed from the results of the Via Lactea-II simulation, with a spherical profile featuring an inner (outer) logarithmic slope of -1.24 (-3) and a 28.1 kpc scale parameter. At variance with the other parts of this thesis, here, the local density  $\rho_{\odot}$  is taken equal to  $0.37 \text{ GeV cm}^{-3}$  and the galactocentric distance of the Earth is  $r_{\odot} = 8.5 \text{ kpc}$ . A discussion of these values can be found in appendixes C.2 and D.3. One should keep in mind that we are in an optimistic scenario. Furthermore, as clumps are treated here as point-like objects<sup>a</sup> located in the galactic plan. Actually putting them above or bellow the plan would not have much impact as long as their distance from the Sun  $D$  is small compared with the diffusive halo half thickness  $L$ .

The annihilation cross-section of the dark matter particles under scrutiny is set equal to  $\langle\sigma v\rangle = 3 \times 10^{-26} \text{ cm}^3 \text{ s}^{-1}$ . This canonical value matches a thermal production of dark matter in the early universe, in the framework of standard cosmology. We also consider 100 GeV and 1 TeV dark matter particles as benchmark cases. Finally, we focused here on leptophilic species and considered either a pure  $e^+e^-$  annihilation final state (positronic line) or an equal production of charged leptons  $e^{\pm} + \mu^{\pm} + \tau^{\pm}$ . We also tried to use models featuring pure  $b\bar{b}$  or  $W^+W^-$  annihilation final state, but we disregard them since the configurations required for the clump to fit the data was then extremely unlikely ( $p < 10^{-6}$ ).

The particle physics framework being set, we perform fits to the PAMELA, ATIC and Fermi data which include a smooth dark matter component plus a contribution from a dark matter subhalo whose luminosity  $L$  and distance from the Sun  $D$  are free parameters. For PAMELA, we compute the positron fraction  $\phi_{e^+}/\phi_{e^+} + \phi_{e^-}$  where we use for  $\phi_{e^-}$  the observed cosmic ray electron flux measured by AMS [8] parametrised by Casadei & Bindi [15]. As regards ATIC and Fermi, we derive the total lepton flux  $\phi_{e^+} + \phi_{e^-}$ , assuming that the electron background  $\phi_{e^-}^{\text{back}}$  is given at high energy by the Casadei & Bindi fit and adding a dark matter contribution equal to  $\phi_{e^+}^{\text{s}} + \phi_{e^+}^{\text{c}}$ . Solar modulation is implemented using the force field approximation (see section 5.4) with a Fisk potential of 300 MV. As far as ATIC is concerned, we reproduce the observed feature

---

<sup>a</sup>The scale radii of the clumps are always much smaller than the typical lepton diffusion length.

in the case of a 1 TeV dark matter particle if we assume a dark matter clump with luminosity  $2.98 \times 10^9 M_{\odot}^2 \text{ pc}^{-3}$  lying at a distance of 1.52 kpc from the Earth. The ATIC excess was reported in [17] where it was interpreted as evidence for a 620 GeV Kaluza-Klein species. We confirm that result in the case of a positronic line. In that case, no satisfying adjustment can be found adding a nearby subhalo, dark matter particle annihilations take place only inside a smooth Galactic dark matter distribution and the required cross-section  $< \sim 10^{-24} \text{ cm}^3 \text{ s}^{-1}$ , *id est* two orders of magnitude above our canonical value. As we shall see in the following, the fit to the Fermi data points towards an incredibly bright clump. Indeed, the feature seen by Fermi is not very peaked and quite spread and requires, because of propagation effect, both a very large mass for the dark matter particle and a quite far away clump. We therefore exclude the combination of a thermal relic density plus a bright clump as a solution to this puzzle and we do not mention this case when dealing with other messengers. All parameters found in the best-fit cases are displayed in Tab. 8.1.

	PAMELA		ATIC	Fermi
$m_{\chi}$ (GeV)	100	1 000	1 000	2500
$e^+/e^-$	$1.22 - 1.07 \cdot 10^7$	$0.78 - 3.56 \cdot 10^9$	$1.52 - 2.98 \cdot 10^9$	$2.68 - 5.53 \cdot 10^{10}$
$e^{\pm} + \mu^{\pm} + \tau^{\pm}$	$0.44 - 2.51 \cdot 10^7$	$0.27 - 9.84 \cdot 10^9$	$0.25 - 8.78 \cdot 10^9$	$2.81 - 2.17 \cdot 10^{11}$

Table 8.1: Best fit values of the  $(D; L)$  couple in units of  $(\text{kpc}; M_{\odot}^2 \text{ pc}^{-3})$  for various dark matter particle masses and annihilation channels.

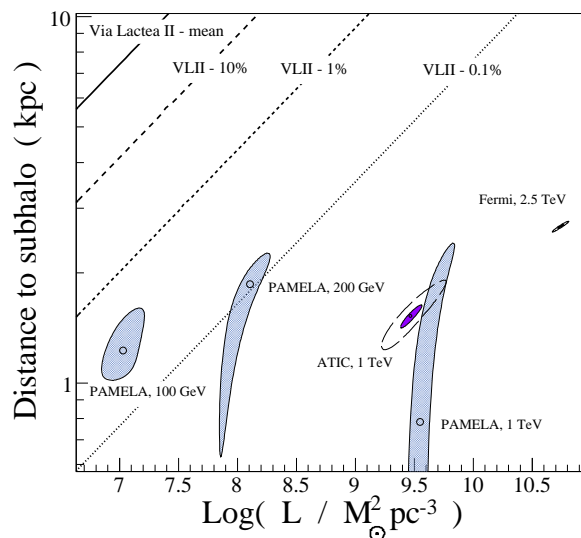


Figure 8.4: Best fit results in a clump luminosity-distance plane for different configurations, together with probabilities inferred from Via Lactea-II results.

Fig. 8.4 shows the probability of having the nearest dark matter clump of luminosity  $L$  within a distance  $D$  from the Sun. The abundance of nearby clumps and their properties are taken directly from the Via Lactea-II (VL-II) simulation [20]. The high mass and force resolution, combined with a physical time step criterion [39], allow VL-II to resolve subhalos

even in the dense environment near the solar circle. The mean separation of subhalos with peak circular velocities  $V_{\max} > 5 \text{ km.s}^{-1}$  is 9.6 kpc and their luminosities are

$$L = 7.91 \times 10^5 M_{\odot}^2 \text{ pc}^{-3} \left( \frac{V_{\max}}{5 \text{ km.s}^{-1}} \right)^3 \sqrt{\frac{c_V}{2 \times 10^6}}. \quad (8.1)$$

For comparison, the smooth VL-II main halo has a luminosity of  $L = 3.4 \times 10^9 M_{\odot}^2 \text{ pc}^{-3}$ , while the total luminosity is about 10 times higher [20]. At a given  $V_{\max}$  we assume a log-normal distribution of luminosities with factor of 3 scatter, motivated by the substantial variance in the concentration  $c_V$  found in nearby subhalos [20]. The bold line gives the median distances calculated from a random sample of observer positions. The long-dashed, dashed and dotted lines stand for the 10th 1st and 0.1st percentiles, respectively. The points represent the locations of the best fits to the data in the  $L - D$  plane while the surrounding contours display the  $1\sigma$  excursions around these best fit values (as well as  $3\sigma$  for ATIC and Fermi). We find that clumps fitting the PAMELA, ATIC and Fermi data are far from the natural values indicated by VL-II. The most probable configuration is the PAMELA fit with a 100 GeV dark matter particle, which is inside the Via Lactea  $3\sigma$  contours. That configuration is found in 0.37% of all realizations. However, this scenario cannot accommodate ATIC data because  $m_{\chi}$  is too small. Increasing the mass of the dark matter particle requires even brighter and less likely clumps at  $D \simeq 1$  kpc. As illustrated by the different PAMELA fit contours of Fig. 8.4, the parameter degeneracy also increases as  $m_{\chi}$  gets higher. Basically, the PAMELA measurements do not constrain the spectral shape of the signal above 100 GeV and leave more lever-arm to the fits when dark matter particles are heavy. For TeV dark matter particles, there are clump properties which reproduce both the ATIC and PAMELA excess (see Fig.8.4), and such a source would be well within the reach of Fermi (Tab. 8.1). However, in the standard cold dark matter halo it is very unlikely to exist ( $p \simeq 3 \times 10^{-5}$ ). A dark matter spike or a higher cross-section would be required to get the needed luminosity from a smaller, more probable nearby subhalo. As shown in Tab. 8.1, the corresponding subhalo is within reach of Fermi. Concerning the best fit to the Fermi data, it points at the need for a clump that should be brighter than the whole Milky Way. We can safely associate a zero probability to this configuration. Note finally that the Via Lactea II contours extrapolate at lower values of the distance and clump luminosity. The corresponding clumps are not of particular interest for this particular study as for mean Via Lactea clumps, the natural luminosity decreases faster than what we gain from placing the clump closer.

This study has been performed based on the results of the Via Lactea II simulation and one could wonder if its conclusions would still hold another N-body simulation would be used. It is not easy to answer this question because it is not usual for the people who work on these simulations to express the clumps distribution in terms of probability of existence as a function of the distance with respect to the Sun as one can see if figure 8.4. However, even though from one simulation to another, there are some differences, especially at very low mass elements, the size of the clumps required by the data being so large, I do not believe that important variations would be observed with another N-body simulation. Of course a simulation including baryons, if it shows that tidal effects are very efficient in destroying the clumps crossing the gas disk, would lead to even more pessimistic conclusions.

As a conclusion, one could say that the optimistic scenario is not ruled out but is extremely

unlikely, it requires both extreme situations for the dark matter distribution in the Galaxy and its particle physics properties. Compared with how natural it was to obtain the same results with classical astrophysical sources, it seems very awkward to persist in this scenario.

### 8.3 A more realistic interpretation

If one considers that all the current data we have can be accounted for by astrophysical sources, cannot we learn something about dark matter nonetheless? More precisely in reference [11], we have wondered if the absence of signal in present cosmic ray data could be of any use for the dark matter particle research at the Large Hadron Collider.

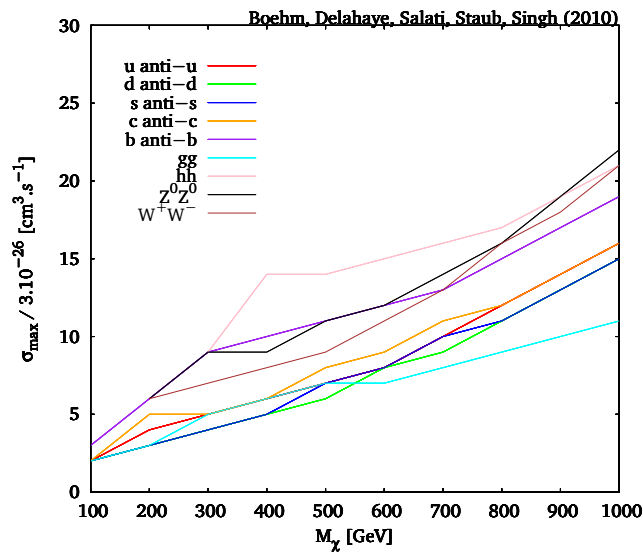


Figure 8.5: Maximum allowed annihilation cross section (in units of  $3 \times 10^{-26} \text{ cm}^3 \text{ s}^{-1}$ ) for each channel, constrained not to exceed the PAMELA anti-proton measurements.

In this Letter, we concentrated on the antiproton measurements which are subject to neither speculation nor controversial interpretation. The lack of excess in antiprotons may suggest that the dark matter particle couplings to quarks must be small. However, in reference [11], we proposed to find what is the maximal coupling that is allowed by the PAMELA antiproton data to verify whether this assertion is true or not.

For simplicity, we based our analysis on a generic dark matter model where the dark matter particle  $\chi$  is directly coupled to a Standard Model quark  $q$  and a heavy coloured partner  $F_q$ . Inspired by supersymmetry, we focused this Letter on a Majorana dark matter particle so  $F_q$  is in fact a scalar (and would be equivalent to a squark in supersymmetry). This approach is generic enough to be applied to other types of dark matter. However a complete survey of the various possibilities (including scalar dark matter species  $\chi$  and fermionic partner  $F_q$ ) was beyond the scope of this work (although we anticipate that the results presented here are fairly general).

In “Standard” supersymmetry, the heavy states  $F_q$  are produced mostly through gluon-gluon fusion proton-proton collisions. They are expected to decay into missing energy (the

dark matter) and a jet (corresponding to the quark  $q$ ) shortly after production. Hence, this channel constitutes an important source for dark matter particles production at the Large Hadron Collider.

However, if the direct dark matter couplings to quarks are larger than usually expected in “standard” supersymmetry, new channels could open up with  $qq$ ,  $q\bar{q}$  and  $qg$  interactions, thus providing new possible signatures and increasing the discovery potential at the Large Hadron Collider. Hence the importance of characterising the direct dark matter couplings to quarks in light of PAMELA antiproton data.

To constrain the dark matter characteristics (mass and properties of the particles to which dark matter is coupled), we proceeded as follows: we first calculated the antiproton flux at the Earth expected from conventional spallations and dark matter annihilations. The latter depends on the  $\chi - q - F_q$  left and right couplings  $c_L^q$  and  $c_R^q$  which we want to constrain from the PAMELA antiproton measurements. We then considered a variety of annihilation channels and derived the maximal cross sections allowed by the PAMELA antiproton data. Results are expressed in units of the canonical thermal value of  $3 \times 10^{-26} \text{ cm}^3 \text{ s}^{-1}$  and referred to as the boost factor hereafter. Because couplings to  $u$ ,  $d$  and  $s$  quarks are already severely constrained by direct detection, we focused on  $c$  and  $b$  quarks. With the help of a Monte Carlo Markov Chain (MCMC), we delineated the region of parameter space which saturates the upper bound on the boost. Finally, we determined the number of events associated with  $qq \rightarrow FF$ ,  $q\bar{q} \rightarrow FF^*$  and  $qg \rightarrow F\chi$  production at the Large Hadron Collider and discussed the prospects for detecting dark matter related signatures at the Large Hadron Collider.

### The PAMELA antiproton constraints

Just like positrons, the antiproton flux at the Earth arises from two sources: secondary antiprotons are produced by the interactions of high energy cosmic ray protons and helium nuclei with the gas of the galactic disc, and primary antiprotons generated by the annihilation of hypothetical dark matter species in the halo of the Milky Way. To compute both signals, we have followed the method described in appendixes B.2 and B.3.2, indeed, antiprotons and protons propagate in the same way in the diffusive halo. As regards the secondary component, we have used the same local proton and helium nuclei fluxes as in Donato *et alii* [22] together with the radial distribution of supernova remnants given by [37] to retropropagate these fluxes all over the diffusive halo.

Concerning the primaries, we have considered a dark matter halo computed by [20] with a local density of  $\rho_{\odot} = 0.3 \text{ GeV cm}^{-3}$ . The distance from the Earth to the Galactic centre was taken to be 8.5 kpc. The annihilation cross section was set to the conventional thermal value mentioned above. We have determined the boost by which that value can be increased without exceeding the PAMELA data. We have scanned the dark matter particle mass from 100 GeV to 1 TeV and considered different annihilation channels. For each channel, the antiproton spectrum before propagation has been calculated with the PYTHIA 6.4 program [36]. The results are summed up in figure 8.5.

These constraints are quite severe. However, antiproton flux calculations suffer from a lot of uncertainties and changing some of the choices we made may affect these results. As recalled in appendix C.2 the local value of the dark matter density is not very well constrained and in fact lies in  $[0.2; 0.9] \text{ GeV.cm}^{-3}$ . The primary antiproton flux being proportional to the square of the local density, one can divide all the results of figure 8.5 by a factor ranging from  $\sim 0.4$

to 9. The other uncertainties are summed up in Tab. 8.2.

	ref	1	2	3	4	5	6	7
100	3	28	2	4	4	6	2	2
200	6	60	3	8	6	11	3	4
300	9	90	4	13	10	18	5	5
400	10	130	4	15	11	22	7	6
500	11	150	4	16	12	23	9	6
600	12	170	4	18	13	26	10	7
700	13	190	5	20	15	29	11	8
800	15	220	6	23	17	33	12	9
900	17	240	6	26	19	38	14	10
1000	19	270	7	29	21	42	16	11

Table 8.2: Maximum boost (*id est* annihilation cross-section in units of the canonical thermal value of  $3 \times 10^{-26} \text{ cm}^3 \text{ s}^{-1}$ ) allowed by the PAMELA antiproton measurements for various dark matter particle masses in the case of annihilation into  $b\bar{b}$  pairs (pink line of figure 8.5) when varying the parameters. Cases 1 and 2 correspond to extreme propagation parameters in agreement with B/C (respectively *min* and *MAX*). For case 2 the boost has been rounded to the closest decade. Cases 3, 4 and 5 correspond to various dark matter halo profiles : NFW [33] (3), Moore [32] (4) and an isothermal cored profile (5) – see table 4.3. Cases 6 and 7 correspond to alternative fits of the injection proton and helium nuclei spectra respectively proposed by [23] and Shikaze *et alii* [35].

One should notice that for most cases, the constraints come from the point of highest energy (61.2 GeV) published by PAMELA. This point is the one that suffers the biggest statistical error and its systematic error is unknown yet. Hence the results may change with future publication of new PAMELA data. Indeed the current data correspond to only 500 days of data collection starting the 15th of June 2006 but the satellite is still in orbit and should carry on taking data for at least few more months. Moreover, the uncertainty related to the injection spectra should diminish as soon as absolute fluxes for protons and antiprotons are published. Finally, new data are also expected from PAMELA for the boron to carbon ratio that should help us limit the uncertainties on propagation parameters. Some of these data have been shown in some conferences but no result has been published yet.

### The MCMC and the allowed region in parameter space

To find the region of parameter space that reproduces the boost factor as determined in the previous section, we performed a Markov Chain Monte Carlo (MCMC) search. The free parameters of our benchmark model are a priori the dark matter mass, the masses of the heavy scalar partners  $F_q$ , and their couplings  $c_L^q$  and  $c_R^q$  to Standard Model quarks  $q$ . Since  $b$ -quarks are a bit easier to tag (and direct detection experiments indicate that the couplings to  $u$ ,  $d$  and  $s$  quarks must be suppressed), we shall only focus on predictions associated with  $b$  quarks. The only free parameters of interest are therefore the mass  $m_{F_b}$  of the  $b$ -coloured state  $F_b$ , the dark matter mass  $m_\chi$  and its couplings to the  $b$  quark, namely  $c_L^b$  and  $c_R^b$ . Our purpose was to explore this four dimensional parameter space in order to delineate the regions where the boost is close to the maximal value allowed by PAMELA. The expression of the annihilation cross section has been borrowed from [12]. The ranges of masses and couplings which we considered

lie between [100, 2500] GeV and [0.01, 3] respectively. A larger upper limit on the couplings would induce a loss of perturbativity.

Translating the maximal boost  $B_{\max}$  found in the previous paragraph into regions of the parameter space is tricky. For this purpose, we have built a Monte Carlo Markov Chain which explores the parameter space and attributes to each of its points a likelihood depending on whether or not the boost is close to the maximal value allowed by PAMELA. This method allows to rapidly delineate the interesting regions. The likelihood is defined as a Gaussian centred on  $B_{\max}$  with width  $v_B = 0.1$ . Results are displayed in the correlation plots of Fig. 8.6. The first four rows correspond to the parameters  $m_\chi$ ,  $m_{F_b}$ ,  $c_L^b$  and  $c_R^b$  of the model while the fifth one is the reconstruction of the boost factor. Notice that the first plot of this row corresponds (as it should) to the  $b\bar{b}$  pink line of figure 8.5.

The panel in the very first line represents the dark matter mass while the last panel of the second, third and fourth rows stands for  $m_{F_b}$ ,  $c_L^b$  and  $c_R^b$  respectively. The first panel of the second line is a correlation plot between  $m_{F_b}$  and  $m_\chi$ . The first (second) plot in the third line features the correlation between  $c_L^b$  and  $m_\chi$  ( $c_L^b$  and  $m_{F_b}$ ) and so on. The dotted lines in all the plots feature the prior distribution while the solid line is the posterior distribution, *id est*, the values of the parameters that are found by the Markov chain. The chain has explored enough points since the prior distributions are indeed rather flat for the four parameters while it matches a Gaussian distribution for the boost. One can also check that the constraint of dark matter stability ( $m_{F_b} > m_\chi$ ) is correctly reproduced in the  $(m_{F_b}, m_\chi)$  plot of the second row.

Points of the parameter space were selected according to how the boost is close to  $B_{\max}$ . The MCMC considers a priori equally light and heavy dark matter particles. But the heavier the dark matter particle, the larger the value of  $B_{\max}$  as is clear in figure 8.5 as well as in the first plot of the fifth row of Fig. 8.6. On the other hand, a heavy dark matter particle means an even heavier coloured partner  $F_b$  and since the annihilation cross section is a decreasing function of  $m_{F_b}$ , a large boost is only recovered for very large values of the couplings  $c_L^b$  and  $c_R^b$ . Hence, we expect the MCMC to select large values for these couplings. This is confirmed by our results since both left and right handed couplings can reach two or three (with 90% and 68% CL respectively). If we consider a larger variance  $v_B$  as in Fig. 8.7, the trend is the same. Although slightly smaller values of the boost  $B$  can be in principle achieved with simultaneously large values of the couplings and mass  $m_{F_b}$ , the latter would have to be larger than the 2.5 TeV limit which we set. Hence, in this case, our Monte Carlo chooses a large value of one of the coupling (e.g.  $c_L^b$ ) together with a smaller value of the other coupling (*exempli gratia*  $c_R^b$ ) and a large value of  $m_{F_b}$  (still within our limits). Our main conclusion is that the PAMELA antiproton observations do not preclude large values for  $c_L^b$  and  $c_R^b$ . Our naive benchmark model provides therefore a simple example where the dark matter particle can be quarkophilic and yet satisfy the PAMELA constraints.

Note that the correlation plots displayed in Fig. 8.6 are obtained by saturating the upper limit on the boost obtained previously. The parameters found in these plots therefore correspond to a large annihilation cross section into quarks, which translates into a relic density smaller than  $\Omega_{dm} h^2 = 0.1099 \pm 0.0062$  [24]. Since our model simply relies on dark matter particle couplings to quarks (we do not invoke the Sommerfeld mechanism for example nor annihilations into heavy gauge bosons), this means that we have delineated the region of the

parameter space where dark matter particles have the “wrong” relic density. Note however that as stressed by Catena *et alii* [16] some modifications to the cosmological model could lead to an agreement. Discovering heavy coloured states at the Large Hadron Collider decaying into jet + missing energy and with properties matching this region of the parameter space would therefore jeopardise conventional dark matter scenarios.

### Heavy states production at the Large Hadron Collider

Since the dark matter particle couplings to  $b$  quarks can be very large, the question of  $F_q$  production at the Large Hadron Collider from quark-quark collisions arises. We were interested in fact in  $bb \rightarrow F_b F_b$  (which may happen if dark matter is a real scalar or, in our case, a Majorana particle),  $b\bar{b} \rightarrow F_b \bar{F}_b$  and  $qg \rightarrow F\chi$ . Interestingly enough, the  $qq \rightarrow FF$  and  $qg \rightarrow F\chi$  cross sections can reach up a few pb or a few hundred fb respectively for large couplings.

Such large cross sections seem rather encouraging. However, to get realistic estimates, one has to take into account the parton distribution function associated with  $b$  quarks and gluons. By focusing on  $b$ , we have definitely considered a case where there is a very large suppression due to the parton distribution function [38]. However, the parton distribution function for  $c$  quarks is also suppressed and the boost factor is not so large. Hence  $b$  quarks are more or less representative of what is to be *at most* expected at the Large Hadron Collider for these types of  $F_b$  production processes, given PAMELA antiproton measurements.

At large  $x$  and  $Q^2$ , convoluting our cross section with the parton distribution function leads to a large suppression of the number of events. We predicted less than ten events for  $pp \rightarrow F_b F_b$  (for a integrated luminosity of  $fb^{-1}$ ) in the region where the  $bb \rightarrow F_b F_b$  process is supposed to be maximal (*id est* for large couplings) [10]. The  $pp \rightarrow F\chi$  cross section is a bit less suppressed because it involves gluon. However, it is still very small (it can reach at most ten  $fb$ , assuming a very small uncertainty on the value of the boost factor). Assuming a greater uncertainty on the boost value does not help. The two cross sections become even smaller since, in this case, larger  $m_{F_b}$  values are preferred when the dark matter couplings to quarks is greater than unity. Both cases lead to a too small number of events to be detected via the decay (jet+missing energy) of the heavy coloured states  $F_b$ . Indeed, they would correspond to pure hadronic final states which are extremely difficult to exploit.

### Conclusion

We found that, the large values of the dark matter particles couplings to quarks notwithstanding, there is very little hope to produce a large number of coloured states  $F_b$  through  $bb$ ,  $b\bar{b}$ ,  $bg$  process in  $pp$  collisions because of the  $b$  quark parton distribution function suppression (less than a few 100 events at the Large Hadron Collider for most of the parameter space under consideration and a luminosity of  $1fb^{-1}$ ). Also, such a final state would be purely hadronic and would be difficult to disentangle from background. Hence, the best channel to constrain the dark matter particle (direct) couplings to quarks in the absence of other signatures may be, indeed, heavy coloured states production via gluon fusion and their decay into jets plus missing energy.

Although there have been many studies advocating leptophilic dark matter particles to fit the PAMELA positron excess, our analysis showed that the PAMELA antiproton measurement also allows for “quarkphilic” dark matter in principle. This property may hold whether dark matter is at the origin of the positron excess or not. To fit both PAMELA antiproton data and positron excess, it therefore seems likely that only the dark matter particle couplings to

gauge boson (the  $W$  in particular) may have to be suppressed. Not only are large dark matter particles couplings to heavy quarks allowed by PAMELA antiproton data but they may also be difficult to constrain using the Large Hadron Collider data since their effect on the cross section can be compensated by very large  $F_q$  masses and is suppressed by heavy quark parton distribution function folding.

This actually constitutes the key point of our analysis and suggests that the dark matter production channel in this simple model will also rely on  $F_q$  production through gluon gluon fusion. Hence, such “quarkophilic” models may be difficult to disentangle from standard supersymmetry, unless one can measure the couplings very accurately. In any case, this analysis shows that even though leptophilic dark matter particles may fit the PAMELA positron excess data, this does not imply that the dark matter couplings to quarks must be suppressed. On the other hand, the strength of the dark matter-quark interactions will remain relatively weak owing to the exchange of heavy messengers  $F_q$ .

Though it is not possible at the moment to firmly decide between both scenarios, the optimistic and the realistic one, one can nevertheless infer interesting information on dark matter: either it is responsible for the PAMELA positron fraction rise and then it must annihilate (or decay) strongly into leptons, or no dark matter signal has been seen yet and one can infer upper limits of its coupling to quarks and gauge bosons.

The main conclusion is however that looking to one species only is not a proper method to search for dark matter signal, it is of utmost importance to cross correlate information from all channels: positrons, electrons, anti-protons,  $\gamma$  rays and radio. This will be the only way to be sure of the source of the signal.

## Bibliography

- [1] Abdo, A. A., Ackermann, M., Ajello, M., *et alii* . 2009, Physical Review Letters, 102, 181101 [179](#), [180](#)
- [2] Adriani, O., Barbarino, G. C., Bazilevskaya, G. A., *et alii* . 2010, ArXiv e-prints [1001.3522](#) [178](#), [181](#)
- [3] Adriani, O., Barbarino, G. C., Bazilevskaya, G. A., *et alii* . 2009, Nature, 458, 607 [178](#)
- [4] Adriani, O., Barbarino, G. C., Bazilevskaya, G. A., *et alii* . 2009, Physical Review Letters, 102, 051101 [178](#)
- [5] Aharonian, F., Akhperjanian, A. G., Anton, G., *et alii* . 2009, A&A, 508, 561 [179](#), [180](#)
- [6] Aharonian, F., Akhperjanian, A. G., Barres de Almeida, U., *et alii* . 2008, Physical Review Letters, 101, 261104 [179](#), [180](#)
- [7] AMS-01 Collaboration, Aguilar, M., Alcaraz, J., *et alii* . 2007, Physics Letters B, 646, 145 [181](#)
- [8] AMS Collaboration, Alcaraz, J., Alpat, B., *et alii* . 2000, Physics Letters B, 494, 193 [181](#), [182](#)

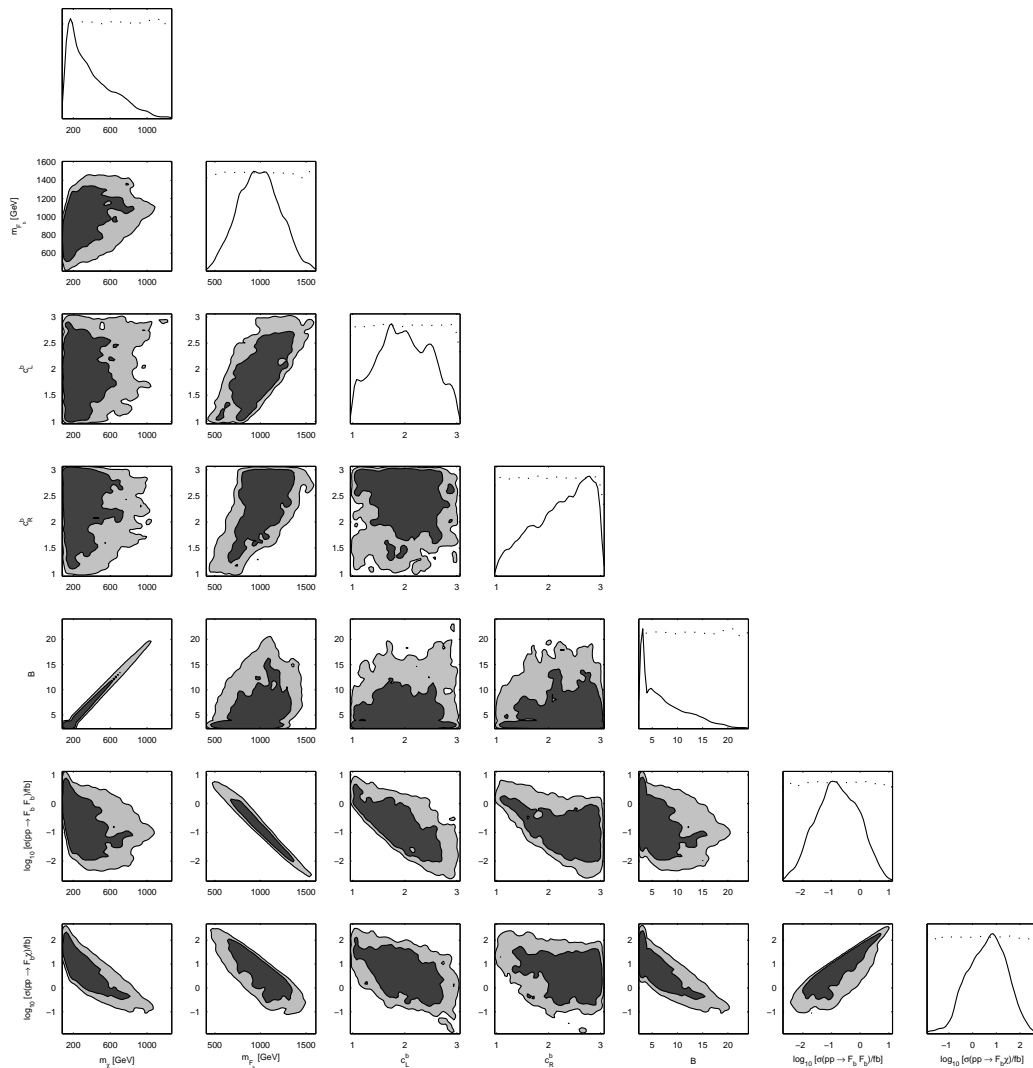


Figure 8.6: The dark matter parameter space is tuned to reproduce the boost factor obtained in figure 8.5 for a  $b\bar{b}$  pair. The central boost value is taken from figure 8.5 while its uncertainty is taken to be  $v_B = 0.1$ . Due to this very small boost uncertainty, one can see the very strong correlation between the boost value and the dark matter mass. The cross sections account for the  $F_b F_b$ ,  $\bar{F}_b F_b$ ,  $F_b \bar{F}_b$  and  $\bar{F}_b \bar{F}_b$  as well as the  $F_b \chi$  and  $\bar{F}_b \chi$  final states respectively. We used the `getdist` routine from the COSMOMC code [30] to make this plot. We used  $\sqrt{s} = 10$  TeV, which should be reached by the Large Hadron Colliders within a few years.

- [9] Barwick, S. W., Beatty, J. J., Bhattacharyya, A., *et alii* . 1997, ApJ, 482, L191+ [181](#)
- [10] Belanger, G., Boudjema, F., Pukhov, A., & Semenov, A. 2007, Comput. Phys. Commun., 177, 894 [189](#)
- [11] Boehm, C., Delahaye, T., Salati, P., Staub, F., & Singh, R. K. 2009, ArXiv e-prints [0907.4511](#) [185](#)

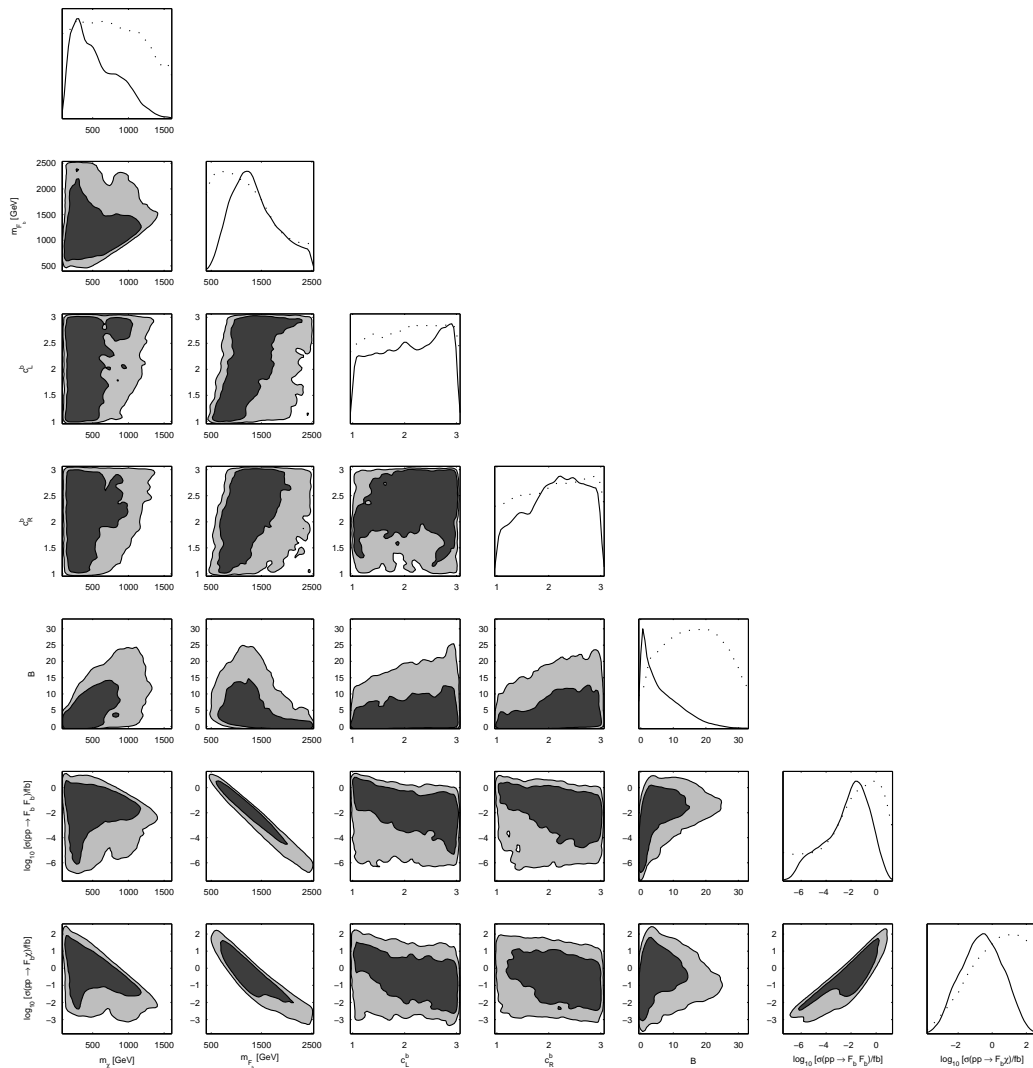


Figure 8.7: The dark matter parameter space is tuned to reproduce the boost factor obtained in figure 8.5 for a  $b\bar{b}$  pair. The central boost value is taken from figure 8.5. Its uncertainty is estimated from the smallest difference between the boost value displayed in the last five columns of Tab. 8.2 and the central value of reference. Whatever the dark matter mass, the uncertainty  $v_B$  thus obtained is much larger than in Fig. 8.6 and one loses the strong correlation between the value of the boost and the dark matter mass. Such “large” values of  $v_B$  relaxes the constraints previously obtained and opens up the parameter space. As a result, large coupling values ( $c_{l,r}^b \in [1, 3]$ ) allow for larger  $m_{F_b}$  values which translate into smaller production cross sections at the Large Hadron Collider. Again, we used  $\sqrt{s}=10$  TeV.

[12] Boehm, C. & Fayet, P. 2004, Nucl. Phys., B683, 219 [187](#)

[13] Bringmann, T., Lavallo, J., & Salati, P. 2009, Phys. Rev. Lett., 103, 161301 [182](#)

[14] Brun, P., Delahaye, T., Diemand, J., Profumo, S., & Salati, P. 2009, Phys. Rev. D, 80, 035023 [182](#)

- [15] Casadei, D. & Bindi, V. 2004, ApJ, 612, 262 [182](#)
- [16] Catena, R., Fornengo, N., Pato, M., Pieri, L., & Masiero, A. 2009, ArXiv e-prints [0912.4421](#) [189](#)
- [17] Chang, J., Adams, J. H., Ahn, H. S., *et alii* . 2008, Nature, 456, 362 [179](#), [183](#)
- [18] Cirelli, M., Kadastik, M., Raidal, M., & Strumia, A. 2009, Nuclear Physics B, 813, 1 [180](#)
- [19] Cumberbatch, D. T. & Silk, J. 2007, Mon. Not. Roy. Astron. Soc., 374, 455 [182](#)
- [20] Diemand, J., Kuhlen, M., Madau, P., *et alii* . 2008, Nature, 454, 735 [182](#), [183](#), [184](#), [186](#)
- [21] Dobler, G., Finkbeiner, D. P., Cholis, I., Slatyer, T. R., & Weiner, N. 2009, ArXiv e-prints [0910.4583](#) [180](#)
- [22] Donato, F., Maurin, D., Brun, P., Delahaye, T., & Salati, P. 2009, Physical Review Letters, 102, 071301 [180](#), [186](#)
- [23] Donato, F., Maurin, D., Salati, P., *et alii* . 2001, ApJ, 563, 172 [187](#)
- [24] Dunkley, J., Komatsu, E., Nolta, M. R., *et alii* . 2009, ApJS, 180, 306 [188](#)
- [25] Finkbeiner, D. P. 2004, ApJ, 614, 186 [180](#)
- [26] Hisano, J., Matsumoto, S., & Nojiri, M. M. 2003, Phys. Rev. D, 67, 075014 [181](#)
- [27] Hooper, D., Finkbeiner, D. P., & Dobler, G. 2007, Phys. Rev. D, 76, 083012 [180](#)
- [28] Hooper, D., Stebbins, A., & Zurek, K. M. 2009, Phys. Rev., D79, 103513 [182](#)
- [29] Lavalle, J., Yuan, Q., Maurin, D., & Bi, X. 2008, A&A, 479, 427 [181](#)
- [30] Lewis, A. & Bridle, S. 2002, Phys. Rev., D66, 103511 [191](#)
- [31] Linden, T. & Profumo, S. 2010, ApJ, 714, L228 [180](#)
- [32] Merritt, D., Graham, A. W., Moore, B., Diemand, J., & Terzić, B. 2006, AJ, 132, 2685 [187](#)
- [33] Navarro, J. F., Frenk, C. S., & White, S. D. M. 1997, ApJ, 490, 493 [187](#)
- [34] Pesce-Rollins, M. & for the Fermi-LAT Collaboration. 2009, ArXiv e-prints [0912.3611](#) [179](#), [180](#)
- [35] Shikaze, Y., Haino, S., Abe, K., *et alii* . 2007, Astroparticle Physics, 28, 154 [187](#)
- [36] Sjostrand, T., Mrenna, S., & Skands, P. Z. 2006, JHEP, 05, 026 [186](#)
- [37] Webber, W. R., Lee, M. A., & Gupta, M. 1992, ApJ, 390, 96 [186](#)
- [38] Whalley, M. R., Bourilkov, D., & Group, R. C. 2005 [189](#)
- [39] Zemp, M., Stadel, J., Moore, B., & Carollo, C. M. 2007, MNRAS, 376, 273 [183](#)



# Conclusion

Da steh ich nun, ich armer Tor,  
Und bin so klug als wie zuvor.

*Goethe in Faust*

The reasons to invoke a non baryonic component of the Universe are so many that even though it has not been detected yet, it seems the most natural explanation to the cosmological and astrophysical issues explained in chapter 1. Not only is it required to solve gravitational problems but also its existence is predicted by many models of particle physics trying to assess the hierarchy problem. Indeed, as explained in chapter 2, consistency of the standard model of particle physics requires new physics at the TeV scale, the new particles of these theories will affect the primordial universe and at least for most models, some amount of it should remain in the present Universe in the form of a dark matter.

Though the different fields of physics that are cosmology and particle physics, point toward the same direction the only way to be sure that we are not victim of a cosmic conspiracy is to detect dark matter. Three categories of detection methods have been exposed

# Appendix A

## Technical details in cosmology

### A.1 Distances in Robertson-Walker metric

It is sometimes convenient to rewrite Robertson-Walker metric of equation 1.2 in a comoving framework:

$$ds^2 = -dt^2 + a^2(t) \left[ d\chi^2 + \begin{cases} \sin^2(\chi) \\ \chi^2 \\ \sinh^2(\chi) \end{cases} (d\theta^2 + \sin^2(\theta)d\phi^2) \right] \text{ for } k = \begin{cases} 1 \\ 0 \\ -1 \end{cases}$$

#### A.1.1 Angular distance

Let us consider an observer at  $(t_0, \chi = 0)$  and two objects emitting light at the same time  $t_1$  from two positions having the same radial coordinate  $\chi_1$  but an angular separation  $\Delta\Theta = \sqrt{\Delta\theta^2 + \sin^2(\theta)\Delta\phi^2}$ . Because they move radially, the original angle between the photons coming from both sources is conserved. The distance between these two objects  $\Delta S$  is then  $a(t_1)\chi_1\Delta\Theta$ . This allows us to define the angular distance:

$$d_A = \frac{\Delta S}{\Delta\Theta} = a(t_1)\chi_1. \quad (\text{A.1})$$

The problem is then to compute  $\chi_1$ . By definition, if a photon comes to us radially, one has:

$$\left| \frac{d\chi}{dt} \right| = \frac{1}{a},$$

which gives, for the comoving distance of the photon emission point:

$$\chi = \int_{t_1}^{t_0} \frac{dt}{a(t)} = \int_{a_1}^{a_0} \frac{da}{a\dot{a}}. \quad (\text{A.2})$$

considering the definition of the redshift  $1 + z = \frac{a_0}{a_1}$  and using Friedmann equation 1.8, it becomes:

$$\chi = \frac{1}{a_0 H_0} \int_{1/(z+1)}^1 \frac{d\hat{a}}{\hat{a}^2 (\Omega_m \hat{a}^{-3} + \frac{\Omega_\gamma}{197} \hat{a}^{-4} + \Omega_\Lambda + (1 - \Omega_T) \hat{a}^{-2})^{1/2}}.$$

If we focus on a Universe where the radiation is under-dominant we have three cases:

For  $\Omega_m + \Omega_\Lambda = \Omega_T \ll 1$

$$\begin{aligned}\chi &\sim \frac{1}{a_0 H_0} \int_{1/(z+1)}^1 \frac{d\hat{a}}{\hat{a}^2 (\Omega_m \hat{a}^{-3} + \hat{a}^{-2})^{1/2}} \\ &\sim \frac{1}{a_0 H_0} \int_{\Omega_m}^1 \frac{d\hat{a}}{\hat{a}} + \frac{1}{a_0 H_0 \sqrt{\Omega_m}} \int_{1/(z+1)}^{\Omega_m} \frac{d\hat{a}}{\hat{a}^{1/2}} \\ &\sim \frac{\ln(1/\Omega_m)}{a_0 H_0} + 2 \frac{\sqrt{\Omega_m} - \sqrt{1/(z+1)}}{a_0 H_0 \sqrt{\Omega_m}}.\end{aligned}$$

For  $\Omega_m + \Omega_\Lambda = \Omega_T = 1$

$$\begin{aligned}\chi &\sim \frac{1}{a_0 H_0} \int_{1/(z+1)}^1 \frac{d\hat{a}}{\hat{a}^2 (\Omega_m \hat{a}^{-3} + (1 - \Omega_m))^{1/2}} \\ &\sim \frac{1}{a_0 H_0 \sqrt{1 - \Omega_m}} \int_x^1 \frac{d\hat{a}}{\hat{a}^2} + \frac{1}{a_0 H_0 \sqrt{\Omega_m}} \int_{1/(z+1)}^x \frac{d\hat{a}}{\hat{a}^{1/2}} \\ &\sim \begin{cases} \frac{1/x - 1}{a_0 H_0 \sqrt{1 - \Omega_m}} + \frac{2\sqrt{x} - 2\sqrt{1/(z+1)}}{a_0 H_0 \sqrt{\Omega_m}} & \text{if } x \leq 1 \\ \frac{2 - 2\sqrt{1/(z+1)}}{a_0 H_0 \sqrt{\Omega_m}} & \text{if } x \geq 1 \end{cases}.\end{aligned}\tag{A.3}$$

where  $x = (\Omega_m/(1 - \Omega_m))^{1/3}$  is the value of  $\hat{a}$  for which the cosmological constant starts to rule over the dust.

For  $\Omega_m + \Omega_\Lambda = \Omega_T \gg 1$ , because the universe still exists today, it means that the curvature domination era has not begun yet. Therefore we require  $\Omega_m \geq \Omega_m + \Omega_\Lambda - 1$  which is equivalent to  $\Omega_\Lambda \leq 1$ . Then we get a lower limit on  $\chi$ :

$$\chi > \frac{1}{a_0 H_0} \int_{1/(z+1)}^1 \frac{d\hat{a}}{(\Omega_m \hat{a})^{1/2}} = \frac{2 - 2\sqrt{1/(z+1)}}{a_0 H_0 \sqrt{\Omega_m}}.$$

### A.1.2 Luminosity distance

The luminosity distance  $d_L$  of a source is defined by the absolute luminosity  $L$  and the received flux  $\phi$  through the following relation:

$$\phi = \frac{L}{4\pi d_L^2}$$

which is consistent with the usual distance in euclidean geometry. In an expanding universe, the energy of the photons is redshifted by a factor  $1/(1+z)$  and the time delay between the

first and the last photon of the received signal is multiplied by a factor  $a_0/a_{emitted} = 1 + z$ . By definition of the coordinates, the surface of the sphere of radial coordinate  $a_0\chi$  is  $4\pi a_0^2 r^2$ . Thus it is easy to see that

$$\phi = \frac{L}{4\pi(1+z)^2 a_0^2 r^2}, \quad (\text{A.4})$$

so that  $d_L = (1+z)a_0 r$ .

Let us consider our comoving radius  $\chi$  again. In the particular case where we are interested in nearby sources, *id est* sources for which the propagation time of the photon from emission to detection is negligible compared with the Hubble time  $t_H = H_0^{-1}$ , it is possible to Taylor expand  $a(t)$ , simply using its first two derivatives given by Friedmann equations 1.5 and 1.6:

$$a(t) = a_0 \left\{ 1 + \left( \frac{t-t_0}{t_H} \right) + \frac{\ddot{a}_0}{2a_0 H_0^2} \left( \frac{t-t_0}{t_H} \right)^2 + o \left( \frac{t-t_0}{t_H} \right)^2 \right\}$$

using the definition of the deceleration parameter  $q_0$  of section 1.1.3.5, we get:

$$a(t) = a_0 \left\{ 1 + \left( \frac{t-t_0}{t_H} \right) - \frac{q_0}{2} \left( \frac{t-t_0}{t_H} \right)^2 + o \left( \frac{t-t_0}{t_H} \right)^2 \right\}$$

and

$$\dot{a}(t) = \frac{a_0}{t_H} \left\{ 1 - q_0 \left( \frac{t-t_0}{t_H} \right) + o \left( \frac{t-t_0}{t_H} \right) \right\}.$$

Using the definition A.2 and using  $\frac{t-t_0}{t_H} \sim \frac{a}{a_0} - 1 \sim -z$ , we get:

$$\begin{aligned} \chi &= \int_{\frac{a_0}{z+1}}^{a_0} \frac{da}{aa_0 H_0 \left\{ 1 - q_0 \left( \frac{t-t_0}{t_H} \right) + o \left( \frac{t-t_0}{t_H} \right) \right\}} \\ &= \frac{1-q_0}{a_0 H_0} \ln(1+z) + \frac{q_0}{a_0 H_0} \left( 1 - \frac{1}{1+z} \right) + o(z^2) \\ &= \frac{z}{a_0 H_0} \left( 1 - \frac{1+q_0}{2} z \right) + o(z^2) \end{aligned}$$

Because, whatever the geometry  $r = \chi + O(\chi^3)$  it is straightforward to get:

$$\begin{aligned} r &= \frac{z}{a_0 H_0} \left\{ 1 - \left( \frac{1+q_0}{2} \right) z \right\} + o(z^2) \quad \text{and} \\ d_L &= \frac{z}{H_0} \left\{ 1 + \left( \frac{1-q_0}{2} \right) z \right\} + o(z^2) \end{aligned} \quad (\text{A.5})$$

### A.1.3 Hubble distance

By definition, the Hubble distance  $d_H$  of a photon emitter is the inverse of the Hubble constant at the time of emission.

$$d_H = \frac{1}{H_0 \sqrt{\Omega_m \hat{a}^{-3} + \Omega_\gamma \hat{a}^{-4} + \Omega_\Lambda + (1 - \Omega_T) \hat{a}^{-2}}}. \quad (\text{A.6})$$

If we focus on a matter dominated Universe we have three cases:

For  $\Omega_m = \Omega_T \ll 1$

$$d_H \sim \frac{\hat{a}}{H_0} \sim \frac{1}{H_0(1+z)}.$$

For  $\Omega_m = \Omega_T = 1$

$$d_H \sim \frac{\hat{a}^{3/2}}{H_0\sqrt{\Omega_m}} \sim \frac{1}{H_0\sqrt{\Omega_m}(1+z)^{3/2}}.$$

For  $\Omega_m = \Omega_T \gg 1$

$$d_H \sim \frac{1}{\sqrt{\Omega_m}H_0\sqrt{\hat{a}^{-3} - \hat{a}^{-2}}} \xrightarrow{z \gg 1} \frac{1}{\sqrt{\Omega_m}H_0(1+z)^{3/2}}.$$

## A.2 Computing the relic density

Let us introduce the phase space density of a particle  $i$ :

$$f_i(\vec{r}, \vec{p}, t) = \frac{dN_i}{d^3r d^3p} \frac{(2\pi\hbar)^3}{g_i}$$

where  $g_i$  stands for the number of spin states of the particle  $i$ . The density  $f_i$  is normalised so that its maximum value is one for a fermion. Before recombination, the Universe is still homogeneous and isotropic hence the  $f_i$ 's only depend on the norm of the impulsion. During thermal equilibrium at temperature  $T$ , quantum statistical physics gives us:

$$f_i(p) = \frac{1}{\exp[(E_p - \mu_i)/T] \pm 1},$$

where the  $+$  sign is for fermions and the  $-$  for bosons. The chemical potential  $\mu_i$  depends on the number of species and the amount of particles versus anti-particles. This allows us to define the particle density  $n_i$ , the energy density  $\rho_i$ , the partial pressure  $p_i$  and with the help of some differential calculus, the entropy density  $s_i$ :

$$n_i = \frac{g_i}{(2\pi\hbar)^3} \int d^3p f_i(p) \tag{A.7}$$

$$\rho_i = \frac{g_i}{(2\pi\hbar)^3} \int d^3p E_p f_i(p) \tag{A.8}$$

$$p_i = \frac{g_i}{(2\pi\hbar)^3} \int d^3p \frac{p^2}{3E_p} f_i(p) \tag{A.9}$$

$$s_i = \frac{\rho_i + p_i - \mu_i n_i}{T}$$

which can be analytically computed in two cases: the relativistic limit (when  $T \gg m_i, \mu_i$ ) and the non relativistic limit ( $m_i - \mu_i \gg T$ ). The results are summed up in Table A.1.

Quantity	relativistic limit	non-relativistic limit
$n(T, \mu)$	$g(1.2/\pi^2)T^3$ ( $\times 3/4$ for fermions)	$g(mT/2\pi)^{3/2}e^{(\mu-m)/T}$
$\rho(T, \mu)$	$g(\pi^2/30)T^4$ ( $\times 7/8$ for fermions)	$(m + 3T/2)n$
$p(T, \mu)$	$\rho/3$	$Tn$
$s(T, \mu)$	$g(2\pi^2/45)T^3$ ( $\times 7/8$ for fermions)	$(m + 5T/2 - \mu)n/T$

Table A.1: Thermodynamical quantities at equilibrium.

From the expression of  $n_i$  it clearly appears that a particle that would become non-relativistic much before decoupling from the ylem would disappear completely because of the exponential behaviour. On the other hand, it can be shown (see section 1.2.1.3) that a particle that would decouple when still relativistic could destroy the galaxies. Hence, for the standard Dark Matter particle, the freeze-out temperature is of order of its mass:  $T_f \sim m_\chi/20$ .

We will consider a curvatureless Universe. The first Friedmann equation 1.5 simplifies into:

$$H^2 = \frac{8\pi G}{3}\rho = \frac{8\pi G}{3}g(T)\frac{\pi^2}{30}T^4.$$

The number of relativistic degrees of freedom  $g(T)$  is the sum of degrees of freedom of bosons plus  $7/8$  times the number of degrees of freedom of fermions that are still in equilibrium with the ylem at temperature  $T$ . It is now possible to write down the equation 1.13 verified by the freeze-out temperature of  $\chi$ :

$$n_\chi(T_f) \sum_{i,j} \langle \sigma_{\chi\chi \rightarrow ij} v \rangle \sim \sqrt{\frac{8\pi G}{3}g(T)} \frac{\pi^2}{30} T_f^2.$$

One particle that we are sure will always be relativistic is the photon hence it is convenient to compute the ratio:

$$\frac{n_\chi(T_f)}{n_\gamma(T_f)} = C \frac{\sqrt{g(T_f)}}{m_\chi \sum_{i,j} \langle \sigma_{\chi\chi \rightarrow ij} v \rangle},$$

where  $C$  takes into account all the numerical constants. After freeze-out, both  $\chi$  particles and photons adiabatically expand. However, for the photon density number, it is important not to forget the decrease of number of degrees of freedom of the ylem between  $\chi$ -freeze-out and today. So:

$$n_\chi(a_0) = C' \frac{n_\gamma(a_0)g_0}{\sqrt{g(T_f)}m_\chi \sum_{i,j} \langle \sigma_{\chi\chi \rightarrow ij} v \rangle},$$

and the relic density parameter  $\Omega_{dm}$  is then simply obtained by multiplying by  $m_\chi$  and dividing by the critical density  $\rho_c$  from equation 1.7.



# Appendix B

## Technical details concerning propagation

### B.1 Bessel expansions

In this paragraph, a proof of the existence of Bessel expansions will be given. Bessel functions are the solutions, found by Bernoulli of Bessel's differential equations:

$$x^2 \frac{d^2 y}{dx^2} + x \frac{dy}{dx} + (x^2 - n^2) y = 0, \quad (\text{B.1})$$

where  $n$  is an integer. This equation is naturally interesting for diffusive problems in cylindrical symmetry, indeed the first two term of the left-hand side are proportional to the radial part of the Laplace operator in cylindrical coordinates. Looking for a solution that can be expanded into a power series, it is easy to find that the functions:

$$J_n(x) = \left(\frac{x}{2}\right)^n \sum_{p=0}^{\infty} \frac{(-1)^p x^{2p}}{2^{2p} p! (n+p)!} \quad (\text{B.2})$$

are solutions of the equation [B.1](#). As these series are alternate, it is possible to show that they have an infinite number of zeros, that, in the case of  $J_0(x)$  will be denoted  $\alpha_i$ . The aim is now to prove that whatever function  $f(x)$  which cancels out at  $x = 1$ , it is possible to find coefficients  $f_n$  such that:  $f(x) = \sum_{n=1}^{n=\infty} f_n J_0(\alpha_n x)$ .

Let  $m$  be an integer, using the classical expression of a Bessel function of equation [B.2](#), calculating the following expression leads to:

$$\begin{aligned} \frac{d}{dx} (x^{-m} J_m(x)) &= \frac{d}{dx} \left( x^{-m} \sum_{p=0}^{\infty} \frac{(-1)^p x^{2p+m}}{2^{2p+m} p! (p+m)!} \right) \\ &= \sum_{p=0}^{\infty} \frac{(-1)^{p+1} x^{2p+1}}{2^{2p+m+1} p! (p+m+1)!} \\ &= -x^{-m} J_{m+1}(x) \end{aligned} \quad (\text{B.3})$$

so for  $m = 0$  one gets:  $J_0'(x) = -J_1(x)$ .

Let us now take  $a \in \mathbb{R}$  and compute:

$$\begin{aligned} & \frac{1}{x} \frac{d}{dx} \left( x \frac{dJ_m(ax)}{dx} \right) + \left( a^2 - \frac{m^2}{x^2} \right) J_m(ax) \\ &= a^2 \left( J_m''(u) + \frac{1}{u} J_m'(u) + \left( 1 - \frac{m^2}{u^2} \right) J_m(u) \right) \quad \text{where } u = ax \\ &= 0 \quad \text{by definition of } J_m(u). \end{aligned}$$

If one takes now the expression of the first line, multiply it by  $J_m(bx)$  where  $b \in \mathbb{R}$  and anti-symmetrises, one gets:

$$\begin{aligned} 0 &= \frac{J_m(bx)}{x} \frac{d}{dx} \left( x \frac{dJ_m(ax)}{dx} \right) + \left( a^2 - \frac{m^2}{x^2} \right) J_m(ax) J_m(bx) \\ &\quad - \frac{J_m(ax)}{x} \frac{d}{dx} \left( x \frac{dJ_m(bx)}{dx} \right) - \left( b^2 - \frac{m^2}{x^2} \right) J_m(ax) J_m(bx). \end{aligned}$$

Hence

$$\frac{d}{dx} (ax J_m(bx) J_m'(ax) - bx J_m(ax) J_m'(bx)) = x(b^2 - a^2) J_m(ax) J_m(bx),$$

which can be integrated between 0 and  $u$  to get:

$$(b^2 - a^2) \int_0^u x J_m(ax) J_m(bx) dx = u((a J_m(bu) J_m'(au) - b J_m(au) J_m'(bu))).$$

Let  $u = 1, m = 0$  and  $a = \alpha_i$  a zero of  $J_0(u)$ .

\*If  $b = \alpha_j \neq \alpha_i$ , a different zero of  $J_0(u)$  one gets:

$$\int_0^1 x J_0(\alpha_i x) J_0(\alpha_j x) dx = \frac{1}{\alpha_j^2 - \alpha_i^2} (\alpha_i J_0(\alpha_j) J_0'(\alpha_i) - \alpha_j J_0(\alpha_i) J_0'(\alpha_j)) = 0.$$

\*If  $b = \alpha_i + \delta$  with  $\delta \rightarrow 0$  then one has:

$$\begin{aligned} \int_0^1 x J_0(\alpha_i x)^2 dx &= \frac{1}{2\alpha_i} \lim_{\delta \rightarrow 0} \frac{1}{\delta} (\alpha_i J_0(\alpha_i + \delta) J_0'(\alpha_i) - (\alpha_i + \delta) J_0(\alpha_i) J_0'(\alpha_i + \delta)) \\ &= \frac{1}{2} \lim_{\delta \rightarrow 0} \frac{1}{\delta} (\delta J_0'(\alpha_i)^2) \\ &= \frac{J_1(\alpha_i)^2}{2} \quad \text{using equation B.3.} \end{aligned}$$

Hence the  $J_0(\alpha_i)$  constitute an orthogonal basis and the decomposition of  $f(x)$  exists and is unique with:

$$f(x) = \sum_{n=1}^{n=\infty} f_n J_0(\alpha_n x) \quad \text{with } f_j(x) = \frac{2}{J_1(\alpha_j)^2} \int_0^1 x f(x) J_0(\alpha_j x) dx, \quad (\text{B.4})$$

where the  $2/J_1(\alpha_j)^2$  is here for the normalisation of the basis.

## B.2 Primary cosmic rays retro-propagation

Secondary electrons and anti-protons are created by cosmic ray protons and  $\alpha$  particles (and also by heavier nuclei but in a negligible amount). In most cases, it is easier to consider that the secondary production is homogeneous throughout the whole Galactic disc. However this approximation is not always valid (especially when dealing with photons). Let us see how to compute the proton flux everywhere in the Galaxy in a consistent scheme, *id est* using the same propagation model for primaries and secondaries and having a primary flux at the Earth position which is in agreement with current data.

When dealing with stable nuclei, steady state can be assumed because their propagation time scale ( $\sim 50$  millions years) is very long compared to the source rate ( $\sim$  a few per century) and rather short with respect to Galactic evolution time ( $\sim 200$  millions years for one Galactic rotation).

The only important energy losses for nuclei are those due to ionisation (see paragraph 5.2). The destruction term is quite important because the interactions between interstellar gas and cosmic rays are quite frequent, though they only take place in the disc:

$$D_p(r, z, E) = 2h\delta(z)\sigma^{coll}v(E)n_H\Psi(r, z = 0, E) = 2h\delta(z)\Gamma^{coll}\Psi(r, z = 0, E), \quad (\text{B.5})$$

where  $n_H \sim 1 \text{ cm}^{-3}$  is the average proton density in the disc,  $2h$  is the thickness of the disc and  $\sigma^{coll}$  is the total collision cross-section. It is convenient to introduce the collision rate  $\Gamma^{coll}$ . Though secondary protons should exist, they are absolutely under-dominant with respect to the primary ones. Hence the source term can be considered as confined in the disc. A priori, there is no reason to believe that supernova remnants produce different proton spectra depending on their position in the Galaxy, hence it is possible to decorrelate energy and space dependence of the source term:

$$Q_p(r, z, E) = 2h\delta(z)Q_p^{tot}(E)f(r), \quad (\text{B.6})$$

where  $f(r)$  is normalised so that  $2\pi \int_0^R r f(r) dr = 1$ . The last term,  $Q_p^{tot}(E)$  is hence the total production rate in the Galaxy of cosmic protons with energy  $E$  per unit of energy  $dE$ . This quantity cannot be measured nor easily estimated, but actually, as we will see later on, it will disappear from our calculus. The propagation equation is hence:

$$V_C \partial_z \Psi - K \Delta \Psi + 2h\delta(z) \partial_E (b^{ion} \Psi - D_{EE} \partial_E \Psi) = 2h\delta(z) Q_p^{tot}(E) f(r) - 2h\delta(z) \Gamma^{coll} \Psi, \quad (\text{B.7})$$

The resolution of this equation starts as usual by a Bessel expansion:

$$V_C \partial_z P_i - K \partial_z^2 P_i + K \frac{\alpha_i^2}{R^2} P_i + 2h\delta(z) \{ \partial_E (b^{ion} P_i - D_{EE} \partial_E P_i) + \Gamma^{coll} P_i \} = 2h\delta(z) Q_p^{tot}(E) q_i, \quad (\text{B.8})$$

where  $P_i$  and  $q_i$  are the Bessel coefficients of  $\Psi$  and  $f$  respectively. For  $z > 0$  the equation is a standard linear differential equation without right-hand side one can solve easily:

$$P_i(z \neq 0, E) = P_i^* \exp \left\{ \frac{V_c |z|}{2K} \right\} \frac{\sinh \left( \frac{\sqrt{\Delta}}{2} (L - z) \right)}{\sinh \left( \frac{\sqrt{\Delta}}{2} L \right)} \quad (\text{B.9})$$

where the discriminant is

$$\Delta = \left(\frac{V_c}{K}\right)^2 + \left(\frac{2\alpha_i}{R}\right)^2 \quad (\text{B.10})$$

and  $P_i^*$  stands for  $P_i(z=0, E)$ . We need now to integrate equation B.9 on a thin vertical layer around the Galactic disc.

$$\int_{-\epsilon}^{\epsilon} dz \left\{ V_C \partial_z P_i - K \partial_z^2 P_i + K \frac{\alpha_i^2}{R^2} P_i \right\} + 2h \left\{ \partial_E (b^{ion} P_i^* - D_{EE} \partial_E P_i^*) + \Gamma^{coll} P_i^* \right\} = 2h Q_p^{tot}(E) q_i. \quad (\text{B.11})$$

When  $\epsilon$  goes to zero, the terms in  $P_i$  and  $\partial_z P_i$  will vanish. However it is not the case for the term in  $\partial_z^2 P_i$ . Indeed,  $\partial_z P_i$  is discontinuous at  $z=0$ . By symmetry of the problem, the particle current along the  $z$  axis has to be null at  $z=0$ :

$$-K \partial_z P_i(O_+, E) + V_c P_i(0_+, E) = 0. \quad (\text{B.12})$$

From this, one easily gets that  $\partial_z P_i(z=0_+) = \frac{V_c}{K} P_i^*$  and

$$\begin{aligned} \int_{-\epsilon}^{\epsilon} \partial_z^2 P_i dz &= 2 (\partial_z P_i(z=\epsilon) - \partial_z P_i(z=0_+)) \\ &= 2 \left( \frac{V_c}{2K} e^{\left\{ \frac{V_c \epsilon}{2K} \right\}} \frac{\sinh\left(\frac{\sqrt{\Delta}}{2}(L-\epsilon)\right)}{\sinh\left(\frac{\sqrt{\Delta}}{2}(L)\right)} - \frac{\sqrt{\Delta}}{2} e^{\left\{ \frac{V_c \epsilon}{2K} \right\}} \frac{\cosh\left(\frac{\sqrt{\Delta}}{2}(L-\epsilon)\right)}{\sinh\left(\frac{\sqrt{\Delta}}{2}(L)\right)} - \frac{V_c}{K} \right) P_i^* \\ &\xrightarrow{\epsilon \rightarrow 0} - \left( \frac{V_c}{K} + \sqrt{\Delta} \coth\left(\frac{\sqrt{\Delta}L}{2}\right) \right) P_i^*. \end{aligned} \quad (\text{B.13})$$

For clarity, let  $A_i$  be  $V_c + 2h\Gamma^{coll} + K\sqrt{\Delta} \coth\left(\frac{\sqrt{\Delta}L}{2}\right)$  so we are left with:

$$A_i P_i^* + 2h \partial_E (b^{ion} P_i^* - D_{EE} \partial_E P_i^*) = 2h Q_p^{tot}(E) q_i. \quad (\text{B.14})$$

If one is interested only in high energy protons, we do not need to consider ionisation losses and reacceleration which occur only at low energy. This is valid for instance for antiprotons which cannot be created by protons of energies lower than 20–30 GeV. Then we trivially have:

$$P_i^* = \frac{2h q_i}{A_i} Q_p^{tot}(E) \quad (\text{B.15})$$

If we forget about  $Q_p^{tot}(E)$ , we have a reduced proton density

$$\Psi_p^0(r, z, E) = \sum_{i=1}^{\infty} J_0\left(\frac{\alpha_i r}{R}\right) \frac{2h q_i}{A_i} \exp\left\{\frac{V_c |z|}{2K}\right\} \frac{\sinh\left(\frac{\sqrt{\Delta}}{2}(L-z)\right)}{\sinh\left(\frac{\sqrt{\Delta}}{2}L\right)} \quad (\text{B.16})$$

and making use of the local measurement of the proton density  $\Psi_p^{exp}(E)$ , we can find

$$Q_p^{tot}(E) = \Psi_p^{exp}(E) / \Psi_p^0(r=R_{\odot}, z=0, E) \quad (\text{B.17})$$

which allows us to compute the proton flux everywhere in the Galaxy. If one really wishes to take into account re-acceleration and energy losses, it is possible to perform a perturbative calculation explained in the next section.

## B.3 Taking into account diffusive reacceleration

### B.3.1 The electron case

I have not been able to find an analytical solution to the full equation of propagation 5.4 for electrons, which accounts for energy losses everywhere in the diffusion halo, however a little trick allows a solution. Indeed, by changing the expression of the energy losses, it is possible to reproduce the same results but with an energy loss term only in the disc. Then we are confronted with the same equation as for the proton case, which after the usual Bessel expansion is equation B.14.

For the reacceleration coefficient, at variance with equation 5.5, the energy dependence has been explicitly shown:  $D_{EE} = K_{EE}\epsilon^{2-\delta}$ .

$$\frac{\tau_e}{2h} \left\{ \frac{\sqrt{\Delta}K_0\epsilon^\delta}{\tanh\left(\frac{\sqrt{\Delta}L}{2}\right)} + V_C \right\} P_i^* - \partial_\epsilon \left\{ \tau_e b_{loss}(\epsilon) P_i^* + \tau_e K_{EE}\epsilon^{2-\delta} \partial_\epsilon P_i^* \right\} = \tau_e q_i(\epsilon). \quad (\text{B.18})$$

To lighten the notations, let:

$$\begin{aligned} A(\epsilon) &= \frac{\tau_e\epsilon}{2h} \left\{ \frac{\sqrt{\Delta}K_0\epsilon^\delta}{\tanh\left(\frac{\sqrt{\Delta}L}{2}\right)} + V_C \right\} \\ \tilde{q}_i &= \tau_e\epsilon q_i(\epsilon) \\ b &= K_{EE}\tau_e \\ x &= \ln(\epsilon) \end{aligned}$$

and equation (B.18) restates as:

$$A(x)P_i^* - \partial_x \left\{ \tau_e b_{loss}(\epsilon) P_i^* + b\epsilon^{1-\delta} \partial_x P_i^* \right\} = \tilde{q}_i. \quad (\text{B.19})$$

To minimise off-diagonal coefficients, one can change variable  $u(\epsilon) = f(\epsilon)P_i^*$  which leads to:

$$\frac{A(x)}{f(x)}u - \partial_x \left\{ \beta(x)u + \gamma(x)\partial_x \frac{u}{f(x)} \right\} = \tilde{q}_i. \quad (\text{B.20})$$

where we have written

$$\begin{aligned} \alpha(x) &= \frac{A(x)}{f(x)}, \\ \beta(x) &= \tau_e \frac{b_{loss}(\epsilon)}{f(x)} \text{ et} \\ \gamma(x) &= b\epsilon^{1-\delta}. \end{aligned}$$

One can now insert a time variation and a discretisation  $^n$  for the time and  $_j$  for energy  $x$ .

$$\frac{u_j^{n+1} - u_j^n}{\Delta t} + \alpha_j \frac{u_j^{n+1} + u_j^n}{2} - \frac{1}{2} \left\{ \frac{J_{j+1/2}^{n+1} - J_{j-1/2}^{n+1}}{\Delta x} + \frac{J_{j+1/2}^n - J_{j-1/2}^n}{\Delta x} \right\} = \tilde{q}_{ij}, \quad (\text{B.21})$$

where  $J$  is the currant :

$$J_{j+1/2}^n = \frac{\beta_j u_j^n + \beta_{j+1} u_{j+1}^n}{2} + \frac{\gamma_j + \gamma_{j+1}}{2} \frac{u_{j+1}^n - u_j^n}{\Delta x}.$$

Equation (B.21) can be written in a matricial form:

$$[\mathbb{I} + \Delta t M] u^{n+1} = [\mathbb{I} - \Delta t M] u^n + \Delta t f \tilde{q}_i, \quad (\text{B.22})$$

with  $M$  tridiagonal matrix of the kind: 
$$\begin{pmatrix} b_0 & c_0 & 0 & \cdots & \cdots \\ a_1 & b_1 & c_1 & 0 & \cdots \\ 0 & \ddots & \ddots & \ddots & 0 \\ \cdots & 0 & a_{J-1} & b_{J-1} & c_{J-1} \\ \cdots & \cdots & 0 & a_J & b_J \end{pmatrix}.$$
 The three vectors  $a$ ,  $b$

and  $c$  have the following form:

$$b_j = \frac{\alpha_j}{2} + \frac{1}{4\Delta x} \left\{ \frac{2\gamma_j + \gamma_{j-1} + \gamma_{j+1}}{f_j \Delta x} \right\}, \quad (\text{B.23})$$

$$a_j = -\frac{1}{4\Delta x} \left\{ -\beta_{j-1} + \frac{\gamma_{j-1} + \gamma_j}{f_{j-1} \Delta x} \right\} \text{ et} \quad (\text{B.24})$$

$$c_j = -\frac{1}{4\Delta x} \left\{ \beta_{j+1} + \frac{\gamma_j + \gamma_{j+1}}{f_{j+1} \Delta x} \right\}. \quad (\text{B.25})$$

In order to keep all coefficients small one need functions  $\gamma$  and  $\beta$  to be small.

It seems that function  $f = \epsilon + \epsilon^\alpha$  allows a rather fast convergence but I would not claim it is the best choice possible.

### First and last lines

Matrix  $M$  cannot be infinite and its extremities should be handled with great care. At very low and at very high energies, diffusive re-acceleration is expected to be very inefficient. If one supposes  $J'_1 = \frac{J_2}{2\Delta x}$  and  $J'_{J-1} = -\frac{J_{J-2}}{2\Delta x}$  one gets:

$$b_0 = \frac{\alpha_1}{2} + \frac{\gamma_2}{4f_2\Delta x^2} \quad c_0 = -\frac{1}{2} \left( \frac{\beta_2}{4\Delta x} + \frac{\gamma_2}{2f_2\Delta x^2} \right) \quad \text{and} \quad (\text{B.26})$$

$$a_J = -\frac{1}{2} \left( \frac{\beta_{J-2}}{4\Delta x} + \frac{\gamma_{J-2}}{2f_{J-2}\Delta x^2} \right) \quad b_J = \frac{\alpha_{J-1}}{2} - \frac{\gamma_{J-2}}{4f_{J-2}\Delta x^2}. \quad (\text{B.27})$$

Everything is now ready to perform a Cranck–Nicholson algorithm. Indeed the matrix  $[\mathbb{I} + \Delta t M]$  is easy to inverse as it is almost diagonal. With a proper choice of  $\Delta t$  the solution converges quite rapidly. The corresponding results can be seen in chapter 5

### B.3.2 The proton case

In the case of protons, complication arises from the fact that the function  $Q_p^{tot}(E)$  is unknown. The solution is to compute it as in equation B.17, reinject it in equation B.14, solve it thanks to the Crank–Nicholson scheme explained in the previous paragraph, and adjust  $Q_p^{tot}(E)$  through:

$$Q_p^{tot\ new}(E) = (\Psi_p^{exp}(E)/\Psi_p^{new}(E)) Q_p^{tot\ old}(E) \quad (\text{B.28})$$

and perform the same process again and again until the convergence is achieved. Though it may sound tedious, a correct algorithm will converge after a few iterations only.

## B.4 Taking into account a local bubble

One could want to consider a local void in two cases, when one wants to take into account the existing local bubble of 100 pc around the Sun for secondary cosmic rays production (as in paragraph 6.1.1.3), or when one wishes to remove the smooth distribution of sources in a region of two kpc to implement point–like sources instead (as in paragraph 6.2.1.2). An absence of source around the Solar position clearly breaks the cylindrical symmetry making the Bessel expansion impossible. We are then left with the Green method only. As propagation itself is not affected, the Green function  $\tilde{G}(\vec{x}_\odot, \tilde{t} \leftarrow \vec{x}_S, \tilde{t}_S)$  is not affected. Neither in the case of a source present everywhere in the diffusion zone (paragraph 5.3.1.2), nor if the sources are in the Galactic disk only (see paragraph 5.3.2). So the halo function  $\tilde{I}(\lambda)$  still has the same definition:

$$\tilde{I}(\lambda) = \int_{\mathcal{D}} S(\vec{x}_S) \tilde{G}(\vec{x}_\odot, \epsilon \leftarrow \vec{x}_S, \epsilon_S) d^3\vec{x}_S. \quad (\text{B.29})$$

The integral is performed over  $\mathcal{D} = (\text{Diffusion zone}) \cap (\text{Source distribution})$ . One could think of taking advantage of the linearity of the diffusion equation (with respect to the source term) by subtracting the result corresponding to the local void. However this method reveals to be extremely costly, as the size of the bubble can be quite small ( $\sim 100$  pc), so the integral would require many very short steps. The correct way to take into account the local void is to limit the integral over the azimuthal angle  $\theta$  to  $[\theta_{min}; 2\pi - \theta_{min}]$  instead of  $[0; 2\pi]$ . So that:

$$\tilde{I}(\lambda) = \int_0^R 2 \int_0^{z_{max}} \left( \int_{\theta_{min}}^{2\pi - \theta_{min}} S(r_S, z_S, \theta_S) \tilde{G}(r_\odot, z_\odot=0, \theta_\odot=0, \epsilon \leftarrow r_S, z_S, \theta_S, \epsilon_S) d\theta_S \right) dz_S r_S dr_S.$$

And  $z_{max}$  is either  $h$  the half thickness of the Galactic disc or  $L$  the half-thickness of the diffusion zone, depending if we are considering sources located in the disc only or not. I do not know any kind of source that is not limited to the Galactic disc and could have a local underdensity, but this does not change the discussion as the implementation would be the same. The expression of the bound  $\theta_{min}$  as a function of  $r_S$  and  $z_S$  depends on the geometrical shape of the void. If the void is a cylinder of radius  $r_b$ , then simply using the fact that:

$$\begin{aligned} r_S^2 &= d^2 + a^2 \\ r_b^2 &= d^2 + (R_\odot - a)^2, \end{aligned}$$

where all the distances are defined in figure B.1, one gets:

$$\cos(\theta_{min}) = \frac{r_S^2 + R_\odot^2 - r_b^2}{2R_\odot r_S}. \quad (\text{B.30})$$

So  $\theta_{min}$  is a function of  $r_S$  only. In the case of a spherical void, it is enough to rescale the size of the bubble for each value of  $z_S$ , *id est* to replace  $r_b$  by  $\sqrt{r_b^2 - z_S^2}$ .

Of course, more complex shapes could be taken into account, or one could also include others voids anywhere in the Galaxy but there is no good motivation for this.

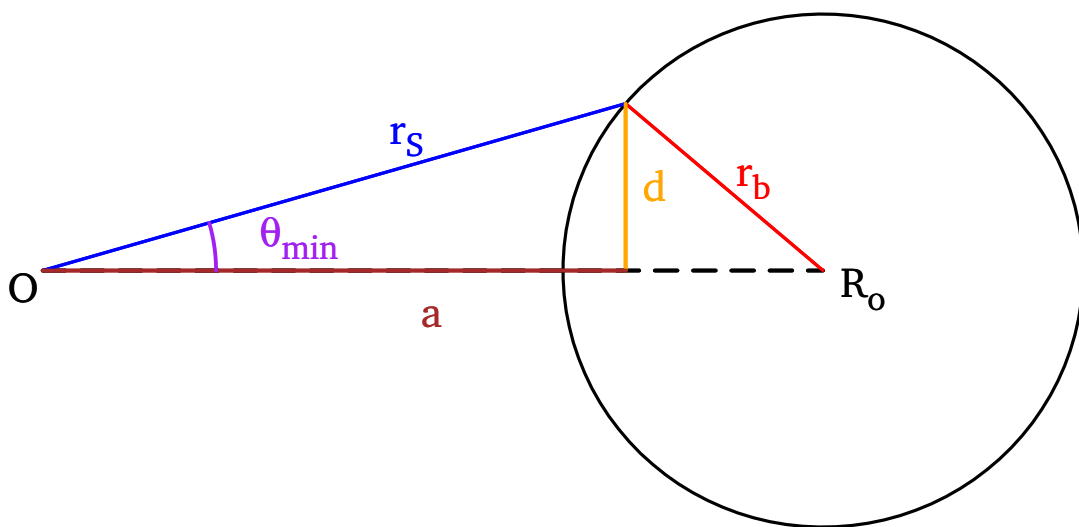


Figure B.1: The geometry of a local void around the Solar position. The scales are not respected on purpose to ensure readability.

## B.5 Taking into account the boundary conditions with the Green method

In order to take into account the boundary conditions with the Green method, it can be convenient to get inspiration from electrostatics.

When an electric charge is placed nearby an infinite electrical conductor plan, it is enough to remove the plan and make the calculus as if there were an opposite charge at the symmetric position of the real one, with respect to the plan. When there are two parallel plans, one needs to consider both images of the charge but also the images of the images and the infinite series of

their images. As the potential goes like  $\frac{1}{r}$  the sum actually converges quite fast and only a few images are necessary. This is even more true for our Green functions which go like  $\exp(-r^2)$ .

The problem is a little more difficult when confronted to a closed electric conductor, like the radial bound of our Galaxy. Because there is only one electrical conductor plan, one need to look for one image only. Let us consider an electric charge  $q$  located in  $S$ , inside a circle of centre  $O$  and radius  $R$ . By reasons of symmetry, we know that the image has to be on the axis linking  $S$  to  $O$ . As illustrated in figure B.2, I call  $r_S$  the distance of the real charge to the centre of the circle, and  $r_{Im}$  the distance of the image  $I$  to  $O$ . In fact there is no reason that the electric charge of the image should be equal to the one of the real one. Let us call it  $q'$ . I want to find the values of  $r_{Im}$  and  $q'$  which allows the electric potential to be zero for all points  $P$  located on the circle.

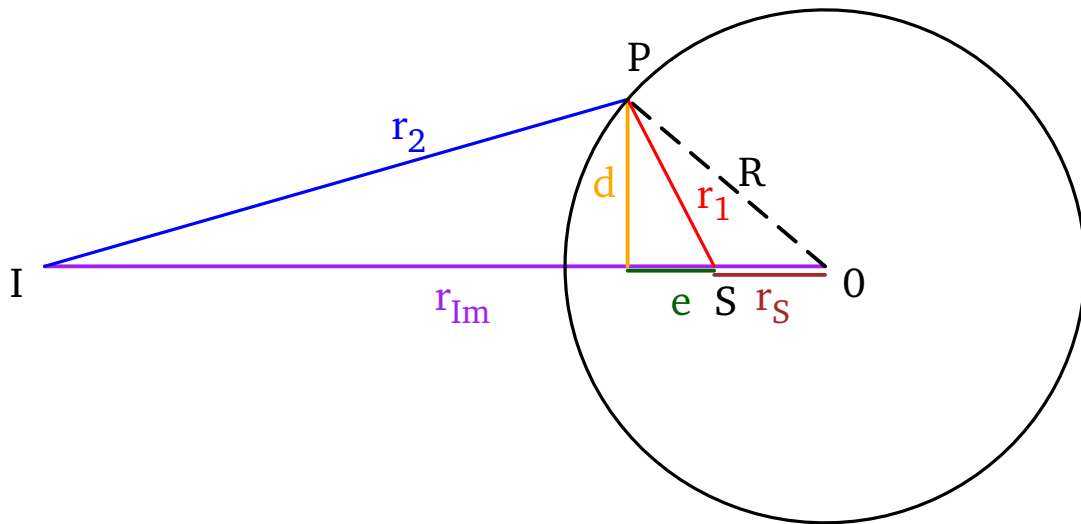


Figure B.2: An electric charge  $q$  is located in  $S$ . Where has to stand the other charge  $q'$  so the potential is null for all points  $P$  located on the circle of radius  $R$ ?

If I call  $r_1$  and  $r_2$  the distances between  $P$  and both charges (real and image respectively), the electric potential being proportional to the ratio of the charge to the distance, the condition that should be fulfilled is:

$$\frac{q}{r_1} = -\frac{q'}{r_2} \text{ or } \frac{r_2}{r_1} = -\frac{q'}{q}. \tag{B.31}$$

Is it possible to find  $I$  so that  $\frac{r_2}{r_1}$  is the same for all  $P$ ? Let us first consider the cases where  $P$  is aligned with  $I$  and  $S$ . If  $P$  is between  $S$  and  $I$ , then:

$$\frac{r_2}{r_1} = \frac{r_{Im} - R}{R - r_S}.$$

Conversely, if  $S$  is between  $I$  and  $P$ , then:

$$\frac{r_2}{r_1} = \frac{r_{Im} + R}{R + r_S}.$$

These two ratios are equal if and only if:

$$(r_{Im} - R)(R + r_S) = (R - r_S)(r_{Im} + R) \iff r_{Im}(R + r_S - R + r_S) = R(R - r_S + R + r_S) \quad (\text{B.32})$$

so  $r_{Im} = \frac{R^2}{r_S}$ . By substituting this value in one or the other of the ratios, one gets

$$\frac{r_2}{r_1} = \frac{R}{r_S}.$$

We need now to verify that this also valid any position of  $P$  on the circle. Using Pythagore's theorem in the three right-triangle of figure B.2, one gets:

$$\begin{aligned} R^2 &= (e + r_S)^2 + d^2 \\ r_1^2 &= e^2 + d^2 \\ r_2^2 &= (r_{Im} - e - r_S)^2 + d^2 \end{aligned} \quad (\text{B.33})$$

What we want to show is that  $\frac{r_2}{r_1} = \frac{R}{r_S}$  or:

$$(r_{Im} - e - r_S)^2 + d^2 = \left(\frac{R}{r_S}\right)^2 (e^2 + d^2) \iff r_{Im}^2 - 2r_{Im}(e + r_S) + R^2 = \frac{R^2}{r_S^2}(R^2 - 2er_S - r_S^2)$$

where on both sides, I have used equation B.33 to get rid of  $d$ . Substituting to  $r_{Im}$ , the value I have found previously, I get:

$$\frac{R^4}{r_S^2} + 2\left(\frac{R^2}{r_S}\right)(e + r_S) + R^2 = \frac{R^4}{r_S^2} - \frac{2eR^2}{r_S} - R^2, \quad (\text{B.34})$$

which, after expanding the parenthesis, reveals to be true. So indeed, if the image satisfies  $r_{Im} = \frac{R^2}{r_S}$  then  $\frac{r_2}{r_1}$  is the same for all  $P$ . So, using equation B.31, this means that putting a charge  $q' = -q\frac{R}{r_S}$  at  $I$  is equivalent as having an electrical conductor on the circle, at least to compute the potential inside it.

How does this translate for the Green propagator? The position of the image is straightforwardly transposed but what is the equivalent of the electric charge? When we dealt with opposite but equal in absolute value charges, like for the vertical bounds, it was trivial we had to subtract the propagators. Obviously it would be a mistake to multiply the propagator of the image by  $\frac{q'}{q}$  otherwise we could get negative propagators in some points. So the only part one can modify is inside the exponential. At fixed distance, the electric potential is proportional to the charge, likewise, at fixed distance the propagator gets larger when  $\lambda$  gets larger. So actually, the  $\lambda$  which is inside the exponential (the other one comes from normalisation and cannot be modified) is the equivalent of the electric charge. So our propagator should be:

$$\tilde{G}_{2D}^r(\vec{r}_\odot, \tilde{t} \leftarrow \vec{r}_S, \tilde{t}_S) = \frac{\theta(\lambda)}{\pi \lambda^2} \left( \exp \left\{ -\frac{(\vec{r}_\odot - \vec{r}_S)^2}{\lambda^2} \right\} - \exp \left\{ -\left(\frac{R}{r_S}\right)^2 \frac{(\vec{r}_\odot - \vec{r}_{im})^2}{\lambda^2} \right\} \right), \quad (\text{B.35})$$

In fact any positive power of  $\lambda$  could have been thought as the equivalent of the electric charge, however it can be easily checked that this is the only solution that vanishes for  $r_S = R$ . When integrated over the full space, one indeed gets 0 (one positive and one negative source) and finally, when compared with the results of the Bessel-Fourier expansion technique, one actually gets the same.

## B.6 Adiabatic losses

Let us try here to justify equations 4.1 and 5.10. Let  $n$  be the particle density in phase space (three dimensions of space and three dimensions of momentum), in a flow of speed  $u$ . In absence of source, particle number conservation implies:

$$0 = \vec{\nabla} \cdot \vec{j},$$

where current  $\vec{j}$  is  $n\vec{u}$ . In both cases we are interested in (Fermi acceleration and convection), the direction of the flow never changes, it is only the norm of  $\vec{u}$  that varies. So, one can write  $\vec{u} = u\vec{e}_x$ , where  $\vec{e}_x$  is a unit vector in the direction of the flow  $x$ . Projecting the previous equation over  $x$  and dividing it by  $nu$ , one gets:

$$\frac{1}{n} \frac{\partial n}{\partial x} = -\frac{1}{u} \frac{\partial u}{\partial x}.$$

If one considers a subset of  $N$  particles, which fill up a volume  $V = N/n$ , one gets:

$$\frac{1}{V} \frac{\partial V}{\partial x} = \frac{1}{u} \frac{\partial u}{\partial x}.$$

Moreover, as there is not energy transfer from the outside of our subset, the volume in phase space is conserved, *id est* :

$$p^3 V = \text{constant}, \quad (\text{B.36})$$

so

$$\frac{1}{V} \frac{\partial V}{\partial x} = \frac{1}{u} \frac{\partial u}{\partial x} = -\frac{3}{p} \frac{\partial p}{\partial x}.$$

Finally, by definition of  $u$  and  $x$ , we have  $u \frac{\partial}{\partial x} = \frac{\partial}{\partial t}$ , so

$$\frac{\partial p}{\partial t} = -\frac{p}{3} \frac{\partial u}{\partial x},$$

and the result is proved.



# Appendix C

## Technical details concerning dark matter distribution

### C.1 The Galactic centre

For some Dark Matter distribution one can find in the literature, like the ones from Navaro, Freack and White or Moore's profile (see equation 4.26), the Dark Matter density is infinite at the centre of the Galaxy. Physically, this is avoided by invoking saturation of annihilation, hence there should be a radius inside which, the density of Dark Matter is constant and not infinite. However the size of this saturation nucleus is very small (of order 1 parsec), much smaller than the increment of our numerical increments in integrals. To avoid non-physical numerical divergences, one can change the function describing the Dark Matter density  $\rho(r)$  for a radius smaller than ( $r_{cutoff} = 100$  or  $500$  pc) by another function  $\rho^*(r)$  the square of which has the same cylindrical integral, is continuous and has a continuous first derivative with function  $\rho$  at  $r_{cutoff}$ . Continuity conditions are quite natural, imposing equality for cylindrical integral of the square of the function corresponds to keep the number of annihilation constant inside the central region. Indeed we do not try to fit rotation curves with a smoother function, but require that the amount of indirect signal and hence of annihilation is constant. One can easily check that the following function satisfies the three conditions mentioned:

$$\rho^*(r) = \rho(r_{cutoff}) \sqrt{1 + a_1 \operatorname{sinc}\left(\pi \frac{r}{r_{cutoff}}\right) + a_2 \operatorname{sinc}\left(2\pi \frac{r}{r_{cutoff}}\right)}, \quad (\text{C.1})$$

where

$$\begin{aligned} a_2 &= 8\gamma \frac{\pi^2 - 9 + 6\gamma}{9(3 - 2\gamma)} \text{ and} \\ a_1 &= a_2 + 2\gamma. \end{aligned}$$

$\gamma$  is 1.5 for Moore's profile and 1.3 for NFW.

## C.2 Determining the local dark matter density

Throughout this work I have always considered that the dark matter local density is  $0.3 \text{ GeV.cm}^{-3}$ , but this is only a conventional value, well spread among the community. This allows easier comparisons among various predictions but should not hide the fact that this value is still unknown.

In 1975, Schmidt [10], using the luminosity function of high-velocity stars, found that the local value of stars is:

$$\rho_{\odot\star} = 1.7 \times 10^{-4} \text{ M}_{\odot}.\text{pc}^{-3} = 6.5 \times 10^{-3} \text{ GeV.cm}^{-3}.$$

Six years later, Caldwell & Ostriker [3], using kinematic measurements of our Galaxy, found that the total local density is:

$$\rho_{\odot} = 6 \times 10^{-3} \text{ M}_{\odot}.\text{pc}^{-3} = 0.23 \text{ GeV.cm}^{-3},$$

proving that stars are clearly not the main Galactic component, even at the Solar location. Later work of Bahcall *et alii* [1] gave a value of

$$\rho_{\odot} = 0.009 \text{ M}_{\odot}.\text{pc}^{-3} = 0.34 \text{ GeV.cm}^{-3}$$

for a rather complex mass distribution (four components, the main one being a Vaucouleur dark matter halo – see section 4.3.1.4). Taking advantage of microlensing data to subtract MACHOs (*id est* dense dark baryonic objects), Gates *et alii* [5] found a value of

$$\rho_{\odot} = 9.2_{-3.1}^{+3.8} \times 10^{-25} \text{ g.cm}^{-3} = 0.50_{-0.17}^{+0.21} \text{ GeV.cm}^{-3},$$

The review from Jungman *et alii* [6], nicely explains these discrepancies, on top uncertainties coming from velocity measurements, the results also depends on the Sun distance to the Galactic centre (see section D.3) and on the model chosen for the distribution. Exploring the allowed ranges for these inputs, Bergström *et alii* [2] concluded that the allowed range for  $\rho_{\odot}$  is 0.2–0.8  $\text{GeV.cm}^{-3}$ . Making use of Markov Chain Monte Carlo method, Widrow *et alii* [13] showed that even when allowing for axisymmetry for the halo, the range for the local density is:

$$\rho_{\odot} = 0.0080 \pm 0.0014 \text{ M}_{\odot}.\text{pc}^{-3} = 0.30 \pm 0.05 \text{ GeV.cm}^{-3}.$$

Very recently, Catena & Ullio [4], taking advantage of recent observational data and of a Markov Chain Monte Carlo method, favoured higher values of the local density:

$$\begin{aligned} \rho_{\odot} &= 0.395 \pm 0.027 \text{ GeV.cm}^{-3} \text{ for an Einasto profile} \\ \rho_{\odot} &= 0.389 \pm 0.025 \text{ GeV.cm}^{-3} \text{ for a NFW profile.} \end{aligned}$$

One can see section 4.3.1.4 for a reminder of these profiles. This results are compatible with those of Strigari & Trotta [11] who claim

$$\rho_{\odot} = 0.32 \pm 0.07 \text{ GeV.cm}^{-3}.$$

However, another recent result is the one from Weber & de Boer [12], which contradicts the both previous ones and claims larger uncertainty with:

$$\rho_{\odot} = 0.3 \pm 0.1 \text{ GeV.cm}^{-3}.$$

Even more recently, using only centrifugal equilibrium, Salucci *et alii* [9] found

$$\rho_{\odot} = 0.43 \pm 0.11 \pm 0.10 \text{ GeV.cm}^{-3}$$

which does not depend on the dark matter halo modelling but on the slope of the circular velocity at the Sun location and the ratio between this radius and the length scale of the stellar exponential disc. This means that using this method, if the observations get more precise, so will be the estimation of the local dark matter density.

This uncertainty is obviously an issue for dark matter detection. Indeed the uncertainty translates linearly for indirect detection for decaying models and for direct detection, and to the square for indirect detection of annihilating dark matter.

### C.3 Boundary conditions of the diffusion equation and dark matter

It has been argued by Perelstein & Shakya [7], that imposing a null density at diffusion zone boundaries, is problematic when confronted with dark matter. Indeed the dark matter halo is supposed much larger than the diffusion zone, so a non-negligible amount of cosmic-rays could be produced outside the diffusion zone. As it is, the diffusion model detailed in this thesis cannot take into account this new component. Also the authors had to modify the diffusion model by adding a vertical variation of the diffusion coefficient  $K_0$ :

$$K_0(z) = \begin{cases} K_0, & \text{if } |z| \leq L; \\ \frac{1}{2}(K_1 + K_0) + \frac{1}{4}(K_1 - K_0) \left[ 3 \cos\left(\frac{|z|-L}{d}\pi\right) - \cos^3\left(\frac{|z|-L}{d}\pi\right) \right], & \text{if } L < |z| \leq L + d; \\ K_1, & \text{if } L + d < |z| \leq D. \end{cases}$$

And now the cosmic ray flux is put to zero at  $|z| = D$  instead of  $L$ . The transition scale  $d$  is taken very short compared with  $L$  and  $D$ . Moreover,  $K_1$  is taken very large ( $\sim 2000 K_0$ ) to describe a free propagation between  $L$  and  $D$ . Their conclusion is that, in the worst case (*id est* when the boundary  $L$  is near: 1 kpc), the correction to the electron/positron flux is at most 17%. Concerning inverse Compton emission, they concluded that the correction could reach 24% in some directions close to the Galactic centre.

However these corrections drop very fast as  $L$  increases. Recent study by Putze *et alii* [8] seems to favour large values of  $L$  so one could believe this issue can be discarded, but one should keep in mind that all the boron to carbon analyses are done by forcing the flux to vanish at  $|z| = L$ . So using the parameter values found by this study on another propagation model such as the one presented by Perelstein & Shakya [7] is not absolutely consistent. Actually little effect is expected on secondary to primary ratios, because both originate from the Galactic disc however changing boundary condition may actually lead to an overestimation of  $L$ . Hence a more thorough study should be done before concluding, using the same model both for secondary to primary ratios and for dark matter.

## Bibliography

- [1] Bahcall, J. N., Soneira, R. M., & Schmidt, M. 1983, *ApJ*, 265, 730 [216](#)
- [2] Bergström, L., Ullio, P., & Buckley, J. H. 1998, *Astroparticle Physics*, 9, 137 [216](#)
- [3] Caldwell, J. A. R. & Ostriker, J. P. 1981, *ApJ*, 251, 61 [216](#)
- [4] Catena, R. & Ullio, P. 2009, *ArXiv e-prints* [0907.0018](#) [216](#)
- [5] Gates, E. I., Gyuk, G., & Turner, M. S. 1995, *ApJ*, 449, L123+ [216](#)
- [6] Jungman, G., Kamionkowski, M., & Griest, K. 1996, *Phys. Rep.*, 267, 195 [216](#)
- [7] Perelstein, M. & Shakya, B. 2010, *ArXiv e-prints* [1002.4588](#) [217](#)
- [8] Putze, A., Derome, L., & Maurin, D. 2010, *ArXiv e-prints* [1001.0551](#) [217](#)
- [9] Salucci, P., Nesti, F., Gentile, G., & Martins, C. F. 2010, *ArXiv e-prints* [1003.3101](#) [217](#)
- [10] Schmidt, M. 1975, *ApJ*, 202, 22 [216](#)
- [11] Strigari, L. E. & Trotta, R. 2009, *Journal of Cosmology and Astro-Particle Physics*, 11, 19 [216](#)
- [12] Weber, M. & de Boer, W. 2010, *A&A*, 509, A25+ [217](#)
- [13] Widrow, L. M., Pym, B., & Dubinski, J. 2008, *ApJ*, 679, 1239 [216](#)

# Appendix D

## Description of the Milky Way

### D.1 Gas distribution

Describing the Galactic gas distribution is not an easy task. Indeed most of the gas is dark and escape detection. The only way to infer the gas distribution is to detect some tracers and to model the relation between these tracers and the gas density and position.

#### D.1.1 Molecular gas distribution

Most of the Galactic gas is in the form of molecular dihydrogen  $\text{H}_2$ . This gas has not a spectroscopy which allows detection. Indeed, it has no permanent electric dipole moment and is usually very cold in the Galaxy. However it is thought that in most molecular clouds in which  $\text{H}_2$  is, there should also be some carbon monoxide. Because it is very asymmetric (oxygen electronegativity is much larger than the one of carbon) it has many excited states. The transition of lower frequency corresponds to a rotational transition referred to as  $1 \rightarrow 0$  which emits at a frequency of 115 GHz. Making use of  $\text{CO}_{1 \rightarrow 0}$  data collection provided by Dame *et alii* [3], Pohl *et alii* [14] were able to produce a CO Galactic map by deconvolving the emission with a dynamical model of the Milky Way. It is sufficient to look at the Doppler shift of the 115 GHz line to infer the speed of the emitter with respect to the Sun. However to find its distance necessitates velocity distribution modelling of the Galaxy. Pohl *et alii* [14] have shown that a full hydrodynamical simulation helps reducing artefacts, but however, some “finger of God” effects remain. The CO maps are available online<sup>a</sup> and an idea of what they look like can be got from figure D.1.

However, from the point of view of cosmic rays, CO is not very interesting. So we need to convert this data into a molecular hydrogen density instead. In the absence of firm assurance, we need to trust that the abundances of both species are proportional. This proportionality factor is often referred to as the X-factor (or  $X_{\text{CO}}$  which actually refers to the proportionality between 115 GHz emission intensity and  $\text{H}_2$  column density). Its local value is  $1.8 \pm 0.3 \times 10^{20} \text{ cm}^{-2} \text{K}^{-1} \text{km}^{-1} \text{s}$  (see reference [3]), but is believed to vary with distance from the Galactic centre. Indeed, where the star population is important and old, the metallicity is quite high. So using the same factor everywhere in the Galaxy could actually lead to an

---

<sup>a</sup><http://cherenkov.physics.iastate.edu/gas/>

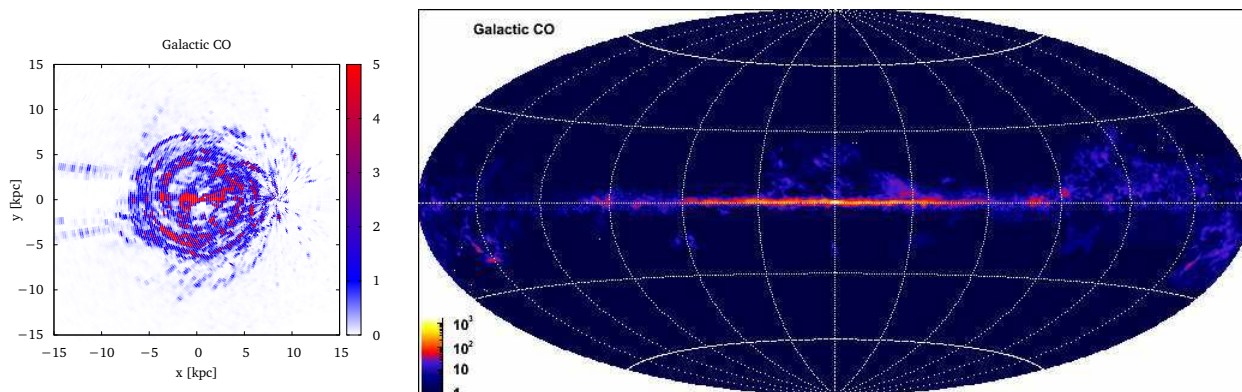


Figure D.1: Carbon monoxide in the Galaxy. *Left*: in the Galactic plan. *Right*: integrated over lines-of-sight from the Earth position.

over-estimation of  $\text{H}_2$  quantity is the Galactic centre and to an under-estimation in the anti-centre. This is a well known fact but its quantification remains an issue, see for instance Strong *et alii* [15].

### D.1.2 Atomic gas distribution

Atomic hydrogen is easier to observe, it has an emission line at 1.4 GHz (or 21 cm) which comes from the transition between the two hyperfine levels of the hydrogen 1s ground state. This line can be used in emission, in absorption or even in self-absorption. Though few recent data exist concerning the Galactic distribution (most of the recent observation focused on extra-galactic observations, see reference [12]).

Using the same method as for the CO, Pohl and Englmaier also produced a HI map which is not public yet but has been kindly given to me for our work on gamma emission. Its appearance is displayed in figure D.2.

Atomic gas is less abundant than molecular gas but populates much higher latitudes so is of utmost importance when dealing with diffuse emission.

### D.1.3 Ionised gas distribution

Ionised hydrogen does not emit nor absorb light, however it is always accompanied by free electrons, which as explained in paragraph D.2 produce Faraday rotation and disperses pulsar light. Using these properties, Cordes & Lazio [2] elaborated a very popular model for HII population in the Galaxy. The Fortran package can be downloaded from their website <sup>b</sup>.

<sup>b</sup><http://tinyurl.com/32t9fk2>

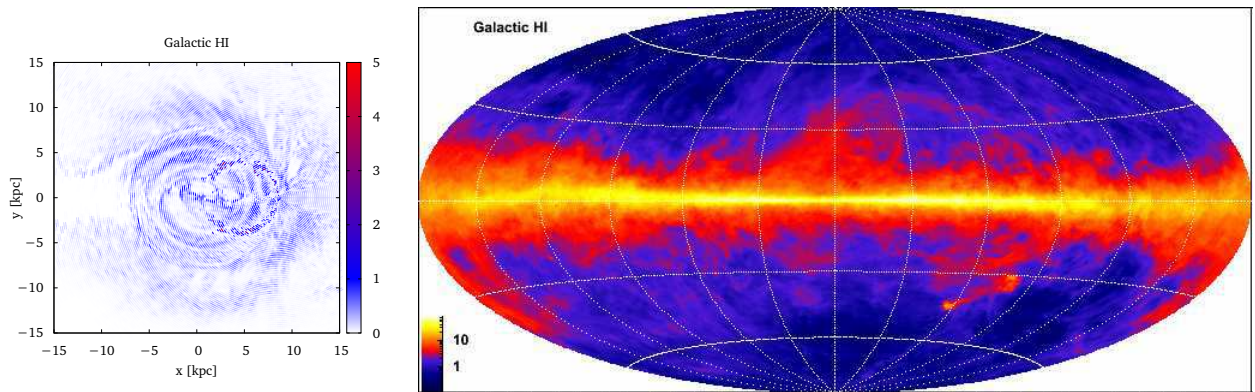


Figure D.2: Atomic hydrogen in the Galaxy. *Left*: in the Galactic plan. *Right*: integrated over lines-of-sight from the Earth position.

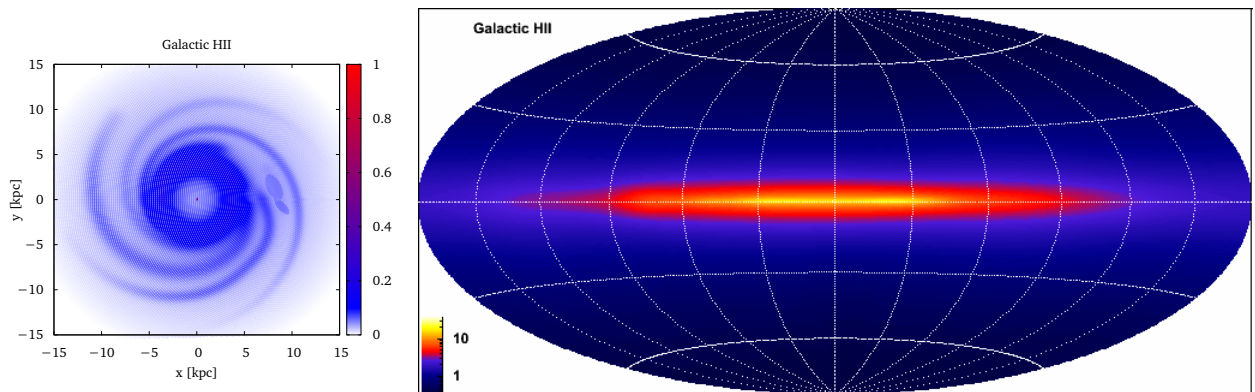


Figure D.3: Ionised hydrogen in the Galaxy. *Left*: in the Galactic plan. *Right*: integrated over lines-of-sight from the Earth position. The void around the Sun position corresponds to a lack of data rather than a real feature.

#### D.1.4 Thin disc approximation

Throughout this work, for proton propagation as well as for secondary electron/positron production, I have used a thin disc approximation. That is, consistently with the model developed and constrained by Maurin *et alii* [11], I have considered that the gas was only in a thin layer of thickness  $2h = 200$  pc with a density of one atom per  $\text{cm}^3$  (0.9 hydrogen and 0.1 helium, in agreement with observations and cosmological predictions). Is this in agreement with the maps presented above?

Table D.1, presents different averages of gas density. It clearly shows that the feature used is incorrect when considering the centre of the Galaxy or the whole Galaxy. However in the Sun vicinity the approximation is correct. Indeed though inside the first 100 pc above and beneath us, the matter is denser than what I have taken as a reference value, it is far from null further. Actually I should have taken  $h = 200$  pc and  $n_H = 0.44 \text{ atom.cm}^{-3}$ , however the

	CO	HI	HII	all
	6.46	0.38	$8.2 \times 10^{-2}$	6.92
$ z  \leq 0.1$ kpc	0.23	0.34	$4.7 \times 10^{-2}$	0.62
	0.17	0.11	$2.5 \times 10^{-2}$	0.30
	4.1	0.28	$6.8 \times 10^{-2}$	4.45
$ z  \leq 0.2$ kpc	0.14	0.27	$4.6 \times 10^{-2}$	0.44
	0.10	0.09	$2.4 \times 10^{-2}$	0.21

Table D.1: Average gas density of each map of this section, and their sum. Either in a layer of 100 pc above and beneath the Galactic plan or 200 pc. For each, the first line correspond the region inside 1 kpc around the Galactic centre, the second line to the region inside 1 kpc around the Sun, and finally the third line corresponds to the full Galaxy ( $r \leq 20$  kpc). All the results are in atom per  $\text{cm}^3$ .

relevant quantity to us is  $2hn_H$ , so actually no large inconsistency has been made there. I have also checked that the density drops very fast in the layer  $200 \text{ pc} \leq |z| \leq 300 \text{ pc}$  to less than  $0.1 \text{ atom.cm}^{-3}$ .

## D.2 The Galactic magnetic field

As very nicely explained by the recent paper by Jaffe *et alii* [6], The Galactic magnetic field can actually be decomposed in three components. The coherent field that varies on very large scales and follows the spiral structure of the Galaxy and the star distribution, the ordered one, that has the same direction as the previous one but has an intensity and a sign which can vary on shorter scales and finally the random/tangled/turbulent field which varies in three dimensions on very short scale.

Various methods exist to size these three components. The first one is to use the synchrotron emission as done for example by Jansson *et alii* [7]. Like explained in section 7.2, propagating cosmic electrons emit synchrotron light, the intensity of which is proportional to the transverse component of the magnetic field with respect to the line-of-sight. Moreover, because synchrotron emission is polarised, it is possible to partially distinguish it from backgrounds such as thermal emission. Though quite useful, this method strongly depends on the cosmic ray model used and this is clearly an issue as large uncertainties affect cosmic ray electron fluxes, some of them due to the Galactic magnetic field. So using magnetic field estimation that rely on electron cosmic ray in order to estimate electron cosmic ray is quite a dangerous game to play and may lead to erroneous results?

Another method uses the Faraday rotation of the linear polarisation of a light source. Free electrons of the ionised gas of the interstellar medium constitute a magnetised plasma which is characterised by a plasma frequency:

$$\nu_p = \sqrt{\frac{e^2 N_e}{4\pi^2 \epsilon_0 m_e}} = 8.98 N_e^{1/2} \text{ Hz},$$

where  $N_e$  is the number of free electron per cubic metre, and a cyclotron frequency (or gyrofrequency), see equation 7.8:

$$\nu_c = \frac{eB}{2\pi m_e} = 2.8B \text{ Hz}, \quad (\text{D.1})$$

where the magnetic field  $B$  is expressed in microGauss. Both frequencies are much less than the typical radio emission. In this medium, electrons propagate by spiral paths about the magnetic field direction. So when an electric excitation, propagating in the same direction as the magnetic field, crosses the medium, right handed and left handed circular polarisations propagate at different speed. When a linearly polarised field crosses the medium, this results in a rotation of its polarisation direction by an angle  $\theta$  which is (see for instance the book of Longair [8] for a detailed proof):

$$\theta = \frac{\pi}{c\nu^2} \int_0^l \nu_p^2 \nu_{c\parallel} dl = 8.12 \times 10^3 \lambda^2 \int_0^l N_e B_{\parallel} dl, \quad (\text{D.2})$$

where  $\nu$  and  $\lambda$  correspond to the frequency and the wavelength of the radio emission and  $B_{\parallel}$  is the magnetic field parallel to the line-of-sight. The quantity  $\theta/\lambda^2$  is often referred to as the *rotation measure* (RM). This quantity leads to the magnetic field but requires a model of the electron density. As explained by Beck *et alii* [1], if electron and magnetic field fluctuations are correlated, this can lead to large errors. An almost model independent measurement is however possible by looking at pulsars. Pulsar emission is highly polarised so rotation measure can be done easily, but because it is a pulsed emission, a dispersion measure is also possible. The group velocity of light in a plasma is given by:

$$v_{gr} = c \sqrt{1 - \left(\frac{\nu_p}{\nu}\right)^2}.$$

At typical radio wavelength ( $\nu \gg \nu_p$ ), this translates into an arrival time of the pulse  $T_a$  equal to:

$$T_a = \int_0^l \frac{dl}{v_{gr}} = 4.15 \times 10^9 \frac{1}{\nu^2} \int_0^l N_e dl. \quad (\text{D.3})$$

Combining both measurements, it is possible to reduce the model dependence with respect to electron distribution over the line-of-sight. Of course if more than one pulsar, with various known distance are on nearby lines-of-sight, then the measure becomes very precise.

Both methods are quite easy to deal with when interested in the coherent component of the magnetic field. However things get a little more complex when working with the ordered and the random fields. Sizing these components requires to compare the various measurements (for instance a low polarisation of a strong synchrotron emission is considered as a probe of a strong random magnetic field). A more detailed discussion can be found in reference [6]. This discussion is summed up in table D.2.

In fact other methods also exist (Zeeman splitting of 21-cm line radiation, polarised dust emission) but present either observational or model bias. Using a Markov Chain Monte Carlo analysis of the available data concerning the quantities of table D.2, Jaffe *et alii* [6] were able to give a 2-D description of the magnetic field of the Galactic plan. The average values they

Methods	Faraday rotation (FR)	$\sigma_{\text{FR}}$	Synchrotron intensity (I)	Synchrotron polarised emission intensity (PI)	$\sigma_{\text{PI}}$
Coherent	$\parallel$	$\emptyset$	$\perp$	$\perp$	$\emptyset$
Ordered	$\emptyset$	$\parallel$	$\perp$	$\perp$	$\emptyset$
Random	$\emptyset$	1	1	$\emptyset$	1

Table D.2: Measurements methods for each magnetic field component.  $\emptyset$  means that the method is not suited to measure this component, 1 means it is,  $\parallel$  means that the method probes only the component of the magnetic field which is parallel to the line-of-sight,  $\perp$  means that it probes only the perpendicular component

found for the three components (Coherent: C; Ordered: O; Random: R) are:

$$\begin{aligned}\langle B_C \rangle &= 1 - 3\mu\text{G} \\ \sqrt{\langle B_O^2 \rangle} &= 0.0 - 3.3\mu\text{G} \\ \sqrt{\langle B_R^2 \rangle} &= 2.1 - 4.2\mu\text{G}\end{aligned}$$

which lead to a quadratic sum of  $\langle B \rangle = 2.3 - 6.1 \mu\text{G}$ . However these results concern the Galactic plan only. The full spatial description they give is displayed in figure D.4. Many works (see for instance Jansson *et alii* [7] who also review other vertical dependences) suggest an exponential decrease of the magnetic field with distance from the Galactic plan  $z$  rather abrupt with a typical scale of order 1 kpc. Averaging over the diffusion zone, this leads to a value of  $0.87 \mu\text{G} \leq \langle B \rangle \leq 2.29 \mu\text{G}$ , which is in good agreement with the upper limit of  $1 \mu\text{G}$  set by Mao *et alii* [10] and used throughout this thesis.

### D.3 Determining the distance of the Sun to the Galactic centre

There are various methods to determine the value of the distance of the Sun to the Galactic centre  $R_\odot$ .

Using proper motion of stars in the Galactic centre region, Ghez *et alii* [4] found a value of  $R_\odot = 8.4 \pm 0.4$  kpc. Using the same method Gillessen *et alii* [5] gave a little more precise result of  $R_\odot = 8.33 \pm 0.35$  kpc.

Making use of recent measurements of parallax, proper motion and line-of-sight velocity of 18 masers, McMillan & Binney [13] showed that the value depends dramatically on the model used for the rotation curve, they hence found that  $R_\odot$  ranges between  $6.7 \pm 0.5$  kpc and  $8.9 \pm 0.9$  kpc.

Using the reddening of RR Lyrae variable stars in the Galactic bulge, Majaess [9] estimated  $R_\odot$  to be  $8.1 \pm 0.6$  kpc. With this method, the errors are due to poor knowledge of light

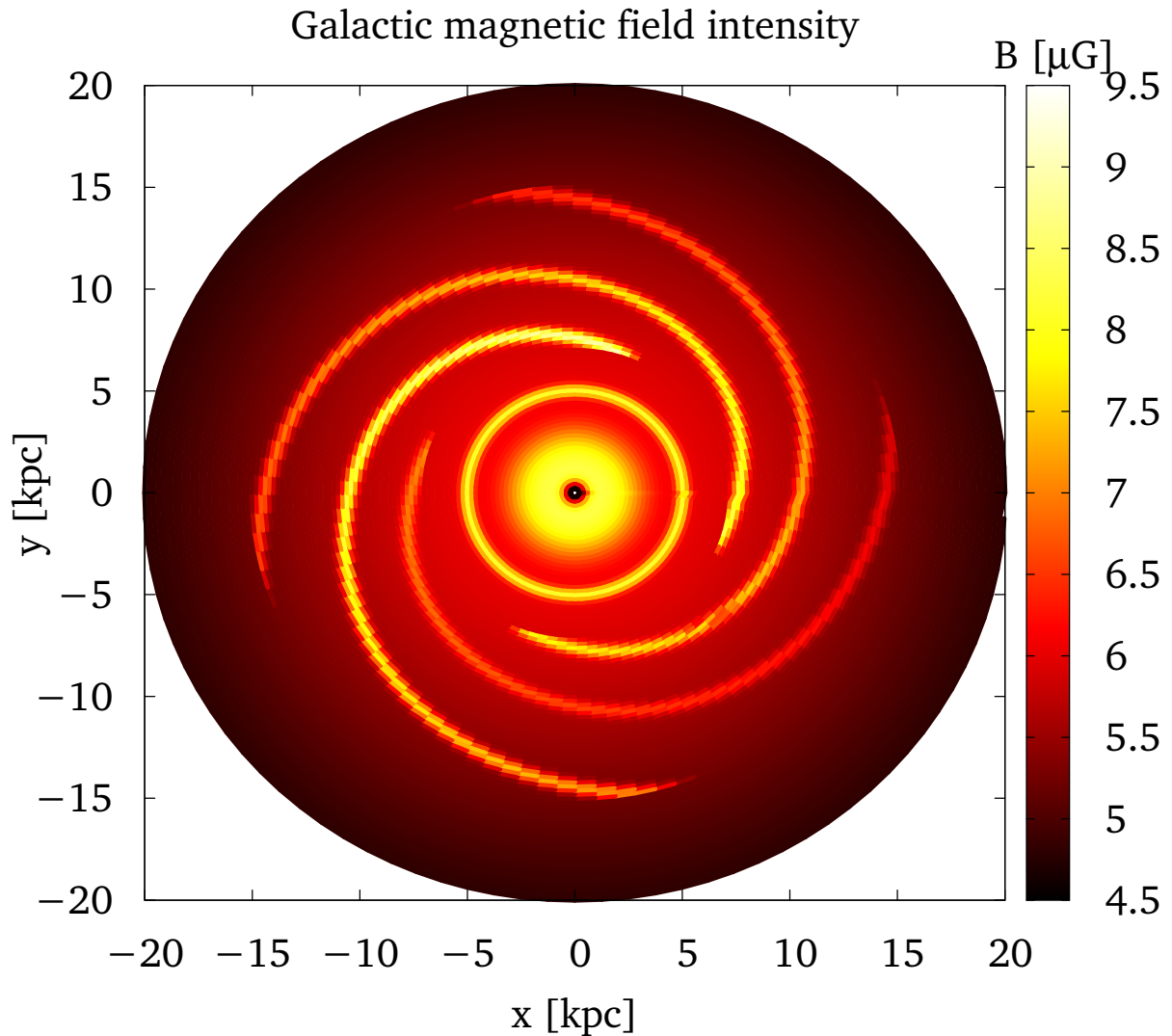


Figure D.4: Absolute value of the Galactic magnetic field, in the plan as in the work of Jaffe *et alii* [6]

extinction and the relation between the distance between a group of star and the Galactic center.

It is surprising to see that such a dramatic astrophysical parameter still suffers such large uncertainties. How does this uncertainty translates into cosmic ray fluxes uncertainty?

The problem is that  $R_{\odot}$  comes into play in many steps of the estimation, from the source distribution functions, to the diffusion boundary conditions but also, when interested in  $\gamma$  rays,

in the gas distributions described above.

## Bibliography

- [1] Beck, R., Shukurov, A., Sokoloff, D., & Wielebinski, R. 2003, *A&A*, 411, 99 [223](#)
- [2] Cordes, J. M. & Lazio, T. J. W. 2002, ArXiv e-prints [astro-ph/0207156](#) [220](#)
- [3] Dame, T. M., Hartmann, D., & Thaddeus, P. 2001, *ApJ*, 547, 792 [219](#)
- [4] Ghez, A. M., Salim, S., Weinberg, N. N., *et alii* . 2008, *ApJ*, 689, 1044 [224](#)
- [5] Gillessen, S., Eisenhauer, F., Trippe, S., *et alii* . 2009, *ApJ*, 692, 1075 [224](#)
- [6] Jaffe, T. R., Leahy, J. P., Banday, A. J., *et alii* . 2010, *MNRAS*, 401, 1013 [222](#), [223](#), [225](#)
- [7] Jansson, R., Farrar, G. R., Waelkens, A. H., & Enßlin, T. A. 2009, *Journal of Cosmology and Astro-Particle Physics*, 7, 21 [222](#), [224](#)
- [8] Longair, M. S. 1994, *High energy astrophysics. Vol.2: Stars, the galaxy and the interstellar medium*, ed. Longair, M. S. [223](#)
- [9] Majaess, D. 2010, *Acta Astronomica*, 60, 55 [224](#)
- [10] Mao, S. A., Gaensler, B. M., Haverkorn, M., *et alii* . 2010, *ApJ*, 714, 1170 [224](#)
- [11] Maurin, D., Donato, F., Taillet, R., & Salati, P. 2001, *ApJ*, 555, 585 [221](#)
- [12] McClure-Griffiths, N. M. 2004, in *Astronomical Society of the Pacific Conference Series, Vol. 317, Milky Way Surveys: The Structure and Evolution of our Galaxy*, ed. D. Clemens, R. Shah, & T. Brainerd, 3–+ [220](#)
- [13] McMillan, P. J. & Binney, J. J. 2010, *MNRAS*, 402, 934 [224](#)
- [14] Pohl, M., Englmaier, P., & Bissantz, N. 2008, *ApJ*, 677, 283 [219](#)
- [15] Strong, A. W., Moskalenko, I. V., Reimer, O., Digel, S., & Diehl, R. 2004, *A&A*, 422, L47 [220](#)



**ABSTRACT :** This thesis is dedicated to the study of propagation of cosmic electrons and positrons in the Milky Way and to the indirect detection of dark matter.

The existence of dark matter is a hypothesis considered as reasonable from the point of view of cosmology, astrophysics and even particle physics. Nevertheless its detection still eludes us and it is not possible to verify this hypothesis by other means than gravitational one. A possible way to detect dark matter is to look for its annihilation or decay products among Galactic cosmic rays.

During the last three years, data concerning cosmic ray electrons and positrons have been accumulated and have reached a remarkable precision. Such a precision requires from us to refine the theoretical models and to quantify the errors.

This thesis addresses the study of all the sources of uncertainties affecting predictions of cosmic electrons and positron fluxes, primary and secondary, classical or from exotic origin. The greatest care has been dedicated to the sources and the propagation in the Galactic halo. Moreover a study of  $\gamma$  and radio emissions associated to these cosmic rays is presented, again with the will of sizing uncertainties. Finally a status of the research for detection of annihilation or decay of Galactic dark matter is presented.

---

**RÉSUMÉ :** Cette thèse est dédiée à l'étude de la propagation des électrons et positrons cosmiques dans la Voie Lactée ainsi qu'à la détection indirecte de matière sombre.

L'existence de la matière sombre dans l'Univers est une hypothèse raisonnable du point de vue de la cosmologie, de l'astrophysique mais également de la physique des particules. Pourtant sa détection nous échappe encore et il n'est pas possible de vérifier la validité de cette hypothèse autrement que par des moyens faisant intervenir la gravitation. L'une des voies possibles pour la détection de la matière sombre et la compréhension de ses propriétés, consiste à chercher les produits de son annihilation ou de sa désintégration dans les rayons cosmiques Galactiques.

Durant ces trois dernières années, les données concernant les flux d'électrons et de positrons cosmiques se sont accumulées et ont atteint des précisions remarquables. Une telle précision expérimentale exige que l'on raffine les modèles théoriques et que l'on quantifie les erreurs.

Cette thèse s'efforce donc de recenser et de quantifier toutes les sources d'incertitudes des prédictions de flux d'électrons et de positrons cosmiques, qu'ils soient primaires ou secondaires, classiques ou exotiques. La plus grande attention a été portée sur les sources et la propagation dans le halo Galactique. De plus, une étude des émissions  $\gamma$  et radio associées à ces rayons cosmiques est présentée, toujours avec la même volonté de mesurer les incertitudes. Enfin, un état des lieux de la recherche de détection de l'annihilation ou de la désintégration de la matière sombre galactique est présenté.

---

**RIASSUNTO :** Questa tesi è dedicata allo studio della propagazione degli elettroni e positroni cosmici nella Via Lattea e alla rivelazione indiretta della materia oscura.

L'esistenza della materia oscura nell'Universo è un'ipotesi importante sia dal punto di vista della cosmologia e dell'astrofisica, sia della fisica delle particelle. Tuttavia la rivelazione della materia oscura ancora ci sfugge, se non attraverso i suoi effetti gravitazionali. Un possibile metodo per rilevare la materia oscura e di capirne le sue proprietà, è di cercare i prodotti della sua annichilazione o decadimento nei raggi cosmici galattici.

Nel corso degli ultimi tre anni, sono stati accumulati molti nuovi dati sui flussi di elettroni e positroni cosmici e le nuove misure hanno cominciato a mostrare dettagli importanti. Le nuove precisioni sperimentali richiedono un miglioramento dei modelli teorici e la determinazione delle loro incertezze.

Questa tesi mira pertanto ad individuare e quantificare tutte le fonti di incertezza nelle previsioni del flusso di elettroni e positroni cosmici, sia primari che secondari, standard o esotici. Molta attenzione è stata rivolta alle sorgenti e alla propagazione nell'alone galattico. Inoltre, viene presentato anche uno studio delle emissioni gamma e radio, sempre nell'ottica di studiarne le incertezze teoriche. Infine, viene discussa una panoramica sulle ricerche per individuare l'annichilazione o il decadimento della materia oscura nell'alone della nostra Galassia.